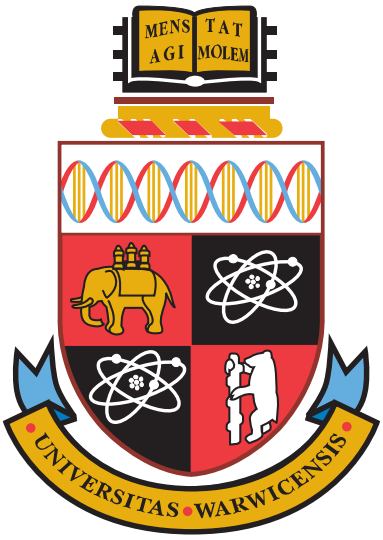

Eclipsing white dwarf binaries

by

Steven Gary Parsons

Thesis

Submitted to the University of Warwick

for the degree of

Doctor of Philosophy

Department of Physics

January 2012

THE UNIVERSITY OF
WARWICK

Contents

List of Tables

List of Figures

Acknowledgments

I am extremely grateful to Prof. Tom Marsh for his support and guidance throughout my PhD. His ability to clearly explain any aspect transformed me from a graduate student into a researcher. His door was always open and I've lost count of the number of hours we've spent discussing various topics.

I thank Prof. Boris Gänsicke, Dr. Chris Copperwheat and Stelios Pyrzas for a great number of enlightening discussions over the years. I would also like to thank the entire ULTRACAM team, particularly Prof. Vik Dhillon, for giving me the opportunity to use ULTRACAM and their trust in leaving it in my hands! There have been several occasions when I've had to call Vik in the middle of the night with some sort of problem and he was always able to solve it.

Finally, I thank my parents for giving me the opportunity to pursue a life of learning, and my examiners Peter Wheatley and Martin Barstow for helping improve the quality of this thesis.

Declarations

I, Steven Parsons, hereby declare that this thesis has not been submitted in any previous application for a higher degree. This thesis represents my own work, except where references to other works are given. The following Chapters are based on refereed publications that I have submitted during my period of study:

Chapter 3 is based on: Parsons S. G., Marsh T. R., Copperwheat C. M., Dhillon V. S., Littlefair S. P., Gänsicke B. T. and Hickman R., "Precise mass and radius values for the white dwarf and low mass M dwarf in the pre-cataclysmic binary NN Serpentis", MNRAS, 402, 2591 (2010).

Chapter 4 is based on: Parsons S. G., Marsh T. R., Gänsicke B. T., Dhillon V. S., Copperwheat C. M., Littlefair S. P., Pyrzas S., Drake A. J., Koester D., Schreiber M. R. and Rebassa-Mansergas A., "The shortest period detached white dwarf + main-sequence binary", MNRAS, 419, 304 (2012).

Chapter 5 is based on: Parsons S. G., Marsh T. R., Gänsicke B. T., Rebassa-Mansergas A., Dhillon V. S., Littlefair S. P., Copperwheat C. M., Hickman R. D. G., Burleigh M. R., Kerry P., Koester D, Nebot Gómez-Morán A., Pyrzas S., Savoury C. D. J., Schreiber M. R., Schmidtobreick L, Schwope A. D., Steele P. R. and Tappert C., "A precision study of two eclipsing white dwarf plus M dwarf binaries", MNRAS, 420, 3281 (2012).

Chapter 6 is based on: Parsons S. G., Marsh T. R., Gänsicke B. T., Drake A. J. and Koester D., "A Deeply Eclipsing Detached Double Helium White Dwarf Binary" ApJ, 735, L30 (2011).

Chapter 7 is based on: Parsons S. G., Marsh T. R., Copperwheat C. M., Dhillon V. S., Littlefair S. P., Hickman R. D. G., Maxted P. F. L., Gänsicke B. T.,

Unda-Sanzana E., Colque J. P., Barraza N., Sánchez N. and Monard L. A. G., "Orbital period variations in eclipsing post-common-envelope binaries", MNRAS, 407, 2362 (2010).

Abstract

Recent years have seen an explosion in the number of eclipsing binaries containing white dwarfs. In the last few years the number of systems has increased from 7 to over 40, thanks mainly to large surveys such as the Sloan Digital Sky Survey and the Catalina Sky Survey. Many of these systems are survivors of the common envelope phase during which the two stars orbit within a single envelope which is rapidly thrown off through loss of energy and angular momentum. Detailed analysis of these systems can yield extremely precise physical parameters for both the white dwarf primary and its companion star. Stellar masses and radii are some of the most fundamental parameters in astronomy and can be used to test models of stellar structure and evolution. They can also be used to constrain the evolutionary history of the binary system offering us the chance to better understand the common envelope phase itself.

In this thesis I present high-precision studies of several eclipsing post common envelope binaries. I use a combination of high-speed photometry and high-resolution spectroscopy to measure the masses and radii of both stars in each system. I compare these results to evolutionary models and theoretical mass-radius relations and find that, on the whole, the measured masses and radii agree well with models. However, the main-sequence companion stars are generally oversized compared to evolutionary models, although this deviation is much less severe at very low masses ($\lesssim 0.1\,\mathrm{M}_{\odot}$). I also find that the measured masses and radii of carbon-oxygen core white dwarfs are in excellent agreement with theoretical models. Conversely, the first ever precision mass-radius measurement of a low-mass helium core white dwarf appears undersized compared to models.

Large scale surveys have also begun to identify double white dwarf eclipsing binaries. In this thesis I present a study of one of these systems and show the potential, as a double-lined spectroscopic binary, of measuring precise parameters for both stars in the future.

Finally, I show that the mid-eclipse times of eclipsing binaries containing white dwarfs can be measured to a high enough precision that we can monitor them for evidence of period changes. I find that many systems show complex variations in their eclipse times and in many cases the only mechanism able to produce these changes is one or more sub-stellar objects in orbit around the binary. However, I show that care must be taken when attempting to detect planets in binary systems using eclipse timings.

Chapter 1

Introduction

1.1 Prelude

The night sky has been used for thousands of years as a calender and navigational tool. In ancient Persia it was also used as an eye test. Mizar, one of the brightest stars in the Plough, has a faint partner named Alcor. The two stars appear virtually indistinguishable except to those with perfect eyesight. These two stars were in fact the first binary stars ever known (a recent study by Mamajek et al. 2010 has shown that these stars actually form part of a sextuplet system). We now know that most stars are part of binary or multiple systems (Iben, 1991). The majority of these stars are sufficiently separated from each other that they will never interact and will evolve in the same manner as an isolated star of the same mass.

Around 25% of binary systems have stars that are close enough to each other that they will interact at some point in their evolution (Willems & Kolb, 2004). This interaction is caused by one or both of the stars filling its Roche lobe and causing material to flow from one star to the other. This process can often lead to a common-envelope (CE) phase. The CE phase gives birth to very close binaries and is thought to lead to the creation of some of the Galaxy's most exotic objects, such as cataclysmic variables (CVs), low-mass X-ray binaries, B-type subdwarfs (sdB stars), double degenerates, short gamma ray burst (GRB) progenitors and millisecond pulsars. The result of binary evolution can affect the global properties of stellar populations, for instance through the iron generated in Type Ia explosions, or the sdB stars responsible for the UV upturn of elliptical galaxies (Han et al., 2007).

Amongst the most common by-products of binary evolution are binaries containing white dwarfs. The most well-known of these are the accreting CVs, but there are much larger populations of detached double white dwarf binaries and white dwarf

plus main-sequence star systems. A small number of these systems are inclined in such a way that, as viewed from Earth, they exhibit eclipses. These detached eclipsing binaries are a primary source of accurate physical properties of stars and stellar remnants. A combination of modeling their light curves and measuring the radial velocities of both components allows us to measure masses and radii to a precision of better than 1 per cent (e.g. Andersen 1991; Southworth et al. 2005; Southworth et al. 2007; Torres et al. 2010). These measurements are crucial for testing theoretical mass-radius relations, which are used in a wide range of astrophysical circumstances such as inferring accurate masses and radii of transiting exoplanets, calibrating stellar evolutionary models and understanding the late evolution of mass transferring binaries such as cataclysmic variables (Littlefair et al. 2008; Savoury et al. 2011). Additionally, the mass-radius relation for white dwarfs has played an important role in estimating the distance to globular clusters (Renzini et al., 1996) and the determination of the age of the galactic disk (Wood, 1992).

Although ubiquitous in the solar neighborhood, the fundamental properties of low-mass M dwarfs are not as well understood as those of more massive stars (Kraus et al., 2011). There is disagreement between models and observations, consistently resulting in radii up to 15 per cent larger and effective temperatures 400K or more below theoretical predictions (Ribas 2006; López-Morales 2007). These inconsistencies are not only seen in M dwarf eclipsing binaries (Bayless & Orosz 2006; Kraus et al. 2011) but also in field stars (Berger et al. 2006; Morales et al. 2008) and the host stars of transiting extra-solar planets (Torres, 2007).

The mass-radius relation for white dwarfs is all but untested observationally. Double white dwarf eclipsing binaries potentially allow extremely precise measurements of white dwarf masses and radii but have only recently been discovered and high precision studies of these systems have yet to be performed. Provencal et al. (1998) used *Hipparcos* parallaxes to determine the radii for white dwarfs in visual binaries, common proper-motion (CPM) systems and field white dwarfs. However, the radius measurements for all of these systems still rely to some extent on model atmosphere calculations. For field white dwarfs the mass determinations are also indirect. Wide, visual binaries containing white dwarfs are a potential source of independent mass-radius measurements. Using *Hubble Space Telescope*/STIS spectra, Barstow et al. (2005) were able to measure the gravitational redshift of the white dwarf in Sirius B (hence the ratio of its mass and radius). They combined this with measurements of its parallax (providing the white dwarf radius) and a model atmosphere analysis of its spectrum in order to find a consistent solution. This approach is less dependent on the white dwarf mass-radius relation, hence providing a test

of it. However, in this case, it is only the gravitational redshift measurement that gives a truly independent mass-radius measurement, since the white dwarf radius determined from its parallax and the spectral modeling still rely to some extent on white dwarf models, and hence the mass-radius relation, therefore this approach is less direct when it comes to testing white dwarf mass-radius relations.

The small size of white dwarfs (roughly Earth-sized) means that the eclipse features are short and sharp. These allow us to measure extremely precise eclipse times. Accurate eclipse timings can reveal period changes; long term period decreases are the result of genuine angular momentum loss from the binary, however, shorter timescale period modulation can be the result of many different mechanisms (see section 1.3). Orbital period variations can give us insights into binary evolution.

This thesis presents high precision studies of eclipsing white dwarf binaries, the main aim being to measure precise model-independent parameters for both stars in the binary. The same data produce very accurate eclipse times which are analysed in search of period changes.

1.2 Binary star evolution

If two stars form a binary system, then their individual evolution may be affected by their companion. The combination of the gravitational potential of each star and the centrifugal potential create the potential of the system, known as the Roche geometry. Close to a star the equipotential surfaces are spherical and material is bound to the star. Further out the influence of the other star distorts the shape of the surfaces. The largest closed equipotential surface of each star is known as its Roche lobe. The lines of Roche equipotential depend only upon the mass ratio, $q = M_1/M_2$, with the scale being set by a, the orbital separation (Warner, 1995), an example of this is shown in Figure 1.1 for a binary with a mass ratio of 0.2.

If the surface of both stars are well within their Roche lobes then they will remain spherical. However, as a star grows larger in radius it will begin to distort to match the equipotentials of its Roche lobe. The star becomes "pear" shaped and points towards its companion. If the star's radius exceeds its Roche lobe then material will be transferred from the Roche lobe filling star to its companion via the inner Lagrangian point (L_1) and mass transfer can being.

If both stars are within their Roche lobes then the binary is considered to be detached. If one component fills its Roche lobe, but not the other, then the binary is semi-detached. If both stars fill their Roche lobes then the binary is a contact binary. An approximate formula (accurate to better than 1%) for the radius of a

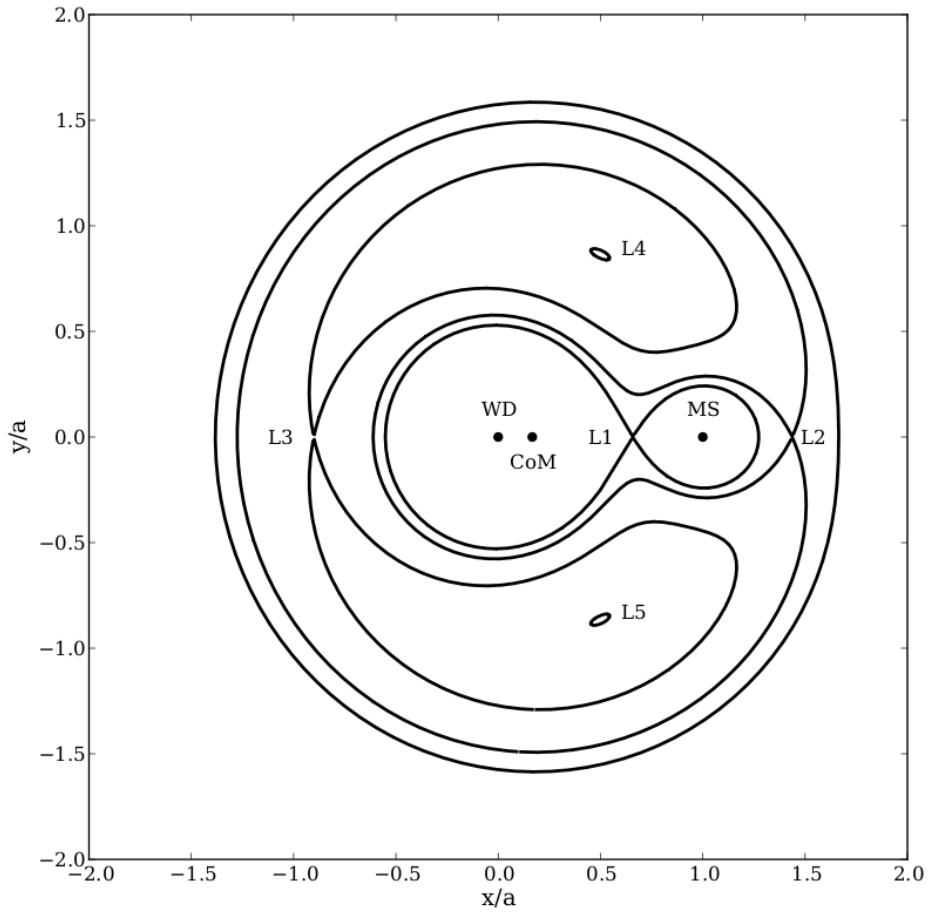

Figure 1.1: A cross section in the orbital plane of a binary with a mass ratio of 0.2, depicting the equipotential surfaces of the Roche geometry. The positions of the white dwarf (WD) and secondary star (MS) are shown as well as the centre of mass (CoM) and the five Lagrangian points (the points at which an object will be theoretically at rest relative to the two stars). The Inner Lagrangian point L_1 lies between the two masses. For the two outer Lagrangian points, L_2 lies behind the smaller mass, on the line determined by the two masses, and L_3 lies behind the larger mass. L_4 and L_5 are positioned at the vertical corners of the two equilateral triangles with as shared base the line between the centres of the two stars, with L_4 leading the motion of the orbit and L_5 lagging behind. The x and y axes are labeled in units of the binary separation a.

sphere containing the same volume as the Roche lobe is (Eggleton, 1983)

$$\frac{R_L}{a} = \frac{0.49\,q^{2/3}}{0.6\,q^{2/3} + \ln\left(1 + q^{1/3}\right)}. \tag{1.1}$$

When the more massive member of a binary system departs from the main sequence and begins to expand, its surface may expand beyond its Roche lobe and material will be transferred to the less massive star. However, in this case material is moving from the more massive star to the less massive one and is therefore gaining angular momentum as it moves away from the centre of mass. To conserve angular momentum the binary separation must decrease, but this also leads to a reduction in the size of the Roche lobe by Equation 1.1.

If the donor has developed a deep convective envelope it can be approximated by a polytrope of index 1.5. In this case the mass-radius relation is $R \propto M^{-1/3}$, hence its radius will expand in response to rapid (adiabatic) mass loss. This decreases the timescale for mass transfer which will be well below the thermal timescale for the companion, even if it is a main-sequence star of comparable mass to the initial mass of the donor (Iben & Livio, 1993). The companion is unable to readjust quickly enough to the additional mass and the accreted material simply piles up into a hot blanket on its surface until it too fills its Roche lobe, at which point a common envelope (CE) develops.

The envelope itself may not necessarily be rotating with the binary and therefore both stars will experience a drag force. This force causes the two stars to spiral inwards. The energetics that result in the ejection of the envelope of material are uncertain (Iben & Livio, 1993). However, a certain fraction of the orbital energy of the binary will be used to eject the common envelope. The parameter usually used to describe this is $\alpha_{\rm CE}$ (Webbink, 1984; de Kool et al., 1987; de Kool, 1992):

$$\frac{GM_i(M_i - M_c)}{R_i} = \alpha_{\rm CE}\lambda\left(\frac{GM_cM_2}{2a_f} - \frac{GM_iM_2}{2a_i}\right), \tag{1.2}$$

where λ is a parameter dependent upon the structure of the star, usually assumed to be constant, e.g. $\lambda = 0.5$ (de Kool et al., 1987). M_i and R_i are the mass and radius of the star at the start of mass transfer, M_c is the core mass of the giant, M_2 is the companion star mass and a_i and a_f are the separation of the two stars before and after the common envelope phase. A value of $\alpha_{\rm CE}$ near unity implies that the envelope was ejected efficiently, causing a small change in the separation of the two stars. A lower value leads to much shorter period binaries; Zorotovic et al. (2010) find that $\alpha_{\rm CE} = 0.2 - 0.3$ can be used to successfully reconstruct

the current population of post common envelope binaries (PCEBs). The common envelope phase is thought to last < 1000 years.

The core composition of the white dwarf that emerges from the CE phase depend upon the evolutionary status of the progenitor star. If the progenitor had not started helium burning then the white dwarf will have a He core with $M_{\rm WD} \lesssim 0.5\,{\rm M}_{\odot}$. If helium burning was achieved then most of the helium would have been converted to carbon and oxygen and the white dwarf will have a C/O core with a mass of $0.5\,{\rm M}_{\odot} \lesssim M_{\rm WD} \lesssim 1.1\,{\rm M}_{\odot}$. For the most massive white dwarfs ($1.1\,{\rm M}_{\odot} \lesssim M_{\rm WD} \lesssim 1.38\,{\rm M}_{\odot}$) the progenitor would have been able to convert most of the C/O to O/Ne and thus the white dwarf will have a O/Ne core.

1.2.1 Post common envelope binaries

Once the common envelope has been expelled the tightly bound binary is revealed containing the core of the giant, which will become a white dwarf, and its main-sequence companion. These binaries have periods of up to a few days.

Until recently only a handful of PCEBs (~ 30) where known (see the catalogue of Schreiber & Gänsicke, 2003). This has now changed thanks mainly to the Sloan Digital Sky Survey (SDSS, York et al. 2000). A dedicated search for white dwarf plus main-sequence binaries in the SDSS spectroscopic survey yielded more than 1600 systems (Rebassa-Mansergas et al., 2007, 2010), of which roughly a third are PCEBs (Schreiber et al., 2008), based on radial velocity variations. The majority of these systems contain low-mass, late-type M dwarfs, while a large percentage of the white dwarfs are also of low mass (Rebassa-Mansergas et al., 2011). The sample of PCEBs has been further increased by long term photometric surveys such as the Catalina Sky Survey (CSS, Drake et al. 2009), which has identified over a dozen new eclipsing systems (Drake et al., 2010), and the Palomar Transient Factory (PTF, Law et al. 2009), which has also found several eclipsing systems with very dominant main-sequence stars (Law et al., 2011).

The two stars in a PCEB will slowly spiral towards each other via the loss of angular momentum (see Section 1.3). Eventually they will get close enough that the companion will start transferring mass onto the white dwarf, forming a CV. Those PCEBs that will reach this stage within a Hubble time are known as Pre-CVs (Schreiber & Gänsicke, 2003).

1.2.2 Double white dwarf binaries

Double white dwarf binaries (DWDs) share a similar evolutionary history to PCEBs. DWDs can be split into two groups which have different properties: the detached and semi-detached DWDs. In most cases DWDs are the result of a second common envelope phase, although an alternative channel for the formation of semi-detached DWDs involves a normal CV in which the mass transfer started from a donor close to the end of core hydrogen burning. In this case, mass transfer uncovers the helium-rich core of the donor and allows the system to avoid the classical period minimum of CVs at about 80 min (Solheim, 2010).

Detached DWDs are simple pairs of white dwarfs slowly spiraling towards each other under the influence of gravitational radiation. The semi-detached DWDs, known as AM CVn stars (see Solheim, 2010, for a recent review), are systems where mass is transferred from a Roche lobe filling hydrogen-deficient star to its more massive white dwarf companion. This mass transfer is stable and AM CVn binaries can reach very short periods, e.g. HM Cnc which has an orbital period of only 5.4 minutes (Israel et al., 2002; Roelofs et al., 2010).

Binary population synthesis studies predict that there are of order 100–300 million detached DWDs in the Galaxy (Han, 1998; Nelemans et al., 2001; Liu et al., 2010; Yu & Jeffery, 2010). They are likely to be the dominant source of background gravitational waves detectable by the proposed space-based gravitational wave interferometer, *LISA* (Hils et al., 1990). The loss of orbital angular momentum via gravitational radiation in these systems will eventually bring the two white dwarfs into contact with one another. Those that achieve this within a Hubble time are possible progenitors of AM CVn binaries, R CrB stars and Type Ia supernovae (Iben & Tutukov, 1984). The coalescence of two low-mass, helium core white dwarfs is also a possible formation channel for the creation of single sdB stars (Webbink, 1984); indeed it may be one of the more important sdB formation channels (Han et al., 2003).

Despite their importance as possible Type Ia supernovae progenitors, very few detached DWDs were known until the 1990s. This is because they are extremely difficult to find, since they appear very similar to single white dwarfs. However, advances in modeling white dwarf spectra lead to the discovery of white dwarfs with masses too low to have formed from single star evolution (Bergeron et al., 1992). Since this work the number of detached DWDs has grown steadily and there are currently ~ 50 systems known (Kilic et al. 2011; Marsh 2011 and references therein). Until recently there were no known eclipsing detached DWDs. This has changed in the last year or so with the discovery of four eclipsing systems by Steinfadt et al.

(2010), Brown et al. (2011) and Vennes et al. (2011b) and an additional system presented in this thesis (Chapter 6).

1.3 Period change mechanisms

Angular momentum loss drives the evolution of close binary stars. For short period systems (< 3 hours) gravitational radiation (Kraft et al. 1962; Faulkner 1971) dominates whilst for longer period systems (> 3 hours) a magnetised stellar wind can extract angular momentum, the so-called magnetic braking mechanism (Verbunt & Zwaan 1981; Rappaport et al. 1983). Accurate eclipse timings can reveal period changes; long term period decreases are the result of angular momentum loss, however, shorter timescale period modulation can be the result of internal processes within the main sequence star, such as Applegate's mechanism (Applegate 1992; see Section 1.3.3), or possible light travel time effects caused by the presence of a third body. Therefore, accurate eclipse timings of binaries can test theories of angular momentum loss as well as theories of stellar structure and potentially identify low mass companions. In this section I summarise the main mechanisms that can produce variations in the observed arrival time of eclipses.

1.3.1 Gravitational radiation

Angular momentum is lost from a binary system via gravitational radiation. The rate of angular momentum loss due to gravitational radiation was presented by Peters & Mathews (1963):

$$\frac{dJ}{dt} = -\frac{32}{5}\frac{G^{7/2}}{c^5}a^{-7/2}M_1^2M_2^2M^{1/2}\,\mathrm{J}, \tag{1.3}$$

where a is the orbital separation, M_1 and M_2 are the primary and secondary star masses and M is the total mass ($M_1 + M_2$).

The relatively low masses of both stars in PCEBs mean that only a very small amount of angular momentum is lost via this mechanism. However, it does affect all binary systems and in some cases (e.g. the detached double white dwarf binaries) is the only mechanism that removes angular momentum from the system.

1.3.2 Magnetic braking

In the magnetic braking mechanism, charged particles from the main sequence star are trapped within its magnetised wind and forced to co-rotate with it. By dragging these particles around, the star transfers angular momentum to them slowing

down its rotation. In close binaries the rotational and orbital periods have become synchronised meaning that the angular momentum is taken from the binary orbit causing the period to decrease. In the disrupted magnetic braking model this process ceases in very low mass stars ($M \lesssim 0.3\mathrm{M}_{\odot}$) as it is hypothesised that they become fully convective in this mass regime and hence the magnetic field is no longer rooted to the stellar core. This model was proposed to explain the cataclysmic variable period gap (a dearth of systems with periods between 2 and 3 hours). At periods of around 3 hours the secondary star becomes fully convective and hence magnetic braking ceases, this reduces the mass transfer rate and eventually causes the donor to shrink back to within its Roche lobe, stopping mass transfer. During this time the period loss is driven solely by gravitational radiation until the secondary star touches its Roche lobe again at a period of around 2 hours. However, it is still unclear how the angular momentum loss changes over the fully convective boundary (Andronov et al., 2003).

Verbunt & Zwaan (1981) calculated the angular momentum loss rate due to magnetic braking to be

$$\frac{dJ}{dt} = -3.8 \times 10^{-23}\mathrm{M}_{\odot}{\mathrm{R}_{\odot}}^{4} M_2 R_2^{\gamma} \omega^3 \,\mathrm{J} \qquad 0 > \gamma > 4 \tag{1.4}$$

where ω is the angular frequency of rotation of the secondary star. γ is a dimensionless parameter which can have a value between 0 and 4, in the context of cataclysmic variable evolution $\gamma = 2$ is frequently used (Schreiber & Gänsicke, 2003). For PCEBs the angular momentum lost via magnetic braking is many orders of magnitude higher than via gravitational braking. However, for many systems the secondary star has a mass less than $0.3\mathrm{M}_{\odot}$ (a fully convective atmosphere) and hence magnetic braking should not be occurring.

1.3.3 Applegate's mechanism

In Applegate's mechanism (Applegate, 1992), as the main sequence star goes through an activity cycle, the outer parts of the star are subject to a magnetic torque changing the distribution of angular momentum and thus its oblateness. The orbit of the stars are gravitationally coupled to variations in their shape hence the period is altered on the same timescale as the activity cycles. This has the effect of modulating the period with fairly large amplitudes ($\Delta P/P \sim 10^{-5}$) over timescales of decades or longer.

We can test whether an observed period change could be caused by Applegate's mechanism by calculating the energy required to drive the change via this

mechanism and comparing it to the total amount of energy available to the main-sequence star. Applegate's equation for the energy required to generate a period change is

$$\Delta E = \Omega_{\rm dr}\Delta J + \frac{\Delta J^2}{2I_{\rm eff}}, \tag{1.5}$$

where $\Omega_{\rm dr}$ is the initial differential rotation which is set to zero since we are after the minimum energy required. The star is separated into a shell and a core, $I_{\rm eff} = I_S I_*/(I_S + I_*)$ is the effective moment of inertia where S stands for the shell and $*$ represents the core. Following the prescription of Applegate (1992) the shell mass is set to $M_S = 0.1{\rm M}_\odot$ meaning that $I_{\rm eff} = 0.5 I_S = (1/3) M_S R_*^2$. The change in angular momentum, ΔJ, is calculated via

$$\Delta J = \frac{-GM^2}{R}\left(\frac{a}{R}\right)^2 \frac{\Delta P}{6\pi}, \tag{1.6}$$

where a is the orbital separation. The energy required for Applegate's mechanism can then be compared with the total energy available to the main sequence star over the time-span of the period change ($\Delta\tau$),

$$E = 4\pi R^2 \sigma T^4 \Delta\tau, \tag{1.7}$$

where T is the temperature of the star and σ is the Stefan-Boltzmann constant. If the total energy available is lower than the minimum required to drive the period change via Applegate's mechanism, then an alternative explanation is required to explain the period change. However, even if the energy is available, it does not necessary mean that it is caused by Applegate's mechanism, only that it is a possible cause.

1.3.4 Third bodies

The presence of a third body results in the central binary being displaced over the orbital period of the third body. This delays or advances eclipse times through variations in light travel time (see Figure 1.2). Since the third body can have a large range of orbital periods these effects can happen over a range of timescales.

1.4 Thesis overview

In this chapter I have introduced detached compact binaries consisting of at least one white dwarf. I have shown that there are still a variety of unsolved problems

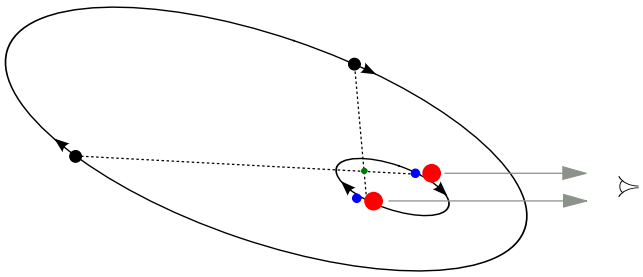

Figure 1.2: An invisible third body (black circle) in orbit around a close binary (blue+red circles) will cause a cyclic period change as observed from Earth. As the central binary moves around the centre of mass of the whole system (green point) it moves slightly further away from, or closer to, Earth. Therefore, the light has more or less distance to travel and as a consequence eclipses are observed to appear later or earlier than predicted.

related to close binary evolution and that eclipsing binaries are a powerful tool to use to help try and solve these problems. I have also shown that there are a variety of mechanisms that can affect the orbital period of a compact binary, both genuine angular momentum loss as well as other quasi-sinusoidal effects, and that the eclipses of compact binaries can be used to detect possible planetary mass companions.

The main aim of this thesis is precision studies of detached white dwarf binaries, both the fundamental stellar parameters as well as precise eclipse timing. I will outline all the tools and methods required to achieve these aims in Chapter 2. In Chapters 3-5 I present the study of a number of eclipsing systems and in each case present some of the most precise mass and radius measurements to date for these kinds of objects. An unexpected outcome of extending these parameter studies to more systems was the discovery of a new eclipsing double white dwarf binary, this study is presented in Chapter 6. Finally, in Chapter 7 I investigate the orbital period variations in a number of close binary systems.

Chapter 2

Methods and Techniques

2.1 Introduction

In this chapter I will outline all the techniques I used to analyse eclipsing white dwarf binaries. I will begin with discussing the basics of collecting and reducing astronomical data. I will then present several important tools for analysing eclipsing binaries with the aim of measuring fundamental parameters.

2.2 Observations and Reductions

2.2.1 Charge Coupled Devices

Charge Coupled Devices (CCDs) are the workhorses of modern astronomy. The low noise level, high quantum efficiency and wide bandpass of CCDs have made them almost ubiquitous. A CCD is a collection of metal-oxide semiconductor (MOS) capacitors in a two dimensional array, known as pixels. When a photon hits a pixel it produces an electron via the photoelectric effect. A voltage applied to the electrodes produces a potential barrier which traps the electron until the CCD is readout.

The CCD readout proceeds in the following way: first, the collected electrons are shifted across the array one column at a time, while the last column is shifted on to the serial register. The electrons are then moved down the serial register to the sense node, where the charge is measured and converted to a digital number, called an analog-to-digital unit (ADU). This process is repeated until the entire CCD is read out. The operation of a CCD can be summarised in the *bucket brigade* analogy, illustrated in Figure 2.1.

The analog to digital conversion process introduces a small amount of noise.

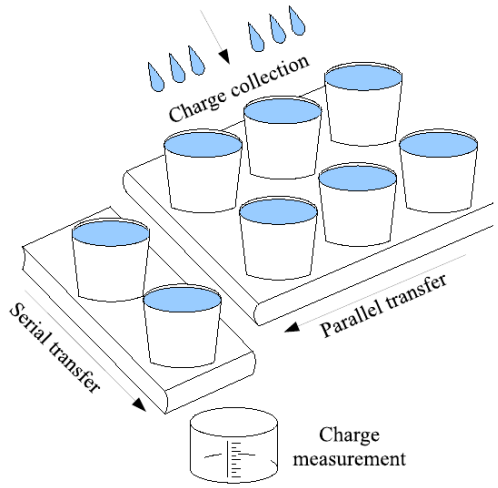

Figure 2.1: The "bucket brigade" analogy for the operation of a CCD. Each bucket (pixel) fills with rainwater (photo-electrons) during an exposure. Once the exposure is finished, each row of buckets is moved down one row at a time onto the serial register. Once on the serial register each bucket is moved to the sense node to measure the amount of rainwater. Figure courtesy of Richard Hickman.

This, combined with the additional noise introduced by spurious electrons in the on-board CCD electronics, is referred to as readout noise.

The charge transfer procedure can be very fast. However, the analog to digital conversion process is much slower and limits the readout speed of a CCD. The time taken for the CCD to readout is known as the dead time and can be quite significant, of the order of $2 - 100$s (depending upon the number of pixels). There are several ways to reduce the dead time; binning can be used to group together several pixels and read them out together. For example, using a 2×2 binning mode will group 4 adjacent pixels together, reducing the overall readout time by a factor of ~ 4. Furthermore, windowing can be used to readout only a specific part of the CCD, the smaller the windows, the shorter the dead time.

Frame transfer CCDs use a different approach. In this case the CCD has an extra unexposed area which can be read whilst the next exposure is being made. In this way the dead time can be greatly reduced. For example, the frame transfer CCDs used by the high-speed camera ULTRACAM (Dhillon et al., 2007) are capable of transferring the frame in milliseconds whilst the time to read the entire CCD is ~ 6 seconds. This means that for exposures of more than 6 seconds the dead time is effectively zero. The CCDs used by ULTRACAM can also be windowed and binned, allowing exposure times much less than 6 seconds with still-negligible dead time.

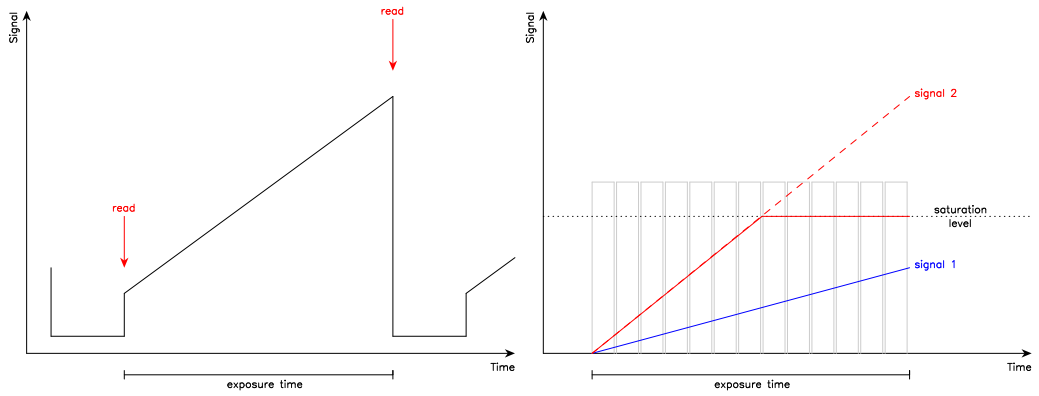

Figure 2.2: Infrared detector readout modes. *Left:* an example of Double Correlated Read mode. The charge is read out at the start and end of the exposure, eliminating any offsets, such as thermal noise. *Right:* an example of Non-Destructive Read. The charge is sampled several times during the exposure and the count level is determined by fitting the slope of the Signal vs. Time. For pixels with high flux (red) only the readout values below the saturation level are taken into account when calculating the slope. The pixel value is then extrapolated to the full exposure time.

2.2.2 Infrared Detectors

Unlike optical CCDs, the charges from individual pixels in infrared detector arrays are not shifted from pixel to pixel during the readout process. Attempts to make charge transfer devices from infrared detector materials have been generally unsuccessful (Joyce, 1992). Instead, each pixel is independently read and each column individually reset. This allows several different readout methods. The two most common infrared detector readout modes are:

Double Correlated Read: In Double Correlated Read (DCR) the voltage is sampled twice, once at the beginning of the exposure and a second time at the end of the exposure. This approach eliminates thermal noise and other offsets, but increases the read noise by $\sqrt{2}$ because the noise from both readouts go into a single image. DCR incurs fewer overheads and thus is suitable where the dominant source of uncertainty is the Poisson noise of the sky emission, e.g. infrared imaging. An example of DCR is shown in the left hand panel of Figure 2.2

Non-Destructive Read: In Non-Destructive Read (NDR) the voltage is sampled many times throughout the exposure, then a linear slope is fitted to the voltage as a function of time. This approach allows one to extend the dynamical range by using a Threshold Limited Integration (TLI). In a TLI the values of saturated pixels are determined by only fitting the voltage values below a certain

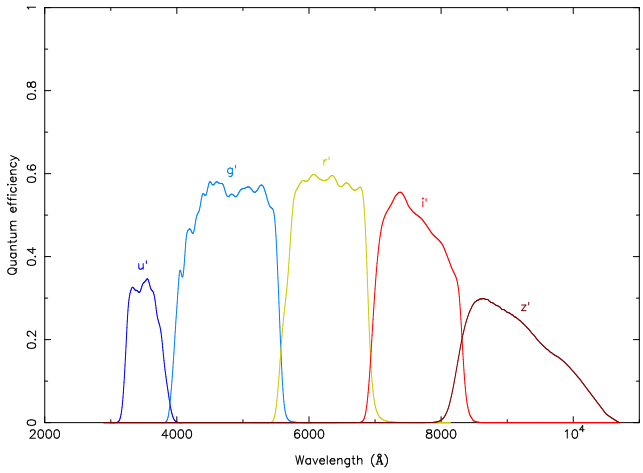

Figure 2.3: ULTRACAM filter profiles (including the quantum efficiency of the detectors). Only light within a specific wavelength range is permitted through to the detector. This allows flux measurements with different instruments to be directly compared.

threshold (close to the detector saturation) and extrapolating to the exposure time. The sampling need not be linear, sampling concentrated towards the beginning and end of the integration minimises the noise and is known as Fowler sampling (Fowler & Gatley, 1990). An example of NDR is shown in the right hand panel of Figure 2.2, with regularly spaced sampling.

The SOFI photometry presented in Chapters 4 and 5 uses DCR mode, whilst the near infrared data from X-Shooter also presented in Chapters 4 and 5 were collected using NDR mode with threshold limited integrations.

2.2.3 Photometry

Photometry is the measurement of the flux of an object. Photometry is particularly important for eclipsing binaries since a long series of images can be used to construct a light curve which can be used to detect variations (e.g. eclipses) in the object's luminosity over time. Flux measurements can be filterless (also known as white light), where all of the light received by the detector is used, or, more commonly, a filter is inserted. A filter only allows light of certain wavelengths through to the detector. For example, the Sloan Digital Sky Survey (SDSS) u-band filter allows the measurement of the flux of an object over the wavelength range of 3000 Å − 4000 Å. The filter profiles for the high-speed camera ULTRACAM are shown in Figure 2.3.

Several calibration steps are required to ensure that the extracted object flux

is accurate. The following sections outline these steps.

Bias subtraction

Since the analog to digital conversion process introduces a small amount of statistical fluctuation in the pixel values, the zero value of the CCD is offset. This avoids potential negative pixel values (which would require a "sign bit" to be used). However, this bias level needs to be subtracted so that errors can be properly determined. This can be estimated by using a bias frame which is a zero exposure-time frame, an example of which is shown in the left hand panel of Figure 2.4. Several bias frames can be combined to reduce the statistical noise and the resultant frame subtracted from the science images.

Bias frames are not possible using infrared detectors since zero second exposures are not possible. Therefore, any bias level is subtracted using dark frames.

Dark-current subtraction

Electrons in the detector can occasionally gain enough thermal energy to jump into the conduction band without the influence of a photon. This extra signal is known as the dark current and can be a substantial source of noise, especially for long exposures. The dark current can be reduced by cooling the detector. An estimate of the dark current can be made using dark frames, which are long exposures with the shutter closed. For CCDs the dark current is proportional to the exposure time, therefore the dark frame can be scaled to match the exposure time of the science image. Infrared detector materials have a dark current that is not linear with time and hence dark frames must be taken with the same exposure time as the science frames. Usually several dark frames are combined to reduce the statistical noise and the resultant frame is subtracted from the science frames. For CCDs the bias level is removed before subtraction whilst the dark frame of an infrared detector acts as both a dark and bias frame.

Flat-fielding

Each pixel in a detector array has a slightly different sensitivity to the pixels around it. Flat fields are used to correct for this effect. A flat field frame is an exposure of a uniform source of light. These are usually a series of exposures of the twilight sky (sky flats) taken with the telescope spiraling to ensure that no stars remain on the same part of the chip. Any counts introduced by stars in the field can then be removed by median averaging the set of flat field frames, this is then normalised to

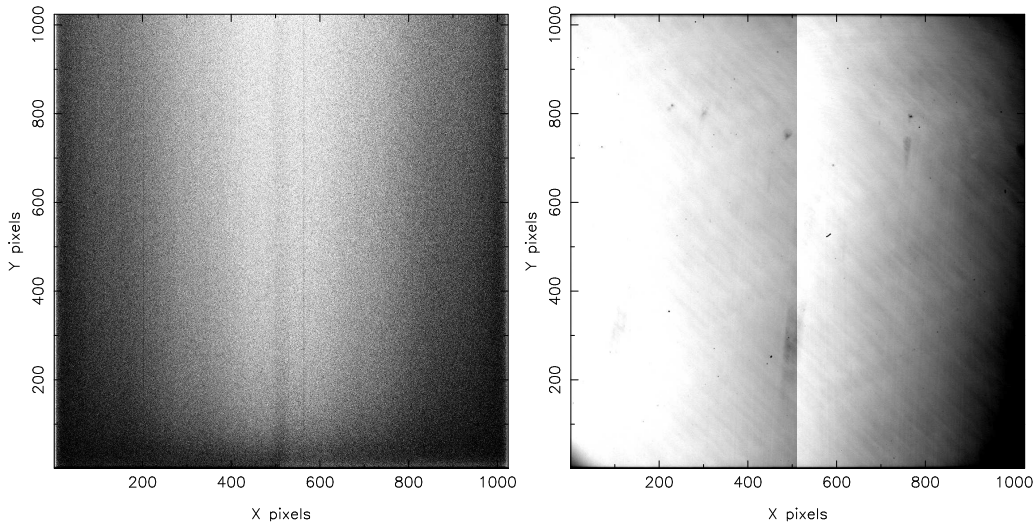

Figure 2.4: *left:* a bias frame from CCD2 of ULTRACAM. The CCD is split into two channels with different bias levels, here the left hand channel has been multiplied up to match the mean level of the right hand one. The difference between the highest and lowest value is only 3%. *Right:* a flat field frame from CCD2 (g' band) of ULTRACAM.

one. All science images are then divided by this frame. Alternately, special flat field screens are provided in many observatories (known as dome flats). An example of a flat field frame is shown in the right hand panel of Figure 2.4.

Aperture photometry

Turning a two dimensional array of numbers into a flux measurement is usually achieved using aperture photometry. An example of aperture photometry is shown in Figure 2.5. It involves picking a small region of pixels (an aperture) that enclose the target. This aperture is usually circular, like those shown in Figure 2.5, to match the star profile. Once we have placed the aperture on the image we simply add up the counts within this window. However, this will also include an offset due to the sky background. The sky background can be estimated by placing a second aperture around the target aperture. This is usually an annulus like those shown in Figure 2.5. The mean of the pixels within this sky aperture is calculated and subtracted from each pixel in the target aperture. A larger sky aperture gives a more reliable estimate of the sky background, but care must be taken that it does not include flux from any other stars, although a mask can be applied to remove any nearby stars.

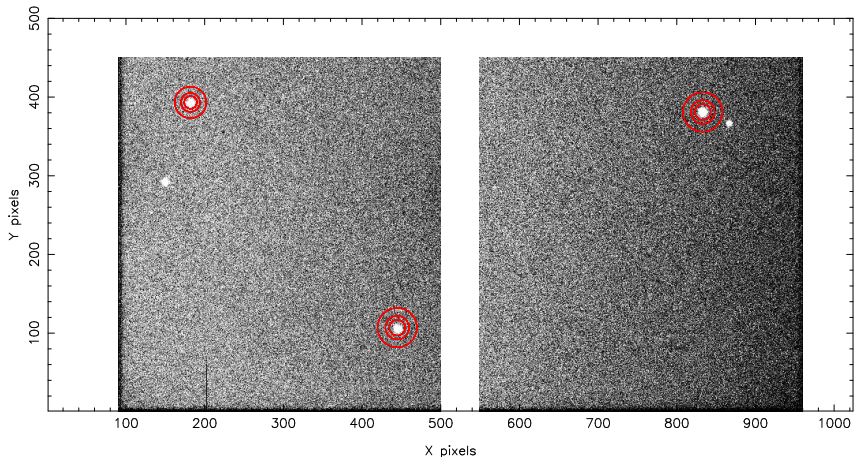

Figure 2.5: An NTT+ULTRACAM g' band image of the sky with several stars visible. The CCD was windowed and only half is shown. Three stars have apertures placed over them. For each star, the smallest circle is the object aperture whilst the two larger circles denote the sky annulus.

The usual way of choosing the size (radius) of the apertures is profile fitting. This approach assumes that the profile of the star resembles some known function (e.g. Gaussian or Moffat functions, the latter based on stellar images (Moffat, 1969)) and thus we can fit the profile to measure variables such as peak intensity and Full-Width at Half-Maximum (FWHM). This allows us to get a good idea of the current atmospheric conditions. The size of the apertures is then based on the FWHM multiplied by a suitable scaling factor. Initially a range of scale factors are used (e.g. ranging from 1.5 to 2.0, in steps of 0.1), then the scale factor that produces the highest signal-to-noise ratio is chosen for the final reduction.

Differential photometry

If we perform aperture photometry of a star over multiple images we can build up a light curve. However, variations in atmospheric conditions (e.g. cloud) can affect the shape of the light curve. This can be corrected for by extracting the flux of a nearby star, known as a comparison star. Dividing the object counts by the comparison star's counts conserves the intrinsic variability of the target but also corrects for variations in conditions. This is known as differential photometry. Care must be taken when choosing a comparison star: it should, if possible, be brighter than the target and have no intrinsic variability itself.

Flux calibration

In some cases it is desirable to turn count values into magnitudes or milli-Janskys (mJy). These values can be compared to external data sets and models. This conversion is achieved using a standard star. Standard stars are relatively bright, non-variable stars with well measured magnitudes in several different bands. The list presented by Smith et al. (2002) is generally used to flux calibrate observations made with the SDSS *ugriz* filters.

The magnitude of the standard star is

$$m_\mu = -2.5 \log_{10}(C_\mu) + x_\mu - \kappa_\mu X, \tag{2.1}$$

where μ represents the filter of interest, C_μ is the counts per second, x_μ is the instrumental zero point, κ_μ is the extinction coefficient in the μ band and X is the airmass.

Since the magnitude of a standard star is known, the only unknowns are the instrumental zero point and the extinction coefficient. A theoretical extinction coefficient can be used but it can also be measured. Using a long observing run (covering a large range in airmass), a linear fit to counts vs. airmass yields the extinction coefficient. Once this is measured the zero point can be obtained and applied to the comparison star and hence the object itself.

To ensure an accurate flux calibration, large apertures must be used to ensure that all the flux is collected. The usual method used to flux calibrate a target's light curves is to use the longest run on the target to determine the comparison star's magnitude. Once determined, the comparison star's magnitude is then fixed and used to flux calibrate all other observations of that target.

2.2.4 Spectroscopy

Spectroscopy involves measuring the flux of an object over a range of wavelengths. This technique can yield information impossible to measure with photometry. Spectroscopic observations are performed using a spectrograph. In a spectrograph the light is first passed through a slit, located at the focus of the telescope. The divergent beam is collimated by a collimator mirror (or lens) and sent to a dispersing element, usually a diffraction grating. The diffracted light is then sent to a camera which focuses it onto a detector (e.g a CCD).

Spectroscopy is a powerful tool for analysing stellar objects and vital for determining binary parameters. However, as with photometry, the data need to be properly calibrated and reduced before any analysis can be performed. The following

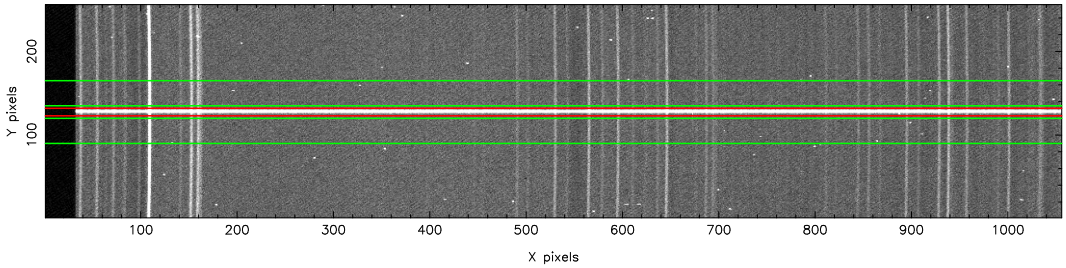

Figure 2.6: Raw image of a stellar spectrum taken using GMOS on the Gemini North Telescope. The star is the bright line across the centre, sky emission lines run perpendicular to it. The dark region $x < 35$ is an overscan region and can be used to estimate the bias level. The sky level will be measured between the green lines whilst the star's flux will be measured between the red lines.

sections outline the calibration steps for reducing spectroscopic data.

Bias and dark-current subtraction

Bias subtraction and dark current removal are performed in the same way as photometric reduction. Most spectrographs have an extended region on the chip which is not exposed to light. This overscan region can be used to measure the bias level for each frame individually (Figure 2.6).

Flat-fielding

The concept of flat-fielding remains the same for spectroscopic data, although there are slight differences. Flat field spectra are usually obtained using a Tungsten lamp located inside the spectrograph. However, the Tungsten spectrum in not flat since it is modulated by its intrinsic, blackbody-like spectrum. Therefore, the flat field frame is collapsed along the spatial direction and the 1D spectrum is fitted with a polynomial. The 2D frame is then divided by the polynomial and applied to the science frames.

Spectrum extraction

Figure 2.6 shows a raw science image obtained with a spectrograph. The target's spectrum runs across the centre of the CCD, although not precisely parallel to the rows due to a small tilt introduced by the optics. A low-order polynomial is fitted to the target spectrum to measure this tilt. Regions either side of the object spectrum are selected to use to measure the sky level (the green regions in Figure 2.6). For each

column a polynomial is fitted to the sky and interpolated in the region containing the target spectrum. A profile is fitted to the target region, this profile is used to assign weights to each pixel. Finally, the background is subtracted and the object extracted using the determined weights in the method outlined by Marsh (1989).

Wavelength calibration

In order to properly analyse the extracted spectrum we need to convert the x-axis from pixels to wavelength. This is achieved by extracting an arc spectrum. These are exposures of emission line lamps with numerous spectral lines with precisely known wavelengths. Examples are CuNe, CuAr or ThAr lamps. The position of each identified line is fitted and compared to the reference wavelength. A polynomial (usually of order 5-7) is fitted to determine the transformation between pixels and wavelength. This transformation is then applied to the science spectra.

Often the arcs will drift during the night, and can be affected by the position of the telescope. Common practice is to observe an arc spectrum both before and after the science exposure and interpolate in time between them for the science spectrum.

Flux calibration

Similar to photometry, the conversion from counts to flux units requires the observation of a standard star. For spectroscopy these spectrophotometric standards are constant stellar sources with well known spectra, observed using a wide slit. The observed spectrum is compared to the template spectrum and the difference is fitted with a spline. The fit is then applied to the science spectra. This approach can remove the instrumental response fairly well. However, since most science spectra are taken with a narrow slit (to achieve the best resolution), some of the light from the target is lost on the slit. These slit losses, and variations in conditions, make absolute flux calibration of variable sources difficult.

One approach to improve the flux calibration of a variable source is to use its light curve. For example, if we fit models to flux calibrated light curves of a source in a number of different filters then we can predict what the flux should be over a range of wavelengths during the spectroscopic observations (if the source's light curve is regular and periodic). Using the known filter profiles we can derive synthetic fluxes from the spectra for those filters and compare them with the photometric models. The difference between the synthetic and model fluxes can then be fitted with a low-order polynomial, which can be applied to the spectrum. This corrects for variable

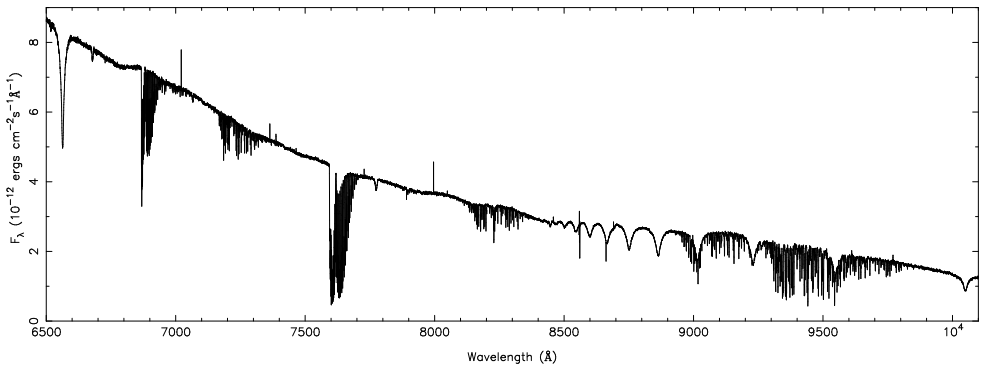

Figure 2.7: A spectrum of the B7 star σ Ari, showing both real features (the hydrogen Paschen series) and telluric absorption features.

extinction across the wavelength range, as well as variations in seeing.

Telluric correction

The Earth's atmosphere is not completely transparent, even in the visual wavelength range. Figure 2.7 shows forests of lines appearing at $\sim$ 6900Å, $\sim$ 7600Å and $\sim$ 9500Å as well as other places throughout the spectrum. These are caused by oxygen and water vapour in the atmosphere and may need to be corrected for in some cases, this is particularly important for the sodium doublet at $\sim$ 8200Å.

Telluric standards are used to correct for these features. These are observations of stars with relatively featureless spectra. The telluric spectrum is continuum normalised, using a spline fit or model spectrum, leaving just the telluric features. One problem is that many of the absorption features are saturated and hence their strength will not be linearly proportional to airmass. This can be somewhat corrected for by using a power law scaling, or trying to minimise the scatter in a well defined telluric region (e.g. the deep feature at $\sim$ 7600Å). This only really works for low to medium resolution data. Applying a telluric correction can restore the original shape of the spectrum, but these regions are much noisier due to the lower number of original counts.

Échelle spectroscopy

Échelle spectrographs work on the same principles as normal slit-based spectrographs but have the advantage of large wavelength coverage and the potential to reach very high resolution. An échelle spectrograph works at very high diffraction orders (e.g. $n \sim 100$) and introduces a cross-disperser to separate and stack the

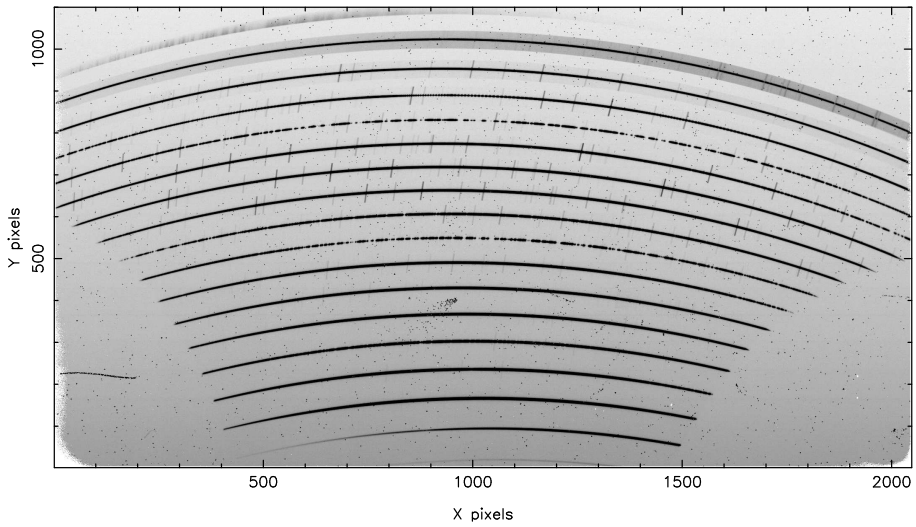

Figure 2.8: A raw échelle spectrum taken using X-Shooter at the VLT. The object spectrum is the dark, highly curved lines in the centre of each order. There are 16 orders in total, with the shortest wavelengths at the bottom. Also visible are a number of sky lines running perpendicular to the objects spectrum. This image covers the NIR region ($1.0 - 2.5$ microns) and the deep J and H atmospheric absorption bands are visible in the 8th and 13th orders up.

orders. An example of a raw échelle spectrum taken using X-Shooter is shown in Figure 2.8. X-Shooter (D'Odorico et al., 2006) is a medium resolution spectrograph and works at diffraction orders of $n \sim 20$ (c.f. the high resolution échelle spectrograph UVES (Dekker et al., 2000) which works at $n \sim 120$). In Figure 2.8, the bottom order is in fact the highest order ($n = 26$) and contains the shortest wavelength information. The order above this ($n = 25$) contains longer wavelength data, but there is a region of wavelength overlap.

Échelle spectroscopy requires two additional steps beyond those used for normal spectroscopy. Firstly, each order must be identified and traced. For the highly curved orders seen in X-Shooter this requires resampling each order. The transformation from pixels to wavelength and slit height must be calculated for each order. Secondly, the orders must be combined. A weighted average is usually used for those wavelengths in the overlap regions.

An échelle grating produces a spectrum that drops as one moves away from the blaze peak, this is known as the blaze function. The left hand panel of Figure 2.9 shows a non-flat fielded spectrum. The peaks are caused by the blaze and are much larger than the genuine stellar features. Applying a flat field correction essentially removes the blaze. However, this removal is not perfect and a residual ripple can

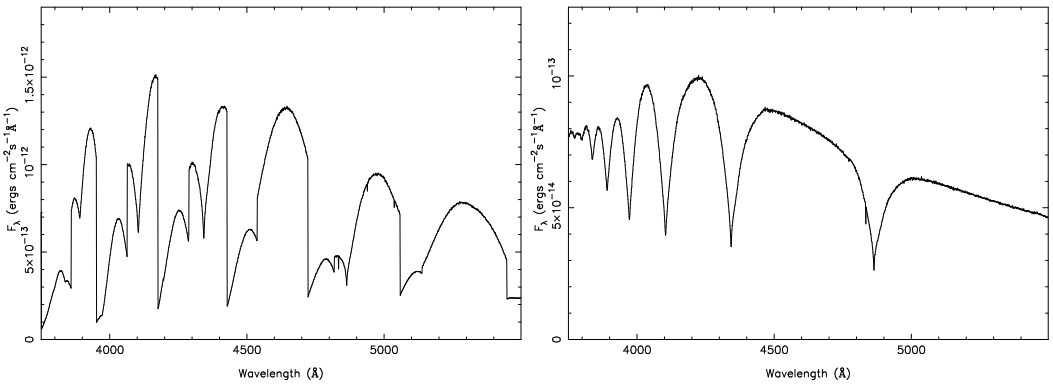

Figure 2.9: *Left:* a non-flat fielded échelle spectrum of a white dwarf. *Right:* the same spectrum but divided by the flat field frame. This demonstrates the importance of using a flat field frame to correct for the blaze function.

often be seen in the final spectrum (this is a particularly large problem for UVES data). We can attempt to remove this ripple by fitting it with a sinusoid of the form

$$\begin{aligned} B(\lambda) &= a_0 + a_1 \sin(2\pi\phi) + a_2\lambda \sin(2\pi\phi) \\ &\quad + a_3 \cos(2\pi\phi) + a_4\lambda \cos(2\pi\phi). \end{aligned} \tag{2.2}$$

The phase (ϕ) can be calculated by identifying the central wavelength of each echelle order. Then using the relation

$$\lambda_n(O - n) = c, \tag{2.3}$$

where c and O are constants and λ_n is the central wavelength of order n, gives us the phase. Since the phase is now known, Equation 2.2 reduces to a simple linear fit.

2.3 General tools

In the following sections I will outline some of the main tools that I use throughout this thesis. These are all techniques used for analysing binary systems.

2.3.1 Measuring radial velocities

One of the main advantages of using spectroscopy is that it allows the study of spectral lines. These lines are not only useful for constraining the physical conditions in a star's atmosphere, but are also extremely important for studying binaries. If

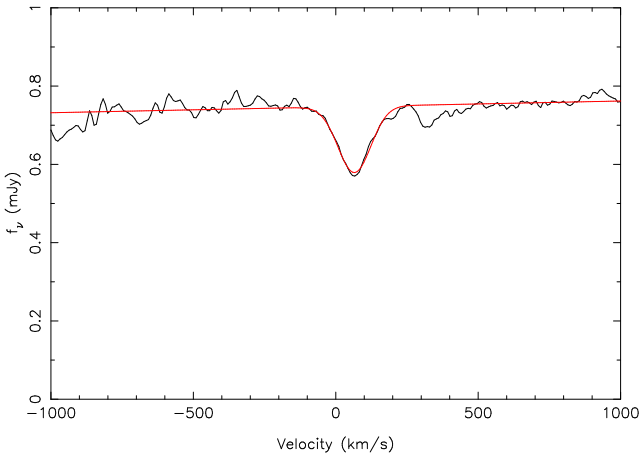

Figure 2.10: Line profile fit to the K I 7699 Å absorption line originating from the secondary star in the eclipsing PCEB SDSS J1212-0123. The line was fitted with a combination of a second-order polynomial and a Gaussian (red line). The velocity scale is centred on the rest wavelength of this line (7698.964Å) and a small shift ($\sim 70\mathrm{km\,s^{-1}}$) is seen in the observed line position.

we spectroscopically observe a binary system over its entire orbit, we will see any spectral lines move. This is because the stars themselves are moving around the centre of mass and thus their spectra will be shifted due to the Dopper effect. This shift will correspond to the radial velocity (the projected velocity in the line of sight) of the star. The velocity of a spectral line can be determined by measuring its central wavelength, λ_{obs}, and comparing it to the lines rest wavelength, λ_0. The velocity of the line is then $V = c\,(\lambda_{\mathrm{obs}} - \lambda_0)\,/\lambda_0$. For circular orbits, the measured velocity of a line will exhibit a sinusoidal variation over the course of an orbit, given by,

$$V(t) = \gamma + K \sin\left(\frac{2\pi(t - T_0)}{P}\right) \tag{2.4}$$

where γ is the systemic velocity, K is the radial velocity, P is the period of the binary and T_0 is the zero-point of the ephemeris (i.e. the centre of the primary eclipse). The ephemerides of all of the systems presented in this thesis are well known from photometry. Therefore, T_0 and P are kept fixed for all radial velocity measurements. However, Equation 2.4 shows that spectral lines can be used to determine the ephemeris of a binary.

In order to measure the radial velocity of a line we need to measure its central wavelength, this is done by fitting the line profile. Figure 2.10 shows a fit to a

potassium absorption line in SDSS J1212-0123 (presented in detail in Chapter 5). In this case I have used a Gaussian profile combined with a second-order polynomial to fit the line. In most cases a Gaussian fit is sufficient. However, the hydrogen Balmer lines seen in white dwarfs are highly pressure broadened due to the high gravity environment in a white dwarf atmosphere. Pressure broadening has a Lorentzian profile, therefore the wings of the line are more affected than the cores, leading to very wide (several thousand $\mathrm{km\,s^{-1}}$) wings in these lines. Fortunately, the lower energy lines in white dwarfs (e.g. Hα) usually display sharp cores ($2-3$Å in width) as the result of non-LTE effects (Greenstein & Peterson, 1973) which are useful for tracing their motion.

As well as the cores of the Balmer lines, white dwarfs in PCEBs often accrete a small amount of the wind from the secondary star. This can create narrow calcium and magnesium absorption lines ideal for radial velocity measurements. The low mass secondary stars in PCEBs are usually M dwarfs and therefore the sodium doublet at $\sim$ 8200Å is usually used to measure their radial velocity. One complication here is that these lines lie in an area of relatively high atmospheric absorption and a telluric correction must be applied. The spectra of M dwarfs also display molecular absorption bands (e.g. TiO). Although these also track the motion of the star, they are highly asymmetric and the central wavelengths are often unknown. Hence profile fitting of these features will not yield particularly accurate radial velocities.

Alternatively, a template spectrum can be used to measure radial velocities by cross correlating it with the observed spectrum. However, given the large number of strong, clean lines present in PCEBs, fitting the line profiles gives results to a similar precision, but is a much faster method then cross correlation.

2.3.2 K_{sec} correction

As well as absorption lines, spectra of PCEBs can contain emission lines. These emission lines usually originate from the heated face of a highly irradiated secondary star (i.e. those systems containing hot white dwarfs).

The centre of light for this reprocessed light will be offset from the centre of mass of the secondary star towards the white dwarf, effectively placing a lower limit on the true radial velocity of the secondary star. For accurate mass determinations the centre of mass radial velocity amplitude is required thus we need to determine the deviation between the reprocessed light centre and the centre of mass for the secondary star, this is known as a K_{sec} correction. This correction can be expressed

analytically as (Wade & Horne, 1988)

$$K_{\rm sec} = \frac{K_{\rm emis}}{1 - f(1+q)\frac{R_{\rm sec}}{a}}, \tag{2.5}$$

where $K_{\rm sec}$ is the centre of mass radial velocity, $K_{\rm emis}$ is the radial velocity of the emission line, q is the mass ratio, $R_{\rm sec}/a$ is the radius of the secondary star scaled by the orbital separation and f is a constant between 0 and 1 which depends upon the location of the centre of light. For $f = 0$ the emission is spread uniformly across the entire surface of the secondary star and therefore the centre of light is the same as the centre of mass. For $f = 1$ all of the flux is assumed to come from the substellar point.

The measured radial velocity amplitude of an emission line will depend upon the optical depths of the line, which will affect the angular distribution of line flux from any given point on the star. This is illustrated in Figure 2.11. Differences in optical depth will also affect the light curve of the line for the same reasons. Figure 2.12 shows the light curve of an optically thick and thin emission line. Therefore, we can use the light curve of a line to determine its optical depth and hence the $K_{\rm sec}$ correction for that line.

We wanted to be able to model optically thin and optically thick emitting regions within one model so that there was a continuous transition from one to the other. To do so we assumed a simple model in which the line emitting region at any point on the secondary behaves as if it had a total vertical optical depth τ_0, and a source function given by an exponential function of vertical optical depth, τ,

$$S(\tau) \propto e^{\beta\tau},$$

where β is a user-defined constant allowing the source function to increase or decrease with optical depth. To prevent divergent integrals, we must have that $\beta < 1$. For $\beta > 0$, the source function increases as one goes further into the star and we expect limb darkening, while $\beta < 0$ gives limb brightening. As $\tau_0 \to 0$, we obtain optically-thin behaviour, thus this two-parameter model gives the desired modeling freedom.

For an incident angle θ such that $\mu = \cos\theta$, the emergent intensity is then given by

$$I(\mu) \propto \int_0^{\tau_0} e^{\beta\tau} e^{-\tau/\mu} \frac{d\tau}{\mu},$$

where the variable of integration τ is the vertical optical depth while the optical

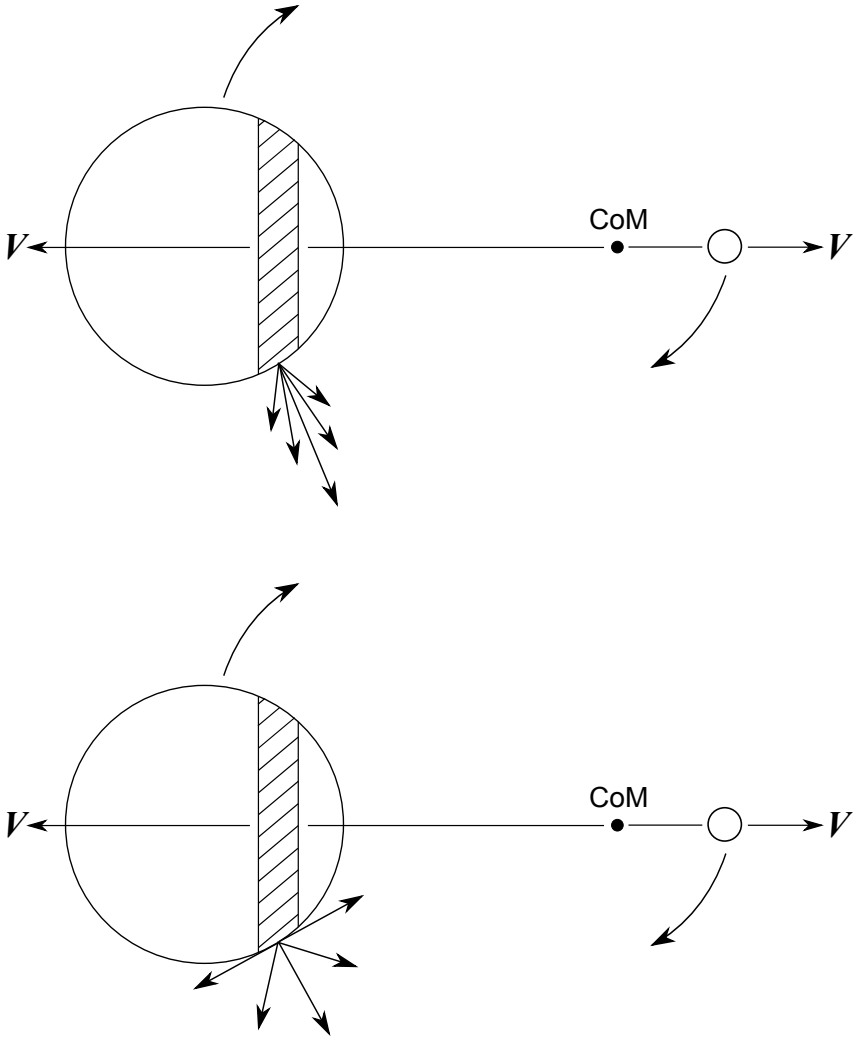

Figure 2.11: Optical depth effects on emission lines. *Top:* In the optically thick case, flux emitted close to the stellar surface is more likely to be absorbed, leading to a higher flux perpendicular to the surface. *Bottom:* In the optically thin case the flux is emitted equally in all directions. This means that, assuming emissivity proportional to the incident flux, at quadrature (phase 0.25 and 0.75) the limb of the irradiated region will be enhanced in the optically thick case, whilst the emission from the substellar point will be enhanced in the optically thin case. This changes the centre of light and thus the measured radial velocity between an optically thick and thin line.

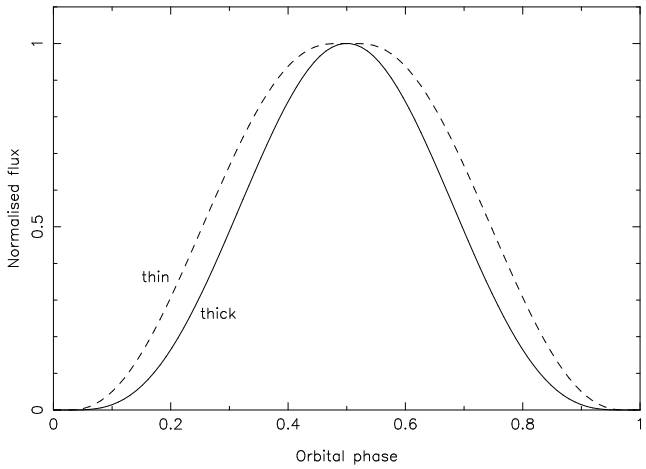

Figure 2.12: The effects of optical depth on the light curve of a line. In the optically thin case the emission is distributed uniformly meaning that the light curve is wider and flatter. In the optically thick case the light emitted at angles close to the stellar surface is reduced, meaning that the brightest region (the substellar point) contributes much less away from phase 0.5, compared to the optically thin case.

depth along the line of sight is τ/μ. Therefore

$$I(\mu) \propto \frac{1 - e^{(\beta - 1/\mu)\tau_0}}{1 - \beta\mu}.$$

In the limit $\tau_0 \to \infty$ we have

$$I(\mu) \propto \frac{1}{1 - \beta\mu},$$

which for small β gives $I(\mu) \propto 1 + \beta\mu$, giving limb-darkening or brightening as expected. In the optically thin limit, $\tau_0 \to 0$,

$$I(\mu) \propto \frac{\tau_0}{\mu}.$$

The μ divides out with the μ factor from Lambert's law, and we find that each unit area contributes equally to all directions, as long as it remains visible. This enhances the star's limb compared to the optically thick case. At quadrature for example, this will enhance emission from the sub-stellar point, leading to a low semi-amplitude.

2.3.3 Time system conversions

One of the oldest branches of astronomy is time keeping. For thousands of years astronomical phenomena have formed the foundations of our time systems: The year

by Earth's orbit around the Sun and the resulting run of the seasons, the month by the Moon's movement around the Earth and the change of the Moon phases, the day by Earth's rotation and the succession of brightness and darkness. Problems arise when high-precision times are required. Not only must one correct for the location on Earth, but one must also correct for the motion of Earth itself. These corrections can be up to several minutes and since we are able to measure eclipse times in PCEBs to sub-second accuracies it is vital that we make these corrections. This section outlines the main time systems used in modern astronomy and their relations to one another.

Universal Time (UT) was introduced in 1926 to replace the less stringent Greenwich Mean Time (GMT). However, this first version of UT, known as UT0, did not take into account the motion of the Earth's poles. Correcting for this effect, one obtains UT1, which is equivalent across the entire surface of the Earth. One problem with UT1 is that the derived length of a second varies noticeably (due to irregularities in the Earths rotation). Therefore, in 1961 Coordinated Universal Time (UTC, a compromise between the English and French acronyms) was devised in which the SI second is the unit of time. UTC and UT1 are kept to within a second of one another by adding or subtracting leap seconds (although none have yet been subtracted). These are inserted into the last minute of June 30th or December 31st. The last leap second (as of 2012) was added on 31st of December 2008.

The SI second is defined as $9,192,631,770$ cycles of a hyperfine transition in the ground state of ^{133}Cs, set to best match the previous definition of a second. Devices that attempt to measure the SI-second are known as atomic clocks. There are many atomic clocks located across the world and the mean time of all of these is known as Atomic Time (TAI). Due to the addition of leap seconds TAI currently (2012) runs 34 seconds ahead of UTC i.e.

$$\mathrm{UTC} = \mathrm{TAI} - N, \tag{2.6}$$

where N is the number of leap seconds.

Terrestrial Time (TT) was introduced in 1991 as a uniform time system (replacing terrestrial dynamical time, which itself had replaced ephemeris time) and was needed to predict the positions of the Sun, Moon and planets. This is because the application of the laws of motion required a smoothly flowing time system. To millisecond accuracy, TT runs parallel to TAI but, for historical reasons, is 32.184 seconds ahead

$$\mathrm{TT} \approx \mathrm{TAI} + 32.184. \tag{2.7}$$

Barycentric Dynamical Time (TDB) is essentially the same as TT (the difference will not exceed 2 milliseconds for several thousand years). TDB accounts for time dilation when calculating orbits and ephemerides. BTDB is TDB corrected for light travel time effects and is equivalent to observations made at the barycentre of the solar system. A similar correction can be made to the heliocentre, which is slightly displaced from the barycentre of the solar system, towards Jupiter.

These time systems allow an observer to say precisely when an event (e.g. an eclipse) occurred. However, the conventional civil calendar is not ideal for calculating the number of days between two events. In 1583 the astronomer and historian Joseph Scaliger devised an absolute day counting system known as Julian Date (JD). He set JD = 0 as noon on the 1st of January 4713 BC. Noon was chosen so that astronomers in Europe performed all of their observations on the same JD. Due to the large number of days that have elapsed since JD = 0 (2,455,562.5 on January 1st 2011) a shortened version known as Modified Julian Date is regularly used,

$$\mathrm{MJD} = \mathrm{JD} - 2400000.5. \tag{2.8}$$

Throughout this thesis times are measured in MJD(UTC) and then converted to MJD(BTDB).

2.3.4 Light curve model fitting

Fitting the light curve of an eclipsing binary is essential if one wants to measure the radii of both stars. There are a number of other methods of determining the radii of stars, for example knowledge of its effective temperature and distance, but none of these techniques are as direct nor assumption-free as using an eclipse light curve.

In eclipsing PCEBs the primary eclipse occurs when the main sequence star passes in front of the white dwarf, as viewed from Earth. The eclipse profile contains two pieces of information: the width of the eclipse and the steepness of the ingress and egress. Unfortunately, there are three unknowns: the radii of the two stars[1] and the orbital inclination. Therefore we have a degeneracy between these three parameters (Ritter & Schroeder, 1979). This is illustrated in Figure 2.13 which shows that the same eclipse shape can be achieved at two different inclinations by varying the radii of both stars.

However, as Figure 2.13 shows, for a given inclination angle we have a unique pair of R_{WD} and R_{sec}. Therefore, only one more piece of information is required to lift this degeneracy. The most direct method is to measure the depth of the

[1] To be exact, eclipses yield the radii scaled by the binary separation R_{WD}/a and R_{sec}/a.

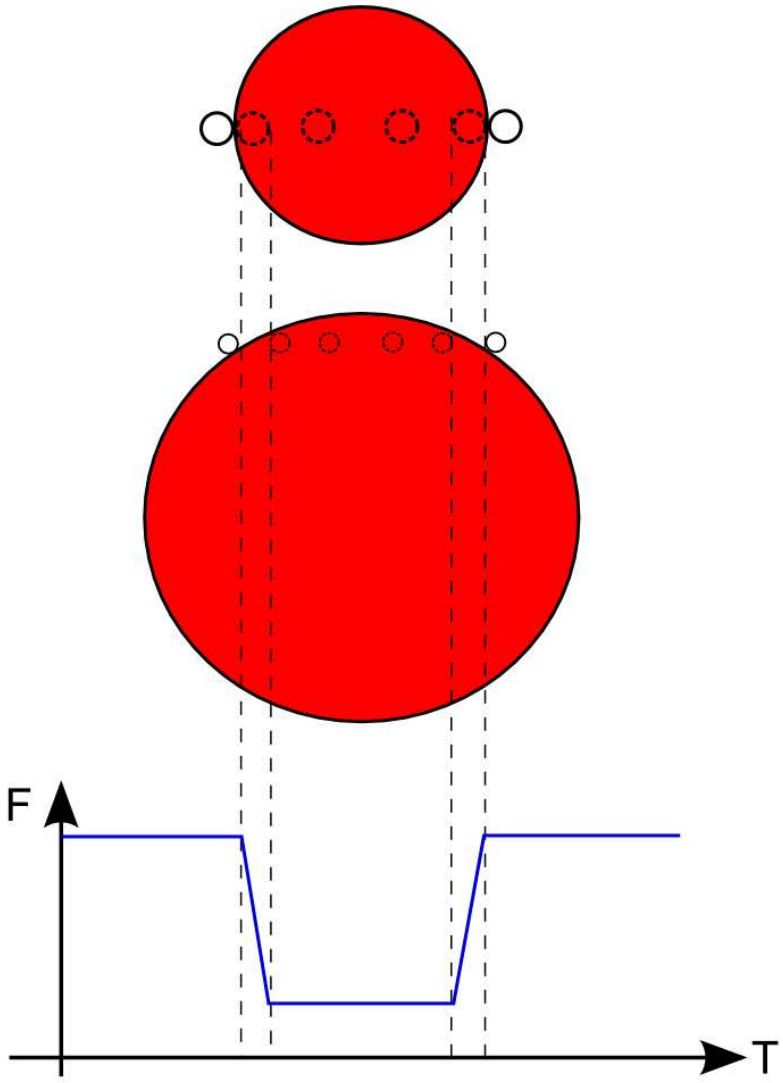

Figure 2.13: The degeneracy between the scaled radii of the two stars and the orbital inclination in an eclipsing PCEB. Moving from a high inclination (top) to a lower inclination (bottom) can still result in the same eclipse profile by increasing the size of the secondary star and decreasing the size of the white dwarf.

secondary eclipse (the transit of the white dwarf across the face of the secondary star). The depth of the secondary eclipse is $(R_{\rm WD}/R_{\rm sec})^2$ which, combined with the primary eclipse fit, allows us to break the degeneracy. This approach will be used in Chapters 3 and 4. The biggest problem with using this approach to break the degeneracy is that the secondary eclipse is very shallow and even in the best cases its depth is $< 2\%$ (see for example Figures 3.11 and 4.3). To detect the secondary eclipse requires $R_{\rm WD}/R_{\rm sec}$ to be as large as possible, meaning large white dwarf radii (i.e. low-mass or hot white dwarfs) and small secondary radii (i.e. very late-type MS stars). Hence, this powerful geometric constraint can only be applied in a very few cases.

There are a number of other methods available which provide constraints to break the degeneracy. If we can identify features from both stars in the spectrum then the fits to both velocities provide the systemic velocities γ for both stars; the difference in systemic velocities, $\gamma_{\rm WD} - \gamma_{\rm sec}$, is usually interpreted as the gravitational redshift of the white dwarf. General relativity tells us that its gravitational redshift of a white dwarf is (Greenstein & Trimble, 1967)

$$V_z = 0.635 \left(\frac{M}{\rm M_\odot}\right)\left(\frac{\rm R_\odot}{R}\right) \,{\rm km\,s^{-1}} \tag{2.9}$$

where M and R are the mass and radius of the white dwarf. Furthermore, if we know the radial velocity amplitudes of the two stars then Kepler's third law tells us

$$M_{\rm WD} = \frac{PK_{\rm sec}(K_{\rm WD}+K_{\rm sec})^2}{2\pi G \sin^3 i} \tag{2.10}$$

where P is the orbital period, and i is the orbital inclination. Therefore for a given inclination we can calculate the mass of the white dwarf via Eq (2.10) and the radius of the white dwarf via a model fitted to the primary eclipse, and thus predict a redshift. Hence we can use the measurement of the gravitational redshift to constrain the inclination by rejecting light curve models which do not satisfy this constraint.

The true gravitational redshift of the white dwarf will actually be slightly higher than the measured value from the spectroscopy. This is because the effects of the secondary star tend to reduce the measured value. Accounting for the presence of the secondary star, the redshift of the white dwarf is in fact

$$V_{z,{\rm WD}} = 0.635\left(\frac{M_{\rm WD}}{R_{\rm WD}} + \frac{M_{\rm sec}}{a}\right) + \frac{(K_{\rm WD}/\sin i)^2}{2c}. \tag{2.11}$$

Similarly, the gravitational redshift of the secondary star is

$$V_{z,\mathrm{sec}} = 0.635 \left(\frac{M_{\mathrm{sec}}}{R_{\mathrm{sec}}} + \frac{M_{\mathrm{WD}}}{a} \right) + \frac{(K_{\mathrm{sec}}/\sin i)^2}{2c}, \tag{2.12}$$

then the value $V_z = V_{z,\mathrm{WD}} - V_{z,\mathrm{sec}}$ is equivalent to the measured redshift from the spectra. In the case of PCEBs this correction is only of the order of 1–2 $\mathrm{km\,s^{-1}}$. This constraint will be used in Chapter 5.

Ellipsoidal modulation is a variation of the out-of-eclipse brightness, arising from the fact that the secondary star is tidally distorted by the white dwarf and hence presents a different area (and hence we observe varying flux) during an orbit. The amplitude of this modulation is related to the mass ratio ($q = M_{\mathrm{sec}}/M_{\mathrm{WD}}$) and R_{sec}. Therefore, if we know q, then the primary eclipse shape combined with the amplitude of the ellipsoidal modulation allows us to break the degeneracy. Examples of ellipsoidal modulation in light curves are shown in Figures 7.3 and 7.4. This method was used by Pyrzas et al. (2012) to measure the masses and radii in the eclipsing PCEB SDSS J1210+3347. Starspots in the surface of the secondary star can affect the amplitude and means that this approach is often unreliable.

LCURVE

I have shown that analysis of the light curve of an eclipsing PCEB gives strong constraints on the system parameters. All of the light curve fitting presented in this thesis was performed using LCURVE written by Tom Marsh (see Copperwheat et al., 2010, for an account). The code produces models for the general case of binaries containing white dwarfs. Several components of the model include accretion phenomena for the analysis of cataclysmic variables. Since PCEBs are detached systems these components are not included.

The program subdivides each star into small elements with a geometry fixed by its radius as measured along the direction of centres towards the other star. Roche geometry distortion and irradiation of the secondary star are included, the irradiation is approximated by $\sigma T'^4_{\mathrm{sec}} = \sigma T^4_{\mathrm{sec}} + A F_{\mathrm{irr}}$ where T'_{sec} is the modified temperature and T_{sec} is the temperature of the unirradiated main-sequence star, σ is the Stefan-Boltzmann constant, A is the fraction of the irradiating flux from the white dwarf absorbed by the secondary star and F_{irr} is the irradiating flux, accounting for the angle of incidence and distance from the white dwarf. Each element, with a vector angle μ towards Earth, has its light contribution altered by

a limb-darkening law such that

$$I(\mu) = 1 - \sum_i a_i (1-\mu)^i, \tag{2.13}$$

where μ is the cosine of the angle between the line of sight and the surface normal, a_i are the limb darkening coefficients, for most cases only one or two coefficients are used. LCURVE also allows an alternative limb-darkening approach based on the 4-coefficient formula of Claret (2000),

$$I(\mu) = 1 - \sum_i a_i (1-\mu^{i/2}). \tag{2.14}$$

The code has two ways to specify the radii: they can be set directly or one can use the third and fourth contact points of the eclipse. In this case the radii are computed, based on a spherical approximation, from two equations:

$$r_2 + r_1 = \sqrt{1 - \sin^2 i \cos^2 2\pi\phi_4}, \tag{2.15}$$

$$r_2 - r_1 = \sqrt{1 - \sin^2 i \cos^2 2\pi\phi_3}. \tag{2.16}$$

In this case, unless the stars are actually spherical ϕ_3 and ϕ_4 are not the true contact points. However, the radii returned will still be precise even in the Roche distorted case. The main advantage of this approach is that the correlation between r_1, r_2 and i is highly curved (particularly in the case of r_2 and i) meaning that most fitting routines will take much longer to explore the full range of possible parameters. Using the contact points instead vastly decreases this curvature, as shown in Figure 2.14, saving a huge amount of CPU time. This is only necessary when using very high S/N data.

There are a number of other parameters used by LCURVE to produce light curves. All the important parameters used to produce the models shown throughout this thesis are listed in Table 2.1.

Fitting routines

We can use LCURVE to produce model light curves and compare these to the actual light curves in order to find the best parameters. The code allows the user to fix a parameter value or allow it to vary. In this thesis three different fitting routines have been used[2].

[2]All the fitting routines are implemented as part of Tom Marsh's LCURVE code

Table 2.1: Parameters needed for LCURVE to create a light curve of an eclipsing PCEB.

Parameter name	Description
Binary and Star:	
q	The mass ratio, $q = M_2/M_1$
i	The inclination
r_1	Radius of star 1 (the white dwarf) scaled by the binary separation ($R_{\rm WD}/a$)
r_2	Radius of star 2 (the secondary star) scaled by the binary separation ($R_{\rm sec}/a$)
ϕ_3	$3^{\rm rd}$ contact point of the eclipse, as star 1 starts to emerge from eclipse
ϕ_4	$4^{\rm th}$ contact point of the eclipse, as star 1 emerges fully from eclipse
T_1	Temperature of star 1 based on a black-body
T_2	Unirradiated temperature of star 2 based on a black-body
$a_{1,i}$	limb-darkening coefficients for star 1
$a_{2,i}$	limb darkening coefficients for star 2
V_s	The sum of the unprojected stellar orbital speeds $V_s = (K_{\rm WD} + K_{\rm sec})/\sin(i)$. Doesn't make much difference to the light curve but can be used to constrain i if $K_{\rm WD}$ and $K_{\rm sec}$ are already known
General:	
T_0	Zero-point of ephemeris, set to the mid-point of the primary eclipse
P	The orbital period
$g_{\rm dark,1}$	The gravitational darkening of star 1, usually set to 0 since the white dwarf is not Roche distorted
$g_{\rm dark,2}$	The gravitational darkening of star 2. Usual values are 0.08 for a convective atmosphere, 0.25 for a radiative atmosphere
A	The fraction of the irradiating flux from star 1 absorbed by star 2
s	A coefficient to add a slope to the light curve. This can help with airmass effects and starspots
Computational:	
Nlat1f	The number of latitude strips used on star 1 around the primary eclipse
Nlat1c	The number of latitude strips used on star 1 away from the primary eclipse
Nlat2f	The number of latitude strips used on star 2 around the secondary eclipse
Nlat2c	The number of latitude strips used on star 2 away from the secondary eclipse
Wavelength	The wavelength to compute the light curve for
roche1	This is set to 1 if Roche distortion of star 1 is needed. This is usually set to 0
roche2	This is set to 1 if Roche distortion of star 2 is needed
eclipse1	This is set to 1 to account for the eclipse of star 1
eclipse2	This is set to 1 to account for the eclipse of star 2
use_radii	If set to 1 then the r_1 and r_2 are used to set the radii. Else ϕ_3 and ϕ_4 are used
limb1	Set to either "Claret" or "Poly" depending upon which limb darkening law is being used for star 1
limb2	Set to either "Claret" or "Poly" depending upon which limb darkening law is being used for star 2

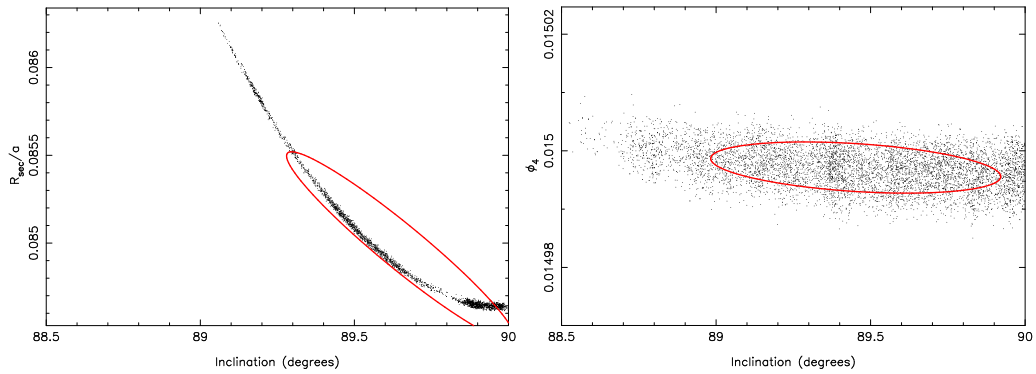

Figure 2.14: *Left:* a fit to the light curve of GK Vir with the radii set directly. In this case there is a highly curved correlation between the radius and the inclination. The red ellipse shows the calculated covariance from the data. In many areas the correlation does not match the calculated covariance and the fitting routine is likely to get stuck, giving erroneous results. *Right:* a fit to the same light curve but using the third and fourth contact points to define the radii. In this case the curvature has been vastly reduced and matches the calculated covariance across the whole inclination range.

The downhill Simplex method (Nelder & Mead, 1965) works with a geometrical object known as a simplex. A simplex has $N+1$ vertices where N is the number of independent variables (e.g. a triangle in two dimensions). The simplex is then moved around (reflected, expanded, contracted etc.) within the parameter space in order to reduce the χ^2. Since this method only requires evaluating the function, not the derivatives, it is robust at finding a minimum. However, it usually requires a large number of function evaluations and thus is slower than other routines. Furthermore, it cannot return an estimate of parameter uncertainties and can easily get caught in local minima. The main advantage of the Simplex routine is that it will converge to a solution over a wide range of initial parameter values, making it the ideal routine to start fitting a light curve with.

The Levenberg-Marquardt method (Press, 2002) is a combination of two minimisation methods: the steepest descent method and the Gauss-Newton method. The routine switches between the steepest descent method (which requires the calculation of the gradient of a function) when the parameters are far from optimal, and the Gauss-Newton method (which assumes that the function is locally quadratic and estimates the minimum) when closer to a minimum. The Levenberg-Marquardt method does have some drawbacks; the convergence will often fail if the initial parameter values were too far from the minimum, it is also unable to distinguish between local or the global minima. However, it can provide both a first estimate of

parameter uncertainties and the correlations between them (a covariance matrix).

The Markov-Chain-Monte-Carlo (MCMC) method (see e.g. Ford, 2006, and references therein for a review) involves making random jumps in the model parameters, with new models being accepted or rejected according to their probability computed as a Bayesian posterior probability. This probability is driven by a combination of χ^2 and, if appropriate, a prior probability (e.g. spectroscopic constraints such as the redshift). A crucial practical consideration of MCMC is the number of steps required to fairly sample the parameter space, which is largely determined by how closely the distribution of parameter jumps matches the underlying distribution. An estimate of the correct distribution can be built up by starting from uncorrelated jumps in the parameters or by using the Levenberg-Marquardt method, after which the covariance matrix can be computed. A covariance matrix is used to define a multivariate normal distribution that is used to make the jumps in a chain. At each stage the actual size of the jumps is scaled by a single factor set to deliver a model acceptance rate of ≈ 25 per cent. When performing a final MCMC run to determine the parameter values and their uncertainties the covariance and scale factor are held fixed. Note that the distribution used for jumping the model parameters does not affect the final parameter distributions, only the time taken to converge towards them.

These three routines naturally lead to the process used to fit the majority of the light curves in this thesis, namely: initially fit the light curve using the Simplex method to find a minimum. Use this result as the starting point for the Levenberg-Marquardt method, which will provide the uncertainties and correlations on the parameters. Use these to start a MCMC chain. Usually a further final MCMC "production" chain is then run, using the updated uncertainties and correlations from the first chain, to give the final parameter values and their uncertainties.

2.4 Summary

In this chapter I have outlined the general tools needed to reduce and analyse both spectroscopic and photometric data. I have also presented several key techniques required to measure precise system parameters (as well as eclipse times). In the following few chapters I will show that by applying these techniques to high quality data can allow us to measure extremely precise physical parameters in eclipsing white dwarf binaries.

Chapter 3

The masses and radii of the stars in NN Ser

3.1 Introduction

In this chapter I begin the precision study of eclipsing PCEBs. This chapter focuses on the system NN Ser in which the secondary eclipse is visible, allowing the inclination to be directly measured. I will apply the techniques described in Chapter 2 to determine precise model-independent masses and radii for both stars in the binary. I will then compare these results with evolutionary models.

3.2 Target information

The PCEB NN Ser (PG 1550+131) is a low mass binary system consisting of a hot white dwarf primary and a cool M dwarf secondary. It was discovered in the Palomar Green Survey (Green et al., 1982) and first studied in detail by Haefner (1989) who presented an optical light curve showing the appearance of a strong heating effect and very deep eclipses (>4.8mag at $\lambda \sim 6500$Å). Haefner identified the system as a pre-cataclysmic binary with an orbital period of 0.13 d. The system parameters were first derived by Wood & Marsh (1991) using low-resolution ultra-violet spectra then refined by Catalan et al. (1994) using higher resolution optical spectroscopy. Haefner et al. (2004) further constrained the system parameters using the FORS instrument at the Very Large Telescope (VLT) in combination with high-speed photometry and phase-resolved spectroscopy. However, they did not detect the secondary eclipse leading them to underestimate the binary inclination and hence overestimate the radius and ultimately the mass of the secondary

Table 3.1: Journal of VLT/UVES spectroscopic observations of NN Ser.

Date	Start (UT)	End (UT)	No. of spectra	Conditions (Transparency, seeing)
30/04/2004	05:15	08:30	40	Fair, ∼2.5 arcsec
01/05/2004	03:14	06:31	40	Variable, 1.2-3.1 arcsec
17/05/2004	03:37	06:58	40	Fair, ∼2.1 arcsec
26/05/2004	00:52	04:14	40	Fair, ∼2.2 arcsec
27/05/2004	03:14	06:42	40	Good, ∼1.1 arcsec
10/06/2004	02:06	05:22	40	Good, ∼1.1 arcsec
12/06/2004	02:39	05:54	40	Fair, ∼2.1 arcsec
15/06/2004	02:41	05:56	40	Good, ∼1.8 arcsec
27/06/2004	03:54	05:11	15	Fair, ∼2.2 arcsec

star. They were also unable to directly measure the radial velocity amplitude of the white dwarf and were forced to rely upon a mass-radius relation for the secondary star. Recently, Brinkworth et al. (2006) performed high time resolution photometry of NN Ser using ULTRACAM mounted on the William Herschel Telescope (WHT). They detected the secondary eclipse leading to a better constraint on the inclination. Since NN Ser belongs to the group of PCEBs which is representative for the progenitors of the current cataclysmic variable (CV) population (Schreiber & Gänsicke, 2003), the system parameters are important from both an evolutionary point of view as well as providing independent measurements of the masses and radii of the system components.

3.3 Observations and their Reduction

3.3.1 Spectroscopy

Spectra were taken in service mode over nine different nights between 2004 April and June using the Ultraviolet and Visual Echelle Spectrograph (UVES) installed at the European Southern Observatory Very Large Telescope (ESO VLT) 8.2-m telescope unit on Cerro Paranal in Chile (Dekker et al., 2000). In total 335 spectra were taken in each arm, details of these observations are listed in Table 3.1. Exposure times of 250.0s and 240.0s were used for the blue and red spectra respectively; these were chosen as a compromise between orbital smearing and signal-to-noise ratio (S/N). The wavelength range covered is 3760–4990Å in the blue arm and 6710–8530 and 8670–10400Å in the red arm. These data were reduced following the methods described in Chapter 2 for échelle spectra (including fitting the blaze function using Equation 2.2). The spectra have a resolution of R∼80,000 in the

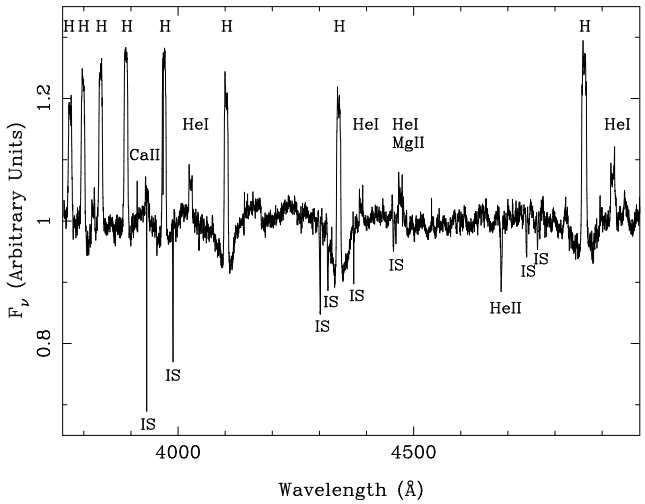

Figure 3.1: Averaged, normalised UVES blue arm spectrum with the blaze removed. IS corresponds to interstellar absorption features. The discontinuity at $\sim$ 4150Å and the emission-like feature at $\sim$ 4820Å are most likely instrumental features or artifacts of the UVES reduction pipeline as they are seen in all 335 spectra.

blue and R$\sim$110,000 in the red. Orbital smearing limits the maximum resolution; at conjunction lines will move by at most $\sim$ 37 km s^{-1}. Since the widths of the lines seen in the spectra are at least $\sim$ 100 km s^{-1}, this effect is not large. The *S/N* becomes progressively worse at longer wavelengths and a large region of the upper red CCD spectra was ignored since there was very little signal. The orbital phase of each spectrum was calculated using the ephemeris of Brinkworth et al. (2006).

The spectral features seen are similar to those reported by Catalan et al. (1994) and Haefner et al. (2004): Balmer lines, which appear as either emission or absorption depending upon the phase, He I and Ca II emission lines and He II 4686 Å in absorption. The Paschen series is also seen in emission in the far red. In addition, Mg II 4481 Å emission is seen as well as a number of fainter Mg II emission lines beyond 7800Å. Weak Fe I emission lines are seen throughout the spectrum and faint C I emission is seen beyond 8300Å (see Table 3.4 for a full list of identified emission lines). The strength of all the emission lines is phase-dependent, peaking at phase 0.5, when the heated face of the secondary star is in full view, then disappearing around the primary eclipse. Several sharp absorption features are observed not to move over the orbital period, these are interstellar absorption features and include interstellar Ca II absorption. The average, continuum normalised UVES blue arm spectrum of NN Ser is shown in Figure 3.1.

Table 3.2: Photometric observations of NN Ser. The primary eclipse occurs at phase 1, 2 etc.

Date	Filters	Telescope	UT start	UT end	Av. exp time (s)	Phase range	Conditions (Transparency, seeing)
17/05/2002	$u'g'r'$	WHT	21:54:40	02:07:54	2.4	0.85–2.13	Good, ∼1.2 arcsec
18/05/2002	$u'g'r'$	WHT	21:21:20	02:13:17	3.9	0.39–1.23	Variable, 1.2-2.4 arcsec
19/05/2002	$u'g'r'$	WHT	23:58:22	00:50:52	2.0	0.93–1.10	Fair, ∼2 arcsec
20/05/2002	$u'g'r'$	WHT	00:58:23	01:57:18	2.3	0.86–1.14	Fair, ∼2 arcsec
19/05/2003	$u'g'z'$	WHT	22:25:33	01:02:25	6.7	0.47–1.12	Variable, 1.5-3 arcsec
21/05/2003	$u'g'i'$	WHT	00:29:00	04:27:32	1.9	0.32–0.59	Excellent, ∼1 arcsec
22/05/2003	$u'g'i'$	WHT	03:24:57	03:50:40	2.0	0.36–1.08	Excellent, <1 arcsec
24/05/2003	$u'g'i'$	WHT	22:58:55	23:33:49	2.0	0.90–1.08	Good, ∼1.2 arcsec
25/05/2003	$u'g'i'$	WHT	01:29:45	02:15:58	2.0	0.39–0.64	Excellent, ∼1 arcsec
03/05/2004	$u'g'i'$	WHT	22:13:44	05:43:11	2.5	0.37–2.27	Variable, 1.2-3.2 arcsec
04/05/2004	$u'g'i'$	WHT	23:18:46	23:56:59	2.5	0.91–1.61	Variable, 1.2-3 arcsec
09/03/2006	$u'g'r'$	WHT	01:02:34	06:46:49	2.0	0.91–2.70	Variable, 1.2-3 arcsec
10/03/2006	$u'g'r'$	WHT	05:01:13	05:50:14	2.0	0.85–1.11	Excellent, <1 arcsec
09/06/2007	$u'g'i'$	VLT	04:59:25	05:46:18	0.9	0.40–0.61	Excellent, ∼1 arcsec
16/06/2007	$u'g'i'$	VLT	03:57:48	04:54:39	2.0	0.86–1.15	Good, ∼1.2 arcsec
17/06/2007	$u'g'i'$	VLT	01:50:16	02:38:09	1.0	0.86–1.11	Excellent, <1 arcsec
07/08/2008	$u'g'r'$	WHT	23:41:29	00:22:46	2.8	0.87–1.07	Excellent, <1 arcsec

3.3.2 Photometry

The photometric data presented in this chapter were collected with the high speed CCD camera ULTRACAM (Dhillon et al., 2007), mounted as a visitor instrument on the 4.2m William Herschel Telescope (WHT) and on the VLT in June 2007. A total of ten observations were made in 2002 and 2003, and these data were supplemented with observations made at a rate of $\sim 1-2$ a year up until 2008. ULTRACAM is a triple beam camera and most of our observations were taken simultaneously through the SDSS u', g' and i' filters (where the prime denotes the ULTRACAM filters, which are slightly different from the SDSS filters). In a number of instances an r' filter was used in place of i'; this was mainly for scheduling reasons. Additionally, a z' filter was used in place of i' for one night in 2003. A complete log of the observations is given in Table 3.2. The data were reduced following the procedure outlined in Chapter 2.

The light curves were corrected for extinction differences by using the comparison star observations. A first-order polynomial was fit to the comparison star photometry in order to determine the comparison star's colours (magnitudes listed in Table 3.3). The colour of the white dwarf in NN Ser was calculated by fitting a zeroth-order polynomial to the flat regions around the primary eclipse with a correction made in the r' and i' bands for the secondary stars contribution (the contribution of the secondary star in the u' and g' bands around the primary eclipse is negligible). The colour dependent difference in extinction coefficients for the com-

Table 3.3: Comparison star magnitudes and positional offsets from NN Ser. There were no i' band observations of star D.

Star	u'	g'	r'	i'	RA off. (arcsec)	Dec off. (arcsec)
A	17.0	15.6	15.8	15.0	-34.1	+2.2
B	16.0	14.7	15.1	14.3	-46.4	+106.7
C	14.6	13.4	13.7	12.8	-114.5	+103.7
D	16.7	14.6	13.7	–	-22.2	-94.1

parison star and NN Ser were then calculated from a theoretical extinction vs. colour plot[1]. The additional extinction correction for NN Ser for each night is then

$$10^{\frac{1}{2.5}(k_N - k_C)X}, \tag{3.1}$$

where k_N is the extinction coefficient for NN Ser, k_C is the extinction coefficient for the comparison and X is the airmass. The value of $k_N - k_C$ for each band was similar for all the comparisons used. In the u' filter $k_N - k_C \sim 0.03$, for the g' band $k_N - k_C \sim 0.02$, for the r' band $k_N - k_C \sim 0.002$ and for the i' band $k_N - k_C \sim 0.0005$.

The flux-calibrated, extinction-corrected light curves for each filter were phase binned using the ephemeris of Brinkworth et al. (2006). Data within each phase bin were averaged using inverse variance weights whereby data with smaller errors are given larger weightings. Smaller bins were used around both the eclipses. The result of this is a set of high signal-to-noise light curves for NN Ser (one for each filter).

3.4 Results

3.4.1 The White Dwarf's Spectrum

In order to recover the white dwarf's spectrum, its radial velocity amplitude must be calculated. Due to the broad nature of the Balmer absorption features and the contamination by emission from the secondary star, we concluded that using the Balmer absorption lines to calculate the radial velocity amplitude of the white dwarf would be likely to give an incorrect result. Fortunately, the narrower He II 4686 Å absorption line is seen in absorption at all phases and no HeII emission is seen at any time throughout the spectra. In addition, there are no nearby features around

[1] theoretical extinction vs. colour plots for ULTRACAM are available at http://garagos.net/dev/ultracam/filters

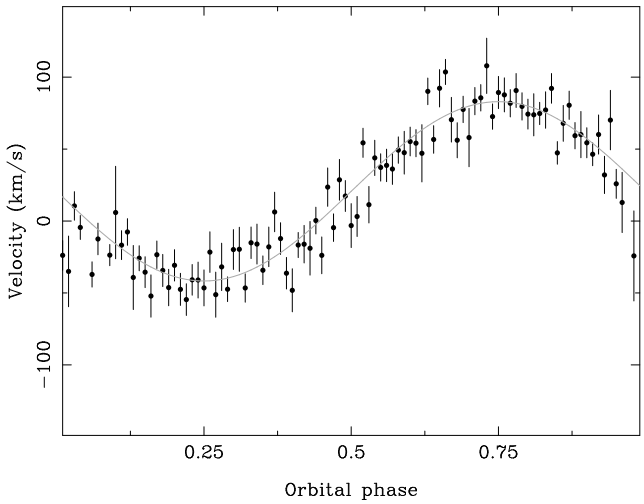

Figure 3.2: Sine curve fit for the He II 4686 Å absorption line fitted with a straight line and a Gaussian. The measured radial velocity amplitude for the primary is $62.3 \pm 1.9\,\mathrm{km\,s^{-1}}$.

the He II 4686 Å line making it a good feature to use to calculate the radial velocity amplitude of the white dwarf; it is indeed the only clean feature from the white dwarf that could be identified. The line was fitted using the method outlined in Section 2.3.

Figure 3.2 shows the fit to the He II 4686 Å velocities. The radial velocity amplitude found is $62.3 \pm 1.9\,\mathrm{km\,s^{-1}}$ significantly smaller than the value of $80.4 \pm 4.1\,\mathrm{km\,s^{-1}}$ calculated indirectly by Haefner et al. (2004) from their light curve analysis as they relied upon a mass-radius relation for the secondary star. The difference is due to their overestimation of the mass of the secondary star by roughly 30%.

Just before and after the primary eclipse the reprocessed light from the secondary star is not yet visible, hence spectra taken at these phases contain just the white dwarf's features. More precise constraints on this range can be made by studying the Balmer lines. The deep wide Balmer absorption lines from the white dwarf are gradually filled in by the emission from the secondary star as the system moves away from the primary eclipse. Multiple Gaussians were fit to the Balmer absorption features, any deviation from this is due to emission from the secondary star which increases the measured velocity amplitude of the lines. Figure 3.3 shows this fit along with the He II 4686 Å radial velocity amplitude fit. No deviation is seen before phase ~ 0.12 and after phase ~ 0.88 hence spectra taken between these phases effectively contain spectral information on the white dwarf only (except those

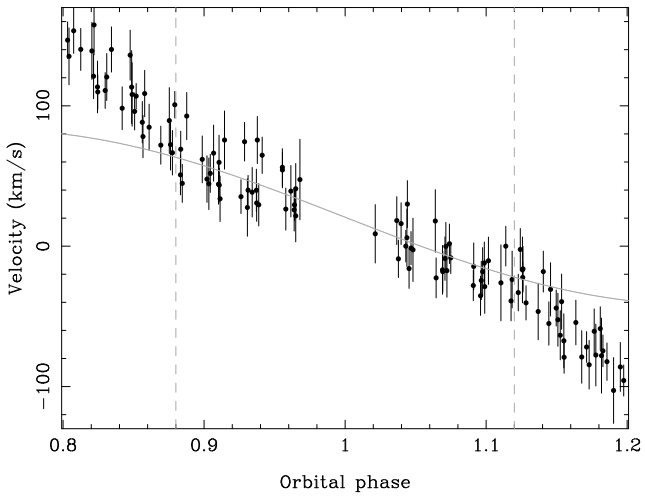

Figure 3.3: Sine curve fit to the Balmer absorption features near the primary eclipse over-plotted with the radial velocity amplitude of the primary calculated using the He II line, the deviations away from the eclipse are caused by emission from the secondary star, hence those spectra within the *dashed* lines contain no emission from the secondary star.

taken during the eclipse).

The spectra were shifted to the white dwarf's frame using the calculated radial velocity amplitude, then the spectra within the phase range quoted were averaged using weights for optimum signal-to-noise (ignoring those spectra taken during the eclipse). The result is the spectrum of the white dwarf component of NN Ser only, as shown in Figure 3.4. A homogeneously-mixed hydrogen and helium atmosphere white dwarf model with a temperature of $57,000K$ and $\log g = 7.5$ was matched to the white dwarf spectrum (also shown in Figure 3.4)[2]. A helium abundance of $4.0 \pm 0.5 \times 10^{-4}$ by number is required to reproduce the measured equivalent width of the He II line (0.25 ± 0.02Å). The result is broadly in agreement with that of Haefner et al. (2004) ($N_{\rm He} = 2 \pm 0.5 \times 10^{-4}$ by number) given that a simplified treatment of the Stark broadening of the He II line was used to calculate the model (TLUSTY, Hubeny 1988, Hubeny & Lanz 1995). The white dwarf spectrum shows only Balmer and He II 4686 Å absorption features (the other sharp absorption features throughout the spectrum are interstellar absorption lines), no absorption lines are seen in the red spectra. This confirms previous results that the classification of the white dwarf is of type DAO1 according to the classification scheme of Sion et al. (1983).

[2]This was performed by B. Gänsicke

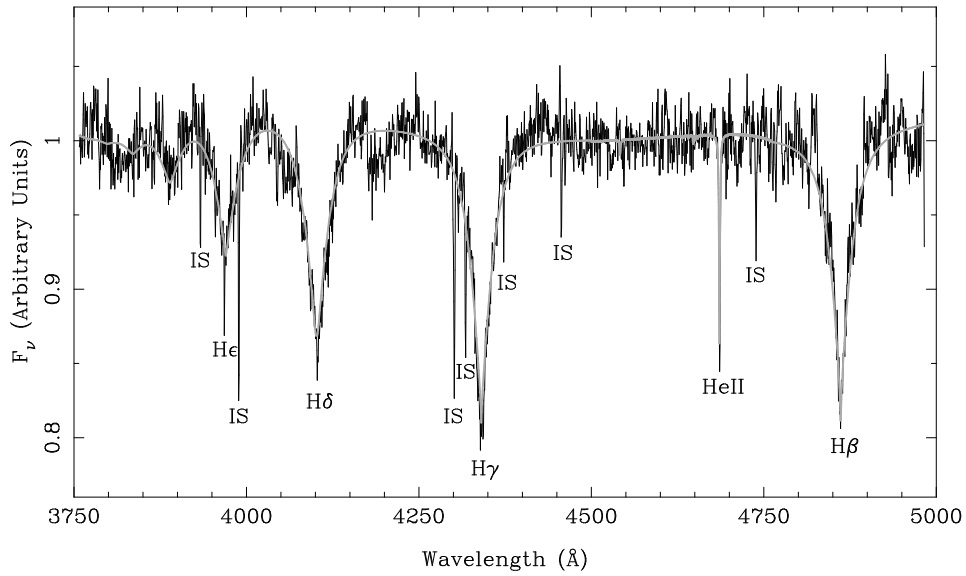

Figure 3.4: Normalised white dwarf spectrum with an over-plotted $T = 57000K$, $\log g = 7.5$ white dwarf model spectrum including homogeneously mixed helium ($N_{\rm He} = 4 \times 10^{-4}$ by number). IS corresponds to interstellar absorption features.

3.4.2 Secondary Star's Spectrum

The most striking features of the UVES spectra are the emission lines arising from the heated face of the secondary star, the most prominent of which are the Balmer lines. Figure 3.5 shows trailed spectra of several lines visible across the spectral range covered. The white dwarf component has been subtracted which creates a peak on the CaII trail that appears to move in anti-phase with the secondary, due to interstellar absorption. The top row shows three Balmer lines (Hδ,Hγ and Hβ) which clearly show reversed cores, becoming more prominent at increasing wavelength. Interestingly, the same effect is not visible in the Paschen series. Large broadening is obvious in all the hydrogen lines compared to the helium and calcium lines.

Radial velocities can be measured from these emission lines using the same method used to fit the white dwarf features. However, as noted in Section 2.3, the measured radial velocity amplitude will be that of the emitting region on the face of the secondary star, hence the radial velocity amplitude of the centre of mass of the secondary star will be larger than that measured from these lines.

The white dwarf component was subtracted from each spectrum and the emission lines fitted. A double Gaussian fit was applied to the double peaked Balmer emission lines, whereby the separation of the two Gaussians was allowed to vary.

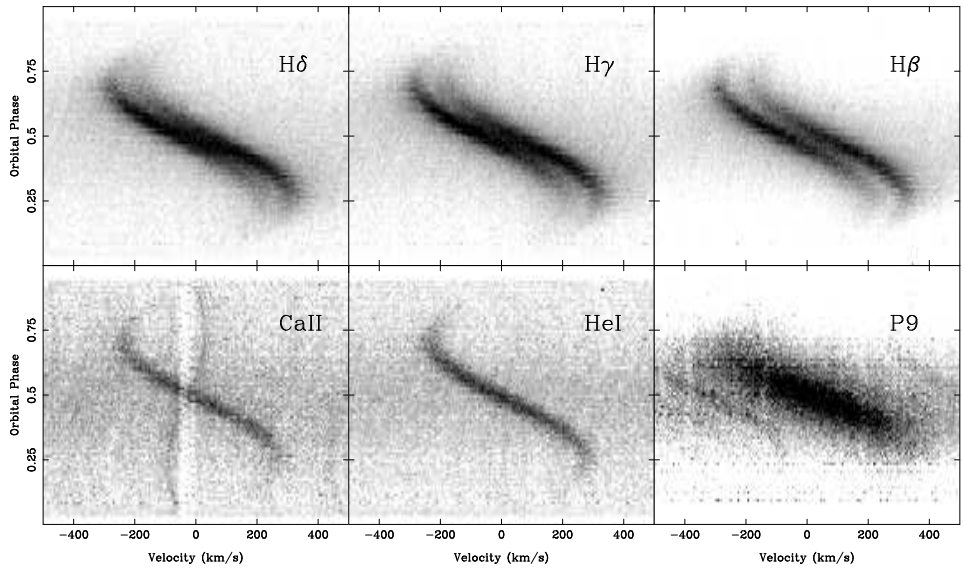

Figure 3.5: Trailed spectra of various lines. The white dwarf component has been subtracted. White represents a value of 0.0 in all trails. For the Balmer lines and the Paschen line, black represents a value of 2.0, for the other lines, black represents a value of 1.0. The subtraction of the white dwarf component creates a peak on the CaII trail due to the presence of interstellar absorption.

Figure 3.6 shows the fit to several lines: all the Balmer lines fitted simultaneously (H11 to Hβ), several He I lines fitted simultaneously and a fit to the Mg II 4481 Å line. All the lines show a similar deviation from a sinusoidal shape at small and large phases (≤ 0.25 and ≥ 0.75). This is because of the non-uniform distribution of flux over the secondary star. The radial velocity amplitude was calculated using only the points between these phases. The measured radial velocity amplitude varies for each line, the Balmer lines showing a larger radial velocity amplitude than most of the other lines. In addition, the radial velocity amplitude of the Balmer lines decreases towards the higher energy states. The spread in measured values is related to the optical depth for each line; as is discussed in Section 2.3.

The Balmer, Mg II and He I lines from the UVES blue spectra were fitted. Furthermore, several He I lines in the red spectra were fit as well as the Paschen lines (P12 to Pϵ). Although several Fe I lines are seen, they are too faint to calculate the radial velocity amplitude of the secondary star reliably. Nonetheless, they do show the same phase dependant variations as all the other emission lines.

In addition to radial velocity information, the widths of the lines were fit. The widths of each of the emission lines vary strongly with phase and noticeable differences are seen between different atomic species. All of the hydrogen lines

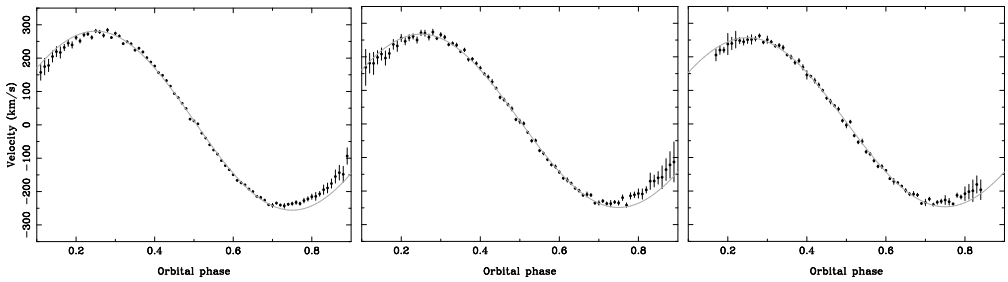

Figure 3.6: Sine curve fits for the Balmer lines (*left*), the three strongest He I lines (*centre*), and the Mg II 4481 Å line (*right*). The lines were fit using a straight line and a Gaussian. The Mg II 4481 Å line becomes too faint before phase 0.15 and after phase 0.85 to fit.

(both Balmer and Paschen lines) show a sharp increase in width around phase 0.1 which flattens off until phase 0.9 where the width falls off sharply. In contrast, the helium and magnesium lines show a gradual increase in width up to phase 0.5, then a gradual decrease. The behaviour of the hydrogen lines may be due to the lines saturating. Figure 3.7 shows the average width of a selection of lines around the secondary eclipse (phase 0.5). The most striking feature is the width of the hydrogen lines which are at least double the width of any other line and reach widths of almost $600\,\mathrm{km\,s^{-1}}$. An interesting trend is seen throughout the Balmer and Paschen series whereby the shorter wavelength lines are wider. The widths of these lines is probably an indication of Stark broadening which affects higher energy states to a larger extent. However, the longer wavelength Balmer lines become wider after Hδ (the slight increase in the width of the Hϵ line is due to the overlapping Ca II 3968 Å line and the nearby He I 3965 Å line), presumably as a result of high optical depth leading to stronger saturation.

To recover the spectrum of the emitting region of the secondary star only, the simultaneous fit to all the He I lines was used to shift the spectra to the frame of the emitting region of the secondary star. This radial velocity amplitude was used because it lies in the centre of the measured amplitudes. The shifted spectra were then averaged, with larger weights given to those spectra taken around phase 0.5 where the reflection effect is greatest. Having previously subtracted the white dwarf's spectrum, the result is the spectrum of only the irradiated part of the secondary star. The UVES blue arm spectrum of the secondary star is shown in Figure 3.8 with the identified lines labeled. As previously mentioned, due to interstellar absorption lines, the subtraction of the white dwarf results in peaks that appear similar to the emission lines in Figure 3.8. These occur just before the

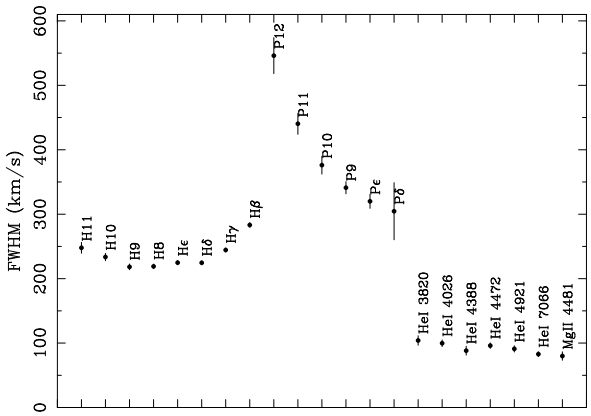

Figure 3.7: Widths of selected lines around the secondary eclipse, where they are at their widest. Note the large difference between the widths of the Hydrogen lines and that of every other species.

He I 4472 Å line and after the He I 4713 Å line.

Once again the inverted core of the Balmer lines is the most striking feature. This can be seen even more clearly in Figure 3.9. For the shorter wavelength lines, there appears to be no core inversion. However, as the wavelength increases the effect becomes more pronounced. The separation between the two peaks in each line increases up to phase 0.5, reaching a maximum separation of $125\,\mathrm{km\,s^{-1}}$ for the Hβ line, the separation decreases symmetrically around phase 0.5. This effect was found to be caused by departure from local thermodynamic equilibrium (LTE) in the upper atmosphere, which causes an over-population of the $n = 2$ energy level of the hydrogen atoms(Barman et al., 2004). Since this occurs high in the atmosphere it is the centre of the line that is affected. It is only seen in the hydrogen lines, and only the Balmer series. The Paschen lines, also shown in Figure 3.9, show no such core inversion.

The trailed spectra of the Balmer lines in Figure 3.5 show, in addition to the core inversion, a clear asymmetry between the two peaks whereby the more shifted peak appears stronger (e.g. the most redshifted peak at phase 0.25 and the most blueshifted at phase 0.75). Barman et al. (2004) found that the line profiles of the hydrogen Balmer emission lines from the heated face have reversed cores, due to non-LTE effects. However, they did not take orbital effects into account, which will introduce an asymmetry into the line profile since at some phases parts of the emission region will not be visible, suppressing the flux at the velocity corresponding to that region. To test if the asymmetry is caused purely by a combination of the non-LTE effects and the orbital motion, a model line profile was used which was

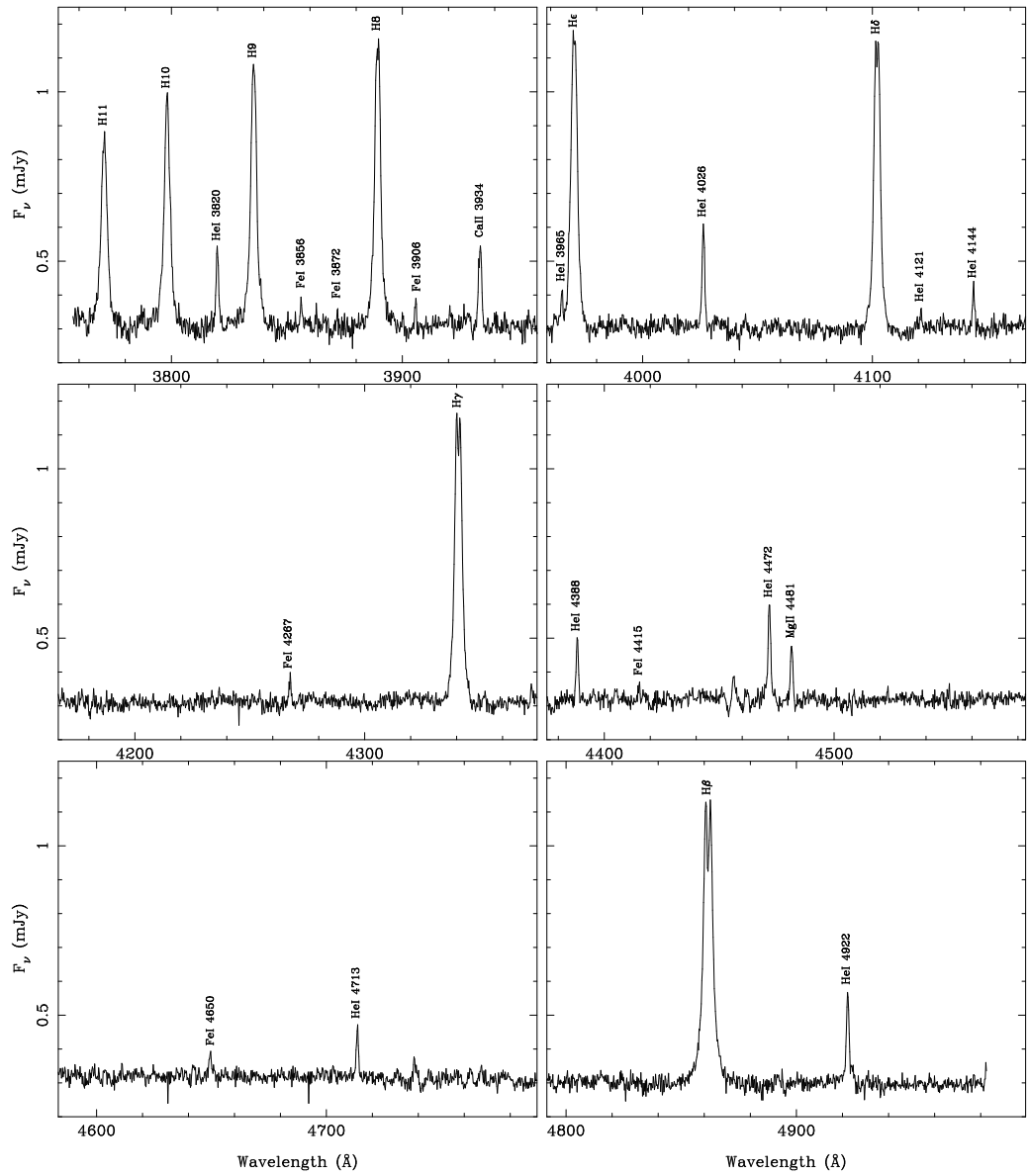

Figure 3.8: Blue spectrum of the heated part of the secondary star. The white dwarf component has been subtracted. The peaks seen just before the He I 4472 Å line and after the He I 4713 Å line are a result of interstellar absorption lines being subtracted off and are not real emission lines.

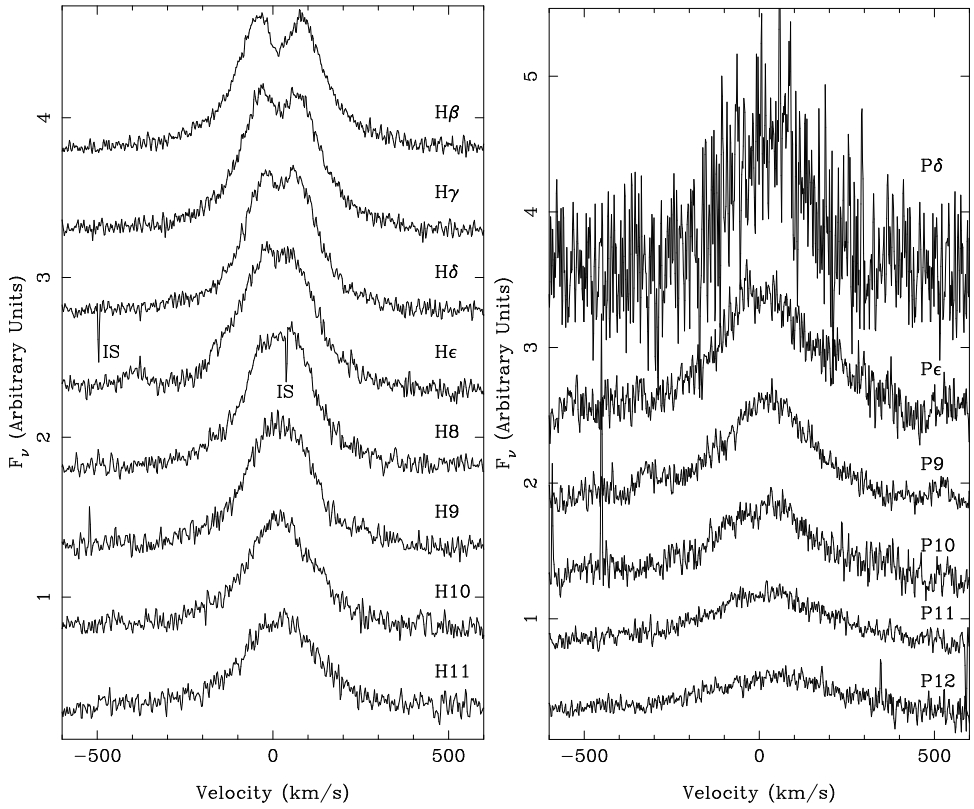

Figure 3.9: *Left*: Profiles of the Balmer lines. IS corresponds to interstellar absorption features. *Right*: Profiles of the Paschen lines. The white dwarf component has been subtracted and the motion of the secondary star removed.

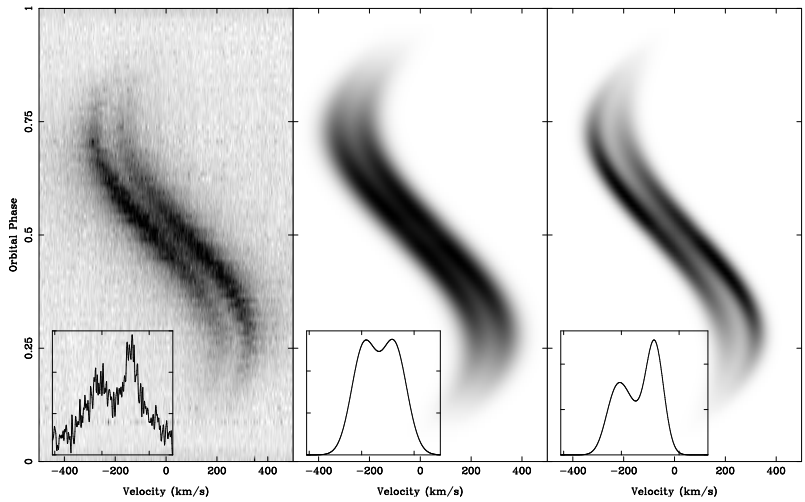

Figure 3.10: *Left*: trailed spectrum of the Hβ line with the white dwarf and continuum subtracted. *Centre*: trailed spectrum of model line profiles convolved with two Gaussians set to reproduce the profile of the Hβ emission line. *Right*: trailed spectrum of a model with a varying line profile across the face of the secondary star, also set to reproduce the profile of the Hβ emission line. Inset on each trail is the profile at phase 0.3; the first model fails to reproduce the observed asymmetry.

similar to the emission line profiles described in Section 2.3. The profile was altered to be double peaked across the surface of the secondary star. This was achieved by convolving the single peaked model with a pair of Gaussians over a full orbital phase, this mimics the reversed core behaviour whilst retaining the orbital effects. The width and separation of the Gaussians was set equal to that measured for the Hβ line. A trailed spectrum of the resulting profile is shown in the central panel of Figure 3.10 next to a trailed spectrum of the Hβ line. The overall shape is similar and there is a small asymmetry, but the effect is far smaller than that seen in the Hβ line, as seen in the profiles at phase 0.3 shown inset.

A possible explanation of the asymmetry is that the optical depth of the line emission varies across the surface of the secondary star. The emission originating from the heavily irradiated region is optically thick (producing the double peaked profile explained by Barman et al. 2004). But further from this region, the irradiation flux decreases and the emission becomes more optically thin, changing the line profile towards a single peak. Since this region of optically thinner emission has a larger radial velocity amplitude, the more shifted peak's emission is increased resulting in the observed asymmetry.

To determine whether optical depth effects are responsible for the observed

asymmetry, the model was adjusted to vary the shape of the line profile across the face of the secondary star. A pair of Gaussians was used that get closer together as the irradiation flux decreases. The result is shown in the right hand panel of Figure 3.10. The model shows better agreement with the Hβ line profile and the asymmetry is visible. Hence it is necessary to allow for the variation in irradiation levels and the non-LTE core reversal in order to model the line profiles in NN Ser.

Non-LTE effects have also been seen in other pre-cataclysmic variable systems such as HS 1857+5144 (Aungwerojwit et al., 2007) where the Hβ and Hγ profiles are clearly double-peaked, V664 Cas and EC 11575–1845 (Exter et al., 2005) both show Stark broadened Balmer line profiles with absorption components. Likewise, double-peaked Balmer line profiles were observed in HS 1136+6646 (Sing et al., 2004) and Feige 24 (Vennes & Thorstensen, 1994); GD 448 (Maxted et al., 1998) also shows an asymmetry between the two peaks of the core-inverted Balmer lines. Since NN Ser is the only system observed with echelle resolution it shows this effect more clearly than any other system.

The secondary star's spectrum contains a large number of emission lines throughout. Each line was identified using rest wavelengths obtained from the National Institute of Standards and Technology[3] (NIST) atomic spectra database. The velocity offset (difference between the rest and measured wavelength) and FWHM of each line were obtained by fitting with a straight line and a Gaussian. The line flux and equivalent width (EW) were also measured. Table 3.4 contains a complete list of all the lines identified. In addition to the already known hydrogen, helium and calcium lines, there are a number of Mg II lines throughout the spectra as well as Fe I lines in the blue spectra and C I lines in the red spectra. The EW of the Balmer lines increases monotonically from H11 to Hβ but the core inversion causes the line flux to level off after the Hϵ line. In addition to the Paschen P12 to Pδ lines, half of the P13 line is seen (cut off by the spectral window used in the UVES upper red chip).

The offsets for each line measured in Table 3.4 combined with the measured offset of the He II absorption line from the white dwarf, give a measurement of the gravitational redshift of the white dwarf. The He II absorption line has an offset of $25.6 \pm 2.7\,\mathrm{km\,s^{-1}}$ measured in the same way as for the emission lines. Taking a weighted average of the emission line velocities gives an offset of $15.1 \pm 0.2\,\mathrm{km\,s^{-1}}$, resulting in a gravitational redshift of $10.5 \pm 2.7\,\mathrm{km\,s^{-1}}$ for the white dwarf. This fairly small redshift is most likely due to the fact that the white dwarf is very hot leading to an inflated radius, as we will see shortly.

[3] http://physics.nist.gov/PhysRefData/ASD/lines_form.html

Table 3.4: Identified emission lines in the UVES spectra. Each line was fitted with a Gaussian to determine the velocity and FWHM.

Line ID	Velocity ($km\,s^{-1}$)	FWHM ($km\,s^{-1}$)	Line Flux (10^{-15} $ergs\,cm^{-2}s^{-1}Å^{-1}$)	Equivalent Width (Å)	comment
H11 3770.634	16.4±1.5	250.7±4.1	3.10(4)	4.36(5)	-
H10 3797.910	12.6±1.1	233.9±2.9	3.46(4)	4.74(5)	-
He I 3819.761	12.4±1.8	107.4±4.5	0.46(2)	0.69(3)	-
H9 3835.397	13.5±0.9	223.1±2.4	4.32(4)	6.30(6)	-
Fe I 3856.327	11.0±3.7	63.2±9.9	0.12(1)	0.20(2)	-
Fe I 3871.749	14.7±2.8	50.0±7.0	0.11(2)	0.20(3)	-
H8 3889.055	14.6±0.7	223.1±1.8	4.46(3)	6.51(4)	-
Fe I 3906.479	10.1±3.6	68.2±8.8	0.22(2)	0.41(4)	-
Ca II 3933.663	-2.9±1.4	106.8±3.7	0.64(2)	1.06(3)	Interstellar absorption present
He I 3964.727	12.2±3.2	85.7±8.0	0.30(2)	0.55(3)	Close to the Hϵ line
Hϵ 3970.074	4.6±0.7	249.4±2.0	5.44(3)	9.59(6)	-
He I 4026.189	14.3±1.0	96.3±2.8	0.71(2)	1.28(3)	-
Hδ 4101.735	17.1±0.6	231.0±1.5	4.72(3)	8.57(5)	-
He I 4120.824	10.3±4.4	73.9±9.8	0.12(1)	0.24(2)	-
He I 4143.759	15.6±2.5	85.2±6.4	0.29(1)	0.59(3)	-
Fe I 4266.964	12.8±4.5	97.9±10.5	0.22(2)	0.49(3)	-
Hγ 4340.465	14.5±0.6	255.9±1.5	4.74(2)	9.40(4)	-
He I 4387.928	18.1±1.4	80.7±3.6	0.34(1)	0.74(2)	-
Fe I 4415.122	15.5±4.4	66.4±11.1	0.18(1)	0.42(2)	-
He I 4471.681	14.5±1.0	86.3±2.5	0.54(2)	1.15(2)	-
Mg II 4481.327	16.9±1.3	89.5±3.5	0.33(1)	0.74(2)	-
Fe I 4649.820	18.9±4.6	80.7±8.8	0.13(1)	0.30(2)	-
He I 4713.146	14.7±1.4	76.6±3.7	0.12(1)	0.57(2)	-
Hβ 4861.327	14.7±0.4	262.0±1.3	4.26(2)	10.34(4)	-
He I 4921.929	16.4±1.0	81.7±2.5	0.39(1)	1.05(2)	-
He I 7065.709	15.4±0.4	78.4±1.1	0.27(3)	1.17(1)	-
He I 7281.349	16.0±0.7	67.3±2.0	0.13(3)	0.64(1)	-
Mg II 7877.051	12.6±3.1	37.1±7.8	0.12(3)	0.23(2)	-
Mg II 7896.368	12.9±2.2	54.8±5.7	0.15(4)	0.30(2)	-
C I 8335.15	9.9±4.1	44.2±6.6	0.11(4)	0.20(3)	-
Ca II 8498.02	14.4±2.7	99.8±8.3	0.14(5)	0.90(3)	-
P12 8750.473	16.6±5.3	402.4±16.8	1.15(2)	5.49(1)	Half of P13 line seen as well
P11 8862.784	16.5±2.7	376.2±8.0	1.68(2)	8.16(9)	-
Ca II 8927.36	18.0±3.6	58.3±9.5	0.13(1)	0.65(5)	-
P10 9014.911	13.1±2.7	280.4±8.1	1.97(2)	10.27(9)	-
C I 9061.43	12.1±4.6	35.6±7.7	0.12(3)	0.28(4)	-
Mg II 9218.248	16.2±2.6	48.9±7.6	0.12(6)	0.51(4)	Close to the P9 line
P9 9229.015	15.1±1.3	316.5±3.6	2.42(2)	11.47(8)	-
Mg II 9244.266	16.0±2.5	44.6±6.4	0.14(3)	0.40(3)	-
C I 9405.73	10.7±5.1	46.0±8.0	0.15(1)	0.87(7)	-
Pϵ 9545.972	16.4±2.3	332.3±6.4	3.39(4)	19.58(7)	-
Pδ 10049.374	18.4±7.4	253.4±22.2	2.7(1)	18.0(7)	Very noisy in the far red

3.5 System Parameters

3.5.1 Light Curve Analysis

The ULTRACAM light curves of NN Ser were fitted using the procedure detailed in Section 2.3 and described in detail in Copperwheat et al. (2010). After a preliminary estimate the mass ratio was fixed at 0.2 (the light curves are only weakly dependent on this parameter), the temperature of the white dwarf fixed at 57,000K (Haefner et al., 2004), the gravity darkening coefficient fixed at 0.08 (the usual value for a convective atmosphere (Lucy, 1967)) and the limb darkening coefficient of the white dwarf fixed at different values for each filter based on a white dwarf model atmosphere with $T_{\rm eff} = 57,000$K and $\log g = 7.46$ using ULTRACAM $u'g'r'i'z'$ filters (Gänsicke et al., 1995). The $\log g$ was obtained from an initial MCMC minimisation of the g' band light curve with the limb darkening coefficient of the white dwarf fixed at a value of 0.2 (the $\log g$ determined from this is very similar to the final value determined later). Changing the $\log g$ by ± 0.1 dex and recomputing the model atmosphere, and hence limb-darkening coefficients, does not have a large effect on the limb-darkening. Furthermore, the final system parameters are only weakly dependent on the limb-darkening coefficients. All other parameters were optimised in the MCMC minimisation. The initial values for the inclination, radii and the temperature of the secondary star were taken from Haefner et al. (2004), the limb darkening coefficient for the secondary star was initially set to zero and the fraction of the irradiating flux from the white dwarf absorbed by the secondary star was initially set to 0.5 (note that the intrinsic flux of the secondary star is negligible).

Since phase-binned light curves were used, T_0 was set to zero but allowed to change while the period was kept fixed at one. The primary and secondary eclipses are the most sensitive regions to the inclination and scaled radii. Hence, in order to determine the most accurate inclination and radii, the data around the two eclipses were given increased weighting in the fit (points with phases between 0.45 and 0.55 and between 0.95 and 0.05 were given twice the weighting of other points). z' band photometry was obtained on only one night and it was of fairly poor quality hence no model was fitted to it. The best fit parameters and their statistical errors are displayed in Table 3.5 along with the linear limb darkening coefficients used for the white dwarf. Figure 3.11 shows the fits to various light curves at different phases. For the secondary eclipse light curves, the same model is over-plotted but with the secondary eclipse turned off, demonstrating the high inclination of this system. The average χ^2, per degree of freedom, for the fits was 1.7 for the g', r' and i' light curves and 2.1 for the u' light curve. The MCMC chains showed no variation beyond that

Table 3.5: Best fit parameters from Markov chain Monte Carlo minimisation for each ULTRACAM light curve. Lin_limb is the linear limb darkening coefficient for the white dwarf which was kept fixed, the values quoted are for a model white dwarf of temperature 57,000K and $\log g = 7.46$. Absorb is the fraction of the irradiating flux from the white dwarf absorbed by the secondary star.

Parameter	u'	g'	r'	i'
Inclination	89.18 ± 0.27	89.67 ± 0.05	89.31 ± 0.21	89.59 ± 0.27
$R_{\rm WD}/a$	0.02262 ± 0.00014	0.02264 ± 0.00002	0.02271 ± 0.00010	0.02257 ± 0.00010
$R_{\rm sec}/a$	0.1660 ± 0.0011	0.1652 ± 0.0001	0.1657 ± 0.0007	0.1654 ± 0.0003
$T_{\rm sec}$	3962 ± 32	3125 ± 10	3108 ± 11	3269 ± 7
Lin_limb$_{\rm WD}$	0.125	0.096	0.074	0.060
Lin_limb$_{\rm sec}$	-1.44 ± 0.13	-0.48 ± 0.03	-0.26 ± 0.02	-0.06 ± 0.03
Absorb	0.899 ± 0.001	0.472 ± 0.001	0.604 ± 0.006	0.651 ± 0.005

expected from statistical variance and the probability distributions are symmetrical and roughly Gaussian.

The errors in Table 3.5 were scaled to give a reduced $\chi^2 = 1$. The inclination was determined by taking a weighted average and is found to be $89.6^\circ \pm 0.2^\circ$. This inclination is much higher than the 84.6° determined by Haefner et al. (2004) but is consistent with the inferred inclination of $\sim 88^\circ$ from Brinkworth et al. (2006). The scaled radius of the white dwarf is $R_{\rm WD}/a = 0.0226 \pm 0.0001$ and the scaled radius of the secondary star is $R_{\rm sec}/a = 0.165 \pm 0.001$. Given our black body assumption, $T_{\rm sec}$ does not represent the true temperature of the secondary star, it is effectively just a scaling factor. An interesting trend is seen in the limb darkening coefficients for the secondary star, which are all negative (limb brightening, although the reflection effect still dominates), the amount of limb brightening decreases with increasing wavelength. This is presumably the result of seeing to different depths at different wavelengths.

Although the ULTRACAM z' photometry was of fairly poor quality (owing to conditions), it was good enough to measure the magnitude of the secondary star during the primary eclipse. A zeroth-order polynomial was fit to the r', i' and z' filter light curves during the primary eclipse. The measured magnitudes were: $r' = 21.8 \pm 0.1$, $i' = 20.4 \pm 0.1$ and $z' = 19.6 \pm 0.1$, which gives colours of $(r' - i')_{\rm sec} = 1.4 \pm 0.1$ and $(i' - z')_{\rm sec} = 0.8 \pm 0.1$ which corresponds to a spectral type of M4 $\pm$ 0.5 (West et al., 2005). This is consistent with the results of Haefner et al. (2004) who fitted the spectral features of the secondary star taken during the primary eclipse to determine a spectral type of M4.75 $\pm$ 0.25.

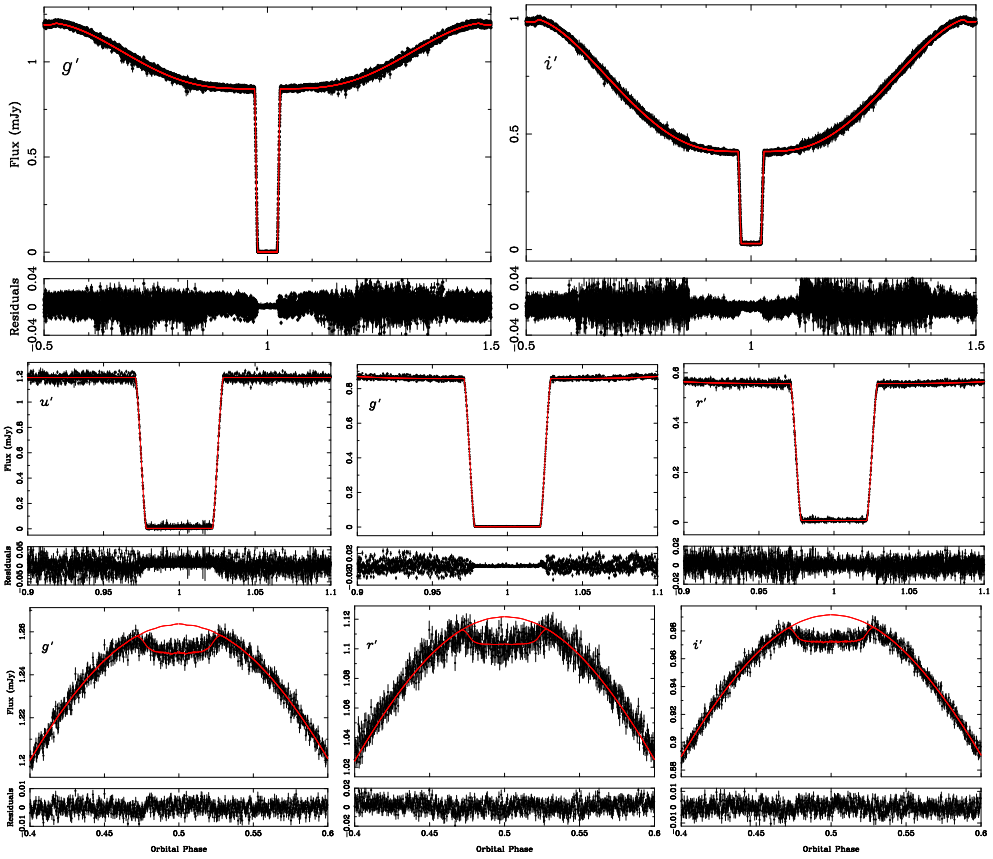

Figure 3.11: Model fits to the ULTRACAM light curves with residuals shown below. *Top*: Full orbital phase. *Centre*: Around the primary eclipse. *Bottom*: Around the secondary eclipse. The light curves have been binned onto a uniform scale hence the regions around phase 0.25 and 0.75 appear noisier because they have been observed less often than the primary and secondary eclipse regions. The secondary eclipse light curves are also shown with a model with no secondary eclipse.

Table 3.6: Distance measurements from each of the ULTRACAM light curves. The absolute magnitudes for the white dwarf in NN Ser were obtained from Holberg & Bergeron (2006) with an error of ±0.1 magnitudes.

Filter	Absolute Magnitude	Measured Magnitude	Extinction (mags)	Distance (pc)
u'	7.264	15.992 ± 0.006	0.258 ± 0.258	494 ± 63
g'	7.740	16.427 ± 0.002	0.190 ± 0.190	501 ± 49
r'	8.279	16.931 ± 0.004	0.138 ± 0.138	505 ± 40
i'	8.666	17.309 ± 0.004	0.104 ± 0.104	510 ± 34
z'	9.025	17.71 ± 0.01	0.074 ± 0.074	527 ± 30

3.5.2 Heating of the Secondary Star

One can make an estimate of the heating effect by comparing the intrinsic luminosity of the secondary star to that received from the white dwarf. The mass-luminosity relation from Scalo et al. (2007), determined by fitting a polynomial to the luminosities and binary star masses compiled by Hillenbrand & White (2004), was used to determine the luminosity of the secondary star as 1.4×10^{-3} $L_\odot$. The luminosity of the white dwarf was calculated using $L_{WD} = 4\pi R^2 \sigma T^4$. Using the radius derived in Section 3.5.4 and the temperature from Haefner et al. (2004) gives the luminosity of the white dwarf as 4.2 $L_\odot$. Using the scaled radius of the secondary star from Table 3.5 translates to the secondary star being hit by over 20 times its own luminosity. Despite this, the colours (hence spectral type) of the unirradiated side are in agreement with the derived mass (Baraffe & Chabrier, 1996) (see Section 3.5.4 for the mass derivation) showing that this extreme heating effect on one hemisphere of the secondary star has no measurable effect on the unirradiated hemisphere.

3.5.3 Distance to NN Ser

Absolute magnitudes for the white dwarf in NN Ser were calculated using a model from Holberg & Bergeron (2006) for a DA white dwarf of mass $0.527 M_\odot$, $\log g = 7.5$ and a temperature of 60,000K which most closely matched the parameters found for NN Ser. An uncertainty of ±0.1 magnitudes was applied to the absolute magnitudes based on the uncertainty in temperature from Haefner et al. (2004) and its effect on the models of Holberg & Bergeron (2006). The magnitudes of the white dwarf in NN Ser were calculated by fitting a zeroth-order polynomial to the flat regions either side of the primary eclipse with a correction made for the flux of the secondary star. The apparent magnitudes were corrected using the reddening value of E(B-V)= 0.05 ± 0.05 from Wood & Marsh (1991) and the conversion of Schlegel et al.

(1998). From these a distance was calculated for each of the ULTRACAM filters. Table 3.6 lists the distances calculated in each of these filters. Using these values gives a distance to NN Ser of 512 ± 43pc consistent with the result of Haefner et al. (2004) of 500 ± 35pc.

The galactic latitude of NN Ser is 45.3° which, combined with the derived distance, gives it a galactic scale height of 364 ± 31pc. The proper motion of NN Ser was retrieved from the US Naval Observatory (USNO) Image and Catalogue Archive. The archive values are $\mu_{\rm RA} = -0.020 \pm 0.003$ and $\mu_{\rm DEC} = -0.056 \pm 0.004$ arcsec / yr. At the derived distance this corresponds to a transverse velocity of $160 \pm 14\,{\rm km\,s^{-1}}$, meaning that NN Ser is likely a thick disc or halo star.

3.5.4 $K_{\rm sec}$ correction

For accurate mass determinations the centre of mass radial velocity amplitude is required thus we need to determine the deviation between the reprocessed light centre and the centre of mass for the secondary star. This is done using the $K_{\rm sec}$ correction method outlined in Section 2.3.2, which requires computing model line profiles from the irradiated face, and from these a light curve.

The code outlined in Section 2.3.2 requires two different sets of information. The first is the physical setup of the system: for these, the light curve model parameters (inclination and scaled radii) were used. The second set of parameters control the resolution of the output. These were set to match the UVES spectra: the line profiles were calculated for phases matching the UVES spectra phases, exposure lengths were set to the same as the UVES blue spectra exposures and sampled in velocity to match the spectra. The profiles are convolved with a Gaussian function, representing the resolution of the spectrograph. In order to match the UVES spectroscopy as closely as possible, the resolution of the spectrograph was calculated by looking at the arc calibration spectra. The intrinsic linewidth of these lines is assumed to be negligible hence the measured linewidth gives an indication of the instrumental resolution, which was found to be 5 $\rm km\,s^{-1}$ (FWHM) for the UVES blue chip.

Figure 3.12 shows the light curve for three different lines over plotted with an optically thick and optically thin model. For the Hβ line, the emission is optically thick, the Mg II line is optically thin and the He I line lies somewhere between these two extremes (the white dwarf component was subtracted from all the light curves). Table 3.7 lists the best fit values for τ_0 and β (see Section 2.3) for each line and the measured and corrected $K_{\rm sec}$ and q values.

The Mg II 4481 Å line appears to be the closest to the optically thin model.

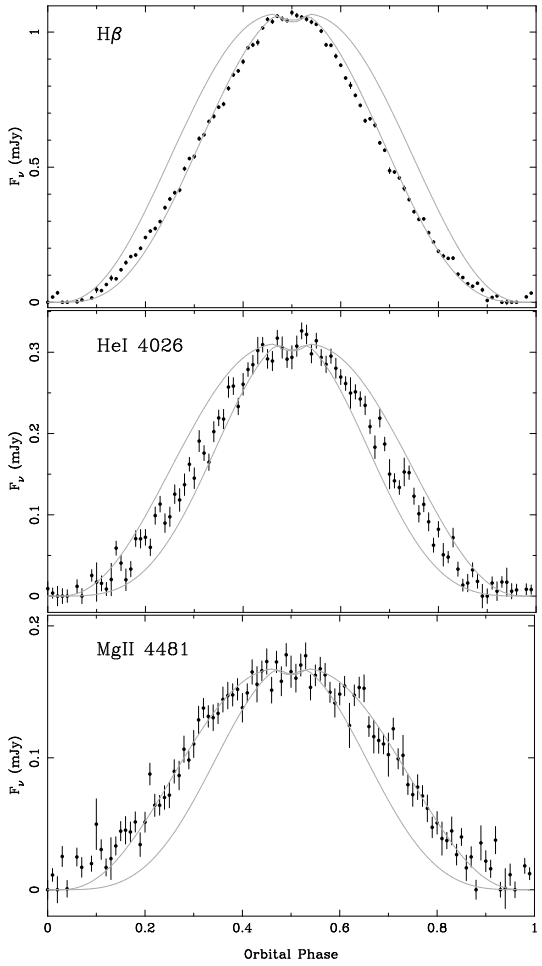

Figure 3.12: Light curves of various lines over-plotted with an optically thick (narrower) and thin (wider) model with the same measured $K_{\rm sec}$ as the line. The model light curves are scaled to match the flux level of the lines around phase 0.5. The Hβ line is optically thick, the Mg II line is optically thin and the He I line is somewhere between thick and thin.

Table 3.7: Measured and corrected values of $K_{\rm sec}$ with the best fit model line profiles parameters, for several lines in the UVES blue spectra.

Line	τ_0	β	$K_{\rm sec,meas}$ km s^{-1}	$K_{\rm sec,corr}$ km s^{-1}	q
He I 3820	2	-0.75	252.2 ± 1.9	296.7 ± 1.9	0.210(6)
He I 4026	1	-3	257.7 ± 1.7	300.1 ± 1.7	0.208(6)
He I 4388	1	-10	249.9 ± 2.0	300.2 ± 2.0	0.208(6)
He I 4472	1	-1.5	263.1 ± 1.8	305.2 ± 1.8	0.204(6)
He I 4922	1	-0.5	255.6 ± 1.8	296.9 ± 1.8	0.210(6)
Hβ	100	-1.5	271.1 ± 1.9	307.6 ± 1.9	0.203(6)
Hγ	100	-1.5	265.1 ± 1.9	302.9 ± 1.9	0.206(6)
Hδ	50	-1.5	265.0 ± 1.9	298.1 ± 1.9	0.209(6)
Hϵ	5	-1.25	263.2 ± 1.9	304.4 ± 1.9	0.205(6)
H8	5	-1	262.5 ± 1.9	303.2 ± 1.9	0.206(6)
H9	2	-0.5	258.1 ± 1.9	297.4 ± 1.9	0.210(6)
H10	2	-0.75	257.2 ± 2.1	299.9 ± 2.1	0.208(6)
H11	1	-2	259.3 ± 2.1	301.2 ± 2.1	0.207(6)
Mg II 4481	0.005	-1.25	252.8 ± 1.8	298.7 ± 1.8	0.209(6)

As such it probably provides the most accurate correction since, in the optically thin case, the angular distribution of the line flux from any given point on the star is even, removing any dependence upon this. Even so, all the corrected values are consistent to within a few km s^{-1}. The first few Balmer lines (Hβ to Hδ) are optically thick but as the series progresses, the lines become more optically thin. There also appears to be a small increase in the value of β throughout the series (with the exception of H10 and H11). The helium lines appear to be somewhere between optically thick and thin.

Figure 3.13 shows the measured values of $K_{\rm sec}$ for several lines from Gaussian fitting in the UVES blue spectra and their corrected values of $K_{\rm sec}$. The spread in values is reduced and the corrected values give a radial velocity amplitude for the secondary star of $K_{\rm sec} = 301\,{\rm km\,s^{-1}}$. The statistical uncertainty is $1\,{\rm km\,s^{-1}}$, however, the error in the correction is dominated by systematic effects from the model and fitting process, for which an error of $3\,{\rm km\,s^{-1}}$ was estimated, based on the scatter seen in Figure 3.13. Some simple considerations can give an idea of the largest possible error that might have been made in correcting the K values. The distance from the centre of the mass to the sub-stellar point in terms of velocity is given by $(K_{\rm WD} + K_{\rm sec})\, R_{\rm sec}/a = 60\,{\rm km\,s^{-1}}$; this is the maximum possible correction. A lower limit comes from assuming the emission to be uniform over the irradiated face of the secondary. Then the centre of light is 0.42 of the way from the centre of

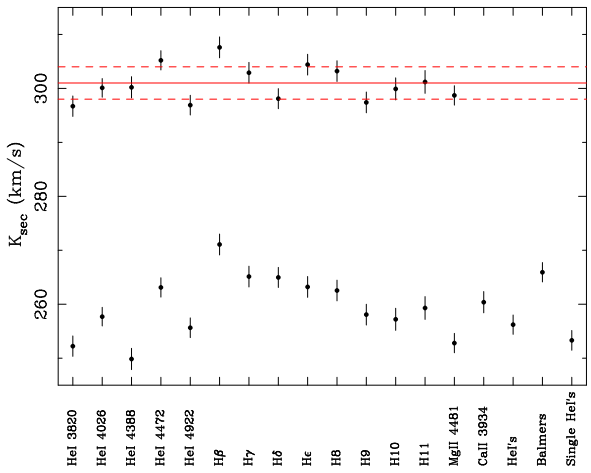

Figure 3.13: *Bottom*: Measured $K_{\rm sec}$ for several lines in the UVES blue spectra from Gaussian fitting and their corrected values (*top*). The Ca II line is contaminated by interstellar absorption which was fitted as an additional Gaussian component and was not corrected. The fit to all the Balmer lines simultaneously is the point labelled 'Balmers'. The point labelled 'HeI's' is a fit to all the visible He I lines whilst the point labelled 'single HeI's' is a fit to only the He I lines which have a single component (i.e. the intensity is not shared by several lines). Our adopted $K_{\rm sec}$ value and uncertainties are shown as red lines.

mass to the sub-stellar point (Wade & Horne, 1988), leading to a lower limit on the correction of $24\,{\rm km\,s^{-1}}$. The corrections from our model range from 33 to $46\,{\rm km\,s^{-1}}$, in the middle of these extremes.

These results imply that the f factor in Equation 2.5 is 0.77 in the optically thin case, and ~ 0.5 in the optically thick case.

From the corrected value of $K_{\rm sec}$ and $K_{\rm WD} = 62.3 \pm 1.9\,{\rm km\,s^{-1}}$ the mass ratio is $q = M_{\rm sec}/M_{\rm WD} = 0.207 \pm 0.006$. Using this, the mass of the white dwarf is then determined using Kepler's third law

$$\frac{PK_{\rm sec}^3}{2\pi G} = \frac{M_{\rm WD}\sin^3 i}{(1+q)^2}, \tag{3.2}$$

using the period (P) from Brinkworth et al. (2006). This gives a value of $M_{\rm WD} = 0.535 \pm 0.012{\rm M}_\odot$. The mass ratio then gives the mass of the secondary star as $M_{\rm sec} = 0.111 \pm 0.004{\rm M}_\odot$. Knowing the masses, the orbital separation is found using

$$a^3 = \frac{G(M_{\rm WD}+M_{\rm sec})P^2}{4\pi^2}, \tag{3.3}$$

which gives a value of $a = 0.934 \pm 0.009{\rm R}_\odot$. Using this gives the radii of the two

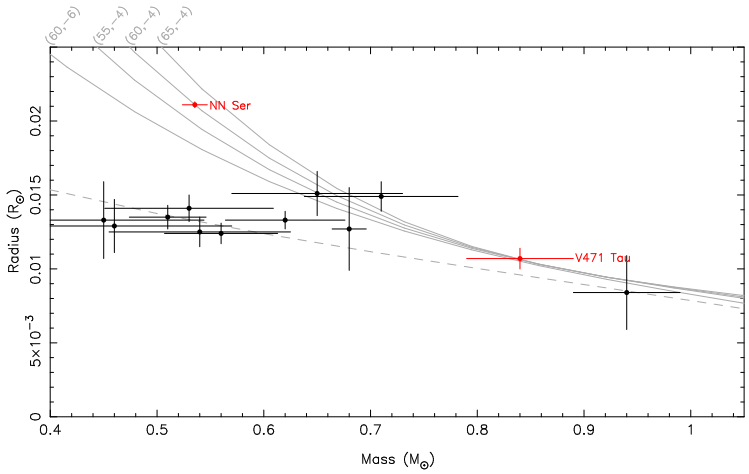

Figure 3.14: Mass-radius plot for white dwarfs measured independent of any mass-radius relations. Data from Holberg et al. (2012) are plotted. The solid lines correspond to different carbon-oxygen core pure hydrogen atmosphere models. The first number is the temperature, in thousands of degrees, the second number is the hydrogen layer thickness (i.e. lines labelled -4 have a thickness of $M_H/M_{WD} = 10^{-4}$) from Benvenuto & Althaus (1999). The dashed line is the zero-temperature mass-radius relation of Eggleton from Verbunt & Rappaport (1988).

stars as $R_{WD} = 0.0211 \pm 0.0002 R_\odot$ and $R_{sec} = 0.154 \pm 0.002 R_\odot$. The radius of the secondary star in our model is measured from the centre of mass towards the white dwarf and hence is larger than the average radius of the secondary star. The radius as measured towards the backside is $R_{sec,back} = 0.153 R_\odot$, the polar radius is $R_{sec,pol} = 0.147 R_\odot$ and perpendicular to these $R_{sec,side} = 0.149 R_\odot$. The volume-averaged radius is $R_{sec,av} = 0.149 \pm 0.002 R_\odot$. The surface gravity of the white dwarf is given by

$$g = \frac{GM_{WD}}{{R_{WD}}^2}, \tag{3.4}$$

which gives a value of $\log g = 7.47 \pm 0.01$.

3.6 Discussion

Figure 3.14 shows the mass and radius of the white dwarf of NN Ser in comparison with other white dwarfs whose mass and radius have been measured independently of any mass-radius relation. The white dwarf in NN Ser is much hotter than the other white dwarfs in Figure 3.14, the mean temperature of the other white dwarfs

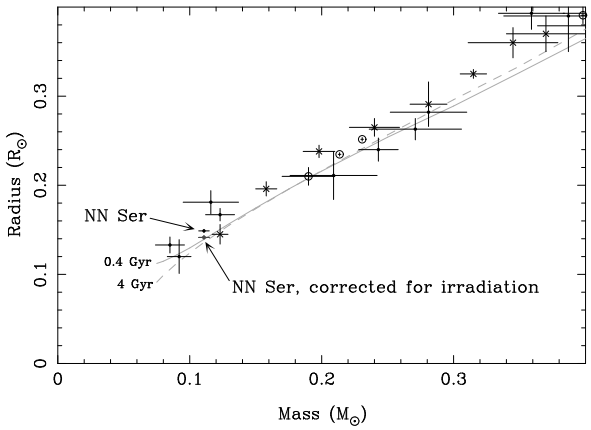

Figure 3.15: Mass-radius plot for low mass stars. Data from López-Morales (2007) and Beatty et al. (2007). The filled circles are secondaries in binaries, the open circles are low mass binaries and the crosses are single stars. The solid line represents the theoretical isochrone model from Baraffe et al. (1998), for an age of 0.4 Gyr, solar metalicity, and mixing length $\alpha = 1.0$, the dotted line is the same but for an age of 4 Gyr. The position of the secondary star in NN Ser is also shown if there were no irradiation effects. The masses of the single stars were determined using mass-luminosity relations.

is $\sim 14,200$K. Also plotted are several mass-radius relations for pure hydrogen atmosphere white dwarfs with different temperatures and hydrogen layer thicknesses from Benvenuto & Althaus (1999). The earlier work from Haefner et al. (2004) and the UVES spectrum of the white dwarf with a model white dwarf spectra over-plotted (Figure 3.4) strongly suggest a temperature for the white dwarf of close to 60,000K (57000 ± 3000K). Assuming the models in Figure 3.14 are correct, the white dwarf in NN Ser shows excellent agreement with having a 'thick' hydrogen layer of fractional mass $M_H/M_{WD} = 10^{-4}$. This is consistent with the inflated radius of the white dwarf due to its high temperature.

Since visual binary systems and common proper-motion systems still rely on model atmosphere calculations to determine radii, the white dwarf in NN Ser is one of the first to have its mass and radius measured independently. O'Brien et al. (2001) determine the mass and radius of both components of the eclipsing PCEB V471 Tau independently. However, since they did not detect a secondary eclipse, they had to rely on less direct methods to determine the radius of the secondary and the inclination. This demonstrates the value of eclipsing PCEBs for investigating the mass-radius relation for white dwarfs.

In addition, the mass and radius of the secondary star have been determined

independently of any mass-radius relation. Since this is a low mass star it helps improve the statistics for these objects and our values are more precise than the majority of comparable measurements. Figure 3.15 shows the position of the secondary star in NN Ser (using the volume-averaged radius) in relation to other low mass stars with masses and radii determined independently of any mass-radius relation (although the masses of the single stars were determined using mass-luminosity relations). For very low mass stars ($M \leq 0.3 M_{\odot}$) the current errors on mass and radius measurements are so large that that one can argue the data are consistent with the low-mass models. However, the secondary star in NN Ser appears to be the first object with errors small enough to show an inconsistency with the models. The measured radius is 10% larger than predicted by the model. However, irradiation increases the radius of the secondary star. For the measured radius of the secondary star in NN Ser, the work of Ritter et al. (2000) and Hameury & Ritter (1997) gives an inflation of 5.6%, based on the difference between the irradiating flux and the secondary star's intrinsic flux. The un-irradiated radius is also shown in Figure 3.15 and is consistent with the models. Hence the secondary star in NN Ser supports the theoretical mass-radius relation for very low mass stars.

Potentially, an initial-final mass relation could be used to estimate the age of NN Ser, but since the system has passed through a common envelope phase its evolution may have been accelerated and the white dwarf may be less massive than a single white dwarf with the same progenitor mass leading to an overestimated age. In addition, the mass of the white dwarf in NN Ser is close to the mean white dwarf mass and the initial-final mass relation is flat in this region. This means a large range of progenitor masses are possible for the white dwarf and hence a large range in age, this means a reliable estimate of the age of NN Ser is not possible. In any case, the position of the un-irradiated secondary star is also consistent with a similarly large range of ages. The mass and radius of the secondary star support the argument of Brinkworth et al. (2006) that it is not capable of generating enough energy to drive period change via Applegate's mechanism (Applegate, 1992).

The system parameters determined for NN Ser are summarised in Table 3.8. Using the UVES spectra, the gravitational redshift of the white dwarf was found to be $10.5 \pm 2.7\,\mathrm{km\,s^{-1}}$. Using the measured mass and radius from Table 3.8 gives a redshift of $16.1\,\mathrm{km\,s^{-1}}$, correcting for the redshift of the secondary star ($0.5\,\mathrm{km\,s^{-1}}$), the difference in transverse Doppler shifts ($0.15\,\mathrm{km\,s^{-1}}$) and the potential at the secondary star owing to the white dwarf ($0.3\,\mathrm{km\,s^{-1}}$) gives a value of $15.2 \pm 0.5\,\mathrm{km\,s^{-1}}$. These two values are only consistent to 2.5 sigma, although in this case, the inflated radius of the white dwarf weakens the constraints of the gravitational redshift. I

Table 3.8: System parameters. (1) this study; (2) Brinkworth et al. (2006); (3) Haefner et al. (2004). WD: white dwarf, Sec: secondary star.

Parameter	Value	Ref.
Period (days)	0.13008017141(17)	(2)
Inclination	$89.6 \pm 0.2^{\circ}$	(1)
Binary separation	0.934 ± 0.009 $R_{\odot}$	(1)
Mass ratio	0.207 ± 0.006	(1)
WD mass	0.535 ± 0.012 $M_{\odot}$	(1)
Sec mass	0.111 ± 0.004 $M_{\odot}$	(1)
WD radius	0.0211 ± 0.0002 $R_{\odot}$	(1)
Sec radius polar	0.147 ± 0.002 $R_{\odot}$	(1)
Sec radius sub-stellar	0.154 ± 0.002 $R_{\odot}$	(1)
Sec radius backside	0.153 ± 0.002 $R_{\odot}$	(1)
Sec radius side	0.149 ± 0.002 $R_{\odot}$	(1)
Sec radius volume-averaged	0.149 ± 0.002 $R_{\odot}$	(1)
WD $\log g$	7.47 ± 0.01	(1)
WD temperature	57000 ± 3000 K	(3)
K_{WD}	$62.3 \pm 1.9\,\mathrm{km\,s^{-1}}$	(1)
K_{sec}	$301 \pm 3\,\mathrm{km\,s^{-1}}$	(1)
WD grav. redshift	$10.5 \pm 2.7\,\mathrm{km\,s^{-1}}$	(1)
WD type	DAO1	(3)
Sec spectral type	$\mathrm{M4} \pm 0.5$	(1)
Distance	512 ± 43 pc	(1)
WD hydrogen layer fractional mass	10^{-4}	(1)

will show in Chapter 5 that there may be some evidence of a slight inconsistency between the spectroscopically measured redshift and that calculated from the radial velocities and light curve fits, although the source of this inconsistency is unknown.

3.7 Summary

In this chapter I have presented high precision mass-radius measurements for both the white dwarf and low-mass M dwarf in the eclipsing PCEB NN Ser. The mass and radius of the white dwarf are consistent with evolutionary models and represent one of the first model-independent tests of white dwarf mass-radius relations. The secondary star is over-inflated compared to evolutionary models of low-mass stars, however, this can be accounted for by correcting for inflation via irradiation from the white dwarf. The mass and radius measurements for the secondary star in NN Ser are amongst the most precise ever for low-mass stars and it is one of the lowest-mass stars to have high-precision measurements.

Chapter 4

The masses and radii of the stars in SDSS J0857+0342

4.1 Introduction

In this chapter I continue the precision study of eclipsing PCEBs. This chapter focuses on the system SDSS J0857+0342 which, like NN Ser, has a visible secondary eclipse. I will apply the techniques described in Chapter 2 to determine precise model-independent masses and radii for both stars in the binary. I will then compare these results with evolutionary models.

4.2 Target information

The subject of this chapter, SDSS J085746.18+034255.3 (henceforth SDSS J0857+0342), was first discovered as a hot ($T_{\rm eff} = 36181 \pm 390$K) white dwarf from the Sloan Digital Sky Survey by Eisenstein et al. (2006). Regular eclipses were observed by Drake et al. (2010) as part of the Catalina Real-time Transient Survey. They determined an orbital period of only 94 minutes making SDSS J0857+0342 the shortest known period, detached, white dwarf / main-sequence binary. There are only a handful of known PCEBs with periods below 2 hours: SDSS J0138-0016 (105 minutes, Becker et al. 2011), SDSS J1329+1230 (116 minutes), WD 0137-349 (116 minutes, Maxted et al. 2006) and SDSS J1611+4640 (118 minutes, Nebot Gómez-Morán et al. 2011). The majority of PCEBs have periods in excess of 3 hours.

Table 4.1: Journal of observations. Exposure times for X-shooter observations are for UVB arm, VIS arm and NIR arm respectively. The primary eclipse occurs at phase 1, 2 etc.

Date at start of run	Instrument	Filter(s)	Start (UT)	Orbital phase	Exposure time (s)	Conditions (Transparency, seeing)
2010/12/03	ULTRACAM	$u'g'r'$	07:14	0.86–1.08	4.0	Excellent, ~ 1 arcsec
2010/12/07	ULTRACAM	$u'g'r'$	06:53	0.95–1.20	4.0	Excellent, ~ 1 arcsec
2010/12/08	ULTRACAM	$u'g'r'$	06:31	0.21–0.63	5.0	Excellent, ~ 1 arcsec
2010/12/09	ULTRACAM	$u'g'i'$	06:49	0.77–1.80	5.0	Excellent, ~ 1 arcsec
2010/12/10	ULTRACAM	$u'g'r'$	06:31	0.93–1.29	4.0	Good, $1.0 - 1.5$ arcsec
2010/12/16	ULTRACAM	$u'g'i'$	04:16	0.68–2.12	4.0	Good, $1.0 - 2.0$ arcsec
2011/01/07	ULTRACAM	$u'g'i'$	06:53	0.54–1.11	4.0	Good, $1.0 - 1.5$ arcsec
2011/01/09	ULTRACAM	$u'g'r'$	04:46	0.70–1.69	4.0	Good, $1.0 - 1.5$ arcsec
2011/01/10	ULTRACAM	$u'g'r'$	04:42	0.03–0.85	4.0	Good, $1.0 - 1.5$ arcsec
2011/01/11	ULTRACAM	$u'g'r'$	03:22	0.53–1.95	4.0	Good, $1.0 - 1.5$ arcsec
2011/02/27	X-shooter	-	03:59	0.94–2.14	191,213,480	Good, $1.0 - 1.5$ arcsec
2011/03/03	X-shooter	-	02:15	0.27–1.35	191,213,480	Good, $1.0 - 1.5$ arcsec
2011/04/06	SOFI	J	00:58	0.72–1.27	15.0	Excellent, < 1 arcsec

4.3 Observations and their reduction

4.3.1 ULTRACAM photometry

SDSS J0857+0342 was observed with ULTRACAM (Dhillon et al., 2007) mounted as a visitor instrument on the New Technology Telescope (NTT) at La Silla, Chile, between December 2010 and January 2011. A complete log of these observations is given in Table 4.1. These data were reduced using the procedure outlined in Chapter 2.

4.3.2 SOFI J band photometry

SDSS J0857+0342 was observed with SOFI mounted at the NTT on the 6th April 2011 (see Table 4.1). The observations were made in fast photometry mode equipped with a J band filter. The detector was windowed to achieve a cycle time of 15 seconds and the telescope was offset every 10 minutes in order to improve sky subtraction. Debiassing (which also removes the dark current) and flatfielding were performed in the standard way. Sky subtraction was achieved by using observations of the sky when the target had been offset. The average sky level was then added back so that we could determine the source flux and its uncertainty with standard aperture photometry, using a variable aperture, within the ULTRACAM pipeline. A comparison star (2MASS $08575095+0340301$, $J = 13.289$) was used to account for variations in observing conditions. Flux calibration was done using the comparison star J band magnitude retrieved from the 2MASS catalogue (Skrutskie et al., 2006).

4.3.3 X-shooter spectroscopy

X-shooter (D'Odorico et al., 2006) service mode observations of SDSS J0857+0342 were obtained in February and March 2011. The observations were designed to cover two entire orbits of the system. Details of these observations are listed in Table 4.1. X-shooter is a medium resolution spectrograph consisting of 3 independent arms that give simultaneous spectra longward of the atmospheric cutoff (0.3 microns) in the UV (the "UVB" arm), optical (the "VIS" arm) and up to 2.5 microns in the near-infrared (the "NIR"arm). We used slit widths of 0.8", 0.9" and 0.9" in X-shooter's three arms and 2×2 binning resulting in a resolution of $R \sim 6,000$. After each exposure we nodded along the slit to help the sky subtraction in the NIR arm. These data were reduced using the procedure outlined in Chapter 2. The K band data are completely dominated by sky noise, the S/N throughout the NIR arm is too low to detect any features from the secondary star.

The ULTRACAM and SOFI light curves were used to flux calibrate the X-shooter spectra. Models were fitted to each of the ULTRACAM light curves (see Section 4.4.2) and the SOFI J-band light curve in order to reproduce the light curve as closely as possible. The model was then used to predict the flux at the times of each of the X-shooter observations. Synthetic fluxes were then derived from the spectra for the ULTRACAM u', g', r', i' and z' filters as well as the SOFI J and H filters. The models were extrapolated to those bands not covered by the photometry. I then calculated the difference between the model and synthetic fluxes and fitted a second-order polynomial to them. This correction was then applied to each spectrum. This corrects for variable extinction across the wavelength range, as well as variations in seeing.

4.4 Results

4.4.1 White dwarf temperature

Eisenstein et al. (2006) and Drake et al. (2010) both determined the temperature of the white dwarf in SDSS J0857+0342 using its SDSS spectra. However, the reprocessed light from the heated face of the secondary star can lead to incorrect results from spectral fitting. Therefore, the X-shooter spectra taken around the eclipse were combined, where the reflection effect is minimal, and used to determine the temperature and $\log g$ values using the method outlined in Rebassa-Mansergas et al. (2007)[1]. Figure 4.1 shows the results of the spectral fit to the white dwarf

[1] This was performed by B. Gänsicke

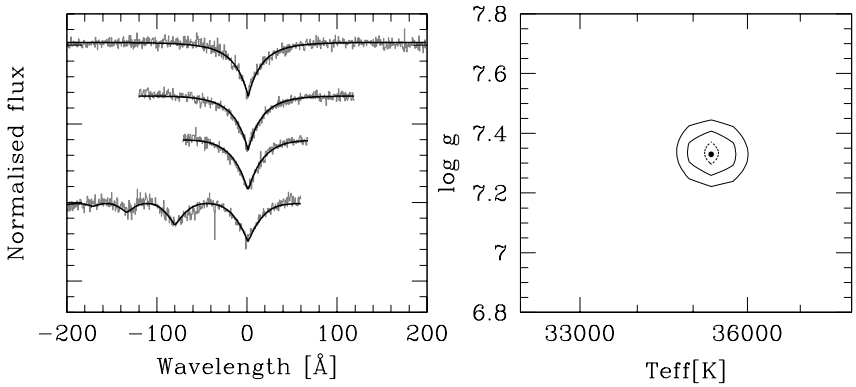

Figure 4.1: Spectral model fit to the white dwarf component of SDSS J0857+0342 from the X-shooter spectroscopy. *Left:* best fit (black lines) to the normalised Hβ to H9 line profiles (gray lines, top to bottom). Interstellar calcium absorption is also visible. *Right:* 1, 2 and 3σ χ^2 contour plots in the $T_{\rm eff} - \log g$ plane to the line profile fits. The intrinsic contribution from the secondary star in this wavelength range is negligible. We remove the reflection component by only selecting those spectra taken around the primary eclipse, where the reflection is minimal.

features. The fit gives a temperature of $35,300 \pm 400$K and a $\log g$ of 7.3 ± 0.1, which is consistent with the light curve model fits and only marginally cooler than the temperature found by fitting the SDSS spectra from Eisenstein et al. (2006) and Drake et al. (2010). The fit also gave a distance to SDSS J0857+0342 of 968 ± 55pc, consistent with previous measurements.

4.4.2 Light curve model fitting

Figure 4.2 shows phase-folded light curves for SDSS J0857+0342 in the ULTRACAM $u'g'r'i'$ bands and the SOFI J band. The deep primary eclipse is clearly visible in all bands; flux is detected in eclipse during the J band eclipse only. A strong reflection effect is also evident in each of the bands caused by reprocessed light from the irradiated face of the secondary star. Also visible is the shallower secondary eclipse which becomes deeper in the redder bands (this phase was not covered by the SOFI observations). The detection of the secondary eclipse allows us to determine the inclination of the system and establish precise scaled radii, $R_{\rm sec}/a$ and $R_{\rm WD}/a$, where a is the orbital separation.

The ULTRACAM light curves of SDSS J0857+0342 were fitted using the procedure detailed in Section 2.3. Each light curve was initially fitted in order to determine the mid-eclipse times and thus an accurate ephemeris. The mid-eclipse

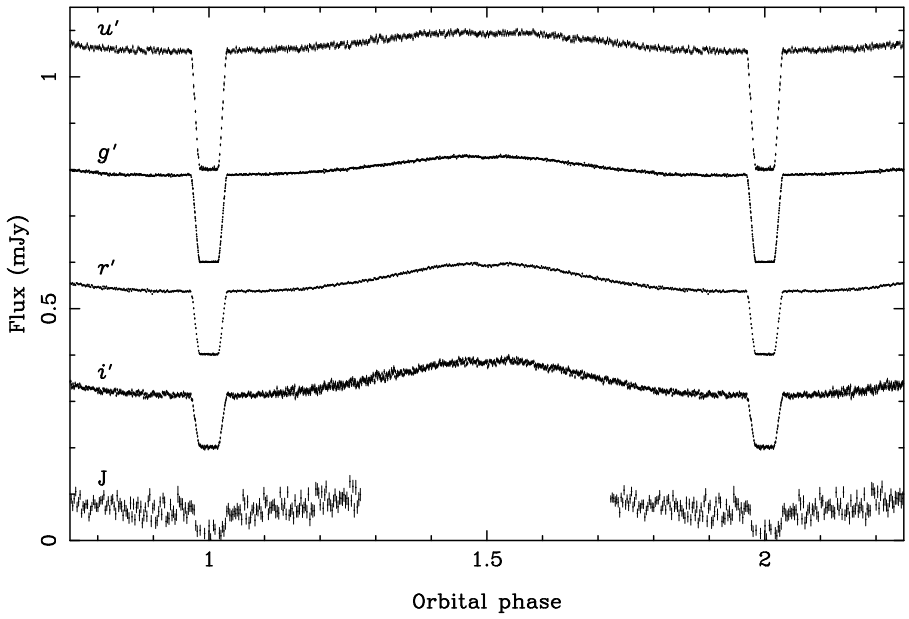

Figure 4.2: *Top to bottom:* phase-folded ULTRACAM $u'g'r'i'$ and SOFI J band light curves of SDSS J0857+0342. The ULTRACAM light curves have been binned by a factor of three. Each light curve is offset by 0.2 mJy from the one below it. The J band light curve has been scaled up by a factor of three for clarity.

times are listed in Table C.19. We update the ephemeris to

$$\mathrm{MJD(BTDB)} = 55552.712\,765\,17(78) + 0.065\,096\,538(3)E,$$

which is consistent with the ephemeris of Drake et al. (2010).

The data were then phase-folded and the period set equal to one for the fit, while the mid-eclipse time was allowed to vary. The mass ratio was kept fixed at 0.13 and the temperature of the white dwarf fixed at 35,300K (see section 4.4.1). The quadratic limb darkening coefficients of the white dwarf were determined based on a white dwarf atmosphere model with a temperature of $T_{\rm eff} = 35,300$K and $\log g = 7.3$ folded through the ULTRACAM $u'g'r'i'$ filter profiles (Gänsicke et al., 1995). The coefficients ($a_{\rm WD}$ and $b_{\rm WD}$) for each filter are listed in Table 4.2 for $I(\mu)/I(1) = 1-a(1-\mu)-b(1-\mu)^2$, where μ is the cosine of the angle between the line of sight and the surface normal; these values were kept fixed. All other parameters were allowed to vary and several MCMC chains were started with different initial parameters in order to check if the results were consistent and that we had found the global minimum.

The best fit parameters and their statistical errors are listed in Table 4.2.

Table 4.2: Parameters from Markov chain Monte Carlo minimisation, some fitted, some fixed a priori. $a_{\rm WD}$ and $b_{\rm WD}$ are the quadratic limb darkening coefficients of the white dwarf, $a_{\rm sec}$ is the linear limb darkening of the secondary star. A is the fraction of the irradiating flux from the white dwarf absorbed by the secondary star.

Parameter	u'	g'	r'	i'
i	86.6 ± 0.5	85.4 ± 0.2	85.5 ± 0.2	84.8 ± 0.5
$r_{\rm WD}/a$	0.0461 ± 0.0012	0.0438 ± 0.0006	0.0431 ± 0.0005	0.0423 ± 0.0013
$r_{\rm sec}/a$	0.180 ± 0.004	0.192 ± 0.003	0.191 ± 0.003	0.203 ± 0.008
$T_{\rm eff,sec}$	4922 ± 97	3575 ± 67	3298 ± 64	3016 ± 104
$a_{\rm WD}$	0.089	0.064	0.057	0.054
$b_{\rm WD}$	0.199	0.178	0.143	0.119
$a_{\rm sec}$	-0.90 ± 0.10	-0.30 ± 0.05	-0.16 ± 0.05	-0.09 ± 0.11
A	0.83 ± 0.02	0.64 ± 0.02	0.78 ± 0.02	0.69 ± 0.06

Figure 4.3 shows the fits to the light curves over the entire orbit as well as zoomed in around the two eclipses. The MCMC chains showed no variation beyond that expected from statistical variance. Since we didn't cover the secondary eclipse in the J band and the S/N of the SOFI data is quite low, we don't fit these data.

The four different bands give consistent results, although the u' band favours a slightly higher inclination but is less constrained due to the shallowness of the secondary eclipse in this band. The faintness of the system in the i' band limits the constraints in this band. The fits give an inclination of $85.5^\circ \pm 0.2^\circ$ and scaled radii of $R_{\rm WD}/a = 0.0436 \pm 0.0004$ and $R_{\rm sec}/a = 0.190 \pm 0.002$. An interesting trend is seen in the limb darkening coefficients for the secondary star, which are all negative (limb brightening) and the amount of limb brightening decreases with increasing wavelength. This is presumably the result of seeing to different depths at different wavelengths; a similar effect was seen with NN Ser in Chapter 3.

4.4.3 Radial Velocities

Figure 4.4 shows an average spectrum of SDSS J0857+0342. The spectral features seen are similar to other PCEBs, namely hydrogen Balmer absorption originating from the white dwarf and emission from the heated face of the secondary star, which disappears around the primary eclipse. Calcium emission is also seen as well as deep interstellar calcium H and K absorption which show no radial velocity variations; no other features from either star are visible. Figure 4.5 shows trailed spectra of the four longest wavelength hydrogen Balmer lines. The emission from the secondary star can be seen as well as the non-LTE absorption core from the white dwarf moving in anti-phase.

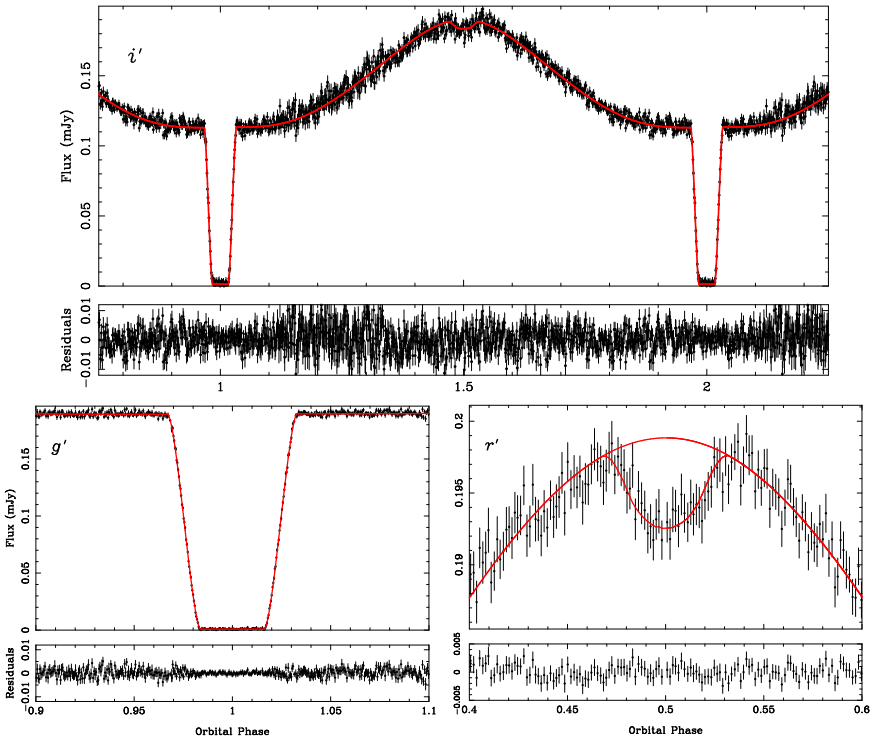

Figure 4.3: Model fits to the ULTRACAM light curves with residuals shown below. *Top*: Full orbit in the i' band. *Bottom left:* The g' band primary eclipse. *Bottom right:* The r' band secondary eclipse, also shown is the same model but without the secondary eclipse.

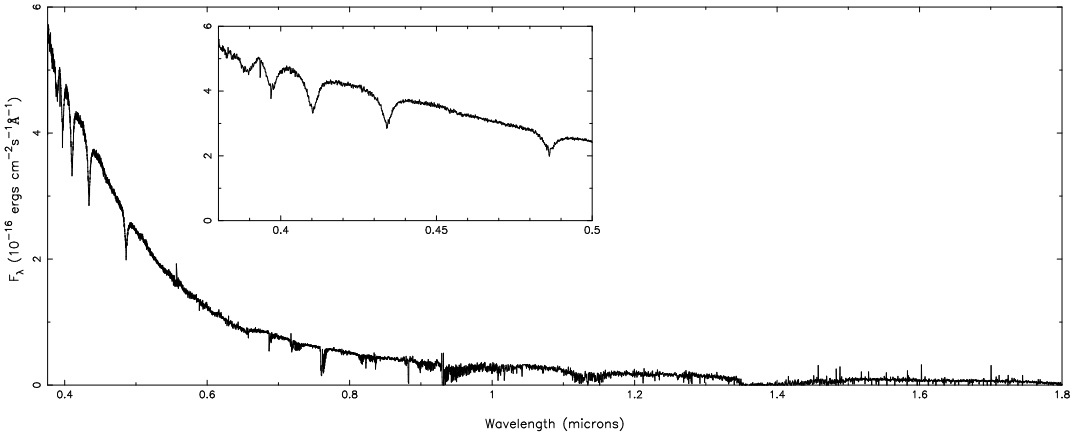

Figure 4.4: Averaged X-shooter spectrum of SDSS J0857+0342. No features from the secondary star are seen in the NIR, the only features visible are telluric or sky lines that have not been completely removed. Those spectra taken during the eclipse were not included in the averaging. Inset is a zoom in on the upper Balmer series; interstellar calcium absorption is also visible.

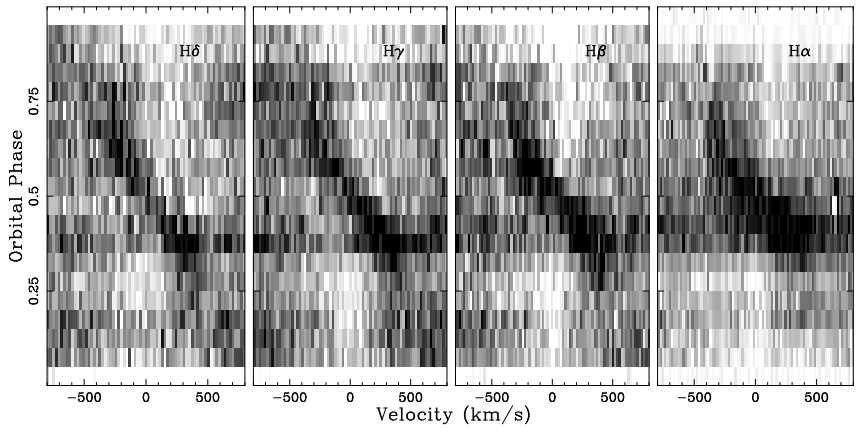

Figure 4.5: Trailed spectrum of the four longest wavelength hydrogen Balmer lines, the scale runs from white (75 per cent of the continuum level) to black (120 per cent of the continuum level). Both white dwarf absorption and secondary star emission components are visible in each line.

The absorption and emission components of each of the Balmer lines were fitted together by simultaneously fitting all of the spectra. This approach was used because the S/N on an individual spectrum was quite low and the absorption from the white dwarf is filled in by the emission component from the secondary star around phase 0.5. Therefore, by fitting all of the spectra simultaneously we obtain a more robust estimate of the radial velocities. The lines were fitted using the techniques described in Section 2.3 (including a broad Gaussian component to account for the wings of the primary star's absorption) and allowed the position of the Gaussians to change velocity according to

$$V = \gamma + K \sin(2\pi\phi),$$

for each star, where γ is the velocity offset of the line from its rest wavelength and ϕ is the orbital phase of the spectrum. We allow the strength of the emission component to vary with orbital phase according to

$$H = H_0 - H_1 \cos(2\pi\phi),$$

which allows the strength to peak at phase 0.5, where the irradiation effect is largest. This approach gave better fits than keeping the strength at a fixed value.

Table 4.3 lists the offsets and radial velocities for the four longest wavelength hydrogen Balmer lines; the shorter wavelength lines were unsuitable for fitting since the emission component is much weaker and the absorption components lack the

Table 4.3: Hydrogen Balmer line offsets and velocities.

Line	$\gamma_{\rm WD}$ ($\rm km\,s^{-1}$)	$K_{\rm WD}$ ($\rm km\,s^{-1}$)	$\gamma_{\rm emis}$ ($\rm km\,s^{-1}$)	$K_{\rm emis}$ ($\rm km\,s^{-1}$)
Hδ	–	–	28.9 ± 4.9	319.4 ± 8.7
Hγ	48.4 ± 8.6	65.9 ± 11.8	25.5 ± 5.3	324.7 ± 8.9
Hβ	50.6 ± 5.8	61.6 ± 8.8	28.5 ± 5.3	343.6 ± 9.8
Hα	42.1 ± 6.3	66.7 ± 10.0	31.8 ± 5.0	336.2 ± 9.9

non-LTE core, this is also the case for the Hδ absorption. The results for each line are consistent, giving values of $K_{\rm WD} = 64 \pm 6\,\rm km\,s^{-1}$ and $K_{\rm emis} = 330 \pm 5\,\rm km\,s^{-1}$. The gravitational redshift of the white dwarf was measured as $z_{\rm WD} = \gamma_{\rm WD} - \gamma_{\rm emis} = 18 \pm 5\,\rm km\,s^{-1}$.

4.4.4 $K_{\rm sec}$ correction

Like NN Ser in Chapter 3, the emission lines in SDSS J0857+0342 originate from the heated face of the secondary star and thus their radial velocities do not represent the true centre of mass radial velocity of the secondary star. However, the low S/N of the data means that the light curves of the lines cannot be used to determine their optical depths. Therefore, an accurate $K_{\rm sec}$ correction is not possible, only a range of possible values for $K_{\rm sec}$.

A lower limit can be obtained by assuming that the emission is uniformly spread over the heated face (in reality it is far more likely to be brighter towards the substellar point where the heating effect is larger). This corresponds to a correction factor of $f = 0.42$ (from Equation 2.5) which gives $K_{\rm sec,min} = 364\,\rm km\,s^{-1}$. An upper limit on the correction factor can be set by using an optically thin correction since this represents a more physical upper limit. This gives a value of $K_{\rm sec,max} = 398\,\rm km\,s^{-1}$ (using $f = 0.77$). The hydrogen Balmer emission is likely to be optically thick, as found for NN Ser in Chapter 3. Besides, I will show in Section 4.5.1 it is the lower limit that is the more important.

Therefore, with the current data the radial velocity semi-amplitude of the centre of mass of the secondary star ($K_{\rm sec}$) lies somewhere between $364\,\rm km\,s^{-1}$ and $398\,\rm km\,s^{-1}$.

Table 4.4: Stellar and binary parameters for SDSS J0857+0342, magnitudes are from SDSS and UKIDSS. The white dwarf temperature and $\log g$ are from the spectroscopic fit. $z_{\rm WD}$ is the measured gravitational redshift of the white dwarf.

Parameter	Value	Parameter	Value
RA	08:57:46.18	$P_{\rm orb}$ (days)	0.065 096 538(3)
Dec	+03:42:55.3	$T_{\rm WD}$ (K)	$35,300 \pm 400$
u'	17.731 ± 0.011	WD $\log g$	7.3 ± 0.1
g'	17.954 ± 0.006	$M_{\rm WD}$ ($M_\odot$)	0.514 ± 0.049
r'	18.256 ± 0.007	$M_{\rm sec}$ ($M_\odot$)	0.087 ± 0.012
i'	18.393 ± 0.011	$R_{\rm WD}$ ($R_\odot$)	0.0247 ± 0.0008
z'	18.536 ± 0.032	$R_{\rm sec}$ ($R_\odot$)	0.1096 ± 0.0038
J	18.184 ± 0.059	a ($R_\odot$)	0.574 ± 0.018
H	18.618 ± 0.160	i (deg)	85.5 ± 0.2
K	18.141 ± 0.174	$K_{\rm WD}$ (km s^{-1})	64 ± 6
d (pc)	968 ± 55	$K_{\rm sec}$ (km s^{-1})	$364 < K < 398$
Sp2	M8 $\pm$ 1	$z_{\rm WD}$ (km s^{-1})	18 ± 5

4.5 Discussion

4.5.1 System parameters

The light curve model fits, radial velocity measurements and Kepler's third law can be combined to determine the masses, radii and orbital separation for SDSS J0857+0342. These are listed in Table 4.4 along with the other system parameters that we have measured.

The largest source of uncertainty is $K_{\rm sec}$ since we were unable to measure it directly. This translates into a large uncertainty in the masses (particularly the white dwarf). The contours in Figure 4.6 show the region of allowed mass and radius for the white dwarf in SDSS J0857+0342 compared to other white dwarfs with measured masses and radii. Also plotted are mass-radius relations for carbon-oxygen core white dwarfs from Benvenuto & Althaus (1999) and helium core white dwarfs from Panei et al. (2007) in the same temperature range as the white dwarf in SDSS J0857+0342. The mass range permitted makes it possible for the white dwarf to have either type of core but the measured radius of the white dwarf places it far above the carbon-oxygen core models, even for very thick hydrogen envelopes. However, it is consistent with a helium core provided that the mass is at the lower end of the permitted range. Therefore, it is most likely that the white dwarf in SDSS J0857+0342 is a helium core white dwarf close to the upper mass limit expected from evolution ($< 0.5 M_\odot$).

The contours in Figure 4.7 show the region of allowed mass and radius for the

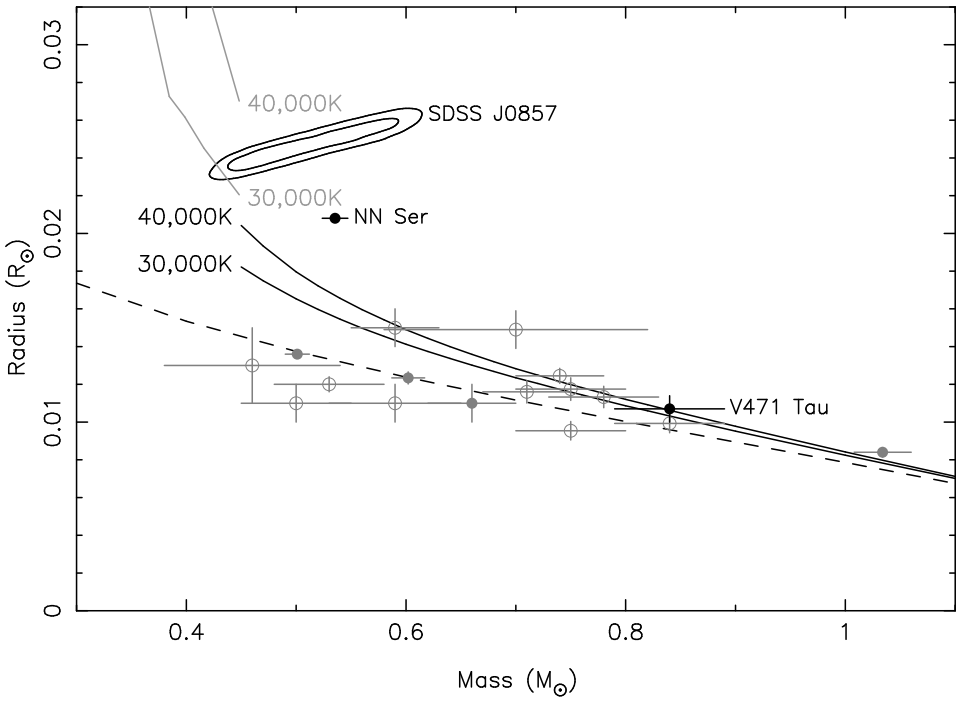

Figure 4.6: Mass-radius plot for white dwarfs. Data from Provencal et al. (1998), Provencal et al. (2002) and Casewell et al. (2009) are plotted. The filled circles are visual binaries and the open circles are common proper-motion systems. The solid dots are from the eclipsing PCEBs NN Ser (Chapter 3) and V471 Tau (O'Brien et al., 2001). The solid black lines correspond to carbon-oxygen core models with temperatures of 30,000K and 40,000K with a hydrogen layer thickness of $M_H/M_{WD} = 10^{-4}$ from Benvenuto & Althaus (1999). The uppermost solid grey lines correspond to helium core models with temperatures of 30,000K and 40,000K from Panei et al. (2007). The dashed line is the zero-temperature mass-radius relation of Eggleton from Verbunt & Rappaport (1988). The contours show the 68 and 95 percentile regions of the masses and radii for the white dwarf in SDSS J0857+0342. For the measured temperature of the white dwarf (35,300K) the measured radius is much larger than predicted from the carbon-oxygen core models but is consistent with the helium core models.

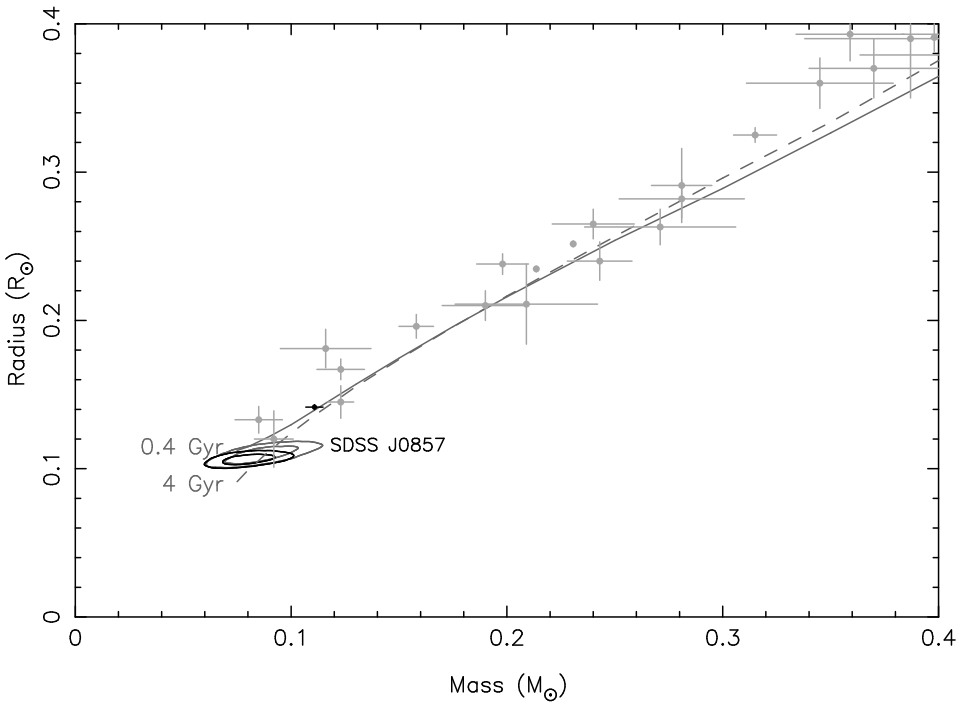

Figure 4.7: Mass-radius plot for low mass stars. Data from López-Morales (2007) and Beatty et al. (2007), also plotted is the mass-radius measurement for the secondary star in NN Ser (black point). The solid line represents the theoretical isochrone model from Baraffe et al. (1998), for an age of 0.4 Gyr, solar metalicity, and mixing length $\alpha = 1.0$, the dashed line is the same but for an age of 4 Gyr. The grey contours show the 68 and 95 percentile regions of the masses and radii for the secondary star in SDSS J0857+0342. The black contours show the same regions if the white dwarf mass is forced to be $< 0.5\mathrm{M}_\odot$.

secondary star in SDSS J0857+0342. The mass range places it close to the hydrogen burning limit and the radius is consistent with the evolutionary models of Baraffe et al. (1998) despite being both heavily irradiated by the nearby white dwarf and rapidly rotating. This result is consistent with that of NN Ser in Chapter 3, implying that very low-mass stars do not appear to be overinflated compared to evolutionary models, in contrast to slightly more massive stars ($\geq 0.3\mathrm{M}_\odot$) (Kraus et al., 2011). The black contours in Figure 4.7 show the region of allowed mass and radius if the white dwarf mass is $< 0.5\mathrm{M}_\odot$ (a helium core), in this case the mass and radius are slightly smaller ($0.08 \pm 0.01\mathrm{M}_\odot$ and $0.106 \pm 0.002\mathrm{R}_\odot$).

The secondary star was detected during the SOFI J band eclipse and its recorded magnitude was $J_{\mathrm{sec}} = 20.9 \pm 0.2$ which, at the distance determined for the white dwarf, gives an absolute magnitude of $M_{J,\mathrm{sec}} = 11.0 \pm 0.2$. This corresponds to

a spectral type of M8 ± 1 (Hawley et al., 2002) and is consistent with the measured mass (Baraffe & Chabrier, 1996).

Using the X-shooter spectra, the gravitational redshift of the white dwarf was found to be $18 \pm 5\,\mathrm{km\,s^{-1}}$. Using the measured mass and radius from Table 4.4 gives a redshift of $13.2\,\mathrm{km\,s^{-1}}$. Correcting the X-shooter measurement for the redshift of the secondary star, the difference in transverse Doppler shifts and the potential at the secondary star owing to the white dwarf gives a value of $12 \pm 1\,\mathrm{km\,s^{-1}}$which is consistent with the measured value although, as with NN Ser in Chapter 3, these two measurements are only just in agreement (2σ).

4.5.2 Evolutionary state

Since SDSS J0857+0342 emerged from the common envelope stage its evolution has been driven by angular momentum loss, which will eventually bring the two stars close enough to initiate mass transfer from the secondary star to the white dwarf. To determine its past and future evolution, the cooling tracks of Panei et al. (2007) were interpolated for a helium core white dwarf with a mass of $0.45\mathrm{M}_{\odot}$. This gives a current cooling age of $\sim 19.5 \times 10^6$ yrs, implying that the system has only recently emerged from the common envelope phase at essentially the current orbital period. An upper limit on the time taken for the system to reach a semi-detached configuration can be made by assuming that the only mechanism of angular momentum loss is via gravitational radiation. If this is the case then mass transfer will begin in $\sim 3.7 \times 10^8$ years (Schreiber & Gänsicke, 2003) once the orbital period has been reduced to 66 minutes (Ritter, 1986). Since there is likely to be some additional angular momentum loss besides gravitational radiation, the true time taken to reach a semi-detached configuration is likely to be lower. SDSS J0857+0342 will start mass transfer below the observed orbital period minimum for CVs (~ 80 minutes), at which point the white dwarf will have cooled to around 13,500K.

Once the binary becomes mass-transferring the secondary star will no longer be in thermal equilibrium and the binary will evolve to longer periods and pass into the "main" CV population (after a brief interval of period reduction as a small amount of mass is lost until the donor becomes a brown dwarf). Therefore, SDSS J0857+0342 is a progenitor for a class of CVs yet to be unambiguously observed: those that began mass transfer from a very low-mass star / brown dwarf donor. The few (non-AM CVn) CVs observed with periods below the minimum were not formed directly from white dwarf / brown dwarf binaries; V485 Cen ($P_{\mathrm{orb}} = 59$ minutes) and EI Psc ($P_{\mathrm{orb}} = 64$ minutes) are both thought to have evolved donor stars in which a large fraction of the hydrogen in the core was processed prior to

mass transfer (Thorstensen et al. 2002; Gänsicke et al. 2003). SDSS J1507 ($P_{\rm orb} = 66$ minutes) was thought to have started mass transfer with a brown dwarf donor (Littlefair et al., 2007) but recent studies have shown that it is more likely to be a halo CV with a low-metalicity, hence higher density donor (Patterson et al. 2008; Uthas et al. 2011). Once it has reached a semi-detached state, SDSS J0857+0342 is likely to take about a Gyr to evolve back towards a period where the shortest period "main" CVs are found (Kolb & Baraffe, 1999).

Our constraints on the system parameters of SDSS J0857+0342 make it likely that the progenitor for this system lay within, or close to, the brown dwarf desert; a paucity of close ($\leq$5AU) brown dwarf companions to main-sequence stars (Grether & Lineweaver, 2006).

4.6 Summary

In this chapter I have used a combination of ULTRACAM and SOFI photometry and X-shooter spectroscopy to constrain the system parameters of the 94 minute orbital period eclipsing PCEB SDSS J0857+0342. The degeneracy between the scaled radii and the orbital inclination was broken by detecting the secondary eclipse and measuring its depth. Unfortunately, a direct measurement of the radial velocity of the secondary star was not possible since no absorption features were visible in the spectra, however, its radial velocity amplitude was constrained using a correction factor applied to the emission lines. It is likely that the white dwarf has a helium core and that the secondary star has a mass that places it at the hydrogen burning limit.

The data also reveal that SDSS J0857+0342 has only recently emerged from the common envelope phase and will reach a semi-detached configuration in $\sim 4\times10^8$ years when it will become a cataclysmic variable with a 66 minute orbital period, at which point its orbital period will increase.

Chapter 5

The masses and radii of the stars in SDSS J1212-0123 and GK Vir

5.1 Introduction

This chapter continues the precision study of eclipsing PCEBs. However, the secondary eclipse is not visible in either of the two systems presented in this chapter, meaning that another approach is needed in order to break the degeneracy between the radii and inclination. Fortunately, the gravitational redshift of the white dwarf is measurable in both cases meaning that it can be used to break the degeneracy using the techniques described in Chapter 2. This results are then compared with evolutionary models.

5.2 Target information

This chapter focuses on two eclipsing PCEBs: SDSS J1212-0123 and GK Vir. The first, SDSS J1212-0123, was initially listed as a quasar candidate from the Sloan Digital Sky Survey by Richards et al. (2004). Silvestri et al. (2006) reclassified it as a white dwarf plus main-sequence binary and eclipses were discovered by Nebot Gómez-Morán et al. (2009) who derived the basic system parameters. However, their analysis was limited by the fact that they did not resolve the white dwarf ingress or egress and could not measure the radial velocity amplitude of the white dwarf. They found that SDSS J1212-0123 contained a relatively hot ($17,700 \pm 300$K) low mass white dwarf with an active M4 main-sequence companion in an $8^{\rm h}3^{\rm m}$ period.

GK Vir (PG 1413 + 015) was discovered by Green et al. (1978) from the Palomar-Green survey for ultraviolet-excess objects (Green et al., 1986). An eclipse was recorded during a subsequent spectroscopic observation. Fulbright et al. (1993) combined the photometry from Green et al. (1978) and high resolution spectroscopy to constrain the system parameters. They found that GK Vir contains a hot DAO white dwarf with a low-mass M3-5 main sequence companion in an $8^{\rm h}16^{\rm m}$ period. However, their lack of radial velocity information limited their analysis.

5.3 Observations and their reduction

5.3.1 ULTRACAM photometry

GK Vir has been observed with ULTRACAM (Dhillon et al., 2007) roughly once a year since 2002, with a couple of gaps in 2005, 2008 and 2009. The data were mainly obtained with ULTRACAM mounted on the WHT but there is also one primary eclipse run from the VLT and several nights worth of NTT data. SDSS J1212-0123 was observed with ULTRACAM mounted on the NTT in April 2010. A complete log of all these observations is given in Table 5.1. All these data were reduced in the standard way, outlined in Chapter 2.

5.3.2 SOFI J-band photometry

GK Vir and SDSS J1212-0123 were observed with SOFI (Moorwood et al., 1998) mounted at the NTT in April 2010 and April 2011. The observations were made in fast photometry mode equipped with a J-band filter. The detector was windowed to achieve a cycle time of $\sim$ 10–15 seconds and the telescope offset every 10 minutes in order to improve sky subtraction. A summary of these observations is given in Table 5.1.

5.3.3 X-shooter spectroscopy

GK Vir and SDSS J1212-0123 were both observed with X-shooter (D'Odorico et al., 2006) mounted at the VLT-UT2 telescope on the night of the 4th of April 2010. Due to the long orbital periods of both systems ($\sim$ 8 hours) the quadrature phases were targeted, since these phases are the most sensitive to the radial velocity amplitude. Details of these observations are listed in Table 5.1. Slit widths of 0.8", 0.9" and 0.9" were used in X-shooter's three arms and binned by a factor of two in the dispersion direction, resulting in a resolution of $R \sim 7,000$. We used exposure times of 300 seconds in the UVB arm, 338 seconds in the VIS arm and 3×100 seconds in the

Table 5.1: Journal of observations. Exposure times for X-shooter observations are for UVB arm, VIS arm and NIR arm respectively. The primary eclipse occurs at phase 1, 2 etc.

Date at start of run	Instrument	Filter(s)	Telescope	Start (UT)	Orbital phase	Exposure time (s)	Conditions (Transparency, seeing)
GK Vir:							
2002/05/19	ULTRACAM	$u'g'r'$	WHT	21:09	0.89–1.02	2.1	Good, ∼1.5 arcsec
2003/05/22	ULTRACAM	$u'g'i'$	WHT	23:25	0.92–1.05	5.0	Excellent, <1 arcsec
2003/05/23	ULTRACAM	$u'g'i'$	WHT	00:31	0.95–1.04	4.0	Excellent, <1 arcsec
2003/05/24	ULTRACAM	$u'g'i'$	WHT	20:51	0.40–0.54	4.0	Good, ∼1.2 arcsec
2004/05/05	ULTRACAM	$u'g'i'$	WHT	01:36	0.84–1.12	3.9	Excellent, ∼1 arcsec
2006/03/11	ULTRACAM	$u'g'r'$	WHT	00:04	0.96–1.08	3.0	Variable, 1-3 arcsec
2006/03/11	ULTRACAM	$u'g'r'$	WHT	04:00	0.43–0.55	3.0	Variable, 1-3 arcsec
2006/03/12	ULTRACAM	$u'g'r'$	WHT	00:35	0.93–1.06	3.0	Excellent, ∼1 arcsec
2006/03/13	ULTRACAM	$u'g'r'$	WHT	01:38	0.96–0.99	3.0	Poor, >3 arcsec
2007/06/18	ULTRACAM	$u'g'i'$	VLT	02:40	0.81–1.14	1.5	Excellent, <1 arcsec
2010/04/05	X-shooter	-	VLT	04:28	0.12–0.26	300,338,100	Excellent, ∼1 arcsec
2010/04/05	X-shooter	-	VLT	07:55	0.53–0.75	300,338,100	Good, ∼1.2 arcsec
2010/04/21	ULTRACAM	$u'g'i'$	NTT	07:18	0.90–1.05	3.0	Good, ∼1.2 arcsec
2010/04/22	ULTRACAM	$u'g'i'$	NTT	04:14	0.45–0.55	3.0	Excellent, ∼1 arcsec
2010/04/23	ULTRACAM	$u'g'i'$	NTT	04:45	0.40–0.55	3.0	Excellent, <1 arcsec
2010/04/25	ULTRACAM	$u'g'i'$	NTT	06:29	0.40–0.55	3.0	Variable, 1-2 arcsec
2010/04/29	SOFI	J	NTT	01:16	0.40–0.55	15.0	Excellent, <1 arcsec
2010/04/30	SOFI	J	NTT	02:17	0.45–0.60	15.0	Good, ∼1.2 arcsec
2010/04/30	SOFI	J	NTT	06:16	0.90–1.05	15.0	Excellent, ∼1 arcsec
2010/05/01	SOFI	J	NTT	02:42	0.40–0.55	15.0	Good, ∼1.2 arcsec
2011/04/02	SOFI	J	NTT	04:05	0.38–0.59	15.0	Excellent, <1 arcsec
2011/04/02	SOFI	J	NTT	08:02	0.86–1.05	15.0	Excellent, <1 arcsec
2011/04/03	SOFI	J	NTT	05:03	0.40–0.61	15.0	Excellent, ∼1 arcsec
2011/04/04	SOFI	J	NTT	05:33	0.37–0.66	15.0	Excellent, ∼1 arcsec
2011/04/05	SOFI	J	NTT	05:56	0.95–1.20	15.0	Excellent, ∼1 arcsec
2011/04/05	SOFI	J	NTT	06:53	0.43–0.69	15.0	Excellent, ∼1 arcsec
2011/04/06	SOFI	J	NTT	03:19	0.90–1.17	15.0	Excellent, <1 arcsec
2011/04/06	SOFI	J	NTT	07:32	0.42–0.62	15.0	Excellent, <1 arcsec
SDSS J1212-0123:							
2010/04/05	X-shooter	-	VLT	00:42	0.57–0.79	300,338,100	Excellent, ∼1 arcsec
2010/04/05	X-shooter	-	VLT	05:57	0.23–0.45	300,338,100	Excellent, ∼1 arcsec
2010/04/22	ULTRACAM	$u'g'i'$	NTT	02:26	0.40–0.55	2.9	Good, ∼1.2 arcsec
2010/04/23	ULTRACAM	$u'g'i'$	NTT	02:46	0.40–0.55	2.9	Excellent, <1 arcsec
2010/04/24	ULTRACAM	$u'g'i'$	NTT	22:57	0.90–1.15	2.9	Good, ∼1.2 arcsec
2010/04/30	SOFI	J	NTT	03:56	0.40–0.55	10.0	Excellent, ∼1 arcsec
2011/04/02	SOFI	J	NTT	01:07	0.43–0.56	10.0	Excellent, <1 arcsec
2011/04/03	SOFI	J	NTT	01:04	0.40–0.61	10.0	Excellent, ∼1 arcsec
2011/04/04	SOFI	J	NTT	01:34	0.44–0.62	10.0	Excellent, ∼1 arcsec
2011/04/05	SOFI	J	NTT	01:04	0.35–0.57	10.0	Excellent, ∼1 arcsec
2011/04/05	SOFI	J	NTT	05:06	0.85–1.06	10.0	Excellent, ∼1 arcsec
2011/04/06	SOFI	J	NTT	01:54	0.43–0.60	10.0	Excellent, <1 arcsec
2011/04/06	SOFI	J	NTT	05:59	0.94–1.12	10.0	Excellent, <1 arcsec

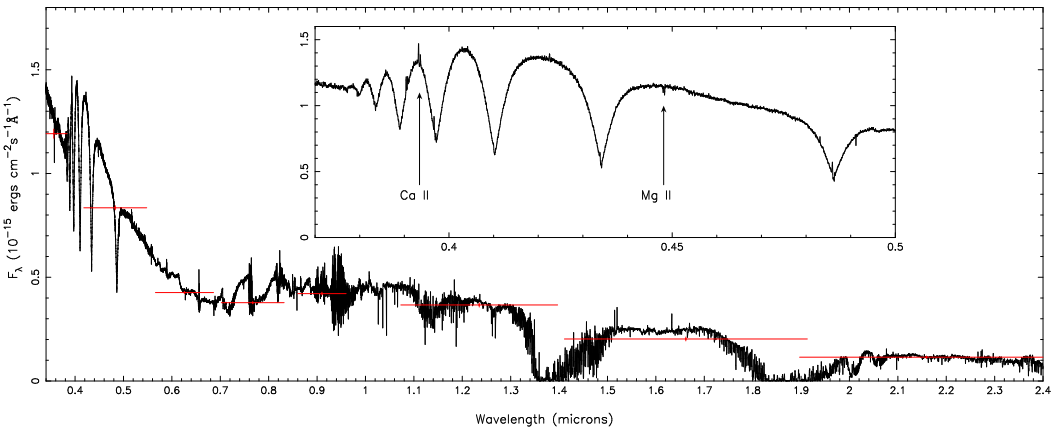

Figure 5.1: Averaged X-shooter spectrum of SDSS J1212-0123. The SDSS $u'g'r'i'z'$ and 2MASS JHK magnitudes and filter widths are also shown. A zoom in on the white dwarf features are shown inset with the narrow Ca II and Mg II absorption features labelled, although the Ca II feature is somewhat filled in by emission from the secondary star (see Figure 5.2).

NIR arm. After each exposure we nodded along the slit to help the sky subtraction in the NIR arm[1]. As with the X-shooter data for SDSS J0857+0342 presented in the previous chapter, the ULTRACAM and SOFI data were used to flux calibrate the X-shooter spectra by fitting models to the photometry and deriving synthetic fluxes from the spectra. This corrects for variable extinction across the wavelength range, as well as variations in seeing.

5.4 Results

5.4.1 SDSS J1212-0123

Spectral features

Figure 5.1 shows an average spectrum of SDSS J1212-0123. The white dwarf dominates the spectrum at wavelengths shorter than 0.55 microns whilst at longer wavelengths the spectral features of the secondary star dominate. There are also numerous emission lines throughout the spectrum originating from the secondary star. Additionally, both Ca II 3934 Å and Mg II 4481 Å absorption from the white dwarf are seen, likely the result of low level accretion from the wind of the secondary star. The fact that absorption features are seen from both stars allows us to measure the radial velocities for both components of the system directly.

[1]data were obtained by A. Rebassa-Mansergas

Atmospheric parameters of the white dwarf

Nebot Gómez-Morán et al. (2009) determined the temperature of the white dwarf in SDSS J1212-0123 by decomposing the SDSS spectrum. The white dwarf's spectrum was computed by removing the M-dwarf contribution from the individual spectra using observations of the M4 star GJ 447, and shifting the residual spectra to the rest frame of the white dwarf, however this does not remove the emission components. The white dwarf spectrum was then fitted[2] following the method outlined in Rebassa-Mansergas et al. (2007, 2010), using a grid of pure hydrogen model atmospheres calculated with the code described by Koester (2010). The cores of the Balmer lines were down-weighted since they are contaminated by emission from the secondary star, the Hα line was not used since the secondary star dominates at this wavelength. The fit gives a temperature of $17,707 \pm 35$K, a surface gravity of $\log g = 7.51 \pm 0.01$ and a distance of 228 ± 5pc, all of which is consistent with the results from Nebot Gómez-Morán et al. (2009) (and from our light curve fit, see Section 5.5). Note that these are purely statistical uncertainties.

Next, the equivalent width of the Mg II 4481 Å absorption line (90 ± 20 mÅ) was fitted by varying the Mg abundance in the synthetic spectrum, keeping $T_{\rm eff}$ and $\log g$ fixed to the values determined above. The best-fit abundance by number is $\log[{\rm Mg/H}] = -5.8 \pm 0.1$, corresponding to $\simeq 4\%$ of the solar value. Figure 5.2 shows the fit to the Mg II 4481 Å line. The Ca K line is significantly contaminated by the emission line of the companion star, however Figure 5.2 illustrates that adopting the Mg abundance for Ca as well matches the observed Ca K line reasonably well.

Since there is no convection zone acting as a reservoir for the accreted elements, the settling times vary throughout the atmosphere. At optical depth $\sim 2/3$, representative for the visible spectrum, the timescale for Mg is a few tens of days (Koester, 2009). The diffusion time scale for the temperature and surface gravity derived above is ~ 2 months (Koester & Wilken, 2006), it is hence plausible to assume accretion-diffusion equilibrium. Hence, $X_{\rm Mg}\rho v_{\rm Mg} = $ constant, with $X_{\rm Mg}$ and $v_{\rm Mg}$ the mass fraction and the diffusion velocity (relative to hydrogen) of Mg, and ρ the mass density. We compute at $\tau_{\rm Ross} \approx 2/3$ that $\rho = 5.23 \times 10^{-8}{\rm g\,cm^{-3}}$, $X_{\rm Mg} = 3.76 \times 10^{-5}$, and $v_{\rm Mg} = 8.48 \times 10^{-2}{\rm cm\,s^{-1}}$, i.e. a mass flux of $1.67 \times 10^{-13}{\rm g\,cm^{-2}s^{-1}}$. Multiplying by the white dwarf surface area, with $R_{\rm WD}$ from Table 5.6, the total mass flux of Mg is $2.9 \times 10^{6}{\rm g\,s^{-1}}$ – which is equal to the mass accretion rate of Mg at the surface of the white dwarf. Assuming that the secondary star transfers material of solar composition, the total accretion rate is then obtained by dividing the Mg rate by the

[2] All of the white dwarf model fitting was performed by B. Gänsicke and D. Koester

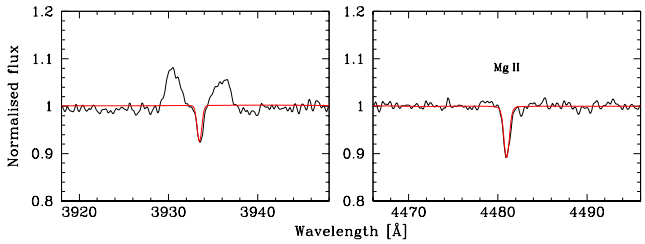

Figure 5.2: The X-shooter spectra of SDSS J1212-0123, averaged in the white dwarf rest-frame and normalised (black) along with the best-fit white dwarf model ($T_{\rm eff}$ = 17707, $\log g$ = 7.51) and log[Mg/H] = −5.8. The Ca K line is contaminated by the emission from the secondary star (which appears shifted/smeared in the rest frame of the white dwarf), however, adopting the same abundance for Ca provides a reasonable match to the photospheric absorption line.

mass fraction of Mg in the Sun, i.e. $\dot{M} \simeq 4.0 \times 10^9 \mathrm{g\,s^{-1}}$ or $6.4 \times 10^{-17} \mathrm{M_\odot\,yr^{-1}}$. This value is right in the middle of the accretion rates calculated for the pre-CVs RR Cae, UZ Sex, EG UMa, LTT 560 and SDSS J121010.1+334722.9 by Debes (2006), Tappert et al. (2011), and Pyrzas et al. (2012), $9 \times 10^{-19} \mathrm{M_\odot\,yr^{-1}}$ to $5 \times 10^{-15} \mathrm{M_\odot\,yr^{-1}}$.

White dwarf radial velocity

The orbital phases of the X-shooter spectra of SDSS J1212-0123 were determined using the ephemeris of Nebot Gómez-Morán et al. (2009). As previously mentioned both Ca II and Mg II absorption from the white dwarf are present. Additionally, the cores of the longer wavelength hydrogen absorption lines (Hδ to Hα) are narrow and suitable for radial velocity measurements.

The radial velocities of the absorption lines were measured by simultaneously fitting all of the spectra. A straight line and Gaussians component was used for each spectrum (including an additional broad Gaussian component to account for the wings of the absorption in the case of the Balmer lines) and allowed the position of the Gaussians to change velocity according to

$$V = \gamma + K \sin(2\pi\phi),$$

for each star, where γ is the velocity offset of the line from its rest wavelength and ϕ is the orbital phase of the spectrum.

The parameters determined from the fits to the white dwarf absorption features are listed in Table 5.2. The fits to several of the absorption features are also shown in Figure 5.3, the fit to the Hα line is also shown in Figure 5.4. Taking

Table 5.2: White dwarf absorption features in SDSS J1212-0123.

Line	$K_{\rm WD}$ (km s^{-1})	$\gamma_{\rm WD}$ (km s^{-1})
Ca II 3933.663	102.71 ± 1.32	37.36 ± 1.12
Hδ 4101.735	106.22 ± 2.21	35.14 ± 1.85
Hγ 4340.465	104.28 ± 1.24	37.43 ± 1.08
Mg II 4481.126	104.53 ± 0.78	35.75 ± 0.67
Hβ 4861.327	105.49 ± 0.93	35.25 ± 0.42
Hα 6562.760	103.32 ± 1.13	38.66 ± 0.97

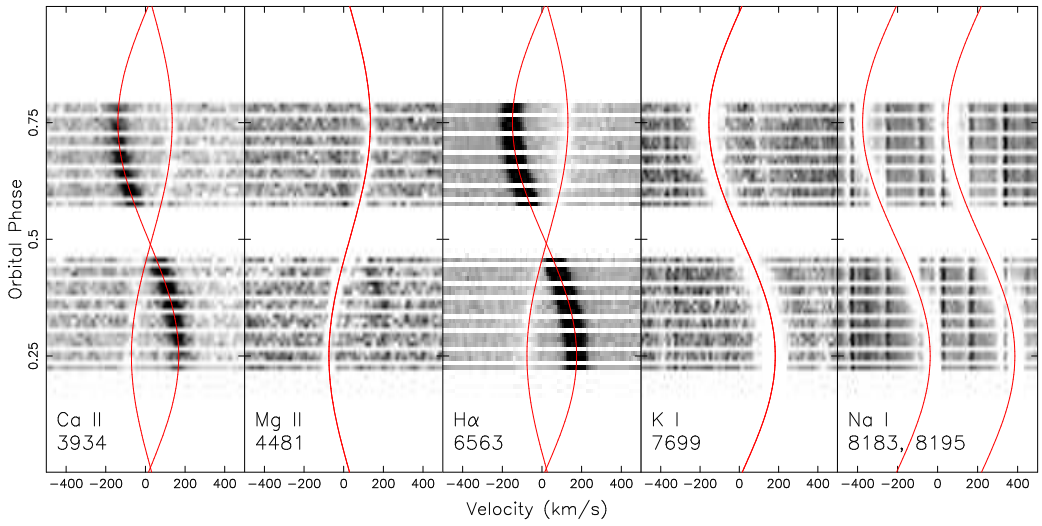

Figure 5.3: Trailed spectra of several lines in SDSS J1212-0123. The grey-scale runs from white (75 per cent of the continuum level) to black (125 per cent of the continuum level). The Ca II 3934 Å line shows an absorption component from the white dwarf and an emission component from the M star. The Mg II 4481 Å line is from the white dwarf, a weak Fe I emission line is also visible. Hα shows both absorption from the white dwarf and emission from the M dwarf. The K I absorption line and the Na I absorption doublet originate from the M star, a telluric correction was applied but artifacts still remain in the Na I trail. The red lines show the best fits to the lines.

a weighted average of the radial velocities gives a radial velocity amplitude of the white dwarf of $K_{\rm WD} = 104.4 \pm 0.5\,{\rm km\,s^{-1}}$.

Secondary star radial velocity

There are both absorption and emission features originating from the secondary star seen in the X-shooter spectra. However, the emission features are due to irradiation from the white dwarf hence they do not track the true radial velocity of the secondary star but the centre of light of the emission region, which will be offset towards the white dwarf. Therefore, only the absorption features yield a direct measurement of the velocity amplitude for the secondary star.

Sodium and Potassium absorption lines are present in the spectra which were fitted in the same way as the white dwarf absorption features. The result of these fits are given in Table 5.3. There were also a number of molecular absorption features which were not fitted due to the uncertainty in their rest wavelengths and their broad, non-Gaussian profiles. Other atomic absorption features are seen at longer wavelengths (for example: the Na I doublet at 2.2 microns) but the S/N of these features are too low to reliably fit them. A weighted average of the radial velocities of the lines in Table 5.3 gives a radial velocity amplitude of the secondary star of $K_{\rm sec} = 168.3 \pm 0.3\,{\rm km\,s^{-1}}$. This is somewhat lower than the value of $K_{\rm sec} = 181 \pm 3\,{\rm km\,s^{-1}}$ found by Nebot Gómez-Morán et al. (2009). To try and resolve this difference the radial velocity data from Nebot Gómez-Morán et al. (2009) was refitted and a $\chi^2 = 25$ was found for the 10 points with 2 variables, implying that they slightly underestimated their error. Accounting for this, their value is consistent with the X-shooter value to within 2.5σ but, based on the higher resolution and additional clean features (not affected by telluric absorption), the X-shooter value for $K_{\rm sec}$ is favoured. I find no evidence that the absorption lines are affected by irradiation from the white dwarf. The equivalent widths of these lines do not vary with phase, as seen in Figure 5.5, and no effects are visible in the radial velocity curves.

The radial velocity amplitudes of all of the identified emission lines were also measured. As in Chapter 5, I allowed the strength of the emission lines to vary with orbital phase according to

$$H = H_0 - H_1 \cos(2\pi\phi),$$

which allows the strength to peak at phase 0.5, where the irradiation effect is largest. This approach gives better fits than keeping the strength at a fixed value.

The results of these fits are given in Table A.1, in the appendix. Figure 5.3

Table 5.3: Secondary star atomic absorption features in SDSS J1212-0123. There are several additional atomic absorption features in the NIR arm spectra but the S/N of these lines are too low to reliably fit them.

Line	$K_{\rm sec}$ ($\rm km\,s^{-1}$)	$\gamma_{\rm sec}$ ($\rm km\,s^{-1}$)
K I 7664.899	169.36 ± 1.13	18.27 ± 0.97
K I 7698.964	169.04 ± 0.83	19.28 ± 0.71
Na I 8183.256	168.77 ± 0.45	18.44 ± 0.38
Na I 8194.824	167.42 ± 0.48	19.52 ± 0.41
Na I 11381.45	165.24 ± 3.86	21.51 ± 3.21
Na I 11403.78	166.87 ± 1.20	19.14 ± 1.07
K I 11690.219	170.22 ± 1.37	20.86 ± 1.24
K I 12432.274	168.63 ± 1.01	19.47 ± 0.88
K I 12522.141	167.40 ± 1.03	21.48 ± 0.72

shows the fits to the Na I doublet as well as several emission lines. The fit to the Na I 8183 Å line is shown in Figure 5.4.

White dwarf's gravitational redshift

In Section 2.3.4 I showed that measuring the gravitational redshift of the white dwarf could enable us to break the degeneracy between the radii and inclination. The gravitational redshift can be measured from the difference in the velocities of the two components ($\gamma_{\rm WD} - \gamma_{\rm sec}$). $\gamma_{\rm sec}$ is tightly constrained due to the large number of emission lines as well as many absorption features. Taking an inverse variance weighted mean of the secondary star line velocities (from Tables 5.3 and A.1) gives $\gamma_{\rm sec} = 19.93 \pm 0.06\,\rm km\,s^{-1}$. $\gamma_{\rm WD}$ was calculated in the same way using the values in Table 5.2 which gave $\gamma_{\rm WD} = 36.0 \pm 0.3\,\rm km\,s^{-1}$. No evidence of pressure shifts is found in these lines, and in any case these are expected to be small for calcium and magnesium (Vennes et al., 2011a).

Using these measurements the gravitational redshift of the white dwarf is $V_z = 16.1 \pm 0.3\,\rm km\,s^{-1}$. As mentioned in Section 2.3.4 the true gravitational redshift of the white dwarf will actually be slightly higher than this value since the measured value includes the effects of the secondary star.

Eclipse time

One eclipse of SDSS J1212-0123 was recorded with ULTRACAM. This provides the first high-precision eclipse time for this system. The SOFI eclipses are not suitable for long term period studies as they are not precisely timed. The eclipse time

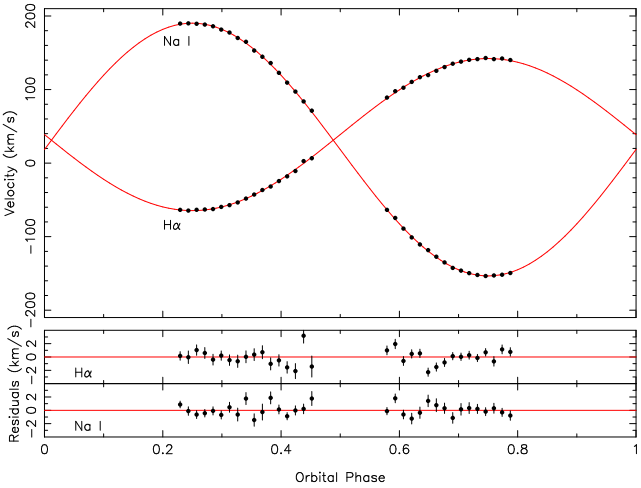

Figure 5.4: Radial velocity fits to the Hα absorption from the white dwarf and Na I 8183 Å absorption from the secondary star in SDSS J1212-0123 with residuals plotted below.

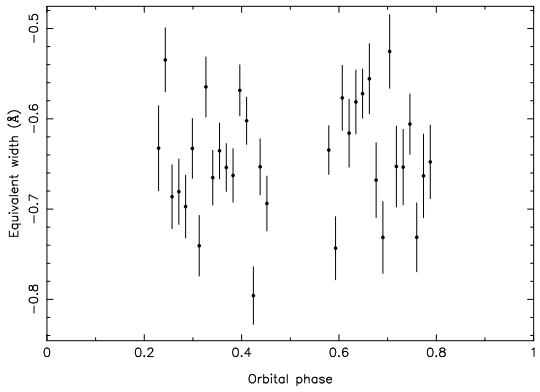

Figure 5.5: Equivalent width variations of the K I 7698.964 Å line in SDSS J1212-0123. The strength of the line does not vary with orbital phase, implying that the irradiating flux from the white dwarf has no effect on the line.

is listed in Table C.17. The new time is consistent with the ephemeris of Nebot Gómez-Morán et al. (2009) and leads to an updated ephemeris of

$$\mathrm{MJD(BTDB)} \;=\; 54104.209\,17(48) + 0.335\,870\,93(13)E.$$

Spectral type of the secondary star

From their spectral decomposition Nebot Gómez-Morán et al. (2009) determined the spectral type of the secondary star in SDSS J1212-0123 to be M4 ± 1. The secondary star was detected during the eclipse in all bands except the u' band giving us multi-colour information. The measured magnitudes of the secondary star are $g' = 19.73 \pm 0.04$, $i' = 17.384 \pm 0.004$ and $J = 14.949 \pm 0.001$. The $i' - J = 2.435 \pm 0.004$ colour implies a spectral type of M4 for the secondary star (Hawley et al. 2002, Table 3), consistent with the result from Nebot Gómez-Morán et al. (2009). The distance determined from the spectroscopic fit (228 ± 5 pc) means that the absolute J band magnitude of the secondary star is $M_J = 8.2$. Using the M_J-spectral type relation from Hawley et al. (2002), also gives a spectral type of M4.

Modelling the light curves

The light curves of SDSS J1212-0123 are characterised by a deep eclipse of the white dwarf (which gets shallower in the longer wavelength bands). There is little variation out of eclipse and there is no evidence of a secondary eclipse in any of the light curves.

The light curves were fitted using the procedure detailed in Section 2.3.4. However, the light curves by themselves are unable to give a unique solution to the radii and inclination. However, using the radial velocity and gravitational redshift constraints from the spectroscopy allows us to break the degeneracy. This is achieved by allowing the mass ratio, q, and velocity scale, V_s to be free parameters in the fit. After a model is computed the radial velocities are calculated via

$$K_{\mathrm{WD}} \;=\; (q/(1+q))V_s \sin i \tag{5.1}$$

$$K_{\mathrm{sec}} \;=\; (1/(1+q))V_s \sin i, \tag{5.2}$$

we can also compute the masses using

$$M = PV_s^3/2\pi G, \tag{5.3}$$

where M is the total system mass. The individual masses are then

$$M_{\rm WD} = M/(1+q) \quad (5.4)$$

$$M_{\rm sec} = qM_{\rm WD}. \quad (5.5)$$

The orbital separation a is then calculated from

$$a = V_s/2\pi P, \quad (5.6)$$

allowing us to calculate the radii of the two stars. Combining all these calculations yields the masses and radii of both stars. We can then use these to calculate the gravitational redshifts using Equation 2.11 and 2.12. The derived gravitational redshift can then be used as a prior constraint during the MCMC minimisation by using it (as well as the fit to the primary eclipse) to decide on the probability of an MCMC jump occurring.

The data were phase folded and the period set equal to one. The temperature of the white dwarf as fixed as 17,900K (from the spectral fit). Quadratic limb darkening coefficients from Claret & Bloemen (2011) for a $T_{\rm eff} = 3000$K, $\log g = 5$ main sequence star were used for the secondary star. The quadratic limb darkening coefficients for the white dwarf were calculated using a white dwarf model with $T_{\rm WD} = 17,900$ and $\log g = 7.53$ (based on our spectroscopic fits) folded through the ULTRACAM u', g', i' and SOFI J filter profiles. For both stars I quote the coefficients a and b where $I(\mu)/I(1) = 1 - a(1-\mu) - b(1-\mu)^2$, where μ is the cosine of the angle between the line of sight and the surface normal. All limb darkening parameters were kept fixed.

The results of a MCMC production run are listed in Table 5.4 along with their 1σ uncertainties, I also list the limb darkening coefficients used for each band. The results from all four bands are consistent. Figure 5.6 shows the fits to the primary eclipses in each band and the residuals to the fits.

5.4.2 GK Vir

Spectral features

Figure 5.7 shows an average X-shooter spectrum of GK Vir. The hot white dwarf dominates the spectrum at wavelengths shorter than 1 micron. In the J band the secondary star contributes roughly 50 per cent of the overall flux. Hydrogen Balmer absorption lines from the white dwarf are visible as well as narrow He II 4686 Å absorption from the white dwarf, making it a DAO white dwarf, as mentioned by

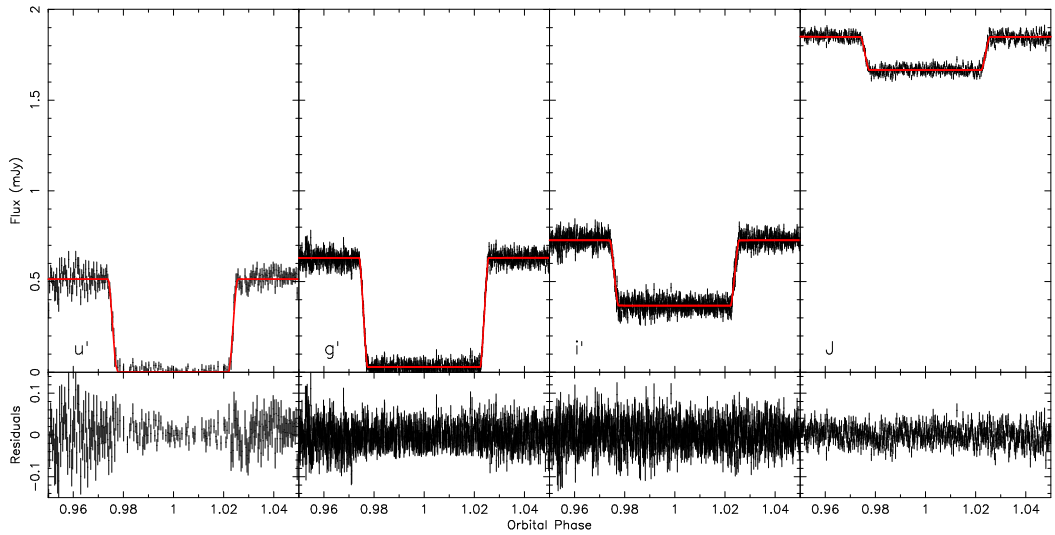

Figure 5.6: ULTRACAM u', g' and i' and SOFI J band primary eclipses of SDSS J1212-0123 with model fits and residuals.

Table 5.4: Parameters from Markov chain Monte Carlo minimisation for SDSS J1212-0123, some fitted, some fixed a priori (those without quoted uncertainties). a and b are the quadratic limb darkening coefficients. A is the fraction of the irradiating flux from the white dwarf absorbed by the secondary star.

Parameter	u'	g'	i'	J
i (deg)	86.1 ± 2.2	85.7 ± 0.6	85.8 ± 0.8	85.5 ± 0.8
$r_{\rm WD}/a$	0.0092 ± 0.0002	0.0092 ± 0.0002	0.0093 ± 0.0002	0.0092 ± 0.0002
$r_{\rm sec}/a$	0.171 ± 0.016	0.171 ± 0.005	0.170 ± 0.006	0.172 ± 0.006
$T_{\rm eff,sec}$ (K)	2618 ± 112	2947 ± 26	3009 ± 41	3342 ± 42
$a_{\rm WD}$	0.2444	0.1340	0.1071	0.0639
$b_{\rm WD}$	0.2256	0.2899	0.1891	0.1342
$a_{\rm sec}$	0.5866	0.6720	0.4193	0.0254
$b_{\rm sec}$	0.2959	0.2660	0.4109	0.4826
A	1.60 ± 0.50	0.81 ± 0.09	0.45 ± 0.03	0.39 ± 0.02

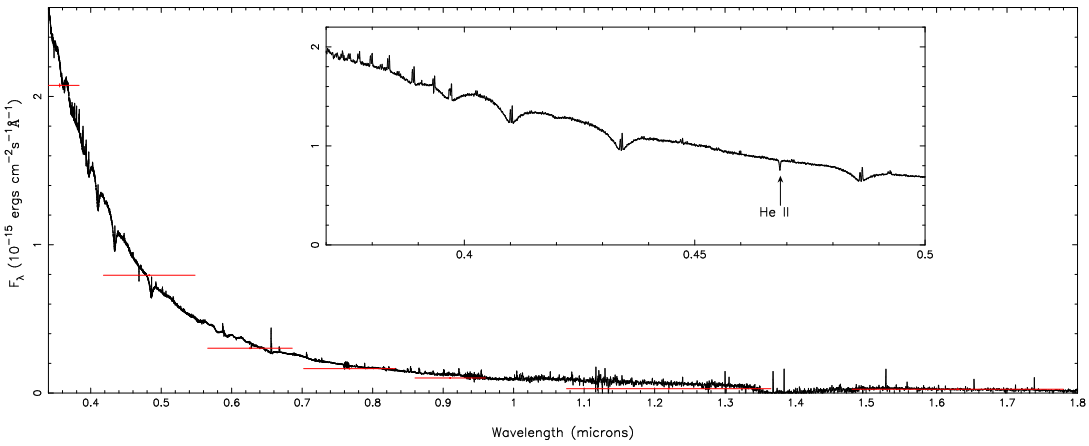

Figure 5.7: Averaged X-shooter spectrum of GK Vir. The SDSS $u'g'r'i'z'$ and UKIDSS JH magnitudes and filter widths are also shown, the UKIDSS J band observations were made during the primary eclipse. A zoom in on the white dwarf features are shown inset with the narrow He II absorption feature labelled.

Fulbright et al. (1993). Numerous emission lines originating from the heated face of the secondary star are seen throughout the spectrum. Na I (8183Å, 8195Å) absorption originating from the secondary star is seen before phase 0.25 but decreases in strength towards phase 0.5 due to the increased ionisation and therefore cannot be used to measure the radial velocity amplitude of the secondary star. No other absorption features for the secondary star are visible.

Atmospheric parameters of the white dwarf

The X-shooter spectrum, averaged in the white dwarf rest-frame, was fitted[3] to obtain an estimate of the effective temperature. As for SDSS J1212-0123, The normalised Balmer lines were fitted, including Hβ to Hζ and the line cores were down-weighted in regions that are noticeably contaminated by emission lines. The best-fit gives a temperature of 55995 ± 673K, a surface gravity of $\log g = 7.68 \pm 0.04$ and a distance of 550 ± 20 pc. These errors are purely statistical, and systematic effects are very likely affecting these results. The X-Shooter data were obtained near the quadrature phases ($\phi \simeq 0.25$ and 0.75, in order to measure $K_{\rm WD}$ and $K_{\rm sec}$), which results in a significant contamination by emission from the strongly irradiated inner hemisphere of the secondary star. Varying the wavelength range around the lines that is down-weighted affects the resulting temperature by several 1000 K. For com-

[3]Fitting performed by B. Gänsicke and D. Koester

parison, the lower-resolution SDSS spectrum of GK Vir was also fitted, obtained near superior conjunction of the companion, and yields a $T_{\rm eff} = 52258 \pm 3131$ K, $\log g = 7.66 \pm 0.18$, and $d = 509 \pm 61$ pc.

Fulbright et al. (1993) analysed a blue spectrum of GK Vir obtained near the eclipse ($\phi \simeq 0.02$), i.e. when the heated inner hemisphere of the companion contributes least to the observed flux. By fitting the Hβ-Hζ Balmer lines and the He II 4686 Å line they determined $T_{\rm eff} = 48800 \pm 1200$ K and $\log g = 7.70 \pm 0.11$. They also modelled the single available far-ultraviolet spectrum of GK Vir, and obtained $T_{\rm eff} = 50000$ K. A major limitation of this spectrum obtained with *IUE* was that the photospheric Lyα line was nearly completely filled in by geocoronal emission. The conclusion is that the effective temperature and distance of the white dwarf GK Vir remains somewhat uncertain, $T_{\rm eff} \simeq 50000$ K and $d \simeq 500 \pm 50$ pc. However, it is reassuring that all the spectroscopic measurements of the surface gravity are consistent with the value that is determined from the light curve fit (see Section 5.5).

Fitting the He II 4686 Å absorption line from the white dwarf gives a helium abundance of $\log[{\rm He/H}] = -2.8 \pm 0.3$ by numbers. Assuming that the secondary star transfers material of solar composition, the total accretion rate is $\dot{M} \simeq 1.4 \times 10^{9} {\rm g\,s^{-1}}$ or $2.2 \times 10^{-17} {\rm M_{\odot}\,yr^{-1}}$, once again consistent with other pre-CVs.

White dwarf radial velocity

Due to the high temperature of the white dwarf, the Balmer lines lack narrow cores and are therefore unsuitable for radial velocity work. The radial velocity of the white dwarf in GK Vir was measured from the He II 4686 Å absorption line using the same technique as used for SDSS J1212-0123. Figure 5.8 shows a trail of the He II line and Figure 5.9 shows the fitted radial velocity curve, which gives a value of $K_{\rm WD} = 38.6 \pm 0.8\,{\rm km\,s^{-1}}$ and a velocity offset of $\gamma_{\rm WD} = -27.2 \pm 0.7\,{\rm km\,s^{-1}}$.

Emission lines

A large number of emission lines are seen in the spectrum of GK Vir caused by the heating of the secondary star by the white dwarf. However, the secondary star in GK Vir receives a much larger irradiating flux to that in SDSS J1212-0123 due to the higher temperature of the white dwarf, therefore a larger number of lines are present and from higher ionised states. Unfortunately the strength of the Na I absorption doublet is too low after phase 0.25 and, combined with the lack of any other absorption features from the secondary star, means that we are unable to get a direct measurement of the radial velocity amplitude of the centre of mass

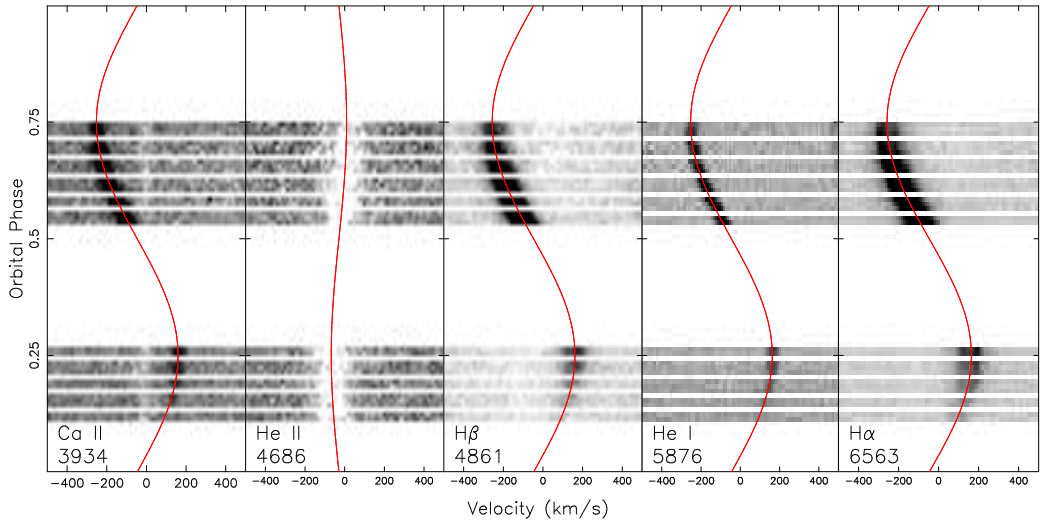

Figure 5.8: Trailed spectra of several lines in GK Vir. The grey-scale runs from white (75 per cent of the continuum level) to black (125 per cent of the continuum level). The Ca II 3934 Å line shows emission from the M star as well as weak interstellar absorption which shows no radial velocity variations. The He II 4686 Å line originates from the white dwarf. The Hβ and Hα emission from the M star shows inverted cores and asymmetric profiles similar to those seen in NN Ser (Chapter 3). The red lines show the best fits to the lines.

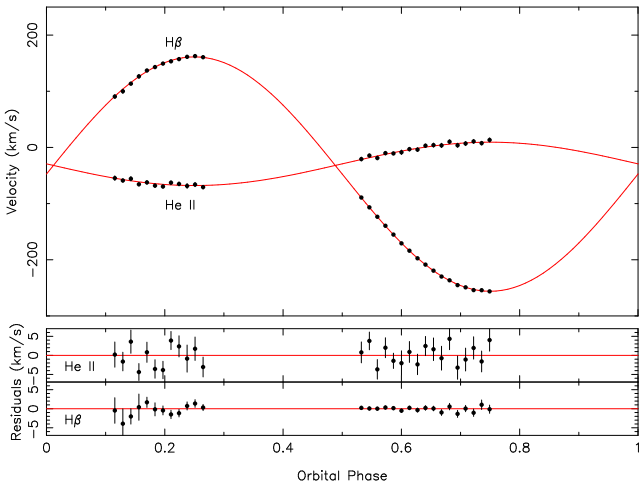

Figure 5.9: Radial velocity fits to the He II 4686 Å absorption from the white dwarf and Hβ emission from the secondary star in GK Vir with residuals plotted below. The emission component does not track the centre of mass of the secondary star.

of the secondary star. The radial velocities and offsets of all of the emission lines identified were measured using the same method used for SDSS J1212-0123, these are listed in Table B.1 in the Appendix. These results give a velocity offset of $\gamma_{\rm sec} = -47.35 \pm 0.05\,{\rm km\,s^{-1}}$, giving a measured redshift for the white dwarf of $V_z = 20.2 \pm 0.7\,{\rm km\,s^{-1}}$.

$K_{\rm sec}$ correction

As previously noted the emission lines in the X-shooter spectra of GK Vir cannot be used to directly measure $K_{\rm sec}$, needed for accurate mass determinations. We need to determine the deviation between the reprocessed light centre and the centre of mass for the secondary star. As with SDSS J0857+0342 in Chapter 4 a direct measurement of the optical depths of each of the emission lines is not possible. This is because, in the case of GK Vir, we lack full orbit light coverage. Therefore, the process used for NN Ser cannot be used here. However, a slightly more sophisticated approach can be used, compared to that used in Chapter 4.

The optical depths of the emission lines in GK Vir can be estimated using the observation of SDSS J1212-0123 and assuming a similar behaviour in the lines. The optical depth of the lines in SDSS J1212-0123 can be determined directly because, in this case, we have a direct measurement of $K_{\rm sec}$. This is done by reversing Equation 2.5 to determine the optical depths. The left hand panel of Figure 5.10 shows where the emission lines lie with respect to the optically thin lower limit

and the optically thick upper limit. The measured radial velocities of the Fe I lines are found to be consistent with them being optically thin. The majority of the emission lines in SDSS J1212-0123 appear to lie somewhere between optically thick and optically thin with the exception of the hydrogen Balmer lines and the calcium H and K lines. For these lines the measured radial velocity is far higher than even the optically thick limit, implying that the emission is more uniformly spread over the surface of the secondary star. This is most likely caused by stellar activity. This is consistent with the observations of several small flares during our photometry and implies that the secondary star in SDSS J1212-0123 is an active star.

From our analysis of the emission lines in SDSS J1212-0123 I make the assumption that the Fe I lines in GK Vir are also optically thin. The radial velocities of these lines can then be used to predict $K_{\rm sec}$ using Equation 2.5 with $f = 0.77$. The radial velocity amplitude of an optically thin line in GK Vir is then $K_{\rm Thin} = 204 \pm 2\,{\rm km\,s^{-1}}$. This result can then be used as a prior constraint in the light curve fitting. The right hand panel of Figure 5.10 shows the radial velocity amplitudes of the emission lines in GK Vir, the dashed lines are based on the results of the light curve fitting. The spread in the emission line radial velocities in GK Vir is relatively small compared to SDSS J1212-0123 because of the small relative size of the secondary star ($R_{\rm sec}/a$).

Spectral type of the secondary star

The secondary star in GK Vir was detected in the r', i' and J band eclipses giving magnitudes of $r' = 21.72 \pm 0.03$, $i' = 19.98 \pm 0.01$ and $J = 17.59 \pm 0.05$. The $r' - i' = 1.74 \pm 0.03$ colour is consistent with a spectral type of M4.5 whilst the $i' - J = 2.39 \pm 0.05$ is closer to a spectral type of M4 (Hawley et al., 2002). Using the distance from the spectroscopic fit (550 ± 20pc) the secondary star has an absolute J band magnitude of $M_J = 8.9$, giving it a spectral type of M4.5 (Hawley et al., 2002), therefore I adopt a spectral type of M4.5 $\pm$ 0.5.

Modelling the light curves

The light curves of GK Vir show a deep eclipse of the white dwarf even in the J band. GK Vir shows a small reflection effect out of eclipse, however no secondary eclipse is detected. The light curves of GK Vir were fitted in the same way as those of SDSS J1212-0123. However, since we lack a direct measurement of $K_{\rm sec}$, the constraint on $K_{\rm Thin}$ was used, combined with Equation 2.5 as well as the $K_{\rm WD}$ and gravitational redshift measurements to constrain the inclination.

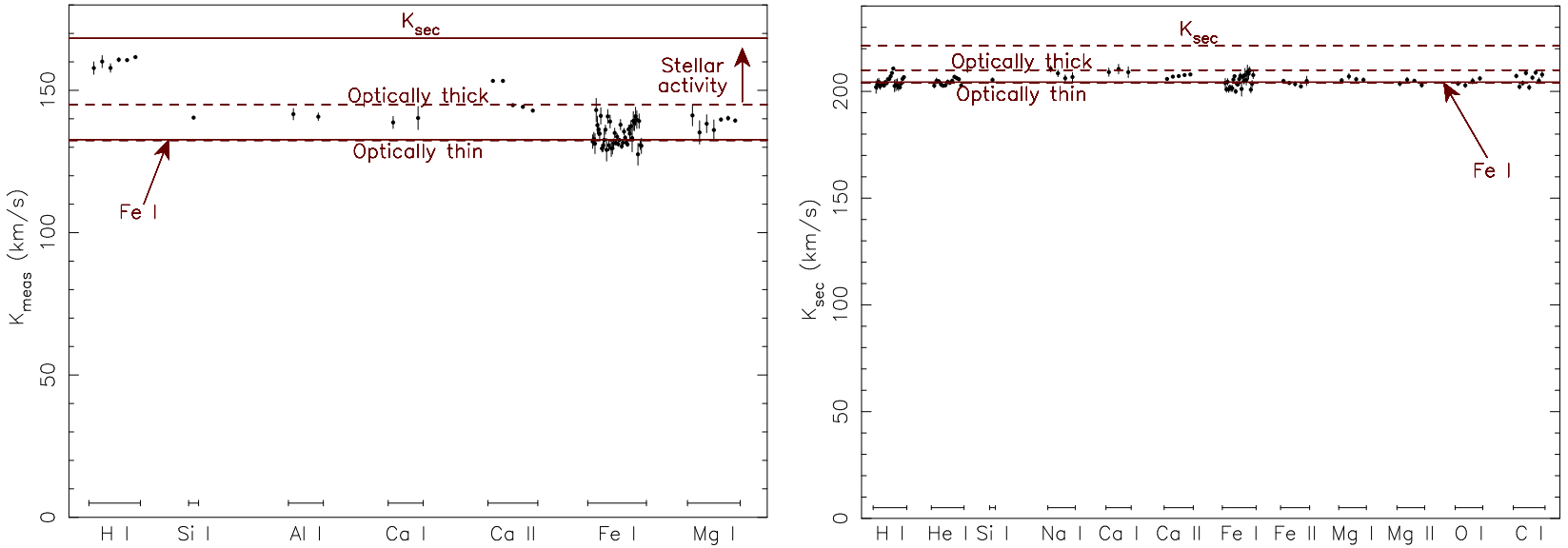

Figure 5.10: *Left:* radial velocities of the emission lines from the secondary star in SDSS J1212-0123. The measured value of centre of mass radial velocity ($K_{\rm sec}$) is also shown. The two dashed lines denote the radial velocity that an optically thick and optically thin line would have. The solid line at $133\,{\rm km\,s^{-1}}$ is a weighted average of the radial velocity amplitudes of the Fe I lines, these appear to be optically thin. The radial velocity amplitudes of the hydrogen Balmer lines and the calcium H and K lines are far above the optically thick limit implying that these lines originate, at least in part, from stellar activity. *Right:* a similar plot but for GK Vir. However, in this case a direct measurement of $K_{\rm sec}$ is not possible from the spectroscopy, but by assuming that the Fe I lines are optically thin a consistent solution is found. The much tighter limits and smaller correction in GK Vir imply that the secondary star is quite small.

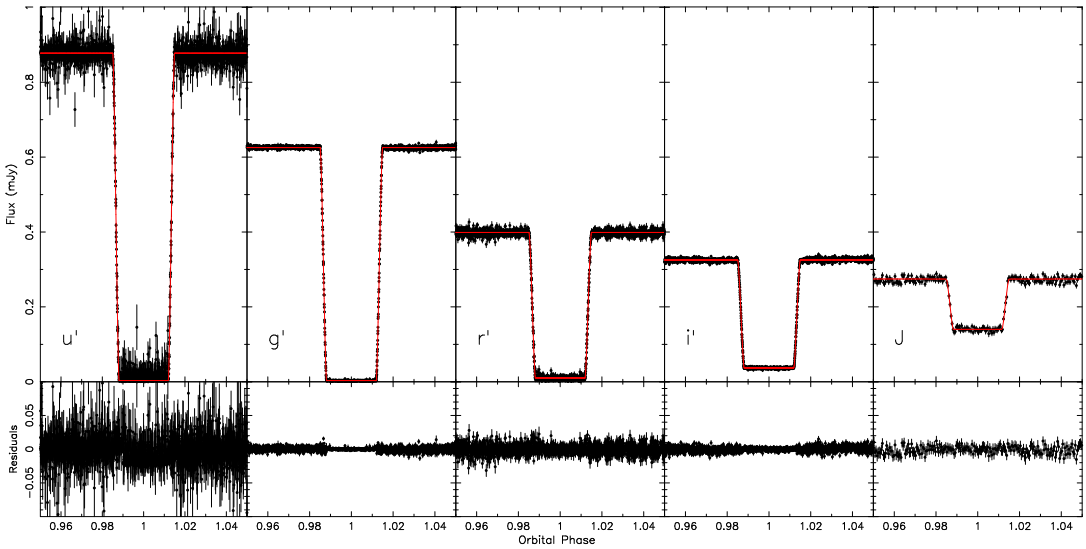

Figure 5.11: Flux calibrated ULTRACAM u', g', r' and i' and SOFI J band primary eclipses of GK Vir with model fits and residuals.

The data were phase binned, using smaller bins on the ingress and egress, and the period kept fixed as one when fitting the light curves. The temperature of the white dwarf was fixed at 55,995K. Quadratic limb darkening coefficients from Claret & Bloemen (2011) for a $T_{\rm eff} = 3000$K, $\log g = 5$ main sequence star were used form the secondary star. Quadratic limb darkening coefficients for the white dwarf were calculated using a white dwarf model with $T_{\rm WD} = 55,995$ and $\log g = 7.68$ based on the spectroscopic fits, folded through the ULTRACAM u', g', r' and i' and SOFI J filter profiles. For both stars I quote the coefficients a and b where $I(\mu)/I(1) = 1 - a(1-\mu) - b(1-\mu)^2$, where μ is the cosine of the angle between the line of sight and the surface normal, all limb darkening parameters were kept fixed. The r' band light curve lacks any out of eclipse information (barring that immediately before and after the eclipse) hence A, the fraction of irradiating flux absorbed by the secondary star, is unconstrained. Therefore, it was kept fixed at 0.4; this parameter has no effect on the radii or inclination.

Figure 5.11 shows the fits to the light curves and the residuals and our final fitted parameters are listed in Table 5.5. The limb darkening coefficients used for each band are also listed.

Table 5.5: Parameters from Markov chain Monte Carlo minimisation for GK Vir, some fitted, some fixed a priori (those without quoted uncertainties). a and b are the quadratic limb darkening coefficients. A is the fraction of the irradiating flux from the white dwarf absorbed by the secondary star, this was kept fixed for the r' band since there is little coverage out-of-eclipse in this band.

Parameter	u'	g'	r'	i'	J
i (deg)	89.5 ± 0.7	89.5 ± 0.6	89.3 ± 0.9	89.2 ± 0.9	88.8 ± 1.4
$r_{\rm WD}/a$	0.0093 ± 0.0002	0.0094 ± 0.0002	0.0093 ± 0.0003	0.0094 ± 0.0003	0.0097 ± 0.0006
$r_{\rm sec}/a$	0.085 ± 0.002	0.085 ± 0.002	0.086 ± 0.002	0.086 ± 0.003	0.088 ± 0.006
$T_{\rm eff,sec}$ (K)	3113 ± 31	3270 ± 12	3224 ± 28	3508 ± 40	4117 ± 139
$a_{\rm WD}$	0.0769	0.0594	0.0505	0.0446	0.0257
$b_{\rm WD}$	0.1393	0.1165	0.0896	0.0736	0.0490
$a_{\rm sec}$	0.5866	0.6720	0.6364	0.4193	0.0254
$b_{\rm sec}$	0.2959	0.2660	0.2521	0.4109	0.4826
A	1.055 ± 0.039	0.551 ± 0.006	0.400	0.263 ± 0.009	0.245 ± 0.032
$K_{\rm sec}$	221.0 ± 2.1	221.2 ± 2.1	221.1 ± 2.1	221.3 ± 2.1	222.5 ± 2.3

5.5 Discussion

The light curve fits combined with Equations (5.3)-(5.6) yield direct measurements for the masses and radii of both components in SDSS J1212-0123 and GK Vir. For the final values and uncertainties I combined the results of all the light curves, however, since they are all constrained by the same spectroscopic information the uncertainties in each light curve fit are not independent. Therefore the results were combined from each light curve in an optimal way by calculating the minimum possible error on each parameter purely from the spectroscopic constraints (i.e. the prior constraint used for fitting all of the light curves) and then combining parameters allowing for the correlated and random noise components. The final parameters for both systems are listed in Table 5.6. The secondary star's shape in both systems is slightly distorted due to the presence of the nearby white dwarf, therefore Table 5.6 lists the radius of the secondary star in various directions. This is a very minor effect in GK Vir whilst the effect is somewhat larger for SDSS J1212-0123, though in both cases the variations are smaller than the uncertainty on the radius from the light curve fits. For my final discussions I adopt the volume-averaged radii.

Figure 5.12 shows the mass-radius plot for white dwarfs. The position of the white dwarfs in SDSS J1212-0123 and GK Vir are shown as well as other accurate white dwarf mass-radius measurements. The measured mass and radius of the white dwarf in GK Vir are consistent with a carbon-oxygen (CO) core white dwarf of the same temperature, with a thick hydrogen envelope ($\rm M_H/M_{WD} = 10^{-4}$). The measured mass and radius of the white dwarf in SDSS J1212-0123 are also consistent with a CO core white dwarf with the same temperature and a thick hydrogen enve-

Table 5.6: System parameters. The surface gravities quoted are from the spectroscopic fit. They are consistent with the measured masses and radii. The accretion rate is that of the material from the wind of the secondary star onto the white dwarf

Parameter	SDSS J1212-0123	GK Vir
Period (days)	0.335 871 14(13)	0.344 330 832 742(99)
Inclination	$85.7^\circ \pm 0.5^\circ$	$89.5^\circ \pm 0.6^\circ$
Binary separation	$1.815 \pm 0.003\,\mathrm{R}_\odot$	$1.82 \pm 0.01\,\mathrm{R}_\odot$
Mass ratio	0.620 ± 0.001	0.174 ± 0.004
WD mass	$0.439 \pm 0.002\,\mathrm{M}_\odot$	$0.564 \pm 0.014\,\mathrm{M}_\odot$
Sec mass	$0.273 \pm 0.002\,\mathrm{M}_\odot$	$0.116 \pm 0.003\,\mathrm{M}_\odot$
WD radius	$0.0168 \pm 0.0003\,\mathrm{R}_\odot$	$0.0170 \pm 0.0004\,\mathrm{R}_\odot$
Sec radius polar	$0.304 \pm 0.007\,\mathrm{R}_\odot$	$0.154 \pm 0.003\,\mathrm{R}_\odot$
Sec radius sub-stellar	$0.310 \pm 0.007\,\mathrm{R}_\odot$	$0.156 \pm 0.003\,\mathrm{R}_\odot$
Sec radius backside	$0.309 \pm 0.007\,\mathrm{R}_\odot$	$0.156 \pm 0.003\,\mathrm{R}_\odot$
Sec radius side	$0.306 \pm 0.007\,\mathrm{R}_\odot$	$0.155 \pm 0.003\,\mathrm{R}_\odot$
Sec radius volume-averaged	$0.306 \pm 0.007\,\mathrm{R}_\odot$	$0.155 \pm 0.003\,\mathrm{R}_\odot$
WD $\log g$	7.51 ± 0.01	7.68 ± 0.04
WD temperature	$17,707 \pm 35$K	$55,995 \pm 673$K
K_{WD}	$104.4 \pm 0.5\,\mathrm{km\,s^{-1}}$	$38.6 \pm 0.8\,\mathrm{km\,s^{-1}}$
K_{sec}	$168.3 \pm 0.3\,\mathrm{km\,s^{-1}}$	$221.6 \pm 2.0\,\mathrm{km\,s^{-1}}$
$V_{z,\mathrm{WD}}$	$16.1 \pm 0.3\,\mathrm{km\,s^{-1}}$	$20.2 \pm 0.7\,\mathrm{km\,s^{-1}}$
Sec spectral type	M4	$\mathrm{M4.5} \pm 0.5$
Distance	$228 \pm 5\,\mathrm{pc}$	$550 \pm 20\,\mathrm{pc}$
Accretion rate	$6.4 \times 10^{-17}\mathrm{M}_\odot\,\mathrm{yr}^{-1}$	$2.2 \times 10^{-17}\mathrm{M}_\odot\,\mathrm{yr}^{-1}$

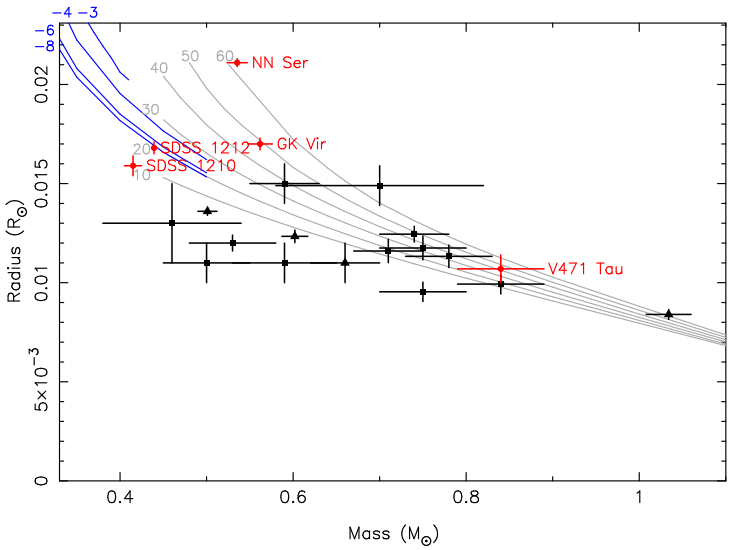

Figure 5.12: Mass-radius plot for white dwarfs. Black points are from Provencal et al. (1998), Provencal et al. (2002) and Casewell et al. (2009). The square points are common proper-motion systems, the triangular points are visual binaries. White dwarfs measurements from PCEBs are shown in red (online version only) from (O'Brien et al., 2001), Chapter 3, Pyrzas et al. (2012) and this work. The grey lines are CO core models with the temperatures labelled in units of 10^3K and with hydrogen layer thicknesses of $M_H/M_{WD} = 10^{-4}$ from Benvenuto & Althaus (1999). The mass and radius of the white dwarf in GK Vir agree well with the 50,000K model. The blue lines are He core models with a temperature of 18,000K and varying hydrogen layer thicknesses labelled by the exponent of the hydrogen layer fraction, from Panei et al. (2007). The mass and radius of the white dwarf in SDSS J1212-0123 is consistent with the CO core models for its temperature but we can rule out a CO core on evolutionary grounds. Therefore the white dwarf in SDSS J1212-0123 is consistent with the He core models only if it has a very thin hydrogen envelope ($M_H/M_{WD} \leq 10^{-6}$).

lope ($M_H/M_{WD} = 10^{-4}$). However, although it is possible to create CO core white dwarfs with masses < 0.5 $M_\odot$ via considerable mass loss along the red giant phase (Prada Moroni & Straniero 2009; Willems & Kolb 2004; Han et al. 2000), doing so in a binary system requires a large initial mass ratio and results in a widening of the orbital separation, hence we would not expect a CO core white dwarf with a mass < 0.5 $M_\odot$ in a close binary system. Therefore the white dwarf in SDSS J1212-0123 should have a He core, as noted by Shen et al. (2009).

Several He core mass-radius relations are shown in Figure 5.12 for a white dwarf with a temperature of 18,000K and varying hydrogen layer thicknesses. The white dwarf in SDSS J1212-0123 is consistent with these relations only if it has a

very thin hydrogen envelope ($M_H/M_{WD} \leq 10^{-6}$). Figure 5.13 shows a zoomed in version of the mass radius plot for the white dwarf in SDSS J1212-0123 as well as the same He core models as Figure 5.12. The black line shows the range of possible masses and radii that the white dwarf in SDSS J1212-0123 could have based on the radial velocities and the primary eclipse shape (i.e. no inclination constraints). The numbers plotted along this line are what the measured gravitational redshift of the white dwarf would need to be in order to give that mass and radius. Previous studies have found that the spectroscopic gravitational redshift measurements are usually slightly inconsistent with mass-radius measurements via other methods (Pyrzas et al. 2012; chapter 3; Maxted et al. 2007) meaning that our inclination constraints may be slightly incorrect. However, Figure 5.13 shows that it is not possible for the white dwarf to have a thick hydrogen envelope ($M_H/M_{WD} > 2 \times 10^{-4}$) even if the inclination is 90°. Current evolutionary models are unable to create He core white dwarfs with such thin hydrogen envelopes, the thinnest envelopes are of the order of $M_H/M_{WD} \sim 3 \times 10^{-4}$ (Althaus et al. 2009; Sarna et al. 2000; Driebe et al. 1998) meaning that, assuming our measured V_z value is accurate, either SDSS J1212-0123 has had a very unusual evolutionary history or that current evolutionary models of He core white dwarfs are incomplete and overestimate their size. Additional He core white dwarf mass-radius measurements should show if this is the case.

Figure 5.14 show the mass-radius plot for low mass stars. The masses and radii of the secondary stars in SDSS J1212-0123 and GK Vir are marked as well as other precise measurements. The mass and radius of the secondary star in SDSS J1212-0123 show that it is over-inflated for its mass compared with evolutionary models by $\sim$ 12 per cent. This discrepancy can be reduced to $\sim$ 9 per cent if the secondary star is active. In this case the radius increases to compensate for loss of radiative efficiency due to starspots and due to a strong magnetic field caused by rapid rotation (Morales et al., 2010; Chabrier et al., 2007). The Balmer emission lines and light curves show evidence of activity from the secondary star in SDSS J1212-0123, therefore these effects can explain some of the discrepancy, however, the star remains oversized. The secondary star in GK Vir is also oversized by $\sim$ 9 per cent, this drops to $\sim$ 6 per cent if it is active, though there is no evidence of activity from this star.

Taking the effects of rotational and tidal perturbations fully into account only causes an increase in the radii of 0.1 per cent for GK Vir and 0.4 per cent for SDSS J1212-0123 (Sirotkin & Kim, 2009) which is not enough to explain the discrepancy.

Irradiation by the white dwarf can cause the secondary star to become in-

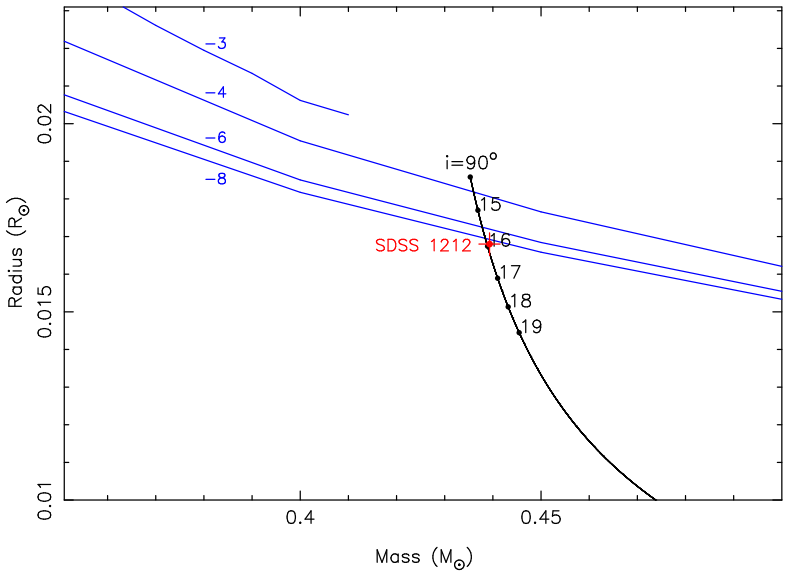

Figure 5.13: Mass-radius plot for the white dwarf in SDSS J1212-0123. The blue lines are He core models with a temperature of 18, 000K and varying hydrogen layer thicknesses labelled by the exponent of the hydrogen layer fraction, from Panei et al. (2007). The black line shows the possible mass and radius range without any constraint on the inclination with 90° at the top. The numbers along this line correspond to the gravitational redshift that the white dwarf would have at that inclination (in $\mathrm{km\,s^{-1}}$). Our measured redshift ($16.1 \pm 0.3\,\mathrm{km\,s^{-1}}$) means that the white dwarf is consistent with models which have a thin hydrogen layer. However, even without any inclination constraints it is not possible for the white dwarf to have a thick ($\mathrm{M_H/M_{WD}} > 2 \times 10^{-4}$) hydrogen layer.

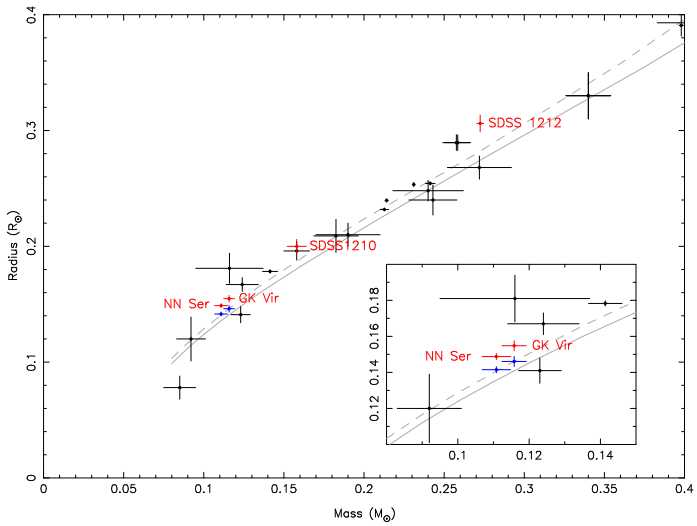

Figure 5.14: Mass-radius plot for low-mass stars. Black points are high-precision measurements taken from Knigge et al. (2011), Carter et al. (2011) and Ofir et al. (2011). The solid line is the 4.0-Gyr isochrone from Baraffe et al. (1998) whilst the dashed line is a 4.0-Gyr model from Morales et al. (2010) which includes the effects of magnetic activity. Low-mass stars from PCEBs are shown in red from Pyrzas et al. (2012), Chapter 3 and this chapter. The blue points show the radii of these stars after correcting for irradiation (negligible for SDSS J1210+3347 and SDSS J1212-0123). The secondary star in GK Vir is consistent with model predictions after correcting for irradiation, however the secondary star in SDSS J1212-0123 is still oversized.

flated by effectively blocking the energy outflow through the surface layers (Ritter et al., 2000). For NN Ser correcting this effect brought the mass and radius measurements into agreement with evolutionary models. For the secondary star in GK Vir I find that irradiation increases its radius by 5.6% (Ritter et al., 2000; Hameury & Ritter, 1997), enough to bring it into agreement with evolutionary models. However, for the far less irradiated secondary star in SDSS J1212-0123 I find an increase of only 0.4% meaning that it is still overinflated. The corrected radii are shown in Figure 5.14

5.6 Summary

In this chapter I have measured precise masses and radii for both components of the eclipsing PCEBs SDSS J1212-0123 and GK Vir. In both cases I used measurements of the gravitational redshift of the white dwarf to constrain the orbital inclination. The mass and radius of the $0.564\,M_{\odot}$ white dwarf in GK Vir are consistent with evolutionary models for a CO core white dwarf with a thick hydrogen envelope. The mass and radius of the white dwarf in SDSS J1212-0123 place it in the crossover region between a CO core white dwarf and a He core white dwarf but a CO core can be excluded on evolutionary grounds. This means that the white dwarf in SDSS J1212-0123 is the first He core white dwarf with precise mass-radius measurements however, it is under-inflated for its temperature unless it has a very thin ($M_H/M_{WD} \lesssim 10^{-6}$) hydrogen envelope, which close binary models are unable to produce. The mass and radius of the secondary star in GK Vir are consistent with evolutionary models after correcting for the effects of irradiation by the white dwarf, however, the measured radius of the secondary star in SDSS J1212-0123 is larger than that predicted by models, even after the effects of activity, rapid rotation and irradiation are taken into account.

Chapter 6

A new double white dwarf eclipsing binary

6.1 Introduction

In this chapter I present a new double white dwarf eclipsing binary. This system is unique among eclipsing double white dwarfs in that both components are visible spectroscopically. This means that precise masses and radii can be measured using the same techniques as those used for the eclipsing PCEBs presented in the previous chapters.

6.2 Target information

The subject of this chapter, CSS 41177 (SDSS J100559.10+224932.2), was listed as a white dwarf plus main sequence binary by Drake et al. (2010). They used a marginal 2MASS detection to infer the presence of a late-type companion though they note that a small faint object could also produce the observed transit signal. CSS 41177 was observed as part of a monitoring campaign for period variations in white dwarf plus main sequence binaries (see Chapter 7). With a better sampled eclipse and detection of the secondary eclipse we realised that it was in fact a detached eclipsing double white dwarf binary, making it only the second known after NLTT 11748 (Steinfadt et al., 2010), but in this case the secondary star contributes 22% of the overall flux (compared to 3% in NLTT 11748). Follow up spectroscopy revealed that CSS 41177 was also a double-lined spectroscopic binary. Since this discovery two more eclipsing double white dwarf binaries have been discovered: SDSS J0654+2844 (Brown et al., 2011) and GALEX J1717+6757 (Vennes et al., 2011b).

6.3 Observations and their Reduction

6.3.1 LT+RISE photometry

Three primary eclipses and two secondary eclipses of CSS 41177 were observed using the LT and RISE (Steele et al., 2004) between February and April 2011. RISE is a high-speed frame transfer CCD camera with a single wideband V+R filter (Steele et al., 2008). All observations were made in 2×2 binning mode, giving a scale of 1.1 arcsec per pixel, and with exposure times of 12-13 seconds.

The raw data are automatically run through a pipeline that debiases, removes a scaled dark frame and flat-fields the data. Aperture photometry was performed using the method outlined in Chapter 2.

6.3.2 Gemini+GMOS spectroscopy

CSS 41177 was observed using GMOS on the 8m Gemini Observatory North telescope (Hook et al., 2004) on 15 March 2011. The R831 grating was used with a 0.5 arcsec slit and 4×2 binning (spatial by spectral) to give a resolution of $R \sim 4400$ centered at Hα. Exposure times of 10 minutes were used, and a total of 17 spectra were recorded, covering an entire orbit. The data were reduced using the methods outlined in Chapter 2.

6.4 Results

6.4.1 Light curve model fitting

The left hand panel of Figure 6.1 shows the LT+RISE photometry of CSS 41177 folded on its 2.78 hour orbital period and binned by a factor of two. Since both eclipses are detected, the light curve information alone constrains the system inclination and the radii scaled by the binary separation. To measure the system parameters the light curve was fitted with the same code and methods outlined in Section 2.3, using MCMC minimisation.

All the times were corrected to Barycentric Dynamical Time (TDB). Each light curve was individually fitted in order to measure mid-eclipse times for the three primary eclipses recorded. The second eclipse recorded was set to cycle number zero. The measured eclipse times are shown in Table 6.1. The zero-point of the ephemeris and the period were allowed to vary in the final fit. The mass ratio was kept fixed as 1.0 (the light curves of this well-detached system are independent of the mass ratio). The quadratic limb darkening coefficients were determined from a pair of

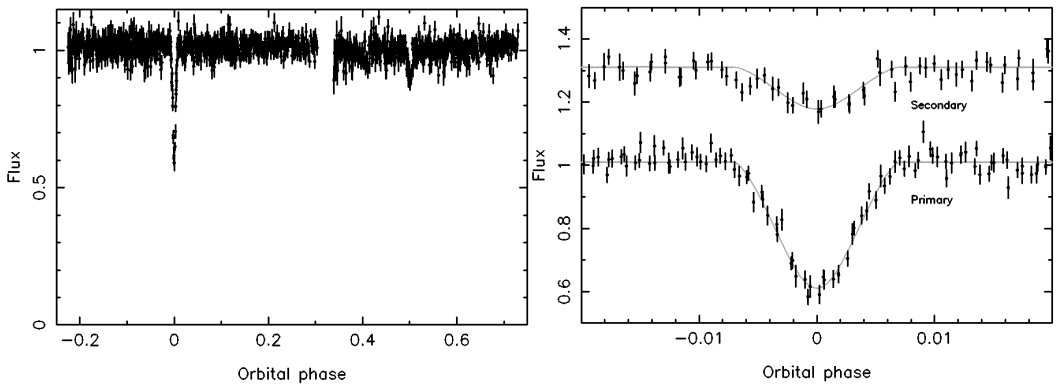

Figure 6.1: *Left:* LT+RISE photometry of CSS 41177 folded on its 2.78 hour orbital period and binned by a factor of two. *Right:* The unbinned primary and secondary eclipse data. The secondary eclipse is shifted back by half a cycle and vertically by 0.3.

Table 6.1: Mid-eclipse times for CSS 41177.

Cycle number	Eclipse time MJD(BTDB)	Uncert MJD(BTDB)
-171	55599.087788	0.000013
0	55618.926463	0.000016
302	55653.963116	0.000020

white dwarf atmosphere models with temperatures of 21,100K and 10,500K and $\log g = 7.3$ (see Section 6.4.2) folded through the RISE filter profile (Gänsicke et al., 1995). The coefficients determined were $a = 0.105$ and $b = 0.228$ for the primary and $a = 0.176$ and $b = 0.288$ for the secondary for $I(\mu)/I(1) = 1 - a(1-\mu) - b(1-\mu)^2$, where μ is the cosine of the angle between the line of sight and the surface normal; these values were kept fixed. The inclination, scaled radii and surface brightness ratio were allowed to vary.

The right hand panel of Figure 6.1 shows the best fit to the RISE photometry around the eclipses. The two eclipses constrain the system inclination to $89.2° \pm 0.3°$. The constraints on the two scaled radii are shown in the left hand panel of Figure 6.4. We also update the ephemeris to

$$\mathrm{MJD(BTDB)} = 55618.926447(9) + 0.116\,015\,49(5)E,$$

which is consistent with the ephemeris of Drake et al. (2010).

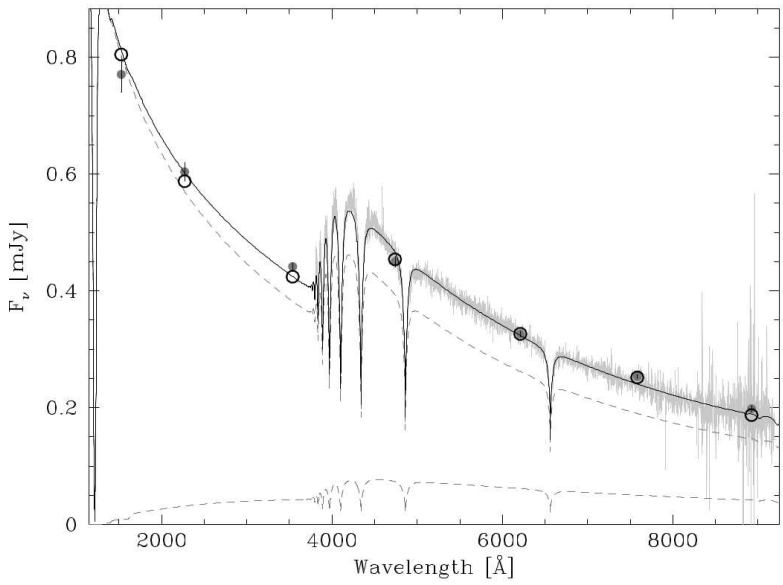

Figure 6.2: SDSS spectrum of CSS 41177 fitted with a combination of a $T_{\rm eff} = 10,500 \pm 500$K (lower dashed line) and a$T_{\rm eff} = 21,100 \pm 800$K (upper dashed line) white dwarf models. The grey points are the observed GALEX ultraviolet and SDSS visual fluxes and the open circles are the fluxes predicted from the fit.

6.4.2 Temperatures

Data from the Sloan Digital Sky Survey (SDSS) were used to determine the temperatures of the two white dwarfs in CSS 41177[1]. Initially, its SDSS spectrum was fitted as a single white dwarf using the models of Koester et al. (2005), which results in a $T_{\rm eff,1} = 21,535 \pm 214$K and $\log g = 7.36 \pm 0.44$. To determine the temperature of both stars better, the SDSS *ugriz* magnitudes were fitted with a composite of two DA white dwarf models, with the additional constraint of the surface brightness ratio $S_1/S_2 = 2.90 \pm 0.23$ in the LT/RISE band, as measured from the light curve. This fit results in $T_{\rm eff,1} = 21,100 \pm 800$K and $T_{\rm eff,2} = 10,500 \pm 500$K, where the quoted errors are estimated, as they correlate with the uncertainties in the surface gravities. The best-fit composite model is shown in Figure 6.2 and reproduces well the observed GALEX ultraviolet fluxes.

6.4.3 Radial velocities

The left hand panel of Figure 6.3 shows the trailed spectrum of CSS 41177 around the Hα line. The non-LTE absorption core from the primary (hotter) star is clearly

[1]This was performed by B. Gänsicke

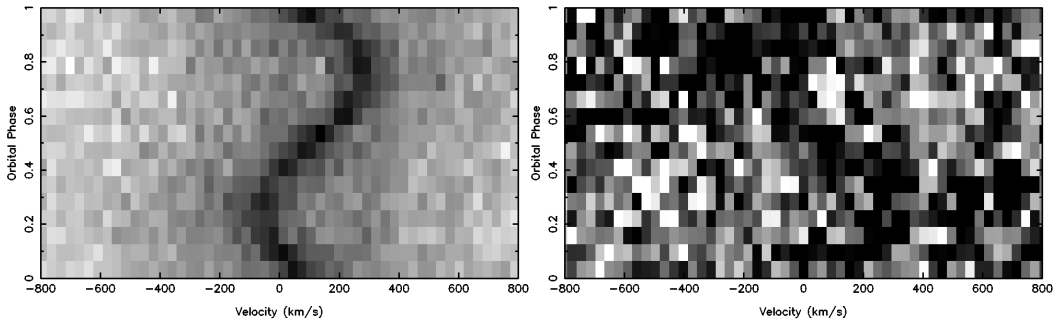

Figure 6.3: *Left:* Trailed spectrum of the Hα line, the scale runs from black (50% of the continuum level) to white (90% of the continuum level). The absorption from the primary star is clearly visible. More subtly absorption from the secondary star is visible moving in anti-phase with the primary stars absorption. *Right:* Same as left hand panel but with the primary stars contribution removed (black is -2% of the continuum, white is 4% of the continuum). The absorption from the secondary star is now visible.

visible. There is also a weaker absorption component moving in anti-phase with the absorption from the primary star originating from the secondary (cooler) star. No other features are visible in the GMOS spectra.

The primary star's absorption was fitted first using the method outlined in Section 2.3. However, the radial velocity measured does not represent the true radial velocity of the primary star as the absorption from the secondary star causes a slight underestimation. Nevertheless, these velocities were used to correct out the motion of the primary star. The shifted spectra were then averaged to obtain the rest-frame spectrum of the primary star, which was then subtracted from all the observed spectra. The result is shown in the right hand panel of Figure 6.3, clearly showing the absorption from the secondary star.

The absorption from the secondary star was fitted in the same way as the primary star. This too underestimated the true velocity since the primary star's contribution had not been completely removed. However, both fits provide us with an initial starting point for K_1 and K_2, the radial velocity amplitudes of both stars. In order to measure accurate radial velocities both absorption components need to be fitted simultaneously. Both lines were fitted together by simultaneously fitting all of the spectra. Each spectrum was fitted using the method from Section 2.3 with an additional broad Gaussian component to account for the wings of the primary star's absorption. The Gaussians were allowed to change position from spectrum-

to-spectrum according to

$$V = \gamma + K \sin(2\pi\phi),$$

for each star, where γ is the offset in the line from its rest wavelength and ϕ is the orbital phase of the spectrum. Due to the faintness of the secondary star's absorption we keep the offset $\gamma_2 = \gamma_1$ to reduce the number of degrees of freedom. All other parameters were initially set to those measured from fitting the lines individually. Levenberg-Marquardt minimisation (Press et al., 1986) was used to fit the data. The resultant fit had a reduced χ^2 of 1.02. The fit resulted in values of $K_1 = 177 \pm 3\mathrm{km\,s^{-1}}$, $K_2 = 181 \pm 20\mathrm{km\,s^{-1}}$ and $\gamma = 109 \pm 2\mathrm{km\,s^{-1}}$. These values imply that CSS 41177 is an equal mass binary (or very close to, given the uncertainty on K_2). CSS 41177 has a relatively small proper motion of $\mu_{\mathrm{RA}} = -0.020 \pm 0.003$ and $\mu_{\mathrm{DEC}} = -0.012 \pm 0.002$ arcsec / yr (retrieved from the US Naval Observatory (USNO) Image and Catalogue Archive) making it likely that it is a member of the Galactic disk.

6.4.4 System Parameters

The RISE photometry constrains i, R_1/a and R_2/a. K_1 and K_2 are constrained from the spectroscopy, therefore we can determine the masses and radii of both white dwarfs using Kepler's third law,

$$\frac{G(M_1 + M_2)}{a^3} = \frac{4\pi^2}{P^2}, \tag{6.1}$$

where P is the orbital period, given the orbital separation from

$$\frac{2\pi}{P}\, a \sin i = K_1 + K_2. \tag{6.2}$$

The masses and radii were determined for each model produced in the MCMC analysis of the light curve using the measured radial velocities and Kepler's laws. The right hand panel of Figure 6.4 shows the regions of allowed masses and radii for both white dwarfs based only upon the photometric and spectroscopic constraints. Also shown are models of helium core white dwarfs with hydrogen layer fractional masses of $\mathrm{M_H/M_*} = 10^{-4}$ (solid lines) and $\mathrm{M_H/M_*} = 10^{-8}$ (dashed lines) from Benvenuto & Althaus (1998) for temperatures of 10,500K (gray) and 21,100K (black) which, given the large uncertainties in our measurements, are consistent with the measured masses and radii. The final system parameters are listed in Table 6.2.

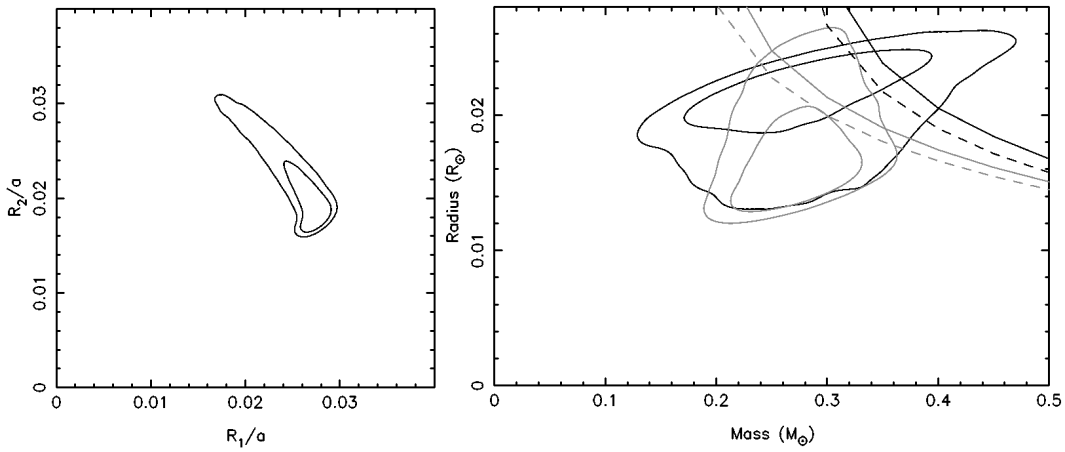

Figure 6.4: *Left:* The contours show the 68 and 95 percentile regions of the scaled radii R_1/a and R_2/a, where a is the orbital separation, constrained by the RISE photometry. *Right:* The contours show the 68 and 95 percentile regions of the masses and radii for the hot (black lines) and cool (gray lines) white dwarfs. Also shown are mass-radius relations for helium core white dwarfs with hydrogen layer fractional masses of $M_H/M_* = 10^{-4}$ (solid lines) and $M_H/M_* = 10^{-8}$ (dashed lines) from Benvenuto & Althaus (1998) for temperatures of 10,500K and 21,100K. The confidence regions shown here are for two parameters jointly and should not be directly compared to the uncertainties in Table 6.2, which are more closely related to single parameter confidence intervals.

Table 6.2: Stellar and binary parameters for CSS 41177

Parameter	Value	Parameter	Value
RA	10:05:59.11	K_1 (km s^{-1})	177 ± 3
Dec	+22:49:32.3	K_2 (km s^{-1})	181 ± 20
GALEX fuv	16.72 ± 0.04	$T_{eff,1}$ (K)	$21,100 \pm 800$
GALEX nuv	16.98 ± 0.03	$T_{eff,2}$ (K)	$10,500 \pm 500$
u	17.317 ± 0.010	M_1 ($M_\odot$)	0.283 ± 0.064
g	17.266 ± 0.005	M_2 ($M_\odot$)	0.274 ± 0.034
r	17.612 ± 0.006	R_1 ($R_\odot$)	0.0210 ± 0.0026
i	17.899 ± 0.008	R_2 ($R_\odot$)	0.0174 ± 0.0031
z	18.151 ± 0.024	a ($R_\odot$)	0.821 ± 0.048
d (pc)	350 ± 13	i (deg)	89.2 ± 0.3
P_{orb} (days)	0.1160156(1)		

6.5 Summary

In this chapter I have shown that the system CSS 41177 is a detached, eclipsing, double white dwarf binary containing two low-mass helium core white dwarfs. The hotter white dwarf has a temperature of $21,100 \pm 800$K and the cooler white dwarf has a temperature of $10,500 \pm 500$K placing it on the red edge of the instability strip.

CSS 41177 is ideally set up to measure precise model-independent masses and radii for both white dwarfs and thus can be used to test white dwarf mass-radius relations. Since the white dwarfs in CSS 41177 have roughly equal masses they will eventually undergo a merger resulting in the formation of a single $\sim 0.6\,M_{\odot}$ sdB star (Han et al., 2003). This will occur in roughly 1.1 Gyr due to the loss of orbital angular momentum via gravitational radiation. The regular eclipse times from CSS 41177 should make it an excellent timing standard for optical astronomy, provided there are no unseen companions.

Chapter 7

Period changes in eclipsing PCEBs

7.1 Introduction

One feature common throughout all eclipsing white dwarf binaries is the sharp eclipse ingress/egress. In the previous chapters I have shown how this can be used to tightly constrain the radii of the two stars. These features also lead to extremely precise eclipse times and in this chapter I present and analyse the period changes that these precise times reveal.

7.2 Observations and their reduction

The observational data set consist of every ULTRACAM observation of an eclipsing PCEBs. These include all of the observations listed in Chapters 3–5 and those listed in Table 7.1. Aperture photometry was performed on all data sets using the procedure outlined in Chapter 2. A notable exception to this was used for the system RX J2130.6+4710 which lies only 12 arcsec away from a bright star (HD 204906, $V = 8.45$). The procedure described in Maxted et al. (2004) was used to correct for the scattered light introduced by this bright star. This involves placing another aperture on the sky at the same distance from the bright star as RX J2130.6+4710 and symmetrically located with respect to the diffraction spikes. The ULTRACAM data were supplemented with the photometry listed in Table 7.2.

Table 7.1: ULTRACAM observations of eclipsing PCEBs not listed elsewhere in this thesis. Primary eclipses occur at phase 1, 2 etc.

Date	Filters	Telescope	UT start	UT end	Av. exp time (s)	Phase range	Conditions (Transparency, seeing)
DE CVn							
22/05/2003	$u'g'i'$	WHT	21:57:16	22:22:44	1.4	0.15–0.18	Good, 1.5"
25/05/2003	$u'g'i'$	WHT	00:34:21	01:44:03	1.4	0.94–1.06	Good, 1.2"
25/05/2003	$u'g'i'$	WHT	22:33:00	23:59:13	1.4	0.44–0.60	Good, 1.2"
04/05/2004	$u'g'i'$	WHT	20:39:25	22:56:47	0.6	0.68–0.96	Excellent, 1.0"
09/03/2006	$u'g'r'$	WHT	23:08:36	01:00:23	1.4	0.90–1.10	Poor, >3"
11/03/2006	$u'g'r'$	WHT	01:35:20	03:00:41	1.2	0.92–1.08	Variable, $1.0 - 3.0$"
12/03/2006	$u'g'r'$	WHT	03:50:25	05:06:55	1.2	0.92–1.07	Good, 1.2"
12/03/2006	$u'g'r'$	WHT	21:40:15	22:30:25	1.2	0.96–1.06	Poor, >3"
QS Vir							
20/05/2002	$u'g'r'$	WHT	20:51:44	00:31:07	1.1	0.48–1.55	Fair, 2.0"
20/05/2003	$u'g'i'$	WHT	23:43:55	00:53:24	2.9	0.93–1.64	Variable, $1.2 - 3.0$"
23/05/2003	$u'g'i'$	WHT	00:39:32	01:35:03	2.9	0.84–1.10	Good, 1.5"
24/05/2003	$u'g'i'$	WHT	22:02:51	22:56:24	2.9	0.38–1.07	Good, 1.2"
13/03/2006	$u'g'r'$	WHT	00:42:35	01:34:29	2.4	0.88–1.09	Fair, 2.0"
RR Cae							
25/11/2005	$u'g'i'$	VLT	00:21:31	01:22:04	0.5	0.42–0.56	Good, 1.5"
26/11/2005	$u'g'i'$	VLT	23:53:01	00:44:38	0.5	0.97–1.06	Good, 1.5"
27/11/2005	$u'g'i'$	VLT	07:04:42	08:16:30	0.5	0.93–1.10	Good, 1.5"
RX J2130.6+4710							
18/05/2003	$u'g'r'$	WHT	02:29:55	05:48:36	1.1	0.97–1.23	Good, 1.2"
25/05/2003	$u'g'i'$	WHT	02:41:38	03:48:08	1.4	0.96–1.03	Excellent, 1.0"
26/05/2003	$u'g'i'$	WHT	03:41:26	04:43:31	1.4	0.95–1.03	Good, 1.5"
13/11/2003	$u'g'r'$	WHT	19:04:41	21:44:06	1.1	0.39–0.59	Good, 1.5"
SDSS J0110+1326							
21/10/2007	$u'g'i'$	WHT	02:46:50	04:32:04	1.2	0.86–1.07	Good, 1.2"
SDSS J0303+0054							
16/10/2007	$u'g'i'$	WHT	02:25:40	03:31:11	5.0	0.89–1.18	Good, 1.2"
17/10/2007	$u'g'i'$	WHT	02:25:04	06:25:18	5.2	0.28–1.52	Good, 1.2"
28/10/2007	$u'g'i'$	WHT	04:40:07	05:36:14	2.3	0.80–1.09	Poor, >3"

Table 7.2: Non-ULTRACAM observations of eclipsing PCEBs. Primary eclipses occur at phase 1, 2 etc.

Date at start of run	Target	Filter/ Instrument	Obs[a]	UT start	UT end	Av. exp time (s)	Phase range	Transparency
10/07/2006	QS Vir	Unfiltered	CBA	17:29:27	18:40:50	30.0	0.80–1.14	Clear
11/07/2006	QS Vir	Unfiltered	CBA	18:52:22	19:57:09	30.0	0.83–1.12	Clear
13/07/2006	QS Vir	Unfiltered	CBA	18:01:30	18:48:48	30.0	0.86–1.07	Clear
18/07/2006	QS Vir	V	CBA	17:19:32	18:26:58	30.0	0.83–1.14	Clear
19/07/2006	QS Vir	V	CBA	18:26:42	19:44:02	30.0	0.77–1.12	Clear
20/07/2006	QS Vir	I	CBA	16:24:46	17:28:17	30.0	0.84–1.13	Clear
23/07/2006	QS Vir	Unfiltered	CBA	16:18:44	20:24:22	30.0	0.71–1.84	Cloudy
29/07/2006	QS Vir	Unfiltered	CBA	17:27:15	18:35:11	30.0	0.82–1.13	Clear
06/02/2008	QS Vir	ULTRASPEC	ESO	07:43:05	08:48:32	0.4	0.90–1.07	Clear
07/02/2008	QS Vir	ULTRASPEC	ESO	05:29:42	06:41:22	2.0	0.91–1.17	Clear
08/02/2008	QS Vir	ULTRASPEC	ESO	06:51:30	07:40:12	2.0	0.87–1.07	Clear
09/02/2008	QS Vir	ULTRASPEC	ESO	08:16:11	08:59:51	2.0	0.89–1.07	Clear
10/06/2009	NN Ser	ULTRASPEC	NTT	04:48:15	04:44:15	1.9	0.91–1.06	Clear
27/01/2010	QS Vir	Unfiltered	OCA	06:22:25	07:58:31	10.0	0.97–1.41	Clear
28/01/2010	QS Vir	Unfiltered	OCA	06:02:14	09:34:46	10.0	0.51–1.49	Clear
30/01/2010	QS Vir	Unfiltered	OCA	06:55:35	08:56:50	10.0	0.02–0.58	Cloudy
31/01/2010	QS Vir	Unfiltered	OCA	06:22:00	09:43:21	10.0	0.50–1.43	Clear
07/02/2010	QS Vir	Unfiltered	OCA	05:40:58	09:11:54	10.0	0.75–1.72	Cloudy
08/02/2010	QS Vir	Unfiltered	OCA	06:07:58	09:44:52	10.0	0.51–1.51	Clear

[a]CBA: Bronberg Observatory, Pretoria, South Africa. ESO: European Southern Observatory 3.6m telescope, La Silla, Chile. NTT: New Technology Telescope, La Silla, Chile. OCA: Observatorio Cerro Armazones, Chile.

7.3 Light Curves

All the data were phase folded using published ephemerides. For light curves with primary eclipses we calculated the observed minus calculated (O-C) eclipse times (see Section 7.4 for eclipse timings) and adjusted the phase of the light curve by the O-C time. For those light curves with no primary eclipse the phase correction was extrapolated from nearby O-C times.

For a given target, data within each phase bin were averaged using inverse variance weights whereby data with smaller errors are given larger weightings; any data affected by flares was removed (see Section 7.3.1). This results in a set of light curves for each target in each band observed. There are u', g' and i' band data for all targets but several have not been observed in the r' band. Figure 7.1 shows the primary eclipses of those systems observed in all four bands, Figure 7.2 shows the primary eclipses of those systems observed in the u', g' and i' bands.

All of these targets have been studied previously and their basic parameters have been determined. Table 7.3 lists these general parameters. Here I briefly introduce each system and describe their light curves.

DE CVn

DE CVn (RX J1326.9 + 4532) is a bright ($V = 12.8$) eclipsing binary consisting of a cool DA white dwarf primary and a M3V red dwarf secondary. It was discovered as an X-ray source by ROSAT (Voges et al., 1999). The period and eclipse depth were first measured by Robb & Greimel (1997). The most recent analysis of this system was carried out by van den Besselaar et al. (2007) who determined the system parameters by combining spectroscopic and photometric observations including ULTRACAM data. Their ULTRACAM data have been included here along with more recent observations.

DE CVn displays large ellipsoidal modulation and regular flaring. Its primary eclipse is shown in Figure 7.1. The secondary star dominates towards the red, therefore the i' band primary eclipse is very shallow.

GK Vir

GK Vir was investigated in detail in Chapter 5, which also contains light curves of the system. No flares have ever been detected in its light curves.

NN Ser

NN Ser was investigated in detail in Chapter 3. A period decrease in this system

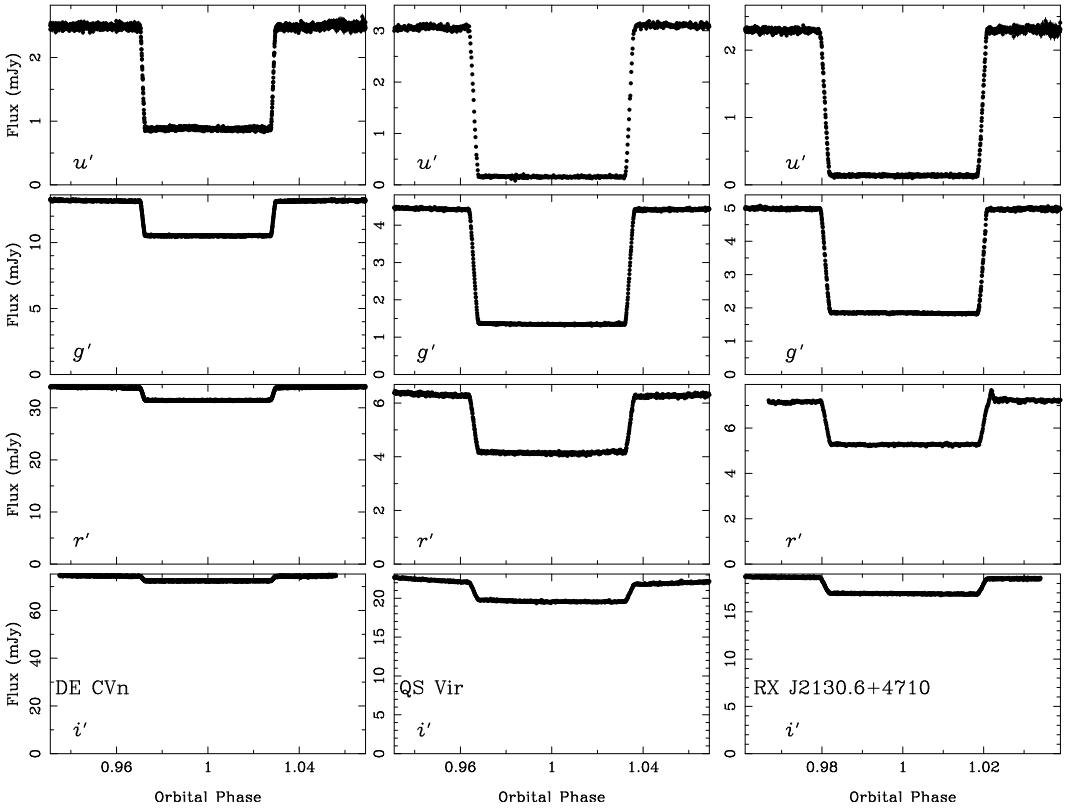

Figure 7.1: Flux calibrated primary eclipses of (*left* to *right*) DE CVn, QS Vir and RX J2130.6+4710 in (*top* to *bottom*) u', g', r' and i' band. Light curves were made by phase folding all available eclipses then combining them. Any flares were removed before the light curves were combined with the exception of RX J2130.6+4710 in the r' band where there was only one eclipse which featured a flare.

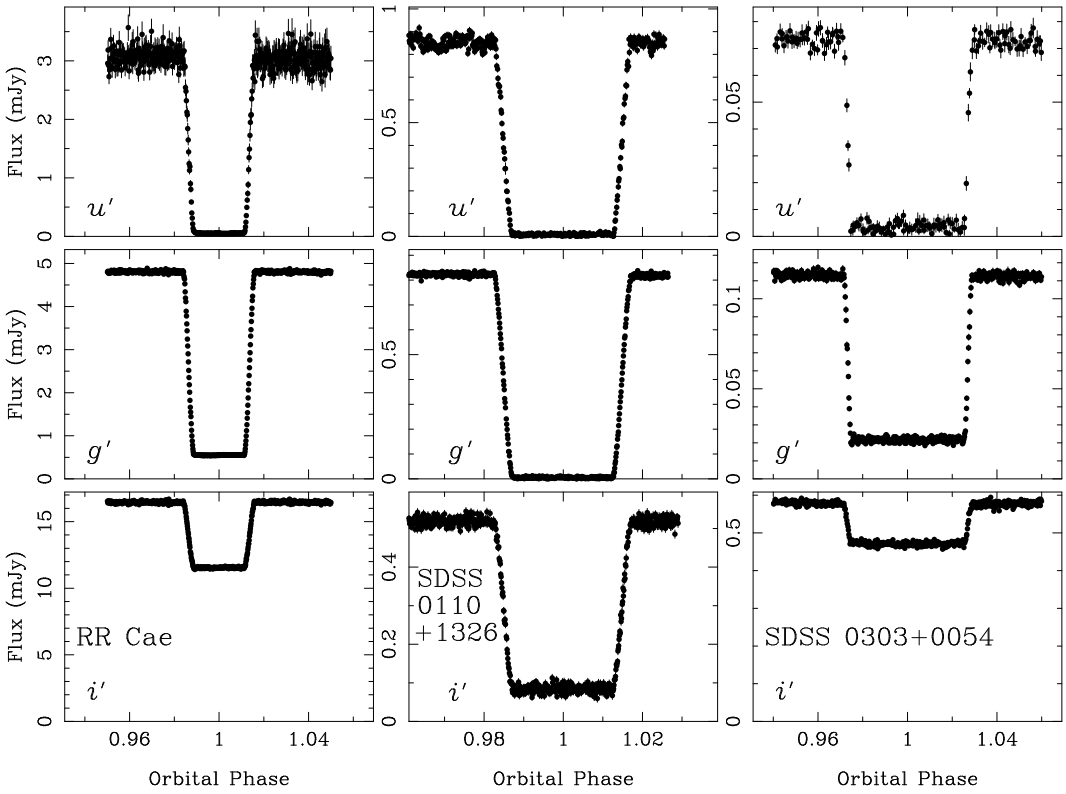

Figure 7.2: Flux calibrated primary eclipses of (*left* to *right*) RR Cae, SDSS J0110+1326 and SDSS J0303+0054 in (*top* to *bottom*) u', g' and i' band. Light curves were made by phase folding all available eclipses then combining them. Any flares were removed before the light curves were combined. A micro-flare occurs during the ingress of the SDSS J0110+1326 eclipse, visible in the u' band light curve.

Table 7.3: Previously determined physical parameters for the eclipsing PCEBs observed with ULTRACAM. Ref.: 1 – Maxted et al. (2004); 2 – van den Besselaar et al. (2007); 3 – Chapter 5; 4 – Pyrzas et al. (2009); 5 – Maxted et al. (2007); 6 – O'Donoghue et al. (2003); 7 – Chapter 3; 8 – Chapter 4.

System	P_{orb} (d)	Out of ecl g'	M_{WD} ($M_\odot$)	R_{WD} ($R_\odot$)	$T_{eff,WD}$ (K)	M_{sec} ($M_\odot$)	R_{sec} ($R_\odot$)	Sp2	Ref.
RX J2130.6+4710	0.5210	14.55	0.554 ± 0.017	0.0137 ± 0.0014	18000 ± 1000	0.555 ± 0.023	0.534 ± 0.017	M3.5–4	(1)
DE CVn	0.3641	13.50	$0.51^{+0.06}_{-0.02}$	$0.0136^{+0.0008}_{-0.0002}$	8000 ± 1000	0.41 ± 0.06	$0.37^{+0.06}_{-0.007}$	M3V	(2)
GK Vir	0.3443	16.81	0.564 ± 0.014	0.0170 ± 0.0004	55000 ± 1200	0.116 ± 0.003	0.155 ± 0.003	$M4.5 \pm 0.5$	(3)
SDSS J1212-0123	0.3359	16.77	0.439 ± 0.002	0.0168 ± 0.0003	$17,707 \pm 35$	0.273 ± 0.002	0.306 ± 0.007	M4	(3)
SDSS J0110+1326	0.3327	16.53	0.47 ± 0.2	$0.0163 - 0.0175$	25900 ± 427	$0.255 - 0.38$	$0.262 - 0.36$	M3–5	(4)
RR Cae	0.3037	14.58	0.44 ± 0.022	0.015 ± 0.0004	7540 ± 175	0.183 ± 0.013	$0.188 - 0.23$	M4	(5)
QS Vir	0.1508	14.68	0.77 ± 0.04	0.011 ± 0.01	14220 ± 300	0.51 ± 0.04	0.42 ± 0.02	M3.5–4	(6)
SDSS J0303+0054	0.1344	18.60	$0.878 - 0.946$	$0.0085 - 0.0093$	< 8000	$0.224 - 0.282$	$0.246 - 0.27$	M4–5	(4)
NN Ser	0.1301	16.43	0.535 ± 0.012	0.0211 ± 0.0002	57000 ± 3000	0.111 ± 0.004	0.149 ± 0.002	$M4 \pm 0.5$	(7)
SDSS J0857+0342	0.0651	17.95	0.514 ± 0.049	0.0247 ± 0.0008	35300 ± 400	0.087 ± 0.012	0.1096 ± 0.0038	$M8 \pm 1$	(8)

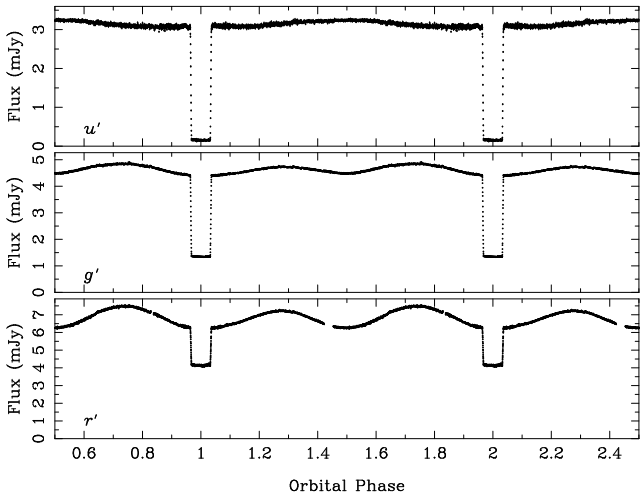

Figure 7.3: Full orbit light curves of QS Vir in (*top* to *bottom*) u', g' and r' band. A small reflection effect is visible in the u' band light curve whilst ellipsoidal modulation is seen in the g' and r' band light curves.

was seen by Brinkworth et al. (2006). Qian et al. (2009) proposed that NN Ser has a sub-stellar companion based on eclipse timings. No flaring events have ever been detected in over 37 hours of ULTRACAM photometry. Light curves of NN Ser were presented in Chapter 3.

QS Vir

QS Vir (EC 13471 − 1258) was discovered in the Edinburgh-Cape faint blue object survey of high galactic latitudes (Kilkenny et al., 1997). The DA white dwarf primary has a companion red dwarf that is close to filling its Roche lobe (O'Donoghue et al., 2003). O'Donoghue et al. (2003) suggested that QS Vir is a hibernating cataclysmic variable. Recently Qian et al. (2010) proposed the existence of a giant planet in this system by analysing the eclipse timings.

QS Vir was regularly observed with ULTRACAM between 2002 and 2006. Due to its short orbital period, it has full phase coverage. The primary eclipse light curves are shown in Figure 7.1, the i' band eclipse shows a clear gradient across the eclipse caused by the varying brightness of the secondary star across its surface. Figure 7.3 shows full orbit light curves in the u', g' and r' bands. A small reflection effect is evident in the u' band with an amplitude of 0.3 mag. Ellipsoidal modulation is seen in the g' and r' bands. QS Vir shows frequent flaring.

RR Cae

Discovered as a high proper motion object by Luyten (1955), RR Cae contains a cool DA white dwarf with a low mass companion and has a deep primary eclipse (Krzeminski, 1984). Recently Maxted et al. (2007) used new photometry and spectroscopy to determine the mass and radius of the secondary star to high precision, they also noted a change in the shape of the primary eclipse from night to night. Zuckerman et al. (2003) detected spectacular metal absorption lines from the white dwarf.

RR Cae has only been observed with ULTRACAM twice, the first observation targeted the secondary eclipse, the second targeted the primary eclipse and recorded two. Unfortunately, RR Cae lacks any nearby bright comparison stars so a fairly dim comparison was used which adds some noise to the light curves in Figure 7.2 particularly in the u' band. RR Cae shows a high level of flaring with flares visible in each of the observations.

RX J2130.6+4710

RX J2130.6+4710 was discovered as a soft X-ray source by the *ROSAT* satellite (Trümper, 1982); it contains a DA white dwarf primary. Maxted et al. (2004) used medium-resolution spectroscopy and ULTRACAM photometry to determine the system parameters. There have been no subsequent observations with ULTRACAM. However, their data are included here for completeness.

RX J2130.6+4710 was observed with ULTRACAM in 2002 and 2003. Three primary eclipses were observed. It shows high levels of flaring. The primary eclipse is shown in Figure 7.1 in each band. The i' band light curve shows a gradient across the eclipse, caused by non-uniform surface brightness over the surface of the secondary star.

SDSS J011009.09+132616.1

SDSS J011009.09 + 132616.1 (WD 0107 + 131, henceforth SDSS J0110+1326) was identified as an eclipsing PCEB from the Sloan Digital Sky Survey (SDSS) by Pyrzas et al. (2009). It contains a DA white dwarf with an M3–M5 companion.

Only one observation of SDSS 0110 + 1326 with ULTRACAM exists. It targeted the primary eclipse as seen in Figure 7.2. There is a small flare on the ingress visible in the u' band light curve, it is also present in the g' band light curve though not visible in Figure 7.2.

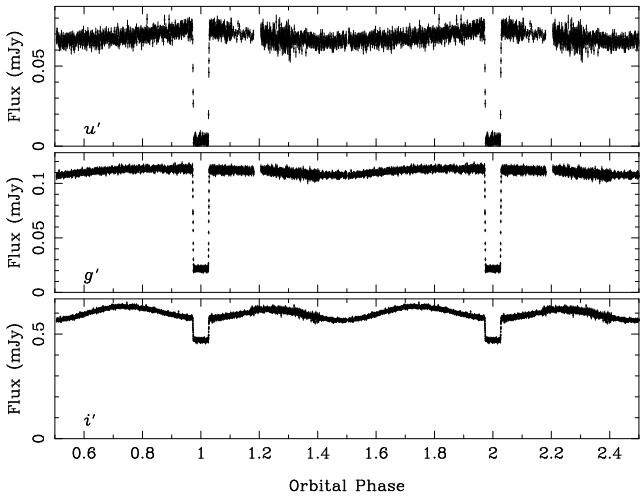

Figure 7.4: Full orbit light curves of SDSS J0303+0054 in (*top* to *bottom*) u', g' and i' band. Ellipsoidal modulation is obvious in the i' band.

SDSS J030308.35+005444.1

SDSS J030308.35 + 005444.1 (henceforth SDSS J0303+0054) was also identified as an eclipsing PCEB by Pyrzas et al. (2009). The DC white dwarf is the most massive white dwarf currently known in an eclipsing PCEB.

SDSS J0303+0054 was observed with ULTRACAM in 2007 October, the first run targeted the primary eclipse, the next covered the full orbital period and also covered a flare just after the primary eclipse. The final run again targeted the primary eclipse (though this final run was compromised by poor conditions). The primary eclipses in the u', g' and i' bands are shown in Figure 7.2. The full orbit light curves in the same bands are shown in Figure 7.4. Ellipsoidal modulation is visible in the i' band, and the u' and g' band light curves show an increase in the flux up to the primary eclipse then a decrease after the eclipse. This is the opposite to what we would expect if there was a reflection effect and implies that the back side of the secondary star is brighter than the side facing the white dwarf. This may be due to the distribution of spots on the secondary star's surface.[1]

SDSS J085746.18+034255.3

SDSS J0857+0342 was investigated in detail in Chapter 4, which also contains light curves of the system. No flares have ever been detected in its light curves.

[1]Further analysis of this system has shown that the white dwarf is magnetic and hence this is the most likely cause of the unusual u' and g' band light curves

Table 7.4: Flaring rates (90% confidence) for our targets during ULTRACAM observations.

System	Flares detected	Hours obs	Flaring rate (hr^{-1})	Period (days)	M_{sec} $M_\odot$
RX J2130.6+4710	2	8.0	$0.05 - 0.38$	0.5210	0.56
QS Vir	2	9.0	$0.04 - 0.33$	0.1508	0.43
DE CVn	2	10.5	$0.04 - 0.29$	0.3641	0.41
SDSS J0110+1326	1	2.0	$0.03 - 1.00$	0.3327	0.32
SDSS J1212-0123	1	4.3	$0.01 - 0.46$	0.3359	0.27
SDSS J0303+0054	1	6.0	$0.01 - 0.33$	0.1344	0.25
RR Cae	2	3.0	$0.13 - 1.00$	0.3037	0.18
GK Vir	0	19.1	$0.00 - 0.16$	0.3443	0.11
NN Ser	0	37.0	$0.00 - 0.08$	0.1301	0.11
SDSS J0857+0342	0	12.4	$0.00 - 0.24$	0.0651	0.09

SDSS J121258.25-012310.2

SDSS J1212-0123 was investigated in detail in Chapter 5, which also contains light curves of the system. One flare was detected during the ULTRACAM observations.

7.3.1 Flaring Rates

Since ULTRACAM acquires simultaneous images in three different bands, the identification of flares is straightforward. This is due to the fact that flares generally appear largest in the u' band and become smaller in redder bands, making identification by eye relatively straightforward. Table 7.4 lists the number of flares detected for each system throughout all ULTRACAM observations and the total number of hours each system has been observed for. The range of flaring rates given in Table 7.4 is the 90% confidence range (5% chance of it being lower or higher, based on Poisson statistics). The ULTRACAM data hint that the flaring rates appear to depend on mass rather than rotation rates. The uncertainty in the flaring rates is a result of the small number of hours that these systems have been observed for.

There are several selection effects to consider: flares are easier to see if the white dwarf is cool (faint) and it may be that more massive stars produce brighter flares and so are more visible. It is also possible that flares have been missed, particularly in the fainter systems, if the light curves are particularly noisy. Longer term monitoring of these and similar systems should determine the parameters that dictate flare rates.

7.4 O-C Diagrams

For each ULTRACAM eclipse recorded, I determined the mid-eclipse time and the scaled secondary star radius ($R_{\rm sec}/a$) using the light curve model outlined in Section 2.3. Changes in the measured size of the secondary star could be due to the presence of starspots which can affect the eclipse time (see Section 7.5.1). Since I am not interested in absolute radii but changes in the secondary stars' radii, the inclination was set to 90° for each system (this includes those systems previously fitted for the parameter studies of Chapters 3–5).

For each target the mass ratio (q), the inclination (i), the white dwarf temperature ($T_{\rm WD}$) and the linear limb darkening coefficients for both the white dwarf and the secondary star were fixed. The mass ratio and white dwarf temperature are taken from previous studies of each system. The linear limb darkening coefficients were set to 0.2 for each star. By setting the inclination to 90°, the measured scaled radii are not true radii but represent lower limits on the scaled radius of the secondary star and upper limits on the scaled radius of the white dwarf. This does not affect variations in the radius of the secondary star.

For each eclipse light curve the scaled radii of both stars were allowed to vary as well as the mid-eclipse time and the temperature of the secondary star. These fits yielded the mid-eclipse times. The light curves were then re-fitted keeping the white dwarf scaled radius fixed as the average from the previous fits. These fits then provide the scaled radius of the secondary star. Each eclipse fit was inspected to ensure a good fit; Figure 7.5 shows a model fit to an eclipse of GK Vir. The radii were not measured for eclipses distorted by the effects of flares. The mid-eclipse time was not measured for those eclipses significantly affected by flares. Some of the systems also show a gradient in the light curves across the eclipse as seen in Figure 7.6 for RX J2130.6+4710, due to the varying brightness of the secondary star across its surface, this was modelled by simply adding a linear slope to the fits.

For most of the systems (with the exception of DE CVn and RR Cae) the scaled radius of the white dwarf determined by fitting the primary eclipses increases as the filter becomes redder. This is due to the fact that the linear limb darkening coefficients of the white dwarf were fixed at 0.2 in all filters. In reality, it is likely that the limb darkening of the white dwarf decreases at longer wavelengths (as was found in the parameter studies of Chapters 3–5), therefore, as seen here, the fits will over-predict the scaled radius of the white dwarf at longer wavelengths. It is interesting to note that the two systems that do not show this trend (DE CVn and RR Cae) contain very cool white dwarfs. Thus, for cool white dwarfs, changes in

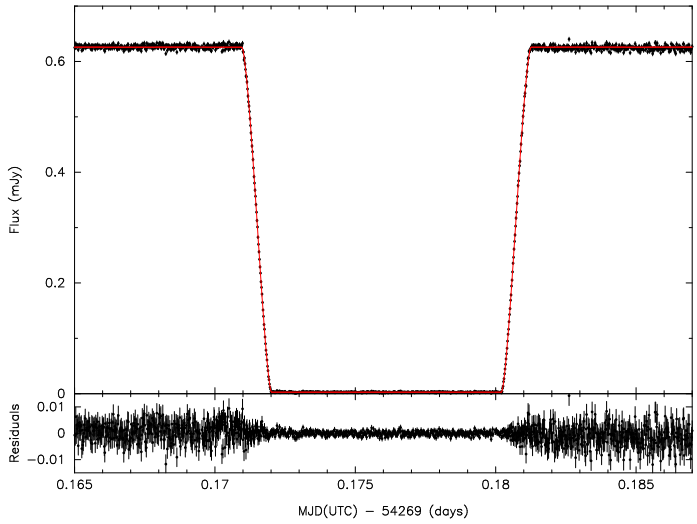

Figure 7.5: Light curve and model fit to the primary eclipse of GK Vir observed on 2007 June 18.

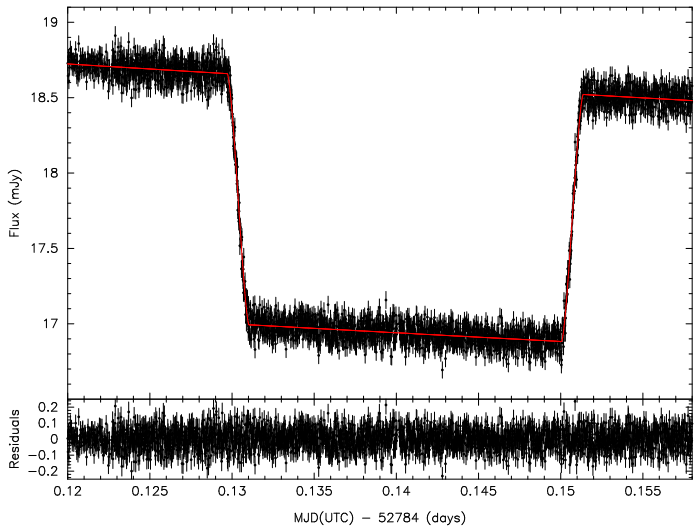

Figure 7.6: Light curve and model fit to the primary eclipse of RX J2130.6+4710 observed on 2003 May 25. A linear slope was added to account for the varying brightness of the secondary star.

wavelength apparently do not affect the linear limb darkening coefficients as much as in hotter white dwarfs.

All mid-eclipse times were corrected to Barycentric Dynamical Time (TDB) and correct for light travel time to the solar system barycentre (BTDB), all times are in MJD. All previous eclipse times were also converted to MJD(BTDB) but I also list the times in MJD(UTC) and the location of each measurement making corrections to Heliocentric Julian Date (HJD), if required, straightforward. Tables containing all the ULTRACAM eclipse times and secondary star scaled radii, as well as previous eclipse times can be found in Appendix 3.

DE CVn

For fitting the primary eclipses of DE CVn the mass ratio was fixed as $q = 0.80$ and the white dwarf temperature fixed as $T_{\rm WD} = 8000$K taken from van den Besselaar et al. (2007). The fits give average white dwarf scaled radii of $R_{\rm WD}/a(u') = 0.00674(4)$, $R_{\rm WD}/a(g') = 0.00682(3)$, $R_{\rm WD}/a(r') = 0.00732(9)$ and $R_{\rm WD}/a(i') = 0.0069(3)$. where the number in parentheses is the 1σ error on the last digit.

Table C.1 lists the mid-eclipse times (in both UTC and BTDB) and the measured secondary star radius for each filter for each eclipse. Older eclipse times for DE CVn are listed in Table C.2 which have barycentrically corrected (I also list the MJD in UTC). Using just the ULTRACAM points the ephemeris for DE CVn is

$$\mathrm{MJD(BTDB)} = 52784.054\,043(1) + 0.364\,139\,3156(5)E,$$

where the numbers in parentheses are the statistical errors on the last digits. This ephemeris is suitable for predicting future eclipse times though stochastic variations make it likely that these errors will under-predict the true variation in eclipse times.

Figure 7.7 shows the O-C plot for the eclipse times of DE CVn. Points with larger error bars have been faded so that any period change is more obvious. Since there are only a few reliable points in the O-C plot no long term period changes are yet visible.

GK Vir

For GK Vir the mass ratio was fixed as $q = 0.174$ and the white dwarf temperature fixed as $T_{\rm WD} = 53000$K from Chapter 5. The inclination was fixed at 90° thus slightly different radii are found from those in Chapter 5 where this was a free parameter. The fits give average white dwarf scaled radii of $R_{\rm WD}/a(u') = 0.00939(3)$, $R_{\rm WD}/a(g') = 0.00949(1)$, $R_{\rm WD}/a(r') = 0.00955(5)$ and $R_{\rm WD}/a(i') = 0.00961(3)$.

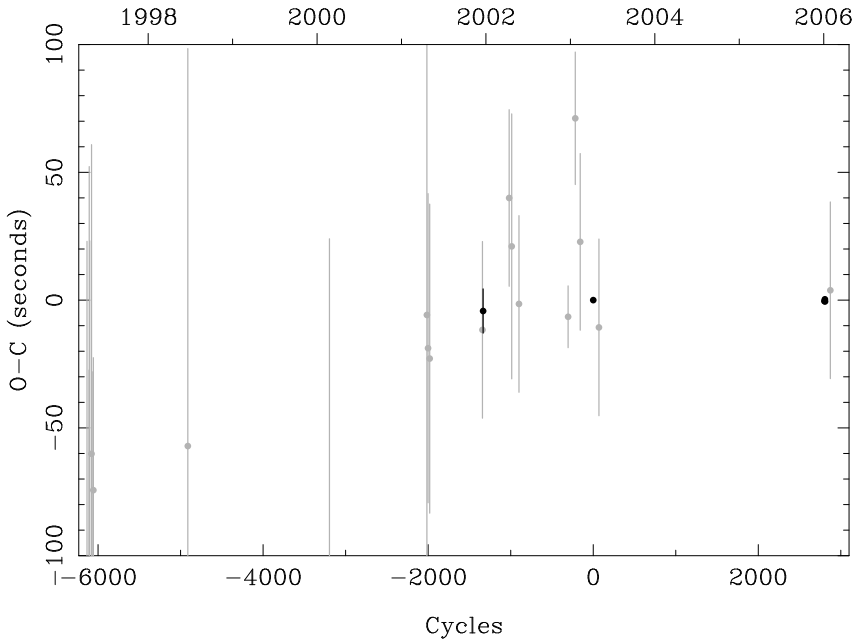

Figure 7.7: O-C diagram for DE CVn with an ephemeris determined from the ULTRACAM points. Previous data are plotted as open circles whilst the ULTRACAM data are plotted as filled circles, their uncertainties are too small to see at this scale. Measurements with larger errors have been faded. The top axis indicates the year of observation.

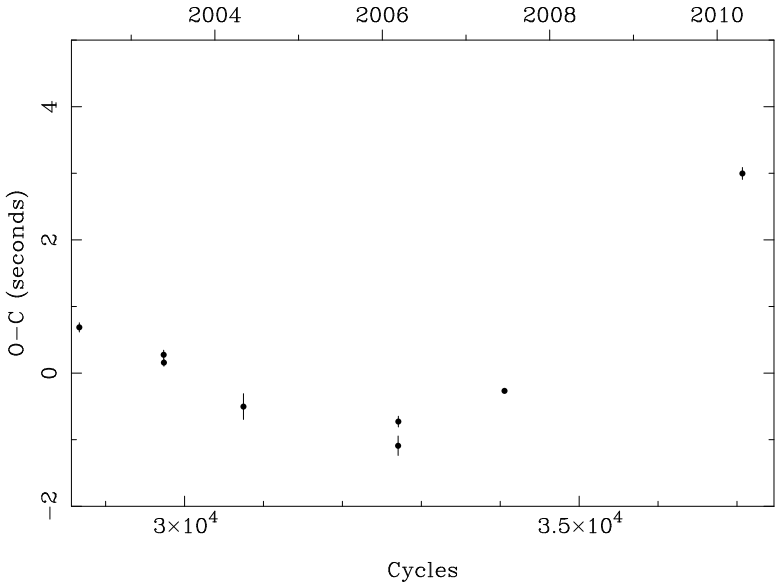

Figure 7.8: O-C diagram for GK Vir zoomed in on the latest ULTRACAM eclipse times. A departure from linearity is seen in the eclipse times. The secondary star is just able to supply the energy required to drive this period change via Applegate's mechanism. However, a third body in orbit around the system is also a possible explanation.

Table C.3 lists the mid-eclipse times and the measured secondary star radius for each filter and for each eclipse. The older eclipse times for GK Vir are listed in Table C.4 from Green et al. (1978), they corrected their times to Barycentric Julian Date but it is likely that the light travel time to the solar system barycentre was not taken into account (as applying this ~ 480 second correction brings them more into line with the new eclipse times). These new eclipse times refine the ephemeris to

$$\mathrm{MJD(BTDB)} \quad = \quad 42543.337\,9121(33) + 0.344\,330\,832\,742(99)E,$$

which is consistent with previous studies. This ephemeris is suitable for predicting future eclipse times but, like DE CVn, larger scale variations may well mean that these errors will under-predict the true variation in eclipse times. Figure 7.8 shows the O-C plot for GK Vir zoomed in on the latest ULTRACAM points. These new times show a clear deviation from linearity, although the magnitude of the period change is small compared to other systems. The secondary star in GK Vir is able to drive this small period change (0.00124 seconds in ~ 8 years) via Applegate's mechanism (Applegate 1992; see Section 1.3), although this is only just the case

if the modified version of Applegate's mechanism presented by Brinkworth et al. (2006) is used. A third body in orbit around the system may also be the cause of the period change. However, longer term monitoring is required in order to discover the true cause.

NN Ser

For fitting the eclipses of NN Ser a mass ratio of $q = 0.207$ and a white dwarf temperature of $T_{\rm WD} = 57000$K was used taken from Chapter 3. From the initial fits I determine the white dwarf scaled radius as $R_{\rm WD}/a(u') = 0.02262(14)$, $R_{\rm WD}/a(g') = 0.02264(2)$, $R_{\rm WD}/a(r') = 0.02271(10)$ and $R_{\rm WD}/a(i') = 0.02257(10)$.

Table C.5 lists the mid-eclipse times and the measured secondary star radius for each filter and for each eclipse. Many of these eclipses are the same as in Brinkworth et al. (2006); the newly calculated eclipse times are consistent with theirs. Also listed are other eclipse times for NN Ser in Table C.6, this table includes previous eclipse times and one additional eclipse time recorded using ULTRASPEC in imaging mode rather than ULTRACAM. The linear ephemeris of Brinkworth et al. (2006)

$$\mathrm{MJD(BTDB)} = 47344.024\,6049(14) + 0.130\,080\,144\,430(36)E$$

was used to determine O-C times.

Qian et al. (2009) proposed the existence of a planet in orbit around NN Ser based on eclipse timings. The top panel of Figure 7.9 shows their sinusoidal fit along with all eclipse times. The new times, which I indicate with arrows, clearly disagree with the sinusoidal fit, hence the third body proposed by Qian et al. (2009) cannot exist, though this does not rule out a third body as the cause of the variations. A fit to just the ULTRACAM points, the centre panel of Figure 7.9, yields a current linear ephemeris of

$$\mathrm{MJD(BTDB)_{UCAM}} = 47344.025\,768\,43(96) + 0.130\,080\,115\,390(20)E.$$

The bottom panel of Figure 7.9 shows the residuals of this fit around the ULTRACAM points. Additional small scale variations are visible in this plot which may be the result of Applegate's mechanism, since the secondary star is able to drive variations on this level.

The period change of NN Ser was analysed by Brinkworth et al. (2006), who determined that Applegate's mechanism fails to explain the large period change. They determined that if magnetic braking is not cut off below $0.3\mathrm{M}_{\odot}$ then it can

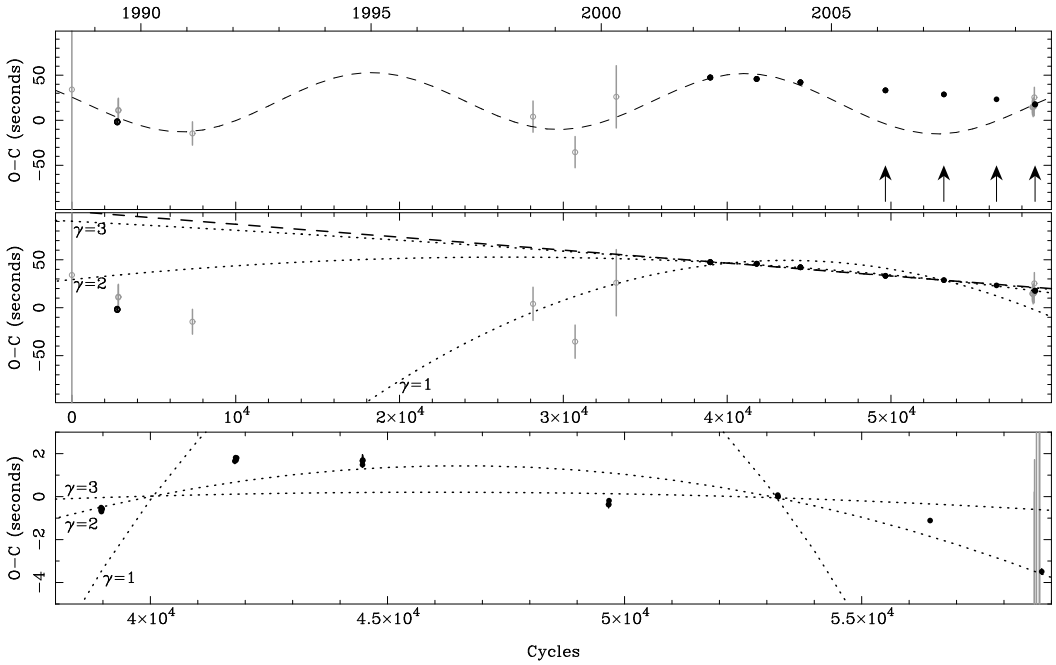

Figure 7.9: *Top:* O-C diagram for NN Ser based on the ephemeris of Brinkworth et al. (2006), with sinusoidal fit from Qian et al. (2009) over plotted. The additional ULTRACAM points, indicated by the arrows, clearly disagree with the fit (the last point coincides with the points from Qian et al. (2009) but has a error comparable in size to the other ULTRACAM points). *Centre:* O-C diagram with a linear fit to just the ULTRACAM points (*dashed* line) and standard magnetic braking models (*dotted* lines). *Bottom:* residuals of the linear fit to the ULTRACAM points with the same magnetic braking models (*dotted* lines). Previous data are plotted as open circles whilst the ULTRACAM data are plotted as filled circles. Measurements with larger errors have been faded.

explain the period change. To see if this is still the case I use the standard magnetic braking relationship from Rappaport et al. (1983)

$$\dot{J} \approx -3.8 \times 10^{-30} \mathrm{M}_{\odot} \mathrm{R}_{\odot}{}^{4} m_2 r_2^{\gamma} \omega^3 \,\mathrm{erg}, \tag{7.1}$$

where m_2 and r_2 are the secondary star's mass and radius and ω is the angular frequency of rotation of the secondary star. γ is a dimensionless parameter which can have a value between 0 and 4. Using the parameters from Chapter 3, Equation 7.1 can be used to determine a quadratic term to the ephemeris. The parabola can the be fitted to the eclipse times. A range of values was used for γ; for $\gamma = 4$ I find that the period change is negligible whilst for $\gamma = 0$ the period change is far higher than observed. The period change resulting from the relationship given by Verbunt & Zwaan (1981) and gravitational radiation (Peters, 1964) give negligible period changes. In the context of cataclysmic variable evolution $\gamma = 2$ is frequently used (Schreiber & Gänsicke, 2003). A good fit to the ULTRACAM points is found with this value. However, this fit passes somewhat above earlier points suggesting $\gamma \sim 1.8$ if this is indeed the explanation. It should be stressed that these relationships are by no means proven but I show them here as a possible explanation for the observed period change.

The analysis of all the eclipse times (including the new times) agrees with the conclusions made by Brinkworth et al. (2006) that the only mechanisms able to explain the observed period change in NN Ser are magnetic braking (provided it is not cut off below $0.3\mathrm{M}_{\odot}$) or perhaps the existence of a third body in a long period orbit around NN Ser.

Since analysing these data, Beuermann et al. (2010) presented additional eclipse times as well as re-analysing some older times. Including our ULTRACAM times, they found good evidence that these eclipse variations could be the result of two planets in orbit around the binary.

QS Vir

A mass ratio of $q = 0.66$ and a white dwarf temperature of $T_{\mathrm{WD}} = 14000$K from O'Donoghue et al. (2003) was used for fitting the eclipses of QS Vir. A slope was also included in the r' and i' band fits. The initial fits give a white dwarf scaled radius of $R_{\mathrm{WD}}/a(u') = 0.01297(7)$, $R_{\mathrm{WD}}/a(g') = 0.01322(5)$, $R_{\mathrm{WD}}/a(r') = 0.01370(12)$ and $R_{\mathrm{WD}}/a(i') = 0.01502(37)$.

Table C.7 lists the eclipse times for QS Vir from the ULTRACAM data, also listed are all previous eclipse times in Table C.8. I convert the O'Donoghue et al.

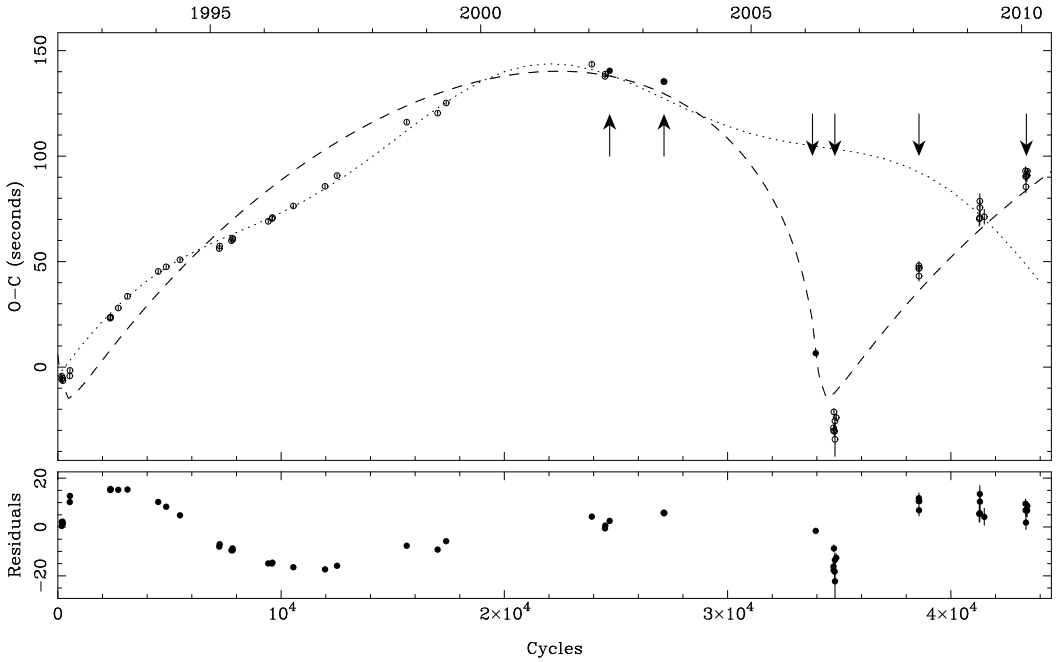

Figure 7.10: *Top:* O-C diagram for QS Vir. The ephemeris was determined by varying the ephemeris of O'Donoghue et al. (2003) in order to fit a third body in an elliptical orbit (*dashed* line). Also included is the sinusoidal fit from Qian et al. (2010) (*dotted* line). The additional eclipse times, indicated by the arrows, clearly disagree with the sinusoidal fit. *Bottom:* residuals of the fit to the third body in an elliptical orbit. The filled circles are the ULTRACAM eclipse points.

(2003) mid-ingress and mid-egress times to mid-eclipse times and correct the times to BTDB. The times from Qian et al. (2010) were converted from UTC to BTDB. For eclipse cycles 43342 and 43362 the observations start during the eclipse therefore the mid-eclipse times were determined by measuring the centre of the egress then applying a correction based on the eclipse model. A minor earthquake occurred during the egress of eclipse cycle 43349 causing the loss of some data, nevertheless enough data were available to determine a mid-eclipse time. The O-C times were found using the linear ephemeris of O'Donoghue et al. (2003) corrected to BTDB,

$$\mathrm{MJD(BTDB)} = 48689.140\,62(1) + 0.150\,757\,525(1)E.$$

The O-C plot for QS Vir is shown in Figure 7.10, the eclipse times show a substantial shift after $\sim 20,000$ cycles. Qian et al. (2010) used their new eclipse times together with previous times and fitted a sinusoid to them. This fit is the dotted line shown in Figure 7.10. Clearly our new eclipse times, indicated by arrows, disagree

strongly with this fit. Hence we conclude that, as with NN Ser, the proposed planet in QS Vir does not exist.

The eclipse times show a complex behaviour. I test whether the maximum period shift ($\sim$0.05 seconds in $\sim$2 years, in the region where the O-C times turn, around cycle number 35,000) could be caused by Applegates mechanism. This was achieved using Equations 1.5 to 1.7 and the mass and radius of the secondary star and orbital separation from O'Donoghue et al. (2003) namely $M = 0.51\mathrm{M}_{\odot}$, $R = 0.42\mathrm{R}_{\odot}$ and $a = 1.28\mathrm{R}_{\odot}$. The result is that the minimum energy required to drive the maximum observed period change in QS Vir is 3.0×10^{40} ergs. The luminosity of the secondary star over the two years supplies 3.5×10^{39} ergs, failing by an order of magnitude to explain the observed period change. This is likely to be even worse if we apply the generalised version of Applegate's calculation introduced in Brinkworth et al. (2006).

Another explanation for the observed shift in eclipse times is a third body. If the third body is in a highly elliptical orbit then for much of its orbit the eclipse times will remain roughly constant but as the third body swings inward the central binary moves towards and away from us quickly resulting in a large, short-lived timing change.

Fitting the eclipse times with an elliptical orbit, allowing the ephemeris of QS Vir to change, results in a third body with a minimum mass of $M \sin i \sim 0.05\mathrm{M}_{\odot}$ in a $\sim$ 14 year orbit with an eccentricity of $\sim$ 0.9 fitting the data reasonably well. This fit is the dashed line in Figure 7.10 for an inclination of 90°. The linear ephemeris obtained from this fit is

$$\mathrm{MJD(BTDB)} = 48689.141\,163(10) + 0.150\,757\,453(1)E.$$

Since this system has undergone substantial evolution the likelihood of a third body in such an orbit is questionable. To see if such an orbit is possible, we must analyse the evolutionary history of QS Vir. I estimate the minimum progenitor mass of the white dwarf to be $\sim 1.8\mathrm{M}_{\odot}$ (Meng et al., 2008), with a core mass equal to the current white dwarf mass ($0.77\mathrm{M}_{\odot}$). This corresponds to a radius on the asymptotic giant branch (AGB) of $\sim 460\mathrm{R}_{\odot}$ (Hurley et al., 2000). The initial separation of the binary can be calculated from the Eggleton (1983) formula

$$R_L = \frac{0.49q^{2/3}a_i}{0.6q^{2/3} + \ln(1 + q^{1/3})} \tag{7.2}$$

and setting $R_L = R_{\mathrm{AGB}}$, where $q = M_{\mathrm{AGB}}/M_2$ and M_2 is the mass of the secondary

star. This gives an initial binary separation of $a_i = 4.4$AU. The fit to the eclipse times implies the current semimajor axis of the third body is ~ 6.4AU. Assuming that the mass loss timescale was much larger than the orbital period, hence an adiabatic change in semimajor axis, implies that the semimajor axis of the third body before the common envelope phase was ~ 3.6AU. By altering the period of QS Vir a longer period fit can be obtained but it requires a similarly high eccentricity and is a slightly poorer fit, and still results in a very small periapsis separation. Since the eccentricity of the third body should have been little affected by the mass loss (Jeans, 1924) all these possible orbits cross the orbit of the secondary star meaning that it is unlikely to have survived for the entire main sequence lifetime of the primary. In addition, since the common envelope must have reached out to at least the secondary star, the orbit of this third body would have taken it into the common envelope resulting in a dramatically different orbit to what we now see.

It also appears doubtful that the third body formed out of the material in the common envelope. A similar mechanism has been used to explain the creation of planets around pulsars (Lin et al., 1991) out of the supernova material. However, the high eccentricity and mass of this object would seem to make creation via such a mechanism unlikely. However, since the dynamics of the system throughout the common envelope phase are subject to large uncertainties, the existence of this third body cannot be ruled out and it remains the only mechanism able to produce such a large period variation.

The residuals of the elliptical orbit fit, shown in the bottom panel of Figure 7.10, still show considerable structure, but they are at a level consistent with Applegate's mechanism. Further monitoring of the eclipse times may reveal the true nature of this remarkable period change.

RR Cae

A mass ratio of $q = 0.42$ and a white dwarf temperature of $T_{\rm WD} = 7540$K was used to fit the two ULTRACAM eclipses of RR Cae (Maxted et al., 2007). The fits give an average white dwarf scaled radius of $R_{\rm WD}/a(u') = 0.01436(18)$, $R_{\rm WD}/a(g') = 0.01448(2)$ and $R_{\rm WD}/a(i') = 0.01433(9)$.

The new ULTRACAM eclipse times and measured secondary star radii are listed in Table C.9 and previous eclipse times are shown in Table C.10. The ephemeris of Maxted et al. (2007),

$$\mathrm{MJD(BTDB)} = 51522.548\,5670(19) + 0.303\,703\,6366(47)E,$$

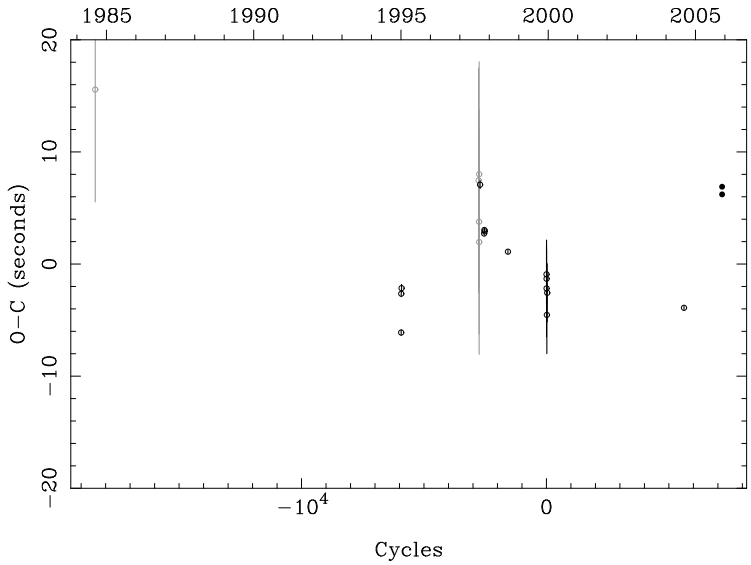

Figure 7.11: O-C diagram for RR Cae based on the ephemeris of Maxted et al. (2007). Previous data are plotted as open circles whilst the ULTRACAM data are plotted as filled circles. Measurements with larger errors have been faded. Eclipse cycle -2760 shows large scatter compared to all the other points hence we do not include it in this figure.

was used to calculate the O-C times.

The O-C plot for RR Cae is shown in Figure 7.11. The secondary star is just to drive the observed period variation (0.006 seconds in ~ 5 years at its maximum). $\sim 3.8 \times 10^{39}$ ergs is required to drive this change and the secondary star is able to supply $\sim 2.4 \times 10^{39}$ ergs which, given the uncertainty in the system parameters and the fact that this is only a rough calculation, demonstrates that Applegate's mechanism is able to explain the observed period change in RR Cae.

It is likely that the eclipse times in RR Cae are being affected by micro-flares that are only visible near the bottom of the primary eclipse. At blue wavelengths these distort the shape of ingress and egress and so produce jitter of up to several seconds in the individual eclipse timings. Further eclipse times may show a discrepancy between the u' band eclipse times and the redder band times.

There is little evidence in the eclipse times of long term period change via angular momentum loss. This is unsurprising given that Maxted et al. (2007) calculated that the period change would be of the order of $5 \times 10^{-14} < \dot{P}/P < 1.4 \times 10^{-13}$ depending upon which magnetic braking prescription is used. However, additional precise eclipse times may reveal this change in the future.

RX J2130.6+4710

The parameters of Maxted et al. (2004) were used to fit the RX J2130.6+4710 eclipses. There are; a mass ratio of $q = 1.00$ and $T_{\rm WD} = 18000$K. A slope was included in the i' band eclipse fits. The initial fits give white dwarf scaled radii of $R_{\rm WD}/a(u') = 0.00768(3)$, $R_{\rm WD}/a(g') = 0.00775(2)$ and $R_{\rm WD}/a(i') = 0.00785(8)$.

The ULTRACAM eclipse times and secondary star radii measurements of RX J2130.6+4710 are shown in Table C.11 and other eclipse times in Table C.12. The eclipse observed in 2002 (cycle -716) featured a flare during the egress, hence the secondary star's radius was not recorded for this eclipse. These eclipses are the same as in Maxted et al. (2004) and are consistent with their results, though a light travel time correction was applied to their times to put them in MJD(BTDB). I re-iterate the warning made in Maxted et al. (2004) that all the eclipse times around cycle -1900 may be in error by a few seconds and should not be used to study any long-term period changes.

The ephemeris of Maxted et al. (2004) was used, corrected to MJD(BTDB)

$$\mathrm{MJD(BTDB)} = 52785.182\,620(2) + 0.521\,035\,625(3)E.$$

The O-C times for RX J2130.6+4710 give an identical plot to that shown in Maxted et al. (2004) since no additional eclipse times are available. Little can be taken from the O-C times since the current number of eclipse times is still quite sparse, hence additional eclipse times are required before any detailed analysis of the period changes can be made.

SDSS J0110+1326

A mass ratio of $q = 0.54$ and a white dwarf temperature of $T_{\rm WD} = 25900$K (Pyrzas et al., 2009) were used to fit the single observed eclipse of SDSS J0110+1326. The white dwarf scaled radii were found to be $R_{\rm WD}/a(u') = 0.01415(16)$, $R_{\rm WD}/a(g') = 0.01431(4)$ and $R_{\rm WD}/a(i') = 0.01426(15)$.

Table C.13 details the ULTRACAM eclipse. Also listed are the previous eclipse times in Table C.14. The O-C times were calculated using the ephemeris of Pyrzas et al. (2009) corrected to MJD(BTDB)

$$\mathrm{MJD(BTDB)} = 53993.948\,65(9) + 0.332\,687\,3(1)E.$$

The ULTRACAM eclipse time is the most accurate published to-date for this system and shows some deviation from the ephemeris, however, given the large errors on

those points used to determine the ephemeris, further accurate eclipse times are likely to greatly improve the ephemeris for SDSS J0110+1326. Since there is only one precise eclipse time the analysis of any period changes in this system will have to wait until further data are available.

SDSS J0303+0054

For SDSS J0303+0054 a mass ratio of $q = 0.28$ was adopted and a white dwarf temperature of $T_{\rm WD} = 8000$K (Pyrzas et al., 2009). The initial fits give white dwarf scaled radii of $R_{\rm WD}/a(u') = 0.0093(7)$, $R_{\rm WD}/a(g') = 0.0098(1)$ and $R_{\rm WD}/a(i') = 0.0100(5)$.

The new ULTRACAM eclipse times and measured secondary star scaled radii are listed in Table C.15, poor conditions led to the loss of data in the u' band during eclipse cycle 3058. All previous eclipse times for SDSS J0303+0054 are listed in Table C.16. The ephemeris of Pyrzas et al. (2009), corrected to MJD(BTDB),

$$\mathrm{MJD(BTDB)} = 53991.117\,18(10) + 0.134\,437\,72(7)E,$$

was used to determine the O-C times. The three new eclipse times are the most accurate for this system so far and, given the large uncertainty in the ephemeris, agree well with previous eclipse times. However, the small number of precise eclipse times means that any long term period changes are not yet visible in the data.

SDSS J0857+0342

The parameters found in Chapter 4 were used to fit the eclipses of SDSS J0857+0342. These were a mass ratio of $q = 0.169$ and a white dwarf temperature of $T_{\rm WD} = 35300$K. The initial fits give white dwarf scaled radii of $R_{\rm WD}/a(u') = 0.04956(3)$, $R_{\rm WD}/a(g') = 0.04967(2)$, $R_{\rm WD}/a(r') = 0.05001(5)$ and $R_{\rm WD}/a(i') = 0.05084(7)$.

Although nine eclipses of SDSS J0857+0342 have been observed, they are only separated by a month and hence no long term period variations are yet visible.

SDSS J1212-0123

For SDSS J1212-0123 the mass ratio was fixed as $q = 0.620$ and the white dwarf temperature fixed as $T_{\rm WD} = 17707$K from Chapter 5. The inclination was fixed at 90° thus slightly different radii are found from those in Chapter 5 where this was a free parameter. The fits give average white dwarf scaled radii of $R_{\rm WD}/a(u') = 0.01023(91)$, $R_{\rm WD}/a(g') = 0.01026(25)$ and $R_{\rm WD}/a(i') = 0.01088(46)$.

Table C.17 details the ULTRACAM eclipse. Also listed are the previous eclipse times in Table C.18. The new time is consistent with the ephemeris of Nebot Gómez-Morán et al. (2009) but since it is of higher precision I use it to update the ephemeris to

$$\text{MJD(BTDB)} \quad = \quad 54104.209\,17(48) + 0.335\,870\,93(13)E.$$

Since this is the first precise eclipse time, no long-term period trend is yet visible in the data.

7.5 Discussion

7.5.1 Variations in Secondary Star Radii

For the systems GK Vir and NN Ser we have accurate measurements of the secondary star's radius spanning eight and six years respectively. The other systems require more measurements before any potential trends can be identified.

A starspot's reduced pressure, density and temperature with respect to its surroundings results in its depression below the surrounding photosphere by several hundreds of kilometres. This effect is known as a Wilson depression. The presence of a Wilson depression on the limb of a secondary star as it occults the primary may cause small changes in the O-C times since it may delay the time of eclipse ingress or advance the time of eclipse egress. Watson & Dhillon (2004) showed that this effect can cause small jitters in the O-C times of up to a few seconds.

A Wilson depression causes a small decrease in the eclipse duration and also displaces the measured centre of the eclipse, hence we would expect that the duration of the eclipse and the jitter in O-C times would be correlated were there Wilson depressions present. For both NN Ser and GK Vir there is no evidence of such a correlation (see Figure 7.12), therefore the eclipse times of these two systems are likely not to be influenced by Wilson depressions. The fact that both of the secondary stars in these systems have never shown any flaring events supports this and shows that both these rapidly rotating stars are remarkably quiet.

Applegate's mechanism can also effect the duration of the eclipse since the result of this mechanism is to alter the oblateness of the star. Applegate (1992) calculated that the deformation of the star, ψ, via this mechanism is

$$\frac{\psi}{R_{\rm sec}} = \frac{1}{3}\frac{\Omega^2 R_{\rm sec}^3}{GM_{\rm sec}} \tag{7.3}$$

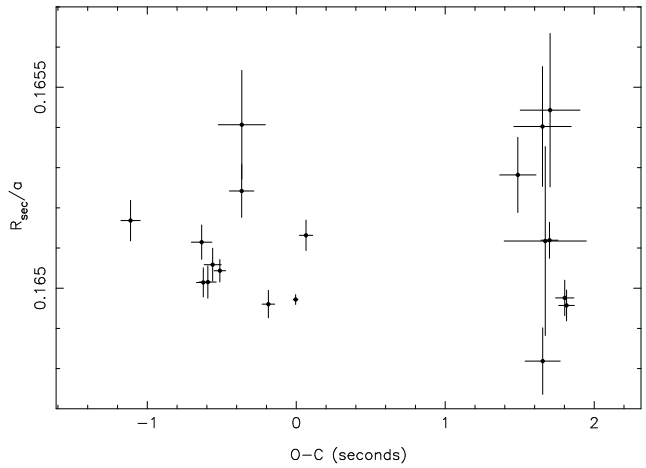

Figure 7.12: Measured g' band secondary star scaled radii (effectively the width of the eclipse) for NN Ser as a function of O-C, based on the ephemeris determined from only these times. No evidence of star spots is seen, which would manifest as a correlation between the O-C times and the measured radius.

where $M_{\rm sec}$ and $R_{\rm sec}$ are the mass and radius of the secondary star and Ω is its angular velocity. However, since this is the deformation at the sub-stellar point and the poles, inclinations where the primary passes across the face of the secondary between these extremes will result in a smaller observed deformation, hence this represents an upper limit. For NN Ser, using the system parameters from Chapter 3 gives a deformation of $\psi \sim 10^{-3} R_{\rm sec}$. Using the parameters from Chapter 5 gives a deformation for GK Vir of $\psi \sim 10^{-4} R_{\rm sec}$.

Figure 7.13 shows the variation in secondary star radius for GK Vir and NN Ser over the period of ULTRACAM observations. For GK Vir, the u' band measurements have been offset by -100 cycles and the red band measurements (r' or i') by +100 cycles. There does not appear to be any obvious variation in the size of the secondary star. However, the 2007 observations made at the VLT ($\sim$ cycle 34000) and are extremely precise with $\Delta R_{\rm sec}/R_{\rm sec} < 10^{-5}$. Additional points with precisions of this order might be able to detect changes in the radius of the secondary star as a result of Applegate's mechanism.

For NN Ser, the u' band measurements have been offset by -200 cycles and the red band measurements (r' or i') by +200 cycles. The measured secondary star scaled radius appears to show a very slight variation of order the size we would expect from Applegate's mechanism however, the errors are too large to be sure. Additional measurements with the accuracy of the best points might reveal any underlying variations.

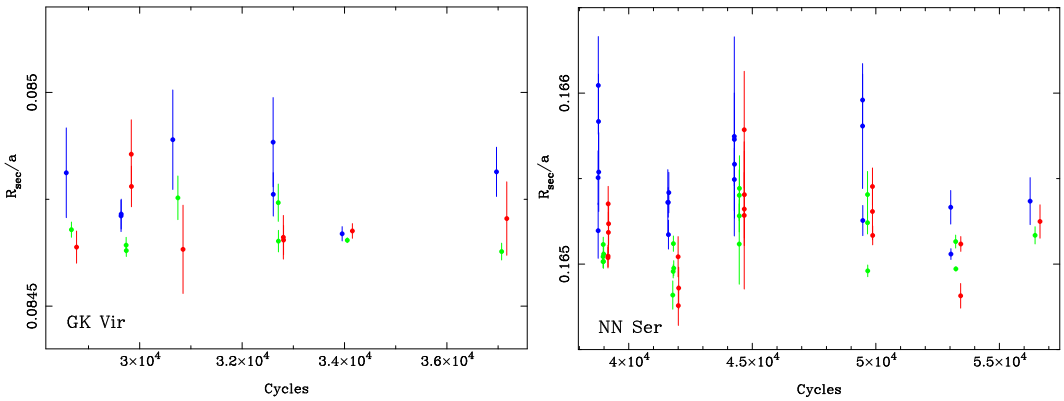

Figure 7.13: Measured secondary star scaled radii for GK Vir (*left*) and NN Ser (*right*). The *blue* points are the u' band measurements and have been offset by -100 cycles for GK Vir and -200 cycles for NN Ser. The *green* points are the g' band measurements and the *red* points are the red band (r' or i') measurements and have been offset by +100 cycles for GK Vir and +200 cycles for NN Ser.

The accuracy of these measurements is encouraging and potentially offers us a method of independently verifying Applegate's mechanism. These two systems are particularly useful in this regard as the secondary stars in both systems show no signs of activity. For those systems that do show substantial activity, such as DE CVn, QS Vir, RR Cae and RX J2130.6+4710, Wilson depressions may affect the eclipses and this may become evident with additional measurements of the width of eclipses. The deformation induced by Applegate's mechanism is also larger for the stars in these systems hence accurate additional monitoring of these systems may identify this effect.

7.5.2 Detecting planets in eclipsing compact binaries

Detection of extrasolar planets via timing observations have been successful around pulsars (see for example Ford et al. 2000 and Konacki & Wolszczan 2003); five planets have been confirmed with this method. Recently these methods have been used to study the eclipse times of compact binaries such as PCEBs since the O-C times in these systems will be affected by the presence of any third body. The possibility of sub-stellar components in these systems suggests intriguing questions about both their history as well as the history of the system as a whole.

However, we have shown that the sub-stellar components suggested as the cause of the O-C variations in NN Ser and QS Vir are incompatible with new eclipse times and hence do not exist. It seems that additional eclipse times invariably

disagree with previous sinusoidal fits, hence regularly sampled eclipse times are essential. This is particularly striking in the case of QS Vir where the previously poorly sampled eclipse times between 2002 and 2009 led Qian et al. (2010) to miss the large deviation from linearity. Similar issues may affect the detection of multiple planets via transit time variations (Watson & Marsh, 2010).

The stability of any additional companions to PCEBs must be studied over the full history of the system. A simple calculation of the orbital configuration of the system before the common envelope phase started will show that some systems cannot have existed during this phase. For example, following the same procedure used to analyse the potential third body found in QS Vir, I take the parameters for the sub-stellar component in NN Ser proposed by Qian et al. (2009) and determine that the semi-major axis of the sub-stellar component before the common envelope phase was ~ 1.6 AU (assuming an adiabatic change in semimajor axis) which was smaller than that of the secondary star (~ 1.8 AU). Therefore the system could not have evolved to its present configuration since these two objects would have had to have crossed each others path. A similar situation is found for the sub-stellar companion thought to exist in QS Vir.

It may be possible to form planets out of the common envelope material thus getting around some of these evolutionary problems, but this mechanism creates additional problems since the created body must still move to its current location.

In light of these findings, I advise caution when using eclipse times of compact binaries to detect planets. Eclipse times must be regularly sampled over long time periods and the history of any third body must be analysed to check its stability. Reliable detections of third-bodies will unfortunately require many decades of monitoring. We also require better understanding of the other processes that can cause period changes. Confirmation of any proposed planetary companions to these systems should currently be made by other methods (radial velocity variations, planetary transits etc.).

7.6 Summary

In this chapter I have shown that very precise eclipse times can be obtained from PCEBs, good enough to observe small variations over several years. Currently, most systems have not be observed over a long enough baseline to detect any period variations. However, all of the systems with long enough baselines (3–4 years) show some sort of deviation from linearity in their eclipse times. For some systems (e.g. RR Cae and GK Vir) the observed variations can be generated via Applegate's

mechanism. However, there are some systems with very large variations that cannot be generated via this mechanism and are most likely caused by additional bodies in orbit around the central binaries.

These new eclipse times also show that the two sub-stellar components proposed to exist in NN Ser and QS Vir do not exist, at least not in the form previously presented. The conclusion is that great care must be taken when attempting to detect planets in binary systems using eclipse timings. All other period change effects must be taken into account. Regularly sampled, long base lines should be used.

Chapter 8

Discussion and Conclusions

8.1 Summary

In this thesis I have presented high precision studies of a number of eclipsing white dwarf binaries. I have used a combination of spectroscopy and photometry to determine the physical parameters of both stars. I have shown that there is a degeneracy between the scaled radii of both stars and the orbital inclination which makes model-independent mass-radius measurements difficult. However, I have also shown that there are a number of methods that can be used to break this degeneracy. First, I presented two systems (NN Ser and SDSS J0857+0342) where the degeneracy was broken by measuring the depth of the secondary eclipse. Then I presented two more systems (GK Vir and SDSS J1212-0123) where the degeneracy was broken by measuring the gravitational redshift of the white dwarf and using it as a prior constraint to the light curve fit. Our project to measure precise parameters in eclipsing PCEBs serendipitously lead to the discovery of only the second known eclipsing double white dwarf binary (CSS 41177). I presented the first data for this system and identified it as a double-lined spectroscopic binary, currently the only known double-lined eclipsing white dwarf binary, and thus a prime target for future high-precision studies.

Using the large amount of photometry already available of eclipsing PCEBs from the high-speed camera ULTRACAM I have measured precise eclipse times for a large number of systems spanning many years. Orbital period variations were found in all the systems with long enough coverage to observe any changes. In most cases the changes were complex and non-sinusoidal. In almost every case Applegate's mechanism fails to provide the energy required to drive these period changes and it is quite possible that many (perhaps even all) of these period variations could be

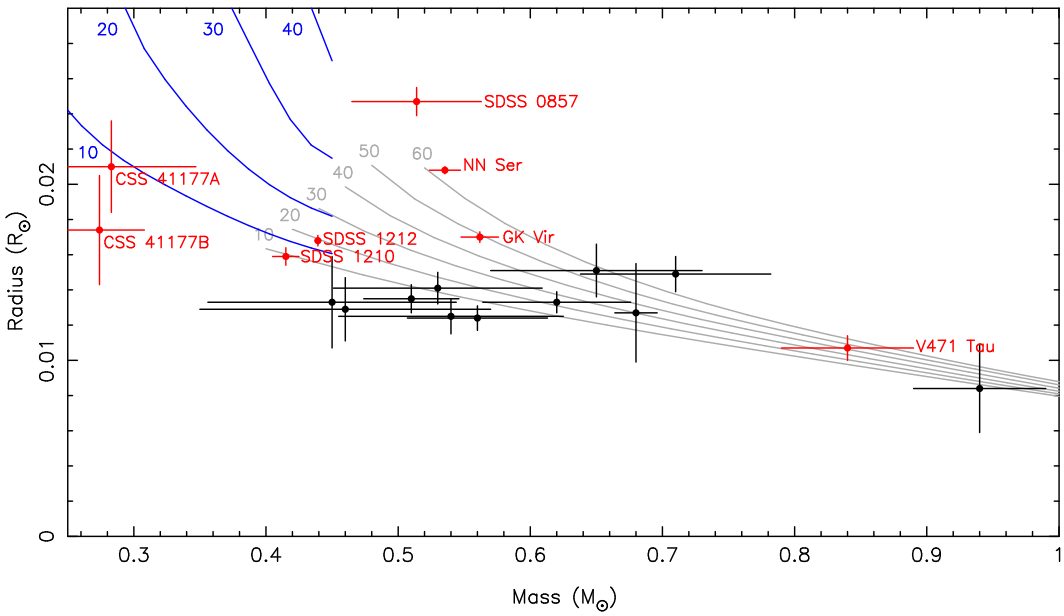

Figure 8.1: Mass-radius plot for white dwarfs. White dwarfs in eclipsing binaries are shown in red, other points are from Holberg et al. (2012). Also shown in grey are mass-radius relations for CO core white dwarfs with thick hydrogen envelopes ($M_H/M_{WD} = 10^{-4}$) and different temperatures (labelled in 10^3K). The blue lines are the same but for He core white dwarfs.

caused by third bodies in orbit around the central binary. However, we have seen that great care must be taken when attempting to detect planets in binary systems using eclipse timings. All other period change effects must be taken into account. Regularly sampled, long base lines should be used.

8.2 Testing mass-radius relations

This thesis has presented some of the first independent mass and radius measurements for white dwarfs. Figure 8.1 summarises the current state of this field. The measurements from white dwarfs in eclipsing binaries are generally much more precise than those from white dwarfs in wide binaries. Furthermore, although the white dwarfs in wide binaries have gravitational redshift measurements (and hence a measure of the ratio of the white dwarf's mass and radius), they have no other independent measurements of the mass and radius. This is because the radius is usually determined from the parallax or from fitting the observed spectral energy distribution of the white dwarf, both of which require using model atmospheres, which depend upon the white dwarf's surface gravity, meaning that the final mass

and radius values are not completely independent.

Although the numbers are small, CO core white dwarfs show very good agreement with evolutionary models, although precise measurements are lacking for cool and high mass CO core white dwarfs. Conversely, most He core mass-radius measurements are still subject to large uncertainties (i.e. the two white dwarfs in CSS 41177). SDSS J1210+3347 (Pyrzas et al., 2012) is likely to be a He core white dwarf but the radius measurement is affected by systematic effects in the light curves. Therefore, although it appears as though its mass and radius are consistent with the models, this is not yet guaranteed. SDSS J1212-0123 is almost certainly a He core white dwarf, as discussed in Chapter 5. However, it is undersized for its mass compared to evolutionary models, unless it has a very thin hydrogen envelope. There is the possibility that the gravitational redshift method, used for breaking the degeneracy between the inclination and radii, is subject to unknown systematic effects. However, even given this uncertainty, the white dwarf would have been undersized even if at an inclination of 90° (and thus as large as possible). Therefore, in order to properly test He core white dwarf mass-radius relations, we not only need to check that the gravitational redshift result of SDSS J1212-0123 is correct, we also need far more precise mass-radius measurements of He core white dwarfs.

I have also shown that eclipsing PCEBs offer the potential to measure extremely precise mass-radius measurements for low mass stars. Figure 8.2 shows independent measurements of masses and radii of low mass stars. The red points are low mass stars in eclipsing PCEBs and are amongst the most precise measurements to date. All of these low mass stars are over-inflated compared to evolutionary models, with the exception of SDSS J0857+0342 where the uncertainties are large. These deviations can be explained, in some cases, as the result of irradiation from the white dwarf. The low mass stars with hot white dwarf companions (NN Ser, GK Vir and SDSS J0857+0342) are hit with high levels of radiation that effectively blocks the energy escaping through the surface layers on the heated side of the star and hence causes the star to slightly inflate. However, this cannot explain the over-inflation of the secondary stars in SDSS J1210+3347 (Pyrzas et al., 2012) or SDSS J1212-0123. More measurements are required in order to see if the models genuinely under-predict the radii of low mass stars. As in the case of SDSS J0857+0342, eclipsing PCEBs are able to probe right down to brown dwarf masses.

The greatest limitation in testing the mass-radius relations for both white dwarfs and low mass stars is the lack of precise measurements. We are in the midst of a rapid increase in the discovery rate of PCEBs as a result of surveys such as the

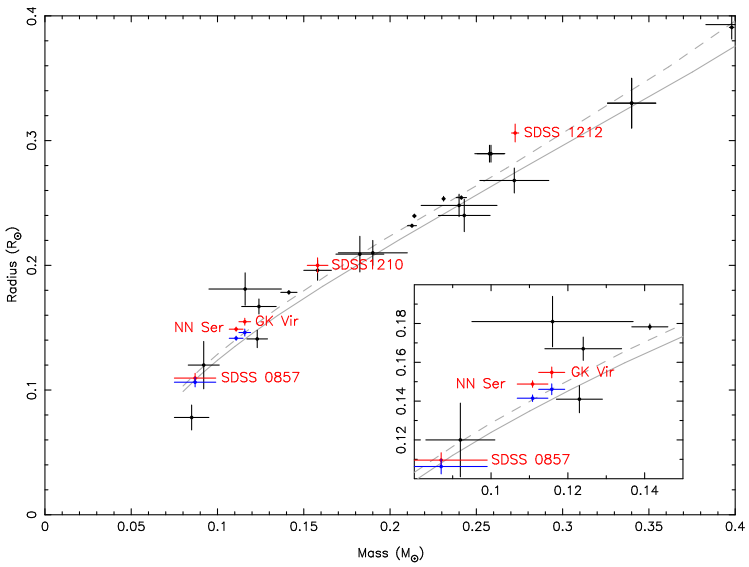

Figure 8.2: Mass-radius plot for low mass stars with independent mass and radius measurements. The blue points are corrected for inflation via irradiation from the white dwarf.

SDSS (Rebassa-Mansergas et al., 2007, 2010; Schreiber et al., 2008) and the Catalina Sky Survey (Drake et al., 2009, 2010), an increase reflected in a corresponding rise in the number of eclipsing systems. We now know of 39 eclipsing PCEBs, 32 of them discovered within the past 3 years alone. Measuring precise parameters in all of these systems would place immensely tight constraints on the evolutionary models of white dwarfs and low mass stars, as well as binary evolution models. However, we have seen that these are difficult measurements to make and many systems are not well suited for these measurements (e.g. only one component is visible spectroscopically). Follow-up high-precision studies of the (now 4) recently discovered eclipsing double white dwarf binaries will also lead to tighter constraints on these models.

8.3 Orbital period variations

I was able to determine extremely precise mid-eclipse times for a large number of eclipsing white dwarf binaries, which I combined with earlier eclipse times (if they existed) to determine any period changes. I found that the conclusions made by Brinkworth et al. (2006) are still true for NN Ser namely, that Applegate's mechanism fails to explain the observed period change but that magnetic braking can,

but given the low mass of the secondary star in NN Ser this requires that magnetic braking is not cut off below $0.3M_{\odot}$ raising problems for cataclysmic variable evolution if true. Further analysis of the eclipse times by Beuermann et al. (2010) have shown that two planetary mass objects in orbit around the central binary are most likely the cause of the period variations.

I have shown that the period variations in RR Cae and GK Vir can just be achieved via Applegate's mechanism, though it is likely that future observations will rule out this mechanism.

I have also presented a 250 second departure from linearity in the eclipse times of QS Vir which is best fit by a combination of a third body ($M \sim 0.05M_{\odot}$) in an eccentric orbit and Applegate's mechanism. A simple analysis of the system's past implies that this potential companion would most likely have interacted with the common envelope making the current system arrangement unlikely. However, given the uncertainties involved in the common envelope stage we cannot rule out the existence of this third body. If confirmed, this third body may offer some insight into common envelope evolution.

The eclipse times also show that the two sub-stellar components previously proposed to exist around NN Ser and QS Vir do not exist, at least in the forms proposed by those authors. The conclusion to draw from this is that great care must be taken when attempting to detect planets in binary systems using eclipse timings.

The possibility of planets around compact binaries is extremely interesting from an evolutionary point of view. How did they survive the common envelope phase? Did they perhaps form out of the large mass ($\sim 1.5M_{\odot}$) ejected during the common-envelope phase, as was suggested by Beuermann et al. (2010) for the possible planets around NN Ser. If this is the case then some of these planets may be very young (e.g. ~ 1 million years old for NN Ser) and may be good candidates for future direct imaging. Other systems may have relatively massive objects in orbit around them (e.g. QS Vir), the radial velocity variations caused by these objects may be observable over many years. However, for now, these systems need to be monitored on a regular basis to build up longer baselines of eclipse times. These can then be used to test if the systems are stable. The double white dwarf binaries will also be extremely useful because if the period changes observed in PCEBs are due to internal processes within the main-sequence stars, then the double white dwarf binaries should show no period variations (except for a gradual decrease caused by angular momentum loss via gravitational radiation).

Appendix A

SDSS J1212-0123 emission lines

Table A.1: Identified emission lines from the secondary star in SDSS J1212-0123. After measuring the radial velocity of a line, the spectra were shifted to remove the motion and averaged. The Equivalent widths were measured from this averaged spectrum.

Line	$\gamma_{\rm sec}$ (km/s)	$K_{\rm meas}$ (km/s)	Equivalent Width (mÅ)
Mg I 3829.355	18.31 ± 2.52	141.19 ± 3.68	72 ± 3
Mg I 3832.299	22.90 ± 3.20	135.22 ± 4.12	60 ± 3
Mg I 3838.292	17.09 ± 2.25	138.27 ± 3.17	67 ± 3
Fe I 3878.573	18.74 ± 1.89	132.01 ± 2.41	83 ± 2
H8 3889.055	17.47 ± 1.73	157.82 ± 2.18	74 ± 3
Si I 3905.523	22.79 ± 0.33	140.42 ± 0.43	248 ± 2
Fe I 3922.911	20.92 ± 1.86	132.93 ± 2.32	41 ± 2
Fe I 3928.083	15.52 ± 2.49	131.28 ± 3.52	37 ± 2
Ca II 3933.663	22.31 ± 0.38	153.32 ± 0.48	386 ± 3
Al I 3944.006	25.21 ± 1.41	141.63 ± 1.99	48 ± 2
Al I 3961.520	19.95 ± 1.01	140.74 ± 1.35	72 ± 2
Ca II 3968.469	21.05 ± 0.53	153.32 ± 0.48	349 ± 3
Hϵ 3970.074	17.03 ± 2.88	160.10 ± 2.13	84 ± 2
Hδ 4101.735	21.62 ± 1.23	157.86 ± 1.53	262 ± 4
Fe I 4143.868	22.17 ± 2.91	143.06 ± 4.15	31 ± 2
Fe I 4216.184	20.09 ± 2.30	137.76 ± 3.16	27 ± 2
Ca I 4226.728	22.94 ± 1.59	138.71 ± 2.13	91 ± 2
Hγ 4340.465	17.31 ± 0.60	160.76 ± 0.76	320 ± 3
Fe I 4375.986	21.88 ± 1.73	136.22 ± 2.20	54 ± 2
Fe I 4427.310	19.64 ± 1.57	134.77 ± 2.09	49 ± 2
Fe I 4461.653	20.38 ± 2.23	141.02 ± 2.91	47 ± 2
Fe I 4482.170	20.86 ± 1.09	129.57 ± 1.22	36 ± 2
Mg I 4571.096	16.38 ± 2.98	136.07 ± 3.55	23 ± 2

continued on the next page...

Table A.1: (. . . continued)

Line	$\gamma_{\rm sec}$ (km/s)	$K_{\rm meas}$ (km/s)	Equivalent Width (mÅ)
Hβ 4861.327	19.97 ± 0.32	160.61 ± 0.40	675 ± 4
Fe I 4924.298	19.42 ± 1.46	130.66 ± 2.18	65 ± 2
Fe I 4939.686	18.22 ± 2.34	132.61 ± 3.18	29 ± 2
Fe I 4957.597	19.55 ± 1.07	136.19 ± 1.63	48 ± 1
Fe I 5006.119	21.48 ± 2.64	129.10 ± 3.95	32 ± 2
Fe I 5012.068	15.55 ± 1.77	140.84 ± 2.42	46 ± 2
Fe I 5041.447	20.98 ± 1.45	130.69 ± 1.91	91 ± 2
Fe I 5051.664	18.19 ± 1.64	139.04 ± 2.28	41 ± 2
Fe I 5079.740	23.25 ± 2.15	129.63 ± 2.89	48 ± 2
Fe I 5083.338	19.40 ± 1.56	129.62 ± 2.01	30 ± 2
Fe I 5107.447	19.03 ± 1.19	131.36 ± 1.63	82 ± 2
Fe I 5110.413	17.30 ± 1.29	135.01 ± 1.71	87 ± 2
Mg I 5167.322	17.26 ± 0.45	139.73 ± 0.59	150 ± 2
Fe I 5168.898	19.56 ± 0.75	131.56 ± 0.96	78 ± 2
Mg I 5172.684	20.00 ± 0.56	140.22 ± 0.78	254 ± 3
Mg I 5183.604	17.46 ± 0.46	139.37 ± 0.62	209 ± 2
Fe I 5227.189	21.54 ± 0.85	133.72 ± 1.16	76 ± 2
Fe I 5269.537	22.13 ± 0.61	131.14 ± 0.85	173 ± 2
Fe I 5328.038	21.83 ± 0.42	132.58 ± 0.58	160 ± 2
Fe I 5341.234	22.18 ± 1.35	137.92 ± 1.86	83 ± 2
Fe I 5371.489	15.66 ± 0.60	130.31 ± 0.82	101 ± 2
Fe I 5397.128	17.84 ± 0.63	131.63 ± 0.87	103 ± 2
Fe I 5405.774	20.25 ± 0.85	135.49 ± 1.16	75 ± 2
Fe I 5429.695	20.10 ± 0.60	133.37 ± 0.84	97 ± 2
Fe I 5446.871	19.61 ± 0.56	131.62 ± 0.74	152 ± 2
Fe I 5455.609	20.32 ± 0.56	130.99 ± 0.76	121 ± 2
Fe I 5497.516	21.74 ± 1.09	136.31 ± 1.49	85 ± 2
Fe I 5501.465	18.64 ± 1.78	134.74 ± 2.46	52 ± 3
Fe I 5506.779	18.37 ± 1.57	137.41 ± 2.02	55 ± 3
Na I 5889.950	20.63 ± 0.84	144.01 ± 1.13	337 ± 7
Na I 5895.924	20.69 ± 1.02	144.35 ± 1.42	204 ± 7
Fe I 6136.994	21.08 ± 3.63	133.25 ± 4.85	149 ± 7
Ca I 6162.170	19.44 ± 2.74	140.27 ± 4.07	65 ± 6
Fe I 6191.588	20.43 ± 2.43	139.27 ± 3.30	87 ± 7
Fe I 6230.723	20.26 ± 2.03	138.54 ± 2.75	92 ± 6
Fe I 6252.555	16.48 ± 2.40	140.87 ± 3.22	52 ± 5
Fe I 6393.601	21.92 ± 2.25	139.69 ± 3.10	65 ± 6
Fe I 6400.001	21.00 ± 2.89	127.53 ± 3.83	89 ± 7
Fe I 6430.846	17.43 ± 1.97	139.20 ± 2.53	84 ± 6
Fe I 6494.980	18.62 ± 1.14	130.75 ± 1.55	106 ± 5
Hα 6562.760	18.91 ± 0.16	161.66 ± 0.20	2894 ± 9

continued on the next page. . .

Table A.1: (. . . continued)

Line	$\gamma_{\rm sec}$ (km/s)	$K_{\rm meas}$ (km/s)	Equivalent Width (mÅ)
Fe I 6677.987	23.21 ± 2.15	130.50 ± 2.70	71 ± 5
Ca II 8498.020	20.35 ± 0.13	144.80 ± 0.18	887 ± 4
Ca II 8542.090	20.13 ± 0.14	144.19 ± 0.20	847 ± 4
Ca II 8662.140	19.87 ± 0.17	142.89 ± 0.23	671 ± 4

Appendix B

GK Vir emission lines

Table B.1: Identified emission lines from the secondary star in GK Vir. P is the hydrogen Paschen series. After measuring the radial velocity of a line, the spectra were shifted to remove the motion and averaged. The Equivalent widths were measured from this averaged spectrum.

Line	$\gamma_{\rm sec}$ (km/s)	$K_{\rm meas}$ (km/s)	Equivalent Width (mÅ)
H16 3703.853	-45.55 ± 2.07	200.01 ± 2.93	68 ± 3
H15 3711.971	-48.49 ± 1.83	203.33 ± 2.49	81 ± 2
Fe I 3719.935	-50.25 ± 1.55	197.94 ± 2.10	29 ± 2
H14 3721.948	-46.01 ± 1.21	204.48 ± 1.71	107 ± 2
H13 3734.372	-49.96 ± 1.01	199.31 ± 1.42	183 ± 2
Fe I 3737.131	-46.50 ± 1.00	199.97 ± 1.40	53 ± 2
H12 3750.152	-46.68 ± 0.73	203.38 ± 1.04	197 ± 2
H11 3770.634	-47.06 ± 0.49	203.61 ± 0.70	239 ± 2
H10 3797.910	-46.32 ± 0.39	202.72 ± 0.55	311 ± 2
He I 3819.761	-48.22 ± 0.73	201.68 ± 1.05	69 ± 2
H9 3835.397	-48.00 ± 0.32	204.37 ± 0.46	331 ± 2
Fe I 3856.371	-46.33 ± 1.11	204.48 ± 1.52	41 ± 2
H8 3889.055	-47.28 ± 0.21	203.86 ± 0.30	457 ± 2
Si I 3905.523	-45.96 ± 0.69	205.38 ± 0.97	58 ± 2
Ca II 3933.663	-46.67 ± 0.28	205.82 ± 0.39	208 ± 2
He I 3964.727	-48.70 ± 0.93	198.93 ± 1.36	44 ± 2
Ca II 3968.469	-46.78 ± 0.31	206.90 ± 0.40	158 ± 2
Hϵ 3970.074	-47.53 ± 0.20	205.75 ± 0.27	529 ± 2
He I 4026.189	-45.77 ± 0.49	204.70 ± 0.70	77 ± 1
Hδ 4101.735	-47.42 ± 0.18	205.81 ± 0.25	659 ± 3
He I 4143.759	-49.44 ± 0.87	198.33 ± 1.18	55 ± 2
Ca I 4226.728	-45.78 ± 1.44	209.03 ± 1.95	36 ± 2
Fe I 4232.726	-47.77 ± 1.15	201.03 ± 1.55	41 ± 2

continued on the next page...

Table B.1: (. . . continued)

Line	$\gamma_{\rm sec}$ (km/s)	$K_{\rm meas}$ (km/s)	Equivalent Width (mÅ)
Fe I 4266.964	-46.93 ± 0.92	198.87 ± 1.26	54 ± 2
Hγ 4340.465	-47.48 ± 0.16	207.11 ± 0.22	842 ± 3
Fe I 4351.544	-48.56 ± 1.04	201.36 ± 1.43	63 ± 2
He I 4387.928	-46.72 ± 0.61	197.68 ± 0.84	84 ± 2
He I 4471.480	-46.99 ± 0.32	202.90 ± 0.46	144 ± 2
Mg II 4481.130	-46.51 ± 0.72	201.59 ± 1.04	71 ± 2
Fe I 4549.467	-46.01 ± 1.05	201.43 ± 1.43	49 ± 2
He I 4713.146	-47.44 ± 0.49	204.45 ± 0.69	75 ± 2
Hβ 4861.327	-47.39 ± 0.16	208.67 ± 0.23	1406 ± 4
He I 4921.929	-48.30 ± 0.30	204.02 ± 0.43	149 ± 2
Fe II 4923.921	-47.35 ± 0.52	204.94 ± 0.73	80 ± 2
Fe I 4957.597	-46.94 ± 0.98	205.54 ± 1.44	59 ± 2
He I 5015.675	-48.93 ± 0.26	205.02 ± 0.37	197 ± 2
Fe II 5018.434	-48.60 ± 0.50	203.93 ± 0.73	105 ± 2
Mg I 5167.322	-49.24 ± 0.63	205.19 ± 0.90	90 ± 2
Fe I 5168.898	-45.00 ± 0.51	207.13 ± 0.73	112 ± 2
Mg I 5172.684	-46.67 ± 0.96	207.01 ± 1.41	127 ± 2
Mg I 5183.604	-48.44 ± 0.66	205.68 ± 0.99	136 ± 3
Fe I 5227.189	-46.44 ± 0.76	200.01 ± 1.10	70 ± 2
Fe I 5269.537	-48.88 ± 0.85	198.55 ± 1.27	92 ± 2
Fe II 5276.002	-48.15 ± 0.77	202.46 ± 1.11	80 ± 2
Fe II 5316.615	-46.43 ± 0.57	201.34 ± 0.82	102 ± 2
Fe I 5328.038	-47.10 ± 0.67	203.37 ± 0.99	126 ± 2
Fe I 5405.774	-48.88 ± 1.95	205.80 ± 1.59	51 ± 2
Fe I 5429.695	-46.80 ± 0.96	207.31 ± 1.43	73 ± 2
Fe I 5434.524	-48.12 ± 2.77	198.15 ± 3.37	25 ± 2
Fe I 5446.871	-45.26 ± 0.97	206.78 ± 1.41	53 ± 2
Fe I 5455.609	-46.39 ± 0.82	204.71 ± 1.20	62 ± 2
He I 5875.618	-47.07 ± 0.29	207.82 ± 0.41	623 ± 7
Na I 5889.950	-48.81 ± 1.07	211.58 ± 1.49	160 ± 8
Na I 5895.924	-49.29 ± 1.13	209.46 ± 1.59	124 ± 8
Fe I 6136.994	-45.82 ± 3.19	207.64 ± 3.19	112 ± 8
Ca I 6162.170	-49.04 ± 2.86	210.47 ± 2.27	31 ± 5
Fe I 6191.588	-48.29 ± 1.77	205.30 ± 2.30	47 ± 7
Mg II 6346.962	-45.17 ± 0.89	203.44 ± 1.21	123 ± 6
Fe I 6393.601	-46.88 ± 2.70	198.16 ± 3.22	50 ± 7
Fe I 6400.001	-46.92 ± 1.74	208.27 ± 2.57	57 ± 6
Fe II 6456.383	-46.43 ± 1.70	204.89 ± 2.21	125 ± 7
Ca I 6462.567	-47.03 ± 1.90	209.01 ± 2.58	37 ± 5
Fe I 6494.980	-46.55 ± 1.30	209.76 ± 1.74	56 ± 5
Hα 6562.760	-46.77 ± 0.25	210.73 ± 0.33	4073 ± 13

continued on the next page. . .

Table B.1: (. . . continued)

Line	$\gamma_{\rm sec}$ (km/s)	$K_{\rm meas}$ (km/s)	Equivalent Width (mÅ)
He I 6678.149	-47.50 ± 0.51	206.26 ± 0.61	645 ± 7
He I 7065.188	-46.25 ± 0.54	205.69 ± 0.64	820 ± 7
He I 7281.349	-48.65 ± 0.64	202.81 ± 0.82	344 ± 8
O I 7771.944	-47.61 ± 0.61	203.64 ± 0.81	223 ± 5
O I 7774.166	-48.06 ± 1.39	202.84 ± 1.12	234 ± 5
O I 7775.388	-46.94 ± 1.55	204.89 ± 1.38	131 ± 5
Mg II 7896.368	-48.23 ± 0.90	202.55 ± 1.30	131 ± 7
Na I 8183.256	-49.93 ± 1.08	206.13 ± 1.62	74 ± 6
Na I 8194.824	-46.10 ± 1.46	206.74 ± 2.13	89 ± 7
Fe I 8327.056	-47.02 ± 1.04	200.82 ± 1.54	158 ± 8
C I 8335.150	-46.96 ± 0.69	207.21 ± 0.94	283 ± 7
O I 8446.359	-47.51 ± 0.73	206.06 ± 0.98	340 ± 9
Ca II 8498.020	-46.89 ± 0.19	207.18 ± 0.27	925 ± 9
Ca II 8542.090	-47.39 ± 0.15	207.64 ± 0.21	1322 ± 9
P14 8598.392	-48.88 ± 2.00	200.56 ± 2.78	256 ± 12
Ca II 8662.140	-47.65 ± 0.19	207.95 ± 0.29	901 ± 9
P13 8665.019	-45.51 ± 1.88	202.98 ± 2.68	489 ± 12
Fe I 8688.625	-48.01 ± 1.07	203.53 ± 1.66	176 ± 9
P12 8750.473	-44.68 ± 1.71	203.42 ± 2.50	719 ± 13
Mg I 8806.757	-46.67 ± 0.72	205.38 ± 0.99	244 ± 8
P11 8862.784	-45.69 ± 1.35	202.23 ± 1.93	1010 ± 13
Ca II 8912.070	-49.99 ± 0.78	202.51 ± 1.19	194 ± 9
Ca II 8927.360	-49.91 ± 0.76	202.22 ± 1.10	207 ± 9
P10 9014.911	-47.08 ± 0.66	201.91 ± 0.95	1337 ± 13
C I 9061.430	-46.69 ± 0.88	202.20 ± 1.12	638 ± 10
C I 9078.280	-46.30 ± 0.85	203.85 ± 1.08	255 ± 9
C I 9088.510	-47.30 ± 0.79	208.63 ± 1.07	378 ± 10
C I 9094.830	-45.99 ± 0.90	201.89 ± 1.19	385 ± 10
C I 9111.800	-48.71 ± 0.79	206.42 ± 1.01	281 ± 9
Fe I 9212.981	-48.42 ± 1.14	207.64 ± 1.67	212 ± 12
Mg II 9218.248	-46.67 ± 0.48	204.95 ± 0.70	493 ± 12
P9 9229.015	-49.80 ± 0.54	203.76 ± 0.78	2079 ± 20
Mg II 9244.266	-46.71 ± 0.63	203.53 ± 0.91	289 ± 11
C I 9405.730	-47.00 ± 0.77	208.83 ± 1.01	799 ± 19
Pϵ 9545.972	-47.40 ± 0.43	205.84 ± 0.62	2825 ± 26
C I 9620.800	-48.95 ± 1.00	204.99 ± 1.41	243 ± 15
C I 9658.440	-45.49 ± 0.99	208.87 ± 1.40	202 ± 18
Pδ 10049.37	-48.12 ± 0.72	206.70 ± 0.65	3576 ± 60

Appendix C

Mid-eclipse times

Table C.1: ULTRACAM eclipse times for DE CVn. The first eclipse (cycle number 0) is the same eclipse as in van den Besselaar et al. (2007), our times are consistent with theirs. All observations were made at the WHT.

Cycle Number	u' eclipse MJD(UTC) MJD(BTDB)	$R_{\rm sec}/a$	g' eclipse MJD(UTC) MJD(BTDB)	$R_{\rm sec}/a$	r'/i'/z eclipse MJD(UTC) MJD(BTDB)	$R_{\rm sec}/a$	Red Filter
0	52784.0518541(18)	0.18109(3)	52784.0518445(13)	0.18110(2)	52784.0518410(68)	0.18113(13)	i'
	52784.0540495(18)		52784.0540400(13)		52784.0540364(68)		
2801	53804.0037989(28)	0.18110(5)	53804.0038091(17)	0.18120(3)	53804.0038027(35)	0.18131(7)	r'
	53804.0082548(28)		53804.0082650(17)		53804.0082586(35)		
2807	53806.1886343(17)	0.18109(3)	53806.1886337(16)	0.18103(3)	53806.1886323(38)	0.18091(7)	r'
	53806.1931064(17)		53806.1931057(16)		53806.1931044(38)		
2809	53806.9168898(76)	0.18142(13)	53806.9169041(33)	0.18120(6)	53806.9168679(90)	0.18143(16)	r'
	53806.9213660(76)		53806.9213803(33)		53806.9213441(90)		

Table C.2: Previous eclipse times for DE CVn. (1) Robb & Greimel (1997), (2) van den Besselaar et al. (2007), (3) Tas et al. (2004)

Cycle Number	Obs[a]	Eclipse time MJD(UTC)	Eclipse time MJD(BTDB)	Uncert MJD	Ref
-6134	UVic	50550.4180	50550.4221	0.0016	(1)
-6109	UVic	50559.5212	50559.5250	0.0016	(1)
-6107	UVic	50560.2500	50560.2538	0.0020	(1)
-6101	UVic	50562.4344	50562.4381	0.0022	(1)
-6079	UVic	50570.4471	50570.4504	0.0014	(1)
-6063	UVic	50576.2725	50576.2756	0.0014	(1)
-6057	UVic	50578.4584	50578.4613	0.0006	(1)
-4912	UVic	50995.4012	50995.4011	0.0018	(2)
-3196	UVic	51620.2591	51620.2636	0.0015	(2)
-2015	UVic	52050.3108	52050.3133	0.0016	(2)
-2001	DAO	52055.4089	52055.4111	0.0007	(2)
-1982	UVic	52062.3280	52062.3297	0.0007	(2)
-1342	MDM	52295.3761	52295.3789	0.0004	(2)
-1334	MDM	52298.2891	52298.2921	0.0001	(2)
-1019	EGE	52412.9940	52412.9965	0.0004	(3)
-988	DAO	52424.2828	52424.2846	0.0006	(2)
-900	MDM	52456.3288	52456.3286	0.0004	(2)
-304	MDM	52673.35212	52673.35562	0.00014	(2)
-217	EGE	52705.0322	52705.0366	0.0003	(3)
-157	EGE	52726.8800	52726.8844	0.0004	(3)
69	MDM	52809.1789	52809.1795	0.0004	(2)
2873	UVic	53830.2220	53830.2263	0.0004	(2)

[a]UVic: Climenhaga Obs, Victoria, Canada. DAO: Dominion Astrophysical Obs, Victoria, Canada. MDM: Michigan-Dartmouth-MIT Obs, Arizona, USA. EGE: Ege University Obs, Turkey.

Table C.3: ULTRACAM eclipse times for GK Vir. All observations were made at the WHT except for cycle number 34054 which was made at the VLT and cycle 37069 at the NTT.

Cycle Number	u' eclipse MJD(UTC) MJD(BTDB)	$R_{\rm sec}/a$	g' eclipse MJD(UTC) MJD(BTDB)	$R_{\rm sec}/a$	r'/i'/z' eclipse MJD(UTC) MJD(BTDB)	$R_{\rm sec}/a$	Red Filter
28666	52413.9197824(54)	0.08481(11)	52413.9197825(9)	0.084679(18)	52413.9197816(19)	0.08464(4)	r'
	52413.9255714(54)		52413.9255716(9)		52413.9255707(19)		
29735	52782.0095805(19)	0.08471(4)	52782.0095823(9)	0.084643(18)	52782.0095818(42)	0.08486(8)	i'
	52782.0152254(19)		52782.0152272(9)		52782.0152267(42)		
29738	52783.0426232(18)	0.08472(3)	52783.0426229(7)	0.084630(14)	52783.0426147(25)	0.08478(5)	i'
	52783.0482188(18)		52783.0482185(7)		52783.0482102(25)		
30746	53130.1274746(58)	0.08489(12)	53130.1274669(27)	0.084753(51)	53130.1274719(56)	0.08463(10)	i'
	53130.1336956(58)		53130.1336878(27)		53130.1336928(56)		
32706	53805.0171937(54)	0.08488(10)	53805.0171856(23)	0.084742(44)	53805.0171828(28)	0.08466(5)	r'
	53805.0221235(54)		53805.0221154(23)		53805.0221125(28)		
32709	53806.0501184(26)	0.08476(5)	53806.0501170(12)	0.084652(25)	53806.0501123(18)	0.08465(3)	r'
	53806.0551144(26)		53806.0551129(12)		53806.0551082(18)		
34054	54269.1761114(8)	0.08467(2)	54269.1761097(3)	0.084654(6)	54269.1761122(9)	0.08468(2)	i'
	54269.1800885(8)		54269.1800868(3)		54269.1800893(9)		
37069	55307.3311816(37)	0.08481(6)	55307.3311758(11)	0.084628(20)	55307.3311777(47)	0.08470(8)	i'
	55307.3375910(37)		55307.3375852(11)		55307.3375871(47)		

Table C.4: Previous eclipse times for GK Vir. We have applied a light travel time correction ($\sim$ 480 seconds) to the times of Green et al. (1978) since it appears they did not make this correction. (1) Green et al. (1978)

Cycle Number	Obs[a]	Eclipse time MJD(UTC)	Eclipse time MJD(BTDB)	Uncert MJD	Ref
-67	Pal	42520.26130	42520.26747	0.00001	(1)
-32	Pal	42532.31292	42532.31905	0.00002	(1)
-29	Pal	42533.34592	42533.35204	0.00009	(1)
0	Pal	42543.33179	42543.33769	0.00001	(1)
3	Pal	42544.36482	42544.37068	0.00001	(1)
851	Pal	42836.35916	42836.36314	0.00006	(1)
1966	Pal	43220.28679	43220.29202	0.00012	(1)
2132	Pal	43277.44522	43277.45101	0.00006	(1)
2896	Pal	43540.51806	43540.51972	0.00012	(1)

[a]Pal: Palomar Obs, California, USA.

Table C.5: ULTRACAM eclipse times for NN Ser. Cycle numbers up to 44480 are the same eclipses as in Brinkworth et al. (2006). Our mid-eclipse times for these eclipses are all consistent with their results. Cycle numbers 53230 and 53237 were observed at the VLT, all others are from the WHT. The *z'* band photometry during cycle 41782 was too poor quality to determine radii.

Cycle Number	*u'* eclipse MJD(UTC) MJD(BTDB)	$R_{\rm sec}/a$	*g'* eclipse MJD(UTC) MJD(BTDB)	$R_{\rm sec}/a$	*r'/i'/z'* eclipse MJD(UTC) MJD(BTDB)	$R_{\rm sec}/a$	Red Filter
38960	52411.9413644(26)	0.16551(16)	52411.9413679(6)	0.16501(4)	52411.9413694(11)	0.16504(6)	r'
	52411.9470531(26)		52411.9470566(6)		52411.9470581(11)		
38961	52412.0714493(27)	0.16520(16)	52412.0714501(5)	0.16504(3)	52412.0714503(12)	0.16505(6)	r'
	52412.0771374(27)		52412.0771382(5)		52412.0771384(12)		
38968	52412.9819958(46)	0.16605(29)	52412.9819913(9)	0.16511(4)	52412.9819897(19)	0.16535(10)	r'
	52412.9877084(46)		52412.9877039(9)		52412.9877023(19)		
38976	52414.0226722(48)	0.16583(28)	52414.0226639(7)	0.16502(4)	52414.0226632(20)	0.16519(12)	r'
	52414.0283472(48)		52414.0283389(7)		52414.0283382(20)		
38984	52415.0633093(39)	0.16554(23)	52415.0633145(7)	0.16506(4)	52415.0633146(22)	0.16524(12)	r'
	52415.0689752(39)		52415.0689804(7)		52415.0689805(22)		
41782	52779.0274986(33)	0.16536(19)	52779.0275064(15)	0.16482(8)	52779.0274749(179)	No data	z'
	52779.0331625(33)		52779.0331703(15)		52779.0331388(179)		
41798	52781.1088076(15)	0.16536(9)	52781.1088073(7)	0.16496(4)	52781.1088090(22)	0.16504(12)	i'
	52781.1144526(15)		52781.1144523(7)		52781.1144540(22)		
41806	52782.1494576(14)	0.16517(8)	52782.1494595(8)	0.16512(4)	52782.1494575(21)	0.16476(12)	i'
	52782.1550908(14)		52782.1550927(8)		52782.1550907(21)		
41820	52783.9706045(21)	0.16542(12)	52783.9706060(8)	0.16498(4)	52783.9706063(23)	0.16486(12)	i'
	52783.9762135(21)		52783.9762150(8)		52783.9762153(23)		
44472	53128.9430722(96)	0.16575(58)	53128.9430788(45)	0.16512(24)	53128.9430789(83)	0.16528(43)	i'
	53128.9486742(96)		53128.9486808(45)		53128.9486809(83)		
44473	53129.0731513(50)	0.16573(27)	53129.0731593(28)	0.16540(15)	53129.0731459(54)	0.16579(34)	i'
	53129.0787552(50)		53129.0787632(28)		53129.0787498(54)		
44474	53129.2032333(33)	0.16549(18)	53129.2032314(17)	0.16528(9)	53129.2032323(40)	0.16532(21)	i'
	53129.2088389(33)		53129.2088370(17)		53129.2088379(40)		
44480	53129.9837007(54)	0.16558(32)	53129.9837076(30)	0.16544(19)	53129.9837008(50)	0.16541(25)	i'
	53129.9893165(54)		53129.9893234(30)		53129.9893166(50)		
49662	53804.0615456(61)	0.16581(37)	53804.0615501(25)	0.16541(13)	53804.0615457(30)	0.16531(17)	r'
	53804.0644522(61)		53804.0644567(25)		53804.0644523(30)		
49663	53804.1916188(26)	0.16596(15)	53804.1916184(12)	0.16524(7)	53804.1916174(19)	0.16545(11)	r'
	53804.1945354(26)		53804.1945350(12)		53804.1945340(19)		
49671	53805.2321817(16)	0.16525(9)	53805.2321827(6)	0.16496(3)	53805.2321818(10)	0.16517(6)	r'
	53805.2351771(16)		53805.2351781(6)		53805.2351772(10)		
53230	54268.1854167(17)	0.16533(10)	54268.1854172(6)	0.16513(4)	54268.1854178(13)	0.16481(7)	i'
	54268.1903109(17)		54268.1903114(6)		54268.1903120(13)		
53237	54269.0960182(6)	0.16506(3)	54269.0960181(2)	0.16497(1)	54269.0960191(8)	0.16512(4)	i'
	54269.1008714(6)		54269.1008713(2)		54269.1008723(8)		
56442	54686.0062951(23)	0.16537(14)	54686.0062944(9)	0.16517(5)	54686.0062964(17)	0.16525(10)	r'
	54686.0076286(23)		54686.0076279(9)		54686.0076299(17)		

Table C.6: Other eclipse times for NN Ser. (1) Haefner (1989), (2) Wood & Marsh (1991), (3) Pigulski & Michalska (2002), (4) Haefner et al. (2004), (5) Qian et al. (2009), (6) Chapter 8.

Cycle Number	Obs[a]	Eclipse time MJD(UTC)	Eclipse time MJD(BTDB)	Uncert MJD	Ref
0	Dan	47344.021	47344.025	0.005	(1)
2760	ESO	47703.041401	47703.045744	0.000002	(4)
2761	ESO	47703.171497	47703.175833	0.000006	(4)
2769	ESO	47704.212182	47704.216460	0.000003	(4)
2776	ESO	47705.122796	47705.127023	0.000003	(4)
2777	ESO	47705.252896	47705.257115	0.000007	(4)
2831	McD	47712.27779	47712.28158	0.00015	(2)
2839	McD	47713.31850	47713.32223	0.00015	(2)
7360	McD	48301.41331	48301.41420	0.00015	(2)
28152	Cal	51006.03704	51006.04050	0.00020	(4)
30721	VLT	51340.21072	51340.21590	0.00020	(4)
33233	Wro	51666.97227	51666.97790	0.00040	(3)
58638	Yun	54971.65784	54971.66350	0.00008	(5)
58645	Yun	54972.56841	54972.57406	0.00010	(5)
58684	Yun	54977.64160	54977.64718	0.00012	(5)
58745	Yun	54985.57668	54985.58208	0.00012	(5)
58753	Yun	54986.61747	54986.62284	0.00013	(5)
58796	NTT	54992.2110071	54992.2161925	0.0000015	(6)

[a]Dan: Danish 1.5m telescope, La Silla, Chile. ESO: European Southern Observatory 3.6m telescope, La Silla, Chile. McD: McDonald Observatory, Texas, USA. Cal: Calar Alto Observatory, Spain. VLT: Very Large Telescope, Cerro Paranal, Chile. Wro: Bialków station, Wrocław University Observatory, Poland. Yun: Lijiang Station, Yunnan Astronomical Observatory, China. NTT: New Technology Telescope, La Silla, Chile.

Table C.7: ULTRACAM eclipse times for QS Vir. All observations were made at the WHT.

Cycle Number	u' eclipse MJD(UTC) MJD(BTDB)	$R_{\rm sec}/a$	g' eclipse MJD(UTC) MJD(BTDB)	$R_{\rm sec}/a$	r'/i'/z' eclipse MJD(UTC) MJD(BTDB)	$R_{\rm sec}/a$	Red Filter
24715	52415.1074646(20)	0.21918(9)	52415.1074644(6)	0.21928(3)	52415.1074622(13)	0.21941(7)	r'
	52415.1133025(20)		52415.1133023(6)		52415.1133001(13)		
27135	52779.9404381(11)	0.21935(5)	52779.9404403(8)	0.21926(4)	52779.9404357(37)	0.21965(18)	i'
	52779.9462791(11)		52779.9462813(8)		52779.9462767(37)		
27149	52782.0511392(32)	0.21975(15)	52782.0511443(18)	0.21972(10)	52782.0511456(40)	0.22022(23)	i'
	52782.0568779(32)		52782.0568830(18)		52782.0568844(40)		
27162	52784.0110903(15)	0.21925(7)	52784.0110936(12)	0.21931(5)	52784.0110852(55)	0.22174(38)	i'
	52784.0167283(15)		52784.0167316(12)		52784.0167232(55)		
33948	53807.0500637(25)	0.21911(12)	53807.0500655(11)	0.21917(5)	53807.0500697(20)	0.21928(10)	r'
	53807.0553148(25)		53807.0553166(11)		53807.0553207(20)		

Table C.8: Other eclipse times for QS Vir. (1) O'Donoghue et al. (2003), (2) Kawka et al. (2002), (3) Chapter 8, (4) Qian et al. (2010).

Cycle Number	Obs[a]	Eclipse time MJD(UTC)	Eclipse time MJD(BTDB)	Uncert MJD	Ref
171	SAAO	48714.91450	48714.92068	0.00001	(1)
172	SAAO	48715.06527	48715.07146	0.00001	(1)
212	SAAO	48721.09541	48721.10174	0.00001	(1)
225	SAAO	48723.05520	48723.06158	0.00001	(1)
535	SAAO	48769.79106	48769.79641	0.00001	(1)
542	SAAO	48770.84646	48770.85174	0.00001	(1)
2347	SAAO	49042.96519	49042.96923	0.00001	(1)
2354	SAAO	49044.02042	49044.02454	0.00001	(1)
2367	SAAO	49045.98011	49045.98439	0.00001	(1)
2705	SAAO	49096.93400	49096.94046	0.00001	(1)
3122	SAAO	49159.80281	49159.80638	0.00001	(1)
4497	SAAO	49367.09788	49367.09801	0.00001	(1)
4855	SAAO	49421.06420	49421.06921	0.00001	(1)
5471	SAAO	49513.93137	49513.93584	0.00001	(1)
7230	SAAO	49779.11374	49779.11826	0.00001	(1)
7249	SAAO	49781.97794	49781.98267	0.00001	(1)
7778	SAAO	49861.72778	49861.73339	0.00001	(1)
7826	SAAO	49868.96457	49868.96976	0.00001	(1)
7831	SAAO	49869.71840	49869.72354	0.00001	(1)
9425	SAAO	50110.02959	50110.03102	0.00001	(1)
9591	SAAO	50135.05298	50135.05677	0.00001	(1)
9611	SAAO	50138.06788	50138.07193	0.00001	(1)
10551	SAAO	50279.78259	50279.78400	0.00001	(1)
11966	SAAO	50493.10273	50493.10590	0.00001	(1)
12508	SAAO	50574.81016	50574.81650	0.00001	(1)
15625	SAAO	51044.72960	51044.72777	0.00001	(1)
17014	SAAO	51254.12438	51254.12992	0.00001	(1)
17391	SAAO	51310.95933	51310.96554	0.00001	(1)
23919	SAAO	52295.10958	52295.11040	0.00001	(1)
24507	MSO	52383.74916	52383.75572	0.00001	(2)
24520	MSO	52385.70902	52385.71558	0.00001	(2)
34742	CBA	53926.754380	53926.756325	0.000017	(3)
34749	CBA	53927.809767	53927.811611	0.000017	(3)
34762	CBA	53929.769906	53929.771562	0.000017	(3)
34795	CBA	53934.745279	53934.746452	0.000029	(3)
38560	ESO	54502.346790	54502.349156	0.000008	(3)
38566	ESO	54503.251262	54503.253715	0.000024	(3)
38580	ESO	54505.361651	54505.364307	0.000011	(3)
41296	Yun	54914.815978	54914.821917	0.000040	(4)
41302	Yun	54915.720447	54915.726426	0.000040	(4)
41495	Yun	54944.816001	54944.822564	0.000040	(4)
43342	OCA	55223.270376	55223.271832	0.000022	(3)
43349	OCA	55224.325543	55224.327104	0.000025	(3)
43362	OCA	55226.285138	55226.286894	0.000033	(3)
43369	OCA	55227.340393	55227.342254	0.000028	(3)
43415	OCA	55234.274562	55234.277101	0.000030	(3)
43422	OCA	55235.329786	55235.332426	0.000014	(3)

[a]SAAO: South African Astronomical Observatory, Sutherland, South Africa. MSO: Mount Stromlo Observatory, Canberra, Australia. CBA: Bronberg Observatory, Pretoria, South Africa. ESO: European Southern Observatory 3.6m telescope, La Silla, Chile. Yun: Yunnan Astronomical Observatory, China. OCA: Observatorio Cerro Armazones, Chile.

Table C.9: ULTRACAM eclipse times for RR Cae. All observations were made at the VLT.

Cycle Number	u' eclipse MJD(UTC) MJD(BTDB)	$R_{\rm sec}/a$	g' eclipse MJD(UTC) MJD(BTDB)	$R_{\rm sec}/a$	r'/i'/z' eclipse MJD(UTC) MJD(BTDB)	$R_{\rm sec}/a$	Red Filter
7173	53701.0121015(19)	0.08632(4)	53701.0121006(8)	0.08632(2)	53701.0121116(34)	0.08604(7)	i'
	53701.0148245(19)		53701.0148236(8)		53701.0148346(34)		
7174	53701.3158207(32)	0.08602(13)	53701.3158174(4)	0.08628(1)	53701.3158130(19)	0.08628(4)	i'
	53701.3185392(32)		53701.3185359(4)		53701.3185315(19)		

Table C.10: Previous eclipse times for RR Cae. (1) Krzeminski (1984), (2) Maxted et al. (2007), (3) Bruch & Diaz (1998)

Cycle Number	Obs[a]	Eclipse time MJD(UTC)	Eclipse time MJD(BTDB)	Uncert MJD	Ref
-18423	LCO	45927.415604	45927.416650	0.000116	(1)
-5932	SAAO	49720.976772	49720.978524	0.000003	(2)
-5929	SAAO	49721.887953	49721.889675	0.000003	(2)
-5916	SAAO	49725.836240	49725.837828	0.000004	(2)
-2770	LNA	50681.288255	50681.289580	0.000116	(3)
-2760	LNA	50684.325599	50684.327030	0.000116	(3)
-2750	LNA	50687.362075	50687.363610	0.000116	(3)
-2747	LNA	50688.273134	50688.274700	0.000116	(3)
-2747	LNA	50688.273204	50688.274770	0.000116	(3)
-2708	SAAO	50700.117255	50700.119201	0.000004	(2)
-2544	SAAO	50749.923693	50749.926547	0.000002	(2)
-2534	SAAO	50752.960724	50752.963587	0.000002	(2)
-2524	SAAO	50755.997756	50756.000622	0.000002	(2)
-1572	SAAO	51045.125194	51045.126463	0.000002	(2)
1	SAAO	51522.849812	51522.852260	0.000030	(2)
5	SAAO	51524.064640	51524.067060	0.000050	(2)
5	SAAO	51524.064650	51524.067070	0.000030	(2)
18	SAAO	51528.012855	51528.015180	0.000040	(2)
31	SAAO	51531.961128	51531.963350	0.000030	(2)
5616	SAAO	53228.147153	53228.148145	0.000002	(2)

[a]LCO: Las Campanas Observatory, Cerro Las Campanas, Chile. SAAO: South African Astronomical Observatory, Sutherland, South Africa. LNA: Laboratorio Nacional de Astrofisica, Pico dos Dias, Brazil.

Table C.11: ULTRACAM eclipse times for RX J2130.6+4710, these are the same eclipses as in Maxted et al. (2004), our measured eclipse times are consistent with theirs. The eclipse of cycle number -716 featured a flare on the egress hence we do not determine secondary star radii for this eclipse. All observations were made at the WHT.

Cycle Number	u' eclipse MJD(UTC) MJD(BTDB)	$R_{\rm sec}/a$	g' eclipse MJD(UTC) MJD(BTDB)	$R_{\rm sec}/a$	r'/i'/z' eclipse MJD(UTC) MJD(BTDB)	$R_{\rm sec}/a$	Red Filter
-716	52412.1216555(21)	No data	52412.1216619(9)	No data	52412.1216707(21)	No data	r'
	52412.1211097(21)		52412.1211161(9)		52412.1211249(21)		
-2	52784.1407462(13)	0.12273(2)	52784.1407520(9)	0.12267(1)	52784.1407419(38)	0.12271(5)	i'
	52784.1405462(13)		52784.1405519(9)		52784.1405418(38)		
0	52785.1827661(13)	0.12268(2)	52785.1827768(11)	0.12272(1)	52785.1827686(42)	0.12262(5)	i'
	52785.1826194(13)		52785.1826302(11)		52785.1826219(42)		

Table C.12: Previous eclipse times for RX J2130.6+4710. These data are not suitable for long-term period studies. (1) Maxted et al. (2004).

Cycle Number	Obs[a]	Eclipse time MJD(UTC)	Eclipse time MJD(BTDB)	Uncert MJD	Ref
-1939	JKT	51774.890168	51774.893803	0.000018	(1)
-1937	JKT	51775.932234	51775.935891	0.000018	(1)
-1935	INT	51776.974257	51776.977936	0.000005	(1)

[a]JKT: Jacobus Kapteyn Telescope, La Palma. INT: Isaac Newton Telescope, La Palma.

Table C.13: ULTRACAM eclipse time for SDSS J0110+1326 made at the WHT.

Cycle Number	u' eclipse MJD(UTC) MJD(BTDB)	$R_{\rm sec}/a$	g' eclipse MJD(UTC) MJD(BTDB)	$R_{\rm sec}/a$	r'/i'/z' eclipse MJD(UTC) MJD(BTDB)	$R_{\rm sec}/a$	Red Filter
1203	54394.1647900(43)	0.09460(7)	54394.1647932(9)	0.09463(2)	54394.1648007(34)	0.09458(7)	i'
	54394.1712500(43)		54394.1712532(9)		54394.1712607(34)		

Table C.14: Previous eclipse times for SDSS J0110+1326. (1) Pyrzas et al. (2009).

Cycle Number	Obs[a]	Eclipse time MJD(UTC)	Eclipse time MJD(BTDB)	Uncert MJD	Ref
0	Cal	53993.94284	53993.94870	0.00020	(1)
3	Cal	53994.94062	53994.94653	0.00020	(1)
6	Cal	53995.93897	53995.94492	0.00020	(1)
1170	Mer	54383.18633	54383.19282	0.00020	(1)

[a]Cal: Calar Alto Observatory, Spain. Mer: Mercator Telescope, La Palma.

Table C.15: ULTRACAM eclipse time for SDSS J0303+0054. Poor observing conditions during eclipse cycle 3058 led to the loss of data in the *u'* band. All readings were taken at the WHT.

Cycle Number	*u'* eclipse MJD(UTC) MJD(BTDB)	$R_{\rm sec}/a$	*g'* eclipse MJD(UTC) MJD(BTDB)	$R_{\rm sec}/a$	*r'/i'/z'* eclipse MJD(UTC) MJD(BTDB)	$R_{\rm sec}/a$	Red Filter
2968	54390.1223164(75)	0.17333(35)	54390.1223205(20)	0.17411(9)	54390.1223114(72)	0.17498(30)	i'
	54390.1282892(75)		54390.1282934(20)		54390.1282842(72)		
2976	54391.1977788(64)	0.17357(54)	54391.1977839(18)	0.17402(9)	54391.1977802(57)	0.17496(34)	i'
	54391.2037850(64)		54391.2037900(18)		54391.2037864(57)		
3058	No data	No data	54402.221443(23)	0.17438(97)	54402.221379(24)	0.1739(11)	i'
	No data		54402.227684(23)		54402.227671(24)		

Table C.16: Previous eclipse times for SDSS J0303+0054. (1) Pyrzas et al. (2009).

Cycle Number	Obs[a]	Eclipse time MJD(UTC)	Eclipse time MJD(BTDB)	Uncert MJD	Ref
0	Cal	53991.11330	53991.11741	0.00020	(1)
14	Cal	53992.99498	53992.99923	0.00020	(1)
23	Cal	53994.20495	53994.20929	0.00020	(1)
44	Cal	53997.02775	53997.03229	0.00020	(1)
2559	Cal	54335.14070	54335.14302	0.00020	(1)
2589	Cal	54339.17315	54339.17583	0.00020	(1)
2960	Mer	54389.04730	54389.05324	0.00020	(1)

[a]Cal: Calar Alto Observatory, Spain. Mer: Mercator Telescope, La Palma.

Table C.17: ULTRACAM eclipse time for SDSS J1212-0123 made at the NTT.

Cycle Number	u' eclipse MJD(UTC) MJD(BTDB)	$R_{\rm sec}/a$	g' eclipse MJD(UTC) MJD(BTDB)	$R_{\rm sec}/a$	r'/i'/z' eclipse MJD(UTC) MJD(BTDB)	$R_{\rm sec}/a$	Red Filter
3593	55310.987623(22)	0.15238(33)	55310.987660(6)	0.15271(10)	55310.987653(11)	0.15215(20)	i'
	55310.993392(22)		55310.993428(6)		55310.993421(11)		

Table C.18: Previous eclipse times for SDSS J1212-0123. (1) Nebot Gómez-Morán et al. (2009).

Cycle Number	Obs[a]	Eclipse time MJD(UTC)	Eclipse time MJD(BTDB)	Uncert MJD	Ref
0	IAC	54104.2075	54104.2092	0.0021	(1)
122	IAC	54145.1802	54145.1854	0.0008	(1)
125	IAC	54146.1877	54146.1929	0.0008	(1)
205	AIP	54173.0565	54173.0628	0.0010	(1)
410	AIP	54241.9131	54241.9170	0.0021	(1)
1455	IAC	54592.8957	54592.9008	0.0014	(1)

[a]IAC: Observatorio del Teide, Spain. AIP: Astrophysical Institute Potsdam, Babelsberg, Germany.

Table C.19: ULTRACAM eclipse time for SDSS J0857+0342 made at the NTT.

Cycle Number	u' eclipse MJD(UTC) MJD(BTDB)	$R_{\rm sec}/a$	g' eclipse MJD(UTC) MJD(BTDB)	$R_{\rm sec}/a$	r'/i'/z' eclipse MJD(UTC) MJD(BTDB)	$R_{\rm sec}/a$	Red Filter
-298	55533.3108562(61)	0.16352(82)	55533.3108608(23)	0.16343(31)	55533.3108550(41)	0.16375(55)	r'
	55533.3139936(61)		55533.3139982(23)		55533.3139924(41)		
-237	55537.2813958(52)	0.16451(63)	55537.2813999(17)	0.16338(19)	55537.2814000(42)	0.16360(55)	r'
	55537.2848789(52)		55537.2848830(17)		55537.2848832(42)		
-206	55539.2992239(62)	0.16388(54)	55539.2992242(27)	0.16291(19)	55539.2992120(77)	0.16423(87)	i'
	55539.3028778(62)		55539.3028781(27)		55539.3028659(77)		
-191	55540.2755867(61)	0.16402(49)	55540.2755875(21)	0.16305(33)	55540.2755931(41)	0.16327(57)	r'
	55540.2793220(61)		55540.2793228(21)		55540.2793283(41)		
-100	55546.1989143(170)	0.16847(123)	55546.1989082(63)	0.16463(86)	55546.1989156(168)	0.16567(103)	i'
	55546.2031232(170)		55546.2031172(63)		55546.2031245(168)		
-99	55546.2639968(72)	0.16625(51)	55546.2639939(21)	0.16275(17)	55546.2639972(74)	0.16513(76)	i'
	55546.2682109(72)		55546.2682079(21)		55546.2682112(74)		
240	55568.3303204(59)	0.16525(60)	55568.3303203(20)	0.16329(10)	55568.3303190(75)	0.16307(52)	i'
	55568.3359333(59)		55568.3359332(20)		55568.3359318(75)		
269	55570.2180257(58)	0.16603(89)	55570.2180263(26)	0.16290(26)	55570.2180310(48)	0.16376(56)	r'
	55570.2237270(58)		55570.2237275(26)		55570.2237323(48)		
299	55572.1708277(65)	0.16558(76)	55572.1708432(25)	0.16265(24)	55572.1708400(44)	0.16315(55)	r'
	55572.1766145(65)		55572.1766301(25)		55572.1766268(44)		

Bibliography

Althaus, L. G., Panei, J. A., Romero, A. D., Rohrmann, R. D., Córsico, A. H., García-Berro, E., Miller Bertolami, M. M., 2009, A&A, 502, 207

Andersen, J., 1991, A&A Rev., 3, 91

Andronov, N., Pinsonneault, M., Sills, A., 2003, ApJ, 582, 358

Applegate, J. H., 1992, ApJ, 385, 621

Aungwerojwit, A., Gänsicke, B. T., Rodríguez-Gil, P., Hagen, H.-J., Giannakis, O., Papadimitriou, C., Allende Prieto, C., Engels, D., 2007, A&A, 469, 297

Baraffe, I., Chabrier, G., 1996, ApJ, 461, L51

Baraffe, I., Chabrier, G., Allard, F., Hauschildt, P. H., 1998, A&A, 337, 403

Barman, T. S., Hauschildt, P. H., Allard, F., 2004, ApJ, 614, 338

Barstow, M. A., Bond, H. E., Holberg, J. B., Burleigh, M. R., Hubeny, I., Koester, D., 2005, MNRAS, 362, 1134

Bayless, A. J., Orosz, J. A., 2006, ApJ, 651, 1155

Beatty, T. G., et al., 2007, ApJ, 663, 573

Becker, A. C., Bochanski, J. J., Hawley, S. L., Ivezić, Ž., Kowalski, A. F., Sesar, B., West, A. A., 2011, ApJ, 731, 17

Benvenuto, O. G., Althaus, L. G., 1998, MNRAS, 293, 177

Benvenuto, O. G., Althaus, L. G., 1999, MNRAS, 303, 30

Berger, D. H., et al., 2006, ApJ, 644, 475

Bergeron, P., Saffer, R. A., Liebert, J., 1992, ApJ, 394, 228

Beuermann, K., et al., 2010, A&A, 521, L60

Brinkworth, C. S., Marsh, T. R., Dhillon, V. S., Knigge, C., 2006, MNRAS, 365, 287

Brown, W. R., Kilic, M., Hermes, J. J., Allende Prieto, C., Kenyon, S. J., Winget, D. E., 2011, ApJ, 737, L23

Bruch, A., Diaz, M. P., 1998, AJ, 116, 908

Carter, J. A., et al., 2011, Science, 331, 562

Casewell, S. L., Dobbie, P. D., Napiwotzki, R., Burleigh, M. R., Barstow, M. A., Jameson, R. F., 2009, MNRAS, 395, 1795

Catalan, M. S., Davey, S. C., Sarna, M. J., Connon-Smith, R., Wood, J. H., 1994, MNRAS, 269, 879

Chabrier, G., Gallardo, J., Baraffe, I., 2007, A&A, 472, L17

Claret, A., 2000, A&A, 363, 1081

Claret, A., Bloemen, S., 2011, A&A, 529, A75

Copperwheat, C. M., Marsh, T. R., Dhillon, V. S., Littlefair, S. P., Hickman, R., Gänsicke, B. T., Southworth, J., 2010, MNRAS, 402, 1824

de Kool, M., 1992, A&A, 261, 188

de Kool, M., van den Heuvel, E. P. J., Pylyser, E., 1987, A&A, 183, 47

Debes, J. H., 2006, ApJ, 652, 636

Dekker, H., D'Odorico, S., Kaufer, A., Delabre, B., Kotzlowski, H., 2000, in Iye, M., Moorwood, A. F., eds., Society of Photo-Optical Instrumentation Engineers (SPIE) Conference Series, vol. 4008 of *Presented at the Society of Photo-Optical Instrumentation Engineers (SPIE) Conference*, p. 534

Dhillon, V. S., et al., 2007, MNRAS, 378, 825

D'Odorico, S., et al., 2006, in Proc. SPIE, vol. 6269, p. 98

Drake, A. J., et al., 2009, ApJ, 696, 870

Drake, A. J., et al., 2010, ArXiv e-prints

Driebe, T., Schoenberner, D., Bloecker, T., Herwig, F., 1998, A&A, 339, 123

Eggleton, P. P., 1983, ApJ, 268, 368

Eisenstein, D. J., et al., 2006, ApJS, 167, 40

Exter, K. M., Pollacco, D. L., Maxted, P. F. L., Napiwotzki, R., Bell, S. A., 2005, MNRAS, 359, 315

Faulkner, J., 1971, ApJ, 170, L99

Ford, E. B., 2006, ApJ, 642, 505

Ford, E. B., Joshi, K. J., Rasio, F. A., Zbarsky, B., 2000, ApJ, 528, 336

Fowler, A. M., Gatley, I., 1990, ApJ, 353, L33

Fulbright, M. S., Liebert, J., Bergeron, P., Green, R., 1993, ApJ, 406, 240

Gänsicke, B. T., Beuermann, K., de Martino, D., 1995, A&A, 303, 127

Gänsicke, B. T., et al., 2003, ApJ, 594, 443

Green, R. F., Richstone, D. O., Schmidt, M., 1978, ApJ, 224, 892

Green, R. F., Ferguson, D. H., Liebert, J., Schmidt, M., 1982, PASP, 94, 560

Green, R. F., Schmidt, M., Liebert, J., 1986, ApJS, 61, 305

Greenstein, J. L., Peterson, D. M., 1973, A&A, 25, 29

Greenstein, J. L., Trimble, V. L., 1967, ApJ, 149, 283

Grether, D., Lineweaver, C. H., 2006, ApJ, 640, 1051

Haefner, R., 1989, A&A, 213, L15

Haefner, R., Fiedler, A., Butler, K., Barwig, H., 2004, A&A, 428, 181

Hameury, J.-M., Ritter, H., 1997, A&AS, 123, 273

Han, Z., 1998, MNRAS, 296, 1019

Han, Z., Tout, C. A., Eggleton, P. P., 2000, MNRAS, 319, 215

Han, Z., Podsiadlowski, P., Maxted, P. F. L., Marsh, T. R., 2003, MNRAS, 341, 669

Han, Z., Podsiadlowski, P., Lynas-Gray, A. E., 2007, MNRAS, 380, 1098

Hawley, S. L., et al., 2002, AJ, 123, 3409

Hillenbrand, L. A., White, R. J., 2004, ApJ, 604, 741

Hils, D., Bender, P. L., Webbink, R. F., 1990, ApJ, 360, 75

Holberg, J. B., Bergeron, P., 2006, AJ, 132, 1221

Holberg, J. B., Oswalt, T. D., Barstow, M. A., 2012, AJ, 143, 68

Hook, I. M., Jørgensen, I., Allington-Smith, J. R., Davies, R. L., Metcalfe, N., Murowinski, R. G., Crampton, D., 2004, PASP, 116, 425

Hubeny, I., 1988, Comput.,Phys.,Comm., 52, 103

Hubeny, I., Lanz, T., 1995, ApJ, 439, 875

Hurley, J. R., Pols, O. R., Tout, C. A., 2000, MNRAS, 315, 543

Iben, Jr., I., 1991, ApJS, 76, 55

Iben, Jr., I., Livio, M., 1993, PASP, 105, 1373

Iben, Jr., I., Tutukov, A. V., 1984, ApJS, 54, 335

Israel, G. L., et al., 2002, A&A, 386, L13

Jeans, J. H., 1924, MNRAS, 85, 2

Joyce, R. R., 1992, in S. B. Howell, ed., Astronomical CCD Observing and Reduction Techniques, vol. 23 of *Astronomical Society of the Pacific Conference Series*, p. 258

Kawka, A., Vennes, S., Koch, R., Williams, A., 2002, AJ, 124, 2853

Kilic, M., Brown, W. R., Allende Prieto, C., Agüeros, M. A., Heinke, C., Kenyon, S. J., 2011, ApJ, 727, 3

Kilkenny, D., O'Donoghue, D., Koen, C., Stobie, R. S., Chen, A., 1997, MNRAS, 287, 867

Knigge, C., Baraffe, I., Patterson, J., 2011, ApJS, 194, 28

Koester, D., 2009, A&A, 498, 517

Koester, D., 2010, Mem. Soc. Astron. Italiana, 81, 921

Koester, D., Wilken, D., 2006, A&A, 453, 1051

Koester, D., Rollenhagen, K., Napiwotzki, R., Voss, B., Christlieb, N., Homeier, D., Reimers, D., 2005, A&A, 432, 1025

Kolb, U., Baraffe, I., 1999, MNRAS, 309, 1034

Konacki, M., Wolszczan, A., 2003, ApJ, 591, L147

Kraft, R. P., Mathews, J., Greenstein, J. L., 1962, ApJ, 136, 312

Kraus, A. L., Tucker, R. A., Thompson, M. I., Craine, E. R., Hillenbrand, L. A., 2011, ApJ, 728, 48

Krzeminski, W., 1984, IAU Circ., 4014, 4

Law, N. M., et al., 2009, PASP, 121, 1395

Law, N. M., et al., 2011, ArXiv e-prints

Lin, D. N. C., Woosley, S. E., Bodenheimer, P. H., 1991, Nature, 353, 827

Littlefair, S. P., Dhillon, V. S., Marsh, T. R., Gänsicke, B. T., Baraffe, I., Watson, C. A., 2007, MNRAS, 381, 827

Littlefair, S. P., Dhillon, V. S., Marsh, T. R., Gänsicke, B. T., Southworth, J., Baraffe, I., Watson, C. A., Copperwheat, C., 2008, MNRAS, 388, 1582

Liu, J., Han, Z., Zhang, F., Zhang, Y., 2010, ApJ, 719, 1546

López-Morales, M., 2007, ApJ, 660, 732

Lucy, L. B., 1967, ZAp, 65, 89

Luyten, W. J., 1955, in Luyten's Five Tenths. (1955), p. 1

Mamajek, E. E., Kenworthy, M. A., Hinz, P. M., Meyer, M. R., 2010, AJ, 139, 919

Marsh, T. R., 1989, PASP, 101, 1032

Marsh, T. R., 2011, Classical and Quantum Gravity, 28, 094019

Maxted, P. F. L., Marsh, T. R., Moran, C., Dhillon, V. S., Hilditch, R. W., 1998, MNRAS, 300, 1225

Maxted, P. F. L., Marsh, T. R., Morales-Rueda, L., Barstow, M. A., Dobbie, P. D., Schreiber, M. R., Dhillon, V. S., Brinkworth, C. S., 2004, MNRAS, 355, 1143

Maxted, P. F. L., Napiwotzki, R., Dobbie, P. D., Burleigh, M. R., 2006, Nature, 442, 543

Maxted, P. F. L., O'Donoghue, D., Morales-Rueda, L., Napiwotzki, R., Smalley, B., 2007, MNRAS, 376, 919

Meng, X., Chen, X., Han, Z., 2008, A&A, 487, 625

Moffat, A. F. J., 1969, A&A, 3, 455

Moorwood, A., Cuby, J.-G., Lidman, C., 1998, The Messenger, 91, 9

Morales, J. C., Ribas, I., Jordi, C., 2008, A&A, 478, 507

Morales, J. C., Gallardo, J., Ribas, I., Jordi, C., Baraffe, I., Chabrier, G., 2010, ApJ, 718, 502

Nebot Gómez-Morán, A., et al., 2009, A&A, 495, 561

Nebot Gómez-Morán, A., et al., 2011, A&A, 536, A43

Nelder, J. A., Mead, R., 1965, The Computer Journal, 7, 308

Nelemans, G., Yungelson, L. R., Portegies Zwart, S. F., 2001, A&A, 375, 890

O'Brien, M. S., Bond, H. E., Sion, E. M., 2001, ApJ, 563, 971

O'Donoghue, D., Koen, C., Kilkenny, D., Stobie, R. S., Koester, D., Bessell, M. S., Hambly, N., MacGillivray, H., 2003, MNRAS, 345, 506

Ofir, A., Gandolfi, D., Buchhave, L., Lacy, C. H. S., Hatzes, A. P., Fridlund, M., 2011, ArXiv e-prints

Panei, J. A., Althaus, L. G., Chen, X., Han, Z., 2007, MNRAS, 382, 779

Patterson, J., Thorstensen, J. R., Knigge, C., 2008, PASP, 120, 510

Peters, P. C., 1964, Physical Review, 136, 1224

Peters, P. C., Mathews, J., 1963, Physical Review, 131, 435

Pigulski, A., Michalska, G., 2002, Information Bulletin on Variable Stars, 5218, 1

Prada Moroni, P. G., Straniero, O., 2009, A&A, 507, 1575

Press, W. H., 2002, Numerical recipes in C++ : the art of scientific computing, Cambridge: University Press, 2002

Press, W. H., Flannery, B. P., Teukolsky, S. A., 1986, Numerical recipes. The art of scientific computing, Cambridge: University Press, 1986

Provencal, J. L., Shipman, H. L., Hog, E., Thejll, P., 1998, ApJ, 494, 759

Provencal, J. L., Shipman, H. L., Koester, D., Wesemael, F., Bergeron, P., 2002, ApJ, 568, 324

Pyrzas, S., et al., 2009, MNRAS, 394, 978

Pyrzas, S., et al., 2012, MNRAS, 419, 817

Qian, S., Dai, Z., Liao, W., Zhu, L., Liu, L., Zhao, E. G., 2009, ApJ, 706, L96

Qian, S., Liao, W., Zhu, L., Dai, Z., Liu, L., He, J., Zhao, E., Li, L., 2010, MNRAS, 401, L34

Rappaport, S., Verbunt, F., Joss, P. C., 1983, ApJ, 275, 713

Rebassa-Mansergas, A., Gänsicke, B. T., Rodríguez-Gil, P., Schreiber, M. R., Koester, D., 2007, MNRAS, 382, 1377

Rebassa-Mansergas, A., Gänsicke, B. T., Schreiber, M. R., Koester, D., Rodríguez-Gil, P., 2010, MNRAS, 402, 620

Rebassa-Mansergas, A., Nebot Gómez-Morán, A., Schreiber, M. R., Girven, J., Gänsicke, B. T., 2011, MNRAS, 413, 1121

Renzini, A., et al., 1996, ApJ, 465, L23

Ribas, I., 2006, Ap&SS, 304, 89

Richards, G. T., et al., 2004, ApJS, 155, 257

Ritter, H., 1986, A&A, 169, 139

Ritter, H., Schroeder, R., 1979, A&A, 76, 168

Ritter, H., Zhang, Z.-Y., Kolb, U., 2000, A&A, 360, 969

Robb, R. M., Greimel, R., 1997, Information Bulletin on Variable Stars, 4486, 1

Roelofs, G. H. A., Rau, A., Marsh, T. R., Steeghs, D., Groot, P. J., Nelemans, G., 2010, ApJ, 711, L138

Sarna, M. J., Ergma, E., Gerškevitš-Antipova, J., 2000, MNRAS, 316, 84

Savoury, C. D. J., et al., 2011, MNRAS, 415, 2025

Scalo, J., et al., 2007, Astrobiology, 7, 85

Schlegel, D. J., Finkbeiner, D. P., Davis, M., 1998, ApJ, 500, 525

Schreiber, M. R., Gänsicke, B. T., 2003, A&A, 406, 305

Schreiber, M. R., Gänsicke, B. T., Southworth, J., Schwope, A. D., Koester, D., 2008, A&A, 484, 441

Shen, K. J., Idan, I., Bildsten, L., 2009, ApJ, 705, 693

Silvestri, N. M., et al., 2006, AJ, 131, 1674

Sing, D. K., et al., 2004, AJ, 127, 2936

Sion, E. M., Greenstein, J. L., Landstreet, J. D., Liebert, J., Shipman, H. L., Wegner, G. A., 1983, ApJ, 269, 253

Sirotkin, F. V., Kim, W.-T., 2009, ApJ, 698, 715

Skrutskie, M. F., et al., 2006, AJ, 131, 1163

Smith, J. A., et al., 2002, AJ, 123, 2121

Solheim, J.-E., 2010, PASP, 122, 1133

Southworth, J., Smalley, B., Maxted, P. F. L., Claret, A., Etzel, P. B., 2005, MNRAS, 363, 529

Southworth, J., Bruntt, H., Buzasi, D. L., 2007, A&A, 467, 1215

Steele, I. A., Bates, S. D., Gibson, N., Keenan, F., Meaburn, J., Mottram, C. J., Pollacco, D., Todd, I., 2008, in Society of Photo-Optical Instrumentation Engineers (SPIE) Conference Series, vol. 7014 of *Presented at the Society of Photo-Optical Instrumentation Engineers (SPIE) Conference*

Steele, I. A., et al., 2004, in J. M. Oschmann Jr., ed., Society of Photo-Optical Instrumentation Engineers (SPIE) Conference Series, vol. 5489 of *Presented at the Society of Photo-Optical Instrumentation Engineers (SPIE) Conference*, p. 679

Steinfadt, J. D. R., Kaplan, D. L., Shporer, A., Bildsten, L., Howell, S. B., 2010, ApJ, 716, L146

Tappert, C., Gänsicke, B. T., Rebassa-Mansergas, A., Schmidtobreick, L., Schreiber, M. R., 2011, A&A, 531, A113

Tas, G., et al., 2004, Information Bulletin on Variable Stars, 5548, 1

Thorstensen, J. R., Fenton, W. H., Patterson, J. O., Kemp, J., Krajci, T., Baraffe, I., 2002, ApJ, 567, L49

Torres, G., 2007, ApJ, 671, L65

Torres, G., Andersen, J., Giménez, A., 2010, A&A Rev., 18, 67

Trümper, J., 1982, Advances in Space Research, 2, 241

Uthas, H., Knigge, C., Long, K. S., Patterson, J., Thorstensen, J., 2011, MNRAS, 414, L85

van den Besselaar, E. J. M., et al., 2007, A&A, 466, 1031

Vennes, S., Thorstensen, J. R., 1994, AJ, 108, 1881

Vennes, S., Kawka, A., Németh, P., 2011a, MNRAS, 413, 2545

Vennes, S., et al., 2011b, ApJ, 737, L16

Verbunt, F., Rappaport, S., 1988, ApJ, 332, 193

Verbunt, F., Zwaan, C., 1981, A&A, 100, L7

Voges, W., et al., 1999, A&A, 349, 389

Wade, R. A., Horne, K., 1988, ApJ, 324, 411

Warner, B., 1995, Cambridge Astrophysics Series, 28

Watson, C. A., Dhillon, V. S., 2004, MNRAS, 351, 110

Watson, C. A., Marsh, T. R., 2010, MNRAS, 405, 2037

Webbink, R. F., 1984, ApJ, 277, 355

West, A. A., Walkowicz, L. M., Hawley, S. L., 2005, PASP, 117, 706

Willems, B., Kolb, U., 2004, A&A, 419, 1057

Wood, J. H., Marsh, T. R., 1991, ApJ, 381, 551

Wood, M. A., 1992, ApJ, 386, 539

York, D. G., et al., 2000, AJ, 120, 1579

Yu, S., Jeffery, C. S., 2010, A&A, 521, A85

Zorotovic, M., Schreiber, M. R., Gänsicke, B. T., Nebot Gómez-Morán, A., 2010, A&A, 520, A86

Zuckerman, B., Koester, D., Reid, I. N., Hünsch, M., 2003, ApJ, 596, 477